

**Energy Dependence Analysis of Neutrino-Nucleus  
Interactions in Scintillator for MINERvA**

**A THESIS  
SUBMITTED TO THE FACULTY OF THE GRADUATE SCHOOL  
OF THE UNIVERSITY OF MINNESOTA  
BY**

**Asit Srivastava**

**IN PARTIAL FULFILLMENT OF THE REQUIREMENTS  
FOR THE DEGREE OF  
MASTER OF SCIENCE**

**Dr. Richard Gran**

**June, 2023**

© Asit Srivastava 2023  
ALL RIGHTS RESERVED

# Acknowledgements

There are many people that have earned my gratitude for their contribution to my time in graduate school. First of all, I would like to thank my graduate advisor Dr. Richard Gran who helped me a lot during the last two years and guided through every step of both academics and research. I also thank MINERvA colleagues for their invaluable input on my work. I would also like to thank the committee members, Dr. Alec Habig and Dr. Marshall Hampton, for their time. I thank my parents for their constant support and motivation.

I thank the National Science Foundation for research assistantship and travel support from grant #2013217. I also thank Mylan and Kathy Radulovich for the Mylan Radulovich Physics Fellowship that was awarded to me to do summer research.

## Abstract

This thesis is on the intrinsic energy dependence in neutrino-nucleus interaction models, especially quasielastic scattering and 2p2h process, and the implications for understanding data from MINERvA, NOvA, and DUNE. Neutrino-nucleus interactions are modeled using five structure functions,  $W_1$ ,  $W_2$ ,  $W_3$ ,  $W_4$  and  $W_5$ , and each structure function contributes differently to the energy dependence once it enters the cross-section calculations. The energy independent term in the calculations contains only  $W_2$  and the next lower order term (of the order  $1/E$ ) contains  $W_3$  also. In this thesis, we show that  $W_2$  is good enough to describe MINERvA data and energy dependence coming from the cross-section directly is small. However,  $W_3$  will be significant for lower energy experiments such as NOvA and DUNE (especially at and below the oscillation maximum). We have also developed a method to extract structure functions directly from MINERvA data though we find that systematic uncertainties present in the data are too big to successfully determine  $1/E$  Term. In addition to this, we have applied muon angle cuts on MINERvA data and MC, which have their own energy dependent effects. An apparent energy dependent discrepancy comes from known shortcomings especially in the pion production model. Finally, because the energy dependence analysis has similarities to the low- $\nu$  method, we have evaluated discrepancies between the data and MC in light of different flux constraint techniques. The results suggest including MINERvA's low- $\nu$  method constraint is an improvement.

# Contents

<b>Acknowledgements</b>	<b>i</b>
<b>Abstract</b>	<b>ii</b>
<b>List of Tables</b>	<b>viii</b>
<b>List of Figures</b>	<b>x</b>
<b>1 Introduction</b>	<b>1</b>
1.1 Standard Model and Types of Neutrinos . . . . .	2
1.2 Definitions of energy transfer and momentum transfer . . . . .	5
1.3 Different types of neutrino-nucleus interactions . . . . .	8
1.3.1 Triangle Diagram . . . . .	8
1.3.2 Quasielastic scattering (QE) . . . . .	10
1.3.3 Delta Resonance and Other Resonances . . . . .	10
1.3.4 Two-particle two-hole (2p2h) Process . . . . .	12
1.3.5 Deep and Shallow Inelastic Scattering (DIS and SIS) . . . . .	13
1.3.6 Coherent Pion Production . . . . .	14
1.4 Introduction to MINERvA Detector . . . . .	15
1.4.1 MINERvA neutrino beam flux . . . . .	16
1.4.2 MINERvA Detector . . . . .	17
1.5 Selection Cuts, Neutrino Flux, Nuclear Effects and Modeling in MINERvA	19
1.5.1 Muon Reconstruction and its limitations . . . . .	19
1.5.2 $\nu - e$ scattering constrained flux is the MINERvA's default flux .	20
1.5.3 Neutrino Event Generators and Nuclear Effects . . . . .	21

1.5.4	Modeling of various neutrino-nucleus interactions in GENIE and MINERvA tunings . . . . .	25
1.6	Prior Work . . . . .	26
<b>2</b>	<b>An Introduction to Structure Functions and their Analysis for QE and 2p2h Process</b>	<b>27</b>
2.1	Introduction to Form Factors . . . . .	29
2.1.1	Introduction to Structure Functions and their energy dependence	31
2.1.2	Llewelyn Smith Model for QE Scattering and Comparison of Form Factors and Structure Functions . . . . .	34
2.2	Analysis of QE structure functions . . . . .	37
2.2.1	Structure Functions in 1D . . . . .	38
2.2.2	Ratios across different energies . . . . .	43
2.2.3	Fractional Contribution of Different Structure Functions in Total Cross-Section . . . . .	46
2.2.4	Structure Functions in 2D . . . . .	51
2.2.5	Ratio of structure functions indicating the energy dependence introduced by RPA . . . . .	54
2.2.6	Energy Dependence coming from RPA and its uniformity across different structure functions . . . . .	57
2.2.7	Fractional Contribution of Structure Functions . . . . .	62
2.3	Analysis of 2p2h Structure Functions . . . . .	66
2.3.1	Structure Functions . . . . .	67
2.3.2	pn and nn contribution in $wv2$ and total cross-section . . . . .	70
2.3.3	Fractional Contribution of Structure Functions . . . . .	73
<b>3</b>	<b>Extraction of Structure Functions from MINERvA MC and Data</b>	<b>78</b>
3.1	Description of the method . . . . .	79
3.2	Differences between Valencia MC and MINERvA MC leading to efficiency correction . . . . .	82
3.3	Extraction from MINERvA MC and Data . . . . .	86
3.4	Are the values after convergence correct? Sensitivity of $1/E$ Coeff. necessitates smaller uncertainties . . . . .	90

<b>4</b>	<b>Muon Angle Analysis and Energy Dependence</b>	<b>93</b>
4.1	Parallel/Longitudinal and Perpendicular Momentum of a Muon . . . . .	94
4.1.1	Expressions for the muon's momentum parallel and transverse to that of the neutrino . . . . .	94
4.1.2	Range of $Q^2$ and $q_3$ . . . . .	95
4.1.3	Variation of $p_{\perp}$ with $q_3$ and $q_0$ . . . . .	97
4.2	Behaviour of $\theta_{\mu}$ with variation of $q_3$ , $q_0$ and $E_{\nu}$ . . . . .	98
4.2.1	Behaviour of $\theta_{\mu}$ with variation in $q_3$ keeping $q_0$ and $E_{\nu}$ fixed . .	98
4.2.2	Behaviour of $\theta_{\mu}$ with variation in $q_0$ keeping $q_3$ and $E_{\nu}$ fixed . .	98
4.2.3	Behaviour of $\theta_{\mu}$ with variation in $E_{\nu}$ keeping $q_0$ and $q_3$ fixed . .	100
4.3	Ineffective angle cuts . . . . .	101
4.4	Energy Dependence Discrepancies when Muon Angle Cuts are applied .	102
4.4.1	Method to test whether energy dependence in data is well-modeled or not . . . . .	103
4.4.2	Smaller angle cuts introduce an additional energy dependence . .	105
4.5	Changing QE axial mass ( $M_A$ ) and RPA effect . . . . .	107
4.5.1	Comparison between the effect of $M_A = 1.08$ GeV and $M_A = 1.24$ GeV on the plot with MINERvA Default $M_A = 0.99$ GeV . . . .	108
4.5.2	Comparison between the effect of $M_A = 1.24$ GeV and RPA ef- fect ( $1\sigma$ away from nominal) on the plot with MINERvA Default $M_A = 0.99$ GeV and nominal RPA . . . . .	110
4.5.3	Varying $M_A$ and RPA effect to observe their effect on the energy dependence discrepancy . . . . .	113
<b>5</b>	<b>Neutrino Flux Analysis</b>	<b>116</b>
5.1	Neutrino Flux Measuring Techniques . . . . .	116
5.2	Rob Fine's Low- $\nu$ Flux and its Analysis . . . . .	119
5.2.1	Angle Acceptance showing up in the data/MC ratio . . . . .	123
5.2.2	Cross-section analysis for the observations of the data/MC ratio	124
5.2.3	Application of low- $\nu$ flux to energy dependence discrepancies . .	126
<b>6</b>	<b>Outer Detector (OD) Analysis</b>	<b>130</b>
6.1	Effect of OD Cuts on Energy Dependence Discrepancy . . . . .	131

6.2	Scanning of Highly Energetic $\pi^+$ entering the Outer Detector . . . . .	133
6.2.1	Scanning results showing that Highly Energetic $\pi^+$ might be over-estimated in MC and/or Highly Energetic Neutral Particles might be underestimated in MC . . . . .	135
6.2.2	Confirming that highly energetic $\pi^+$ are oversimulated and highly energetic neutral particles are well-modeled . . . . .	137
<b>7</b>	<b>Pion Kinetic Energy based Reweighting</b>	<b>141</b>
7.1	Reweighting events in MC based on the kinetic energy of pions . . . . .	141
7.2	Final State Interactions of a $\pi^+$ . . . . .	143
7.3	Determining that FSI of $\pi^+$ is not a major source of the discrepancy . . . . .	148
7.3.1	Breakdown of $\pi^+$ FSI into individual modes for MidEnu and HighEnu separately . . . . .	148
7.3.2	Reweighting events based on individual FSI fates . . . . .	151
7.4	Explanation of why the ratio HighEnu(MC)/MidEnu(MC) goes up when High KE $\pi^+$ events are reweighted . . . . .	153
7.5	Reweighting both Low and High KE $\pi^+$ . . . . .	154
7.6	Application of $\pi^+$ KE reweight to smaller muon angle cuts . . . . .	158
7.6.1	Effect of $\pi^+$ reweight on energy dependence discrepancies present in High $q_3$ range and smaller angle cuts . . . . .	158
7.6.2	Effect of $\pi^+$ reweight on energy dependence discrepancies present in Mid $q_3$ range and smaller angle cuts . . . . .	160
7.7	Delta resonance as the major source of pion production . . . . .	162
<b>8</b>	<b>Conclusion and Discussion</b>	<b>168</b>
	<b>References</b>	<b>170</b>
	<b>Appendix A. Individual Terms of Different Orders of Neutrino Energy in QE Scattering and 2p2h Process</b>	<b>179</b>
A.1	Individual energy terms of $ww2$ and $ww3$ in QE scattering . . . . .	180
A.2	Individual energy terms of $ww2$ and $ww3$ in 2p2h process . . . . .	181

Appendix B. Non-unique Convergence in the Extraction of $En$ . <i>Ind.</i> <i>Term</i> and $1/E$ <i>Coeff.</i>	184
Appendix C. Derivation of the relation between $Q^2$ , $E_\nu$ , $E_\mu$ , $p_\mu$ and $\theta_\mu$	188
Appendix D. Parametrization of Rob Fine's low- $\nu$ flux	190
Appendix E. Energy dependence discrepancy corresponding to muon angle cut 6 to 8 degrees reduced by reweighting $\pi^+$	192

# List of Tables

2.1	Fractional contribution of different structure functions in total cross-section for 3 GeV and 5 GeV neutrinos for different values of $Q^2$ (in $\text{GeV}^2$ ) . . . . .	48
2.2	Fractional contribution of all the structure functions in total cross section for 3 GeV and 5 GeV neutrinos as $Q^2 \rightarrow 0$ . . . . .	49
3.1	Flux in each bin in the energy range 5-7 GeV . . . . .	81
3.2	<i>En. Ind. Term</i> obtained from Valencia code for QE scattering and 2p2h process expressed per neutron corresponding to 3 GeV neutrinos for Low $q_3$ , Mid $q_3$ and High $q_3$ in the unit $10^{-39} \text{ cm}^2$ . . . . .	83
3.3	<i>1/E Coeff.</i> obtained from Valencia Code for QE Scattering and 2p2h Process expressed per neutron corresponding to 3 GeV neutrinos for Low $q_3$ , Mid $q_3$ and High $q_3$ in the unit $10^{-39} \text{ cm}^2\text{-GeV}$ . . . . .	83
3.4	<i>En. Ind. Term</i> and <i>1/E Coeff.</i> for both MINERvA MC and data for Low $q_3$ in the units $10^{-39} \text{ cm}^2$ and $10^{-39} \text{ cm}^2\text{-GeV}$ respectively . . . . .	86
3.5	<i>En. Ind. Term</i> and <i>1/E Coeff.</i> for both MINERvA MC and data for Mid $q_3$ in the units $10^{-39} \text{ cm}^2$ and $10^{-39} \text{ cm}^2\text{-GeV}$ respectively . . . . .	86
3.6	<i>En. Ind. Term</i> and <i>1/E Coeff.</i> for both MINERvA MC and data for High $q_3$ in the units $10^{-39} \text{ cm}^2$ and $10^{-39} \text{ cm}^2\text{-GeV}$ respectively . . . . .	87
3.7	<i>En. Ind. Term</i> and <i>1/E Coeff.</i> for both MINERvA MC and data for Low $q_3$ in the units $10^{-39} \text{ cm}^2$ and $10^{-39} \text{ cm}^2\text{-GeV}$ respectively after reweighting the number of events . . . . .	89
3.8	<i>En. Ind. Term</i> and <i>1/E Coeff.</i> for both MINERvA MC and data for Mid $q_3$ in the units $10^{-39} \text{ cm}^2$ and $10^{-39} \text{ cm}^2\text{-GeV}$ respectively after reweighting the number of events . . . . .	89

3.9	<i>En. Ind. Term</i> and <i>1/E Coeff.</i> for both MINERvA MC and data for High $q_3$ in the units $10^{-39}$ cm <sup>2</sup> and $10^{-39}$ cm <sup>2</sup> -GeV respectively after reweighting the number of events . . . . .	90
4.1	Range of $Q^2$ (in $GeV^2$ ) for $q_0 = 0.8$ $GeV$ . . . . .	96
4.2	Range of $q_3$ (in $GeV$ ) for $q_0 = 0.8$ $GeV$ . . . . .	96
4.3	Maximum angle in an energy range and $q_3$ range, and the corresponding ineffective angle cuts . . . . .	102
5.1	Comparison of <i>1/E Coeff.</i> and <i>1/E Term</i> at 3 GeV with <i>En. Ind. Term</i> for Low $q_3$ , Mid $q_3$ and High $q_3$ . . . . .	125
6.1	Scanning result of 350 events each for events with outer detector energy greater than 100 MeV for the presence of a charged hadron in OD . . .	136
6.2	Percentage of events with outer detector energy greater than 100 MeV and having a neutral particle in OD by subtraction . . . . .	137
6.3	Total number of events (POT-normalized) in the scanning region . . . .	137
6.4	Number of events with charged hadrons or neutral particles in OD having outer detector energy greater than 100 MeV in the scanning region . . .	138
6.5	Comparison of number of events between Data and MC . . . . .	138
7.1	Variation of energy transfer with a change in muon angle corresponding to High $q_3$ for MidEnu and HighEnu represented by 6 GeV and 10 GeV respectively . . . . .	154
7.2	Various interactions producing High KE $\pi^+$ in the discrepancy region $0.2$ GeV $\leq$ energy in tracker $\leq 0.3$ GeV and muon angle cut of 0 to 5 degrees corresponding to MidEnu and HighEnu for High $q_3$ range . . . .	164

# List of Figures

1.1	Standard Model of Elementary particles . . . . .	3
1.2	Feynman diagram of quasielastic scattering . . . . .	5
1.3	Separate Triangle diagrams with two independent quantities, $W$ and $Q^2$ . . . . .	9
1.4	Feynman diagram of quasielastic scattering . . . . .	10
1.5	Feynman diagram of delta resonance . . . . .	11
1.6	Feynman diagram of 2p2h process on np pair, where proton is the spectator nucleon. A variant happens when the spectator nucleon is a neutron. . . . .	13
1.7	Feynman diagram of deep inelastic scattering . . . . .	14
1.8	Feynman diagram of coherent pion production . . . . .	15
1.9	NuMI beamline at Fermilab used to generate a neutrino beam that enters the MINERvA detector (not shown) located a few tens of meters downstream of the final muon monitor . . . . .	16
1.10	Front and Elevation View of MINERvA Detector . . . . .	17
1.11	Default MINERvA flux before applying neutrino-electron scattering constraints . . . . .	21
2.1	An incident particle beam traveling in the differential area ( $d\sigma$ ) scatters in the differential angle ( $d\theta$ ) . . . . .	28
2.2	Double differential cross-section depicting Fermi motion when a neutrino undergoes QE scattering with a nucleon . . . . .	39
2.3	Single-differential cross-section per nucleus goes to zero around $Q^2 = 6.53$ GeV <sup>2</sup> for 3 GeV neutrino . . . . .	40
2.4	Structure functions (wint's) for 3 GeV neutrinos. The cross section is the simple sum of the five panels, where $W_2$ is by far the largest at this energy. . . . .	42

2.5	Ratio of structure function contributions 5 GeV / 3 GeV. The ratios are 1.0, 0.6, and 0.36 until about $Q^2 = 4 \text{ GeV}^2$ when the ratio is affected by the kinematic boundary visible in the 2D plots in the earlier figure. . . .	44
2.6	Ratio of $d\sigma/dQ^2$ for 5 GeV/3 GeV neutrinos drops by about 6% in the range $Q^2 < 1.5 \text{ GeV}^2$ . . . . .	45
2.7	The first three structure functions and the total cross-section for 3 GeV and 5 GeV neutrinos . . . . .	47
2.8	Fractional contribution of the first three structure functions in the total cross-section for 3 and 5 GeV neutrinos . . . . .	47
2.9	Fractional contribution of the fourth and fifth structure functions in the total cross-section for 3 and 5 GeV neutrinos . . . . .	49
2.10	Ratio of contribution of the fifth (scaled by -1) and the second structure functions in the total cross-section for 3 and 5 GeV neutrinos . . . . .	51
2.11	The first three structure function terms for 3 GeV neutrinos . . . . .	52
2.12	Energy Independent Term and $1/E$ Term for 3 GeV neutrinos . . . . .	53
2.13	Ratio of structure function contributions 5 GeV / 3 GeV. The ratios show a slight variation from their constant values of 0.36 and 0.6, and a slight variation along the $q_3$ -axis. . . . .	56
2.14	Single differential cross-section comparison of free nucleon (times 6), carbon nucleus ( $^{12}C$ ) with RPA OFF and RPA ON . . . . .	57
2.15	Ratio of structure functions between 5 GeV and 3 GeV neutrinos with RPA OFF. The gradient has disappeared in the ratios of $ww1$ , $ww4$ and $ww5$ . The ratios of $ww2$ and $ww3$ are also no longer varying with $q_3$ . . .	59
2.16	Ratio of structure functions between RPA ON and RPA OFF at 3 GeV	61
2.17	Comparison of the effect of RPA across $ww2$ and $ww3$ for 3 GeV . . . .	62
2.18	Fractional contribution of structure functions in total cross section (totalXS) of QE scattering for 3 GeV and 5 GeV neutrinos. Caution, the color scale changes from plot to plot, so blue to red in one plot shows the trend but are not the same values as in another plot. . . . .	64

2.19	Fractional contribution of Energy Independent Term and $1/E$ Term for 3 GeV and 5 GeV neutrinos. The middle plot is zoomed in on the lowest $q_3$ , and here $1/E$ Term goes negative, so the plotting package colors all the zero values blue in that case. . . . .	65
2.20	The first three structure function terms for 3 GeV neutrinos . . . . .	68
2.21	Energy Independent Term and $1/E$ Term for 3 GeV neutrinos. As with other 2D plots, the plot on the right has substantial negative components, and the graphic program displays 0.0 as an orange color instead of white. . . . .	69
2.22	Breakdown of $ww2$ into $ww2pn$ and $ww2nn$ for 3 GeV neutrinos . . . . .	71
2.23	Fractional contribution of $ww2pn$ and $ww2nn$ in totalXS (pn + nn) for 3 GeV neutrinos . . . . .	72
2.24	Fractional contribution of pn (total) and nn (total) in totalXS (pn + nn) for 3 GeV neutrinos . . . . .	73
2.25	Fractional contribution of structure functions in total cross section (totalXS) for 2p2h process corresponding to 3 GeV and 5 GeV neutrinos . . . . .	74
2.26	Fractional contribution of Energy Independent Term and $1/E$ Term for 3 GeV and 5 GeV neutrinos. The right plot has negative values along the diagonal, and the value zero is represented by orange rather than white. . . . .	76
3.1	Efficiency for antineutrino interactions as a function of antimuon angle . . . . .	85
4.1	Muon angle first increases and then decreases with an increase in energy transfer. The lower plots zoom in on the details and have different vertical scales. . . . .	100
4.2	Plots of the ratios HighEnu/MidEnu and MidEnu/Low Enu for three different ranges of $q_3$ with the default muon angle cut of 20 deg. . . . .	104
4.3	Plots of the ratios HighEnu/MidEnu High $q_3$ with the angle cut of 0 to 10 degrees, 0 to 5 degrees and 5 to 10 degrees. There is a large energy dependence discrepancy in the middle plot. . . . .	106
4.4	Plots of HighEnu for High $q_3$ and muon angle cut 0 to 10 degrees to draw a comparison between three different quasielastic axial masses . . . . .	109
4.5	Plots of MidEnu for High $q_3$ and muon angle cut 0 to 10 degrees to draw a comparison between three different quasielastic axial masses . . . . .	109

4.6	Increasing $M_A$ brings the data/MC down by the largest amount in High $q_3$ . Reducing RPA brings the data/MC down by the largest amount in Low $q_3$ . Plots are of HighEnu High $q_3$ , Mid $q_3$ and Low $q_3$ with a muon angle cut of 0 to 10 degrees. . . . .	111
4.7	Increasing $M_A$ brings the data/MC down by the largest amount in High $q_3$ . Reducing RPA brings the data/MC down by the largest amount in Low $q_3$ . Plots are of MidEnu High $q_3$ , Mid $q_3$ and Low $q_3$ with a muon angle cut of 0 to 10 degrees. . . . .	112
4.8	Plots of HighEnu and MidEnu in High $q_3$ range when a muon angle cut of 0 to 5 degrees is applied showing that the discrepancy region is populated by QE events only in HighEnu. QE events do not pass the angle cut in MidEnu . . . . .	114
4.9	Plots of HighEnu and MidEnu in High $q_3$ range when a muon angle cut of 0 to 5 degrees is applied showing that the discrepancy region is reduced by a small amount when the $M_A$ and RPA effect in QE are changed . .	115
5.1	Rob Fine's low- $\nu$ flux estimate expressed as a ratio of low- $\nu$ flux to the MINERvA's default $\nu - e$ scattering flux . . . . .	119
5.2	Rob Fine's low- $\nu$ flux parametrization . . . . .	120
5.3	Comparison of data and MC for two different fluxes by dividing three-momentum transfer into three different ranges . . . . .	122
5.4	Energy dependence discrepancy present corresponding to MidEnu and HighEnu in High $q_3$ range for muon angle cuts 0 to 2 deg. and 2 to 4 deg.	128
5.5	Rob Fine's low- $\nu$ flux to analyze the energy dependence discrepancy present corresponding to MidEnu and HighEnu in High $q_3$ range for muon angle cuts 0 to 2 deg. and 2 to 4 deg. . . . .	129
6.1	Energy dependence discrepancy corresponding to HighEnu and MidEnu in High $q_3$ range with muon angle cut of 0 to 5 degrees . . . . .	131
6.2	Plots of HighEnu and MidEnu in High $q_3$ range with muon angle cut 0 to 5 degrees and OD events cut above the OD energy mentioned . . . .	132
6.3	Plots of HighEnu and MidEnu in High $q_3$ range with muon angle cut 0 to 5 degrees and OD events cut above and below 100 MeV respectively .	133

6.4	An example of overlay, neutron and pion in Outer Detector as viewed in Arachne . . . . .	135
6.5	Plots of MidEnu and HighEnu in High $q_3$ range with muon angle cut 0 to 5 degrees depicting the contribution of individual processes (QE, Delta Resonance, 2p2h, SIS) when cuts are applied for outer detector energies	139
6.6	Plots of HighEnu and MidEnu in High $q_3$ range with muon angle cut 0 to 5 degrees and no OD cut with events reweighted by 0.5 remain unchanged if maximum neutron kinetic energy is greater than a certain minimum energy . . . . .	140
7.1	Differential cross-section with respect to pion KE is represented by solid point. Its comparison with different versions of GENIE, NEUT and GiBUU shows that none of them define the data perfectly. . . . .	142
7.2	Plots of MidEnu and HighEnu in High $q_3$ range with muon angle cut of 0 to 5 degrees (no OD cut) are reweighted if the kinetic energy of the most energetic pion in the final state is greater than 150 MeV. . . . .	143
7.3	Plots of MidEnu and HighEnu in High $q_3$ range with muon angle cut 0 to 5 degrees and OD cuts broken down into $\pi^+$ fates . . . . .	146
7.4	Plots of ME and HE High $q_3$ with muon angle cut 0 to 5 degrees and OD cuts broken down into $\pi^+$ fates such that a $\pi^+$ is in the final state. . . .	147
7.5	Plots of MidEnu and HighEnu in High $q_3$ range with muon angle cut 0 to 5 degrees and no OD cuts broken down into $\pi^+$ fates such that the events with the most energetic $\pi^+$ having kinetic energy greater than 150 MeV are reweighted by 50% . . . . .	149
7.6	Plots of MidEnu and HighEnu in High $q_3$ range with muon angle cut 0 to 5 degrees and no OD cuts broken down into $\pi^+$ fates as a function of the kinetic energy of the most energetic $\pi^+$ . . . . .	150
7.7	Plots of MidEnu and HighEnu in High $q_3$ range with muon angle cut 0 to 5 degrees with different processes reweighted by 50% if the kinetic energy of the most energetic $\pi^+$ is greater than 150 MeV . . . . .	152
7.8	Plots of MidEnu and HighEnu in High $q_3$ range with muon angle cut of 0 to 5 degrees with Low KE $\pi^+$ (KE < 100 MeV) reweighted by 1.5 and/or High KE $\pi^+$ (KE > 150 MeV) reweighted by 0.5 . . . . .	155

7.9	Double Ratio Plot for MidEnu and HighEnu in High $q_3$ range with muon angle cut of 0 to 5 degrees with Low KE $\pi^+$ (KE < 100 MeV) reweighted by 1.5 and/or High KE $\pi^+$ (KE > 150 MeV) reweighted by 0.5 . . . . .	157
7.10	Discrepancies present in smaller muon angle cuts for MidEnu and HighEnu in High $q_3$ range, and their reduction after reweighting only High KE $\pi^+$ and both Low and High KE $\pi^+$ . . . . .	159
7.11	Plots of MidEnu and HighEnu in Mid $q_3$ range with muon angle cut of 0 to 5 degrees with High KE $\pi^+$ , and both Low KE and High KE $\pi^+$ reweighted . . . . .	160
7.12	Discrepancies present in smaller muon angle cuts for MidEnu and HighEnu in Mid $q_3$ range, and their reduction after reweighting only High KE $\pi^+$ and both Low and High KE $\pi^+$ . . . . .	161
7.13	MidEnu and HighEnu in High $q_3$ range with muon angle cut of 0 to 5 degrees depicting the contribution of various neutrino-nucleus interactions	163
7.14	MidEnu and HighEnu in Mid $q_3$ range with muon angle cut of 0 to 5 degrees depicting the contribution of various neutrino-nucleus interactions	163
7.15	Plot of MidEnu and HighEnu in High $q_3$ range with muon angle cut of 0 to 5 degrees with delta resonance reweighted by 50% if it produces a $\pi^+$ with KE > 150 MeV compared with the default discrepancy plot and all events reweighted plot . . . . .	165
7.16	Plot of MidEnu and HighEnu in High $q_3$ range with muon angle cut of 0 to 5 degrees with all resonances reweighted by 50% if it produces a $\pi^+$ with KE > 150 MeV compared with the default discrepancy plot and all events reweighted plot . . . . .	166
A.1	Terms of different orders of neutrino energy present in $ww2$ for QE scattering . . . . .	180
A.2	Terms of different orders of neutrino energy present in $ww3$ for QE scattering . . . . .	181
A.3	Terms of different orders of neutrino energy present in $ww2$ for 2p2h process	182
A.4	Terms of different orders of neutrino energy present in $ww3$ for 2p2h process	183

E.1	Plots of LowE <sub>nu</sub> and MidE <sub>nu</sub> in High $q_3$ range with muon angle cut of 6 to 8 degrees comparing the reweight of only High KE $\pi^+$ and both Low and High KE $\pi^+$ with the plot having default pion weight . . . . .	193
E.2	Plots of LowE <sub>nu</sub> and MidE <sub>nu</sub> in Mid $q_3$ range with muon angle cut of 6 to 8 degrees comparing the reweight of only High KE $\pi^+$ and both Low and High KE $\pi^+$ with the plot having default pion weight . . . . .	193

# Chapter 1

## Introduction

This work is on the energy dependence of neutrino-nucleus interactions at low three-momentum transfer. It starts with defining the meaning of an interaction cross-section and how it can be expressed in terms of structure functions. These structure functions have various orders of energy dependence attached and this energy dependence can be easily studied for quasielastic scattering and 2p2h process. The Valencia group has a widely used model for these two processes and we are able to run their code and extract the corresponding structure functions. There are six structure functions in total and five of them enter into the expression of cross-section for a neutrino-nucleus interaction. It will be shown in Chapter 2 that the second structure function is a large enough fraction of the total to describe MINERvA data and the third structure function gains importance in lower energy experiments.

These structure functions can be extracted from the MINERvA data directly. Exploring how to do this required several interrelated studies that are the second half of the thesis and are presented one per chapter. Chapter 3 describes the method to do the extraction and also discusses its limitations due to uncertainties present in experimental data. Charged-current neutrino-nucleus interactions which form a core of this work always produce a muon and this muon can travel at any angle with respect to the neutrino beam but the MINERvA experiment accepts muons up to only 20 degrees. The analysis of muon angle and how this angle is tied to the energy dependence of a neutrino-nucleus interaction is discussed in Chapter 4. The default flux of MINERvA

was obtained using a beam simulation and improved using  $\nu - e$  scattering constraints. Chapter 5 discusses the implications of flux obtained by low- $\nu$  technique and compares it with the default flux and finds that the expression of Low  $q_3$  data in this thesis is consistent with the low- $\nu$  constrained flux. As mentioned before, muon angle is tied to the energy dependence. Thus, applying muon angle cuts, which means selecting muons traveling at an angle in a specific range, can be instrumental in studying whether energy dependence is well-modeled or not. Although it is well-modeled for a wide range of neutrino energies, there are some specific muon angle cuts which reveal a discrepancy in energy dependence between MINERvA data and Monte Carlo (MC) simulations. Outer Detector Analysis discussed in Chapter 6 shows that highly energetic pions are somewhat responsible for this discrepancy. Chapter 7 takes this one step further and investigates how much low energy pions contribute to this discrepancy. Chapter 8 wraps up the thesis with conclusion and discussion.

## 1.1 Standard Model and Types of Neutrinos

The world is made up of particles and particles interact with each other via four fundamental forces: gravity, electromagnetic interaction, strong interaction and weak interaction. Each force is mediated by a different kind of particle.

According to quantum field theory, every particle is an excitation of a quantum field pervading the universe. So, particle physics experts are extra careful in using the word “particles”. However, for the purpose of this thesis, a particle is simply a fundamental entity in the universe. Particles can be created, and they propagate relativistically through physical media, decay, and interact with other particles, electrons, and nuclei. From the perspective of this thesis, the clue that they are not classical billiard ball objects is that their interactions are probabilistic rather than deterministic.

Now, every particle carries some parameters to define it. Some of them are mass, electric charge, color charge, spin and isospin. The classical analogue of spin is the number of rotations a particle must make about its axis before it looks the same again. A particle of spin  $1/2$  such as an electron has to make 2 complete rotations while a particle

of spin 1 has to make only one rotation. Spin-based categorization divides particles into bosons (particles with integer spins) such as pions, kaons and photons, and fermions (particles with half-integer spins) such as quarks, protons, neutrons, electrons, muons and neutrinos.

The other classification is based on whether they interact via strong interaction or not. If they do, they are called hadrons and if they don't, they are called leptons. Before going further, it is helpful to include the following picture for an easier explanation. It is taken from Wikipedia [1].

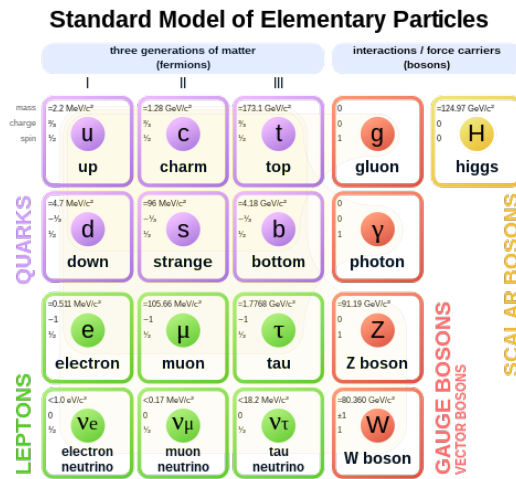


Figure 1.1: Standard Model of Elementary particles

The figure classifies particles into matter particles and force carriers. The matter particles are further divided into quarks which are combined into hadrons and leptons which have no substructure.

Neutrinos are leptons, which means that they do not interact via strong interaction. They are almost massless and the only possible form of interaction for them is weak interaction mediated by W and Z bosons. There are three kinds of neutrinos: electron neutrino, muon neutrino and tau neutrino. Each type of neutrino and its associated charged lepton within a single generation form a pair. Muon neutrino pairs with muon

and this pair of leptons is the most important lepton pair in this thesis.

The other kind of fundamental particles are quarks. Quarks make up protons and neutrons, which further make up a nucleus. Protons and neutrons are also called nucleons as they are found inside a nucleus. They can interact via all four fundamental interactions. Particles consisting of quarks are called hadrons. The terms “baryons” and “mesons” are used at a few places in this thesis. Baryons are the particles made up of three quarks such as protons, neutrons and delta baryons. Mesons are made up of one quark and one antiquark such as pions and kaons.

Standard Model has been successful in explaining a lot of experimental results and has also made predictions that were further verified by experiments. However, recent observations such as neutrino oscillations are beyond the Standard Model. The original Standard Model had neutrinos but they were supposed to be massless. Another missing theory in Standard Model is that of gravity. Physicists are still trying to unify gravity with other fundamental forces. Theories like String Theory boast of this unification but there is no experimental evidence of String Theory. Standard Model also does not include dark matter and dark energy, which cosmologists propose make up 95% of our universe. Possibly involving additional particles or force carriers, searches for dark matter and dark energy are still going on. Understanding neutrino interactions are also important to constrain backgrounds for dark matter experiments.

Some of the other important applications of neutrino study are

- Explanation of matter-antimatter asymmetry: A hypothesis is that when Big Bang happened, equal amount of matter and antimatter was created. However, our universe consists of mostly matter. This asymmetry has a connection to neutrino and antineutrino oscillations. Neutrino experiments are trying to find out if neutrino and antineutrino oscillate at a different rate. If they do oscillate at a different rate, which is technically called CP violation, it can be a key to understanding the matter-antimatter asymmetry [2].
- Elements in the universe: A heavy star ends its life in a supernova, releasing much

of its gravitational energy in the form of neutrinos. They are detected before the optical light, and in addition to being the early warning, they carry information about the supernova collapse mechanisms and heavy element formation [3].

- Cosmic Neutrino Background ( $C\nu B$ ):  $C\nu B$  is the universe's background radiation which separated from the matter just 1 second after the Big Bang [4]. On the contrary, the Cosmic Microwave Background (CMB) originated when the universe was 380,000 years old. Thus,  $C\nu B$  presents an opportunity to study an even earlier universe. However, detecting such neutrinos would be an extremely difficult task due to their low temperature and number density. PTOLEMY project is proposed to make it possible using a tritium target for neutrino detection [5].

## 1.2 Definitions of energy transfer and momentum transfer

There are two kinds of neutrino-nucleus interactions: charged-current interactions and neutral-current interactions. In a charged-current interaction, a neutrino interacts with a nucleon, changing the neutrino into its charged lepton partner. When a muon neutrino interacts, a muon is produced. In a neutral-current interaction, a neutrino interacts with a nucleus but it does not change into a charged lepton and exits as the same neutrino with some hadrons. This thesis deals with charged-current neutrino-nucleus interactions with a muon neutrino beam. The simplest neutrino-nucleus interaction is quasielastic scattering. It involves the interaction of a neutrino with a neutron, changing the neutrino into a negatively charged muon, changing the neutron into positively charged proton, and ejecting it from the nucleus. This interaction happens inside a nucleus since free neutrons do not exist. The Feynman diagram for this interaction ( $\nu_\mu + n \rightarrow \mu^- + p$ ) is

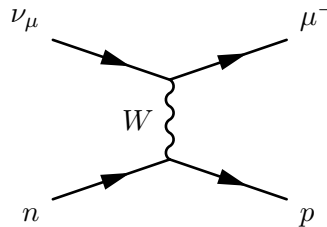


Figure 1.2: Feynman diagram of quasielastic scattering

The Feynman diagram of a charged-current neutrino-nucleus interaction can visually be divided into two systems: lepton system and hadron system. The theoretical expressions that describe the interactions also explicitly combine descriptions of lepton and hadron system. Lepton system consists of a muon neutrino and a muon. In general, the hadron system contains the nucleon with which a neutrino interacts, whatever it changed into, and can further include decay products and/or additional particle production.

The incoming neutrino can be described by a relativistic momentum four-vector as  $(E_\nu, \vec{p}_\nu)$ , where  $E_\nu$  is the neutrino energy and  $\vec{p}_\nu$  is its three-momentum vector. Similarly, the four-vector of the muon can be written as  $(E_\mu, \vec{p}_\mu)$ , where  $E_\mu$  is the muon energy and  $\vec{p}_\mu$  is its three-momentum vector. Since the four-momentum is conserved at the lepton system vertex, thus energy and momentum conserved separately, the momentum transfer four-vector ( $q$ ), basically the four-momentum carried by the W boson from lepton system to hadron system, is given by

$$q = (E_\nu - E_\mu, \vec{p}_\nu - \vec{p}_\mu). \quad (1.1)$$

Similarly, energy transfer is given by

$$q_0 = E_\nu - E_\mu. \quad (1.2)$$

Sometimes, energy transfer is also symbolised by  $\nu$  and  $\omega$ . The quantity  $\nu$  is actually a relativistic invariant, which evaluates to the energy transfer in the lab frame. These alternative symbols will rarely be used in this thesis to avoid confusion, but they are in common use in the literature for high energy neutrino-quark and electron-nucleus scattering respectively. Also, three-momentum transfer is given by

$$\vec{q} = \vec{p}_\nu - \vec{p}_\mu. \quad (1.3)$$

Due to energy conservation and momentum conservation at the hadron system vertex, energy transfer and momentum transfer are also given by  $q_0 = E_p - E_n$  and  $\vec{q} = \vec{p}_p - \vec{p}_n$ , where  $E_p$ ,  $E_n$ ,  $\vec{p}_p$  and  $\vec{p}_n$  are proton energy, neutron energy, three-momentum vector of proton (or a more complicated outgoing hadron system) and three-momentum

vector of neutron. In the approximation that the struck neutron was at rest,  $q_3$  and  $q_0$  are known simply from measuring the hadron system.

The magnitude of the three-momentum transfer is symbolised by  $q_3$  or  $|\vec{q}|$ . The use of symbols  $q_3$  and  $q_0$  is more common and natural for use in computer codes than the other notations, and directly reflect the four-vector nature, and so are becoming more widely used in the literature. The magnitude squared of four-momentum transfer is

$$q^2 = q_0^2 - q_3^2. \quad (1.4)$$

Since W boson is a virtual particle mediating the weak interaction,  $q^2$  is negative. For the convenience, a different symbol,  $Q^2$ , is used. It is equal to the negative of the four-momentum transfer squared. Its expression is

$$Q^2 = q_3^2 - q_0^2. \quad (1.5)$$

Since  $Q^2 > 0$ ,  $q_0$  is always less than  $q_3$ . This can be clearly seen in the plots in the upcoming chapters where the cross-section is 0 whenever  $q_0 > q_3$ . Since  $Q^2$  is a relativistic invariant, it is the only kinematic quantity a theory needs to describe the kinematics of scattering of two point particles. Two quantities are needed for all other interactions, such as with nuclei or when treating composite particles, and the pair  $q_0$  and  $q_3$  are often chosen.

For the purpose of this thesis, I have chosen three bins of  $q_3$  with bin width 0.4 GeV. They are labeled as Low  $q_3$  (0.0 - 0.4 GeV), Mid  $q_3$  (0.4 - 0.8 GeV) and High  $q_3$  (0.8 - 1.2 GeV). It is possible to choose bins with smaller bin width such as those chosen by Ascencio *et al.* [6].

Before going further, an important quantity called invariant mass of the hadron system ( $W$ ) and its square must be defined. If the hadron system is just a single particle, then its invariant mass  $M$  is simply also this quantity  $W$ . If it is a system of multiple particles, their four-vectors can simply be summed and the invariant mass of the result is obtained in the usual way. In addition, if  $p$  is the four-momentum vector of

the struck nucleon and  $q$  is the four-momentum transfer, then momentum conservation implies that the four-momentum of the hadron produced would be  $(p + q)$ . Then,  $W^2$  is the magnitude squared of this quantity. Mathematically, it is

$$W^2 = (p + q)^2. \quad (1.6)$$

When the struck nucleon is at rest,  $W^2$  takes the following simple form

$$W^2 = m_N^2 - Q^2 + 2m_N q_0 \quad (1.7)$$

where  $m_N$  is the mass of the struck nucleon.

Natural units are used everywhere in this thesis, which means speed of light in vacuum ( $c$ ) is set to 1. Energy, momentum and mass will be stated in MeV or GeV units.

### 1.3 Different types of neutrino-nucleus interactions

The quasielastic scattering is the simplest interaction of a neutrino and a nucleon inside the nucleus, but there are more. For the work in this thesis, the production of a nucleon resonance is an important variation, as are reactions on two nucleons at once, knocking them both out and producing two “holes” in the nucleus, sometimes called the 2-particle, 2-hole (2p2h) process and sometimes called a Meson Exchange Current (MEC) process.

#### 1.3.1 Triangle Diagram

The kinematics of different interaction processes can be summarized using the triangle diagram which is a MINERvA jargon. It is used to refer to a plot which shows the cross-section, the relative probability or event rate of a particular interaction at a particular pair of kinematics, on a 2D plot, where  $q_3$  is on the horizontal axis and  $q_0$  is on the vertical axis. An example of the triangle diagram is taken from [7] and these diagrams were originally introduced by Gran *et al.* in [8].

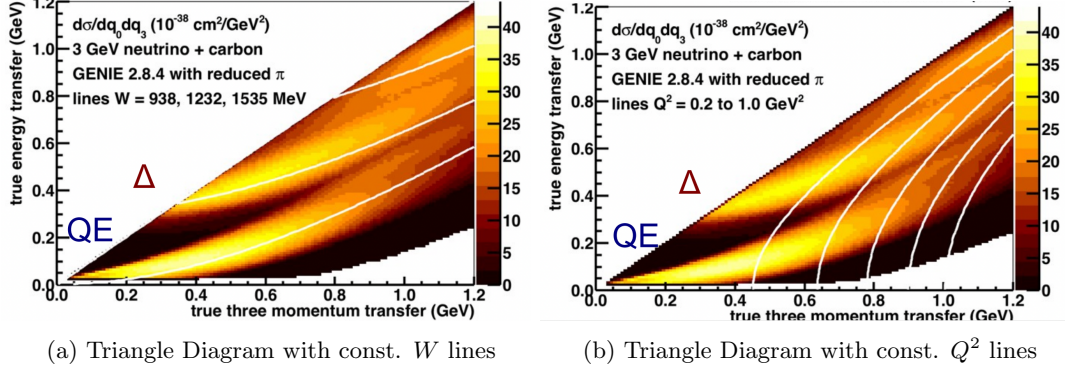


Figure 1.3: Separate Triangle diagrams with two independent quantities,  $W$  and  $Q^2$

Both the triangle diagrams shown in the figure above represent the same cross-section. The difference is in the constant lines drawn on them. These diagrams treat  $q_3$  and  $q_0$  as independent quantities. Other quantities such as  $W$  and  $Q^2$  can also be treated as two independent quantities and cross-section can be defined with respect to them. However, this work uses  $q_3$  and  $q_0$  only except for a specific section in Chapter 2 where the cross-section of quasielastic scattering on a free nucleon is defined with respect to  $Q^2$ .  $W$  is fixed and equal to 938 MeV for such kind of interaction.

The first triangle diagram has the value of  $W$  increasing in the upward direction. The first line corresponds to  $W = 938$  MeV, which is also the mass of a nucleon. This line corresponds to quasielastic scattering. It would be an infinitesimally thin line when a neutrino undergoes quasielastic scattering on a free nucleon. Inside a nucleus, nucleons are in motion and due to that motion, this line has a small width as shown for carbon in the diagram. The second line corresponds to  $W = 1232$  MeV. It is the first resonance, called delta resonance, which is just an excited state of a nucleon. The third line corresponds to  $W = 1535$  MeV and it corresponds to a higher resonance.

The second triangle diagram has the value of  $Q^2$  increasing in the right direction from  $0.2 \text{ GeV}^2$  to  $1.0 \text{ GeV}^2$  in the steps of  $0.2 \text{ GeV}^2$ . The diagonal of the triangle diagram corresponds to an extreme limit of  $Q^2$ , where its value is 0 which corresponds to equations 1.4 and 1.5 when  $q_0 = q_3$ . Later in this thesis, there will be 1D plots with

an estimator for energy transfer  $q_0$  on the horizontal axis for a fixed range of  $q_3$ . In those plots, the high energy transfers on the right correspond to the lowest  $Q^2$ .

### 1.3.2 Quasielastic scattering (QE)

Quasielastic scattering is defined as the interaction of a neutrino with a neutron resulting in the production of a charged lepton and a proton. It can be written as follows for a muon neutrino beam



Its Feynman diagram, also shown in the previous section, is

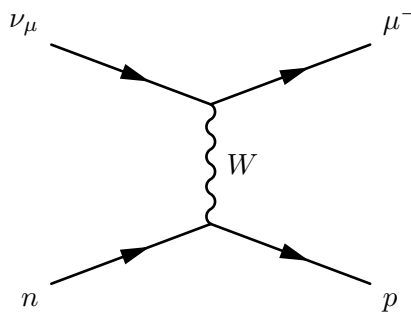


Figure 1.4: Feynman diagram of quasielastic scattering

Quasielastic scattering usually happens when the energy transfer and the momentum transfer is low enough so that a neutrino can eject only a single nucleon out of a nucleus. That's why it lies at the bottom of the triangle diagram as shown in Fig. 1.3. Its invariant mass ( $W$ ) is 938 MeV.

### 1.3.3 Delta Resonance and Other Resonances

Delta resonance happens when a neutrino interacts with a nucleon and produces a muon and a delta baryon with  $W$  equal to 1232 MeV. Delta baryon is unstable and it always decays to hadrons. There are four kinds of delta baryons:  $\Delta^{++}$ ,  $\Delta^+$ ,  $\Delta^0$  and  $\Delta^-$  with the quark content as  $uuu$ ,  $uud$ ,  $udd$ , and  $ddd$  respectively, where  $u$  represents an up quark and  $d$  represents a down quark. The middle two quark contents are the same as proton and neutron, so effectively the delta resonance is the first excited state of a

nucleon. Similar to the states of a Lithium atom, the Pauli exclusion principle prevents three up quarks or three down quarks from being in the same lowest “orbital” so the delta is the lowest energy configuration for those.

$\Delta^{++}$  and  $\Delta^+$  are produced when a neutrino interacts and exchanges one unit positive charge with a proton and a neutron respectively.  $\Delta^0$  and  $\Delta^-$  are produced when an antineutrino interacts with a proton and a neutron respectively. The delta interaction of a neutrino with nucleons is as follows:

$$\nu_\mu + p \rightarrow \mu^- + \Delta^{++} \quad (1.9)$$

$$\nu_\mu + n \rightarrow \mu^- + \Delta^+ \quad (1.10)$$

The decay modes of  $\Delta^{++}$  and  $\Delta^+$  are as follows:

$$\Delta^{++} \rightarrow \pi^+ + p \quad (1.11)$$

$$\Delta^+ \rightarrow \pi^0 + p \quad (1.12)$$

$$\rightarrow \pi^+ + n \quad (1.13)$$

$$\rightarrow \gamma + p \quad (1.14)$$

The decay of  $\Delta^+$  has only a small chance of decaying into a photon and a proton. The other two are its dominant decay modes.

The Feynman diagram of delta resonance is

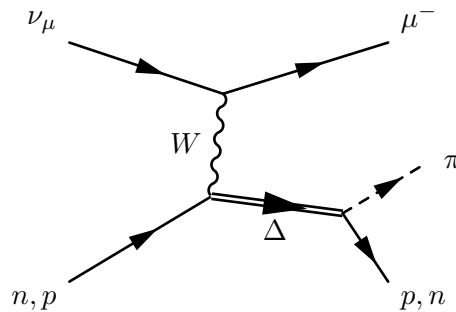
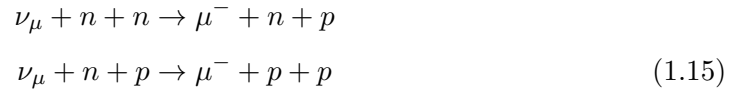


Figure 1.5: Feynman diagram of delta resonance

Delta resonance is the first resonance. Higher resonances such as 1535 MeV also exist but they correspond to the regions of high energy and momentum transfer. Additional resonances are modeled up to about 1700 MeV after which individual resonances are no longer observed and there is a continuum of interaction kinematics called deep inelastic scattering.

#### 1.3.4 Two-particle two-hole (2p2h) Process

QE scattering and delta resonance can occur on both a free nucleon and a bound nucleon since they require only one nucleon. On the other hand, two-particle two-hole process happens only on bound nucleons. In this process, a neutrino interacts with two nucleons together. There can be two free nucleons in nature but 2p2h process happens when two nucleons have short-range correlations between them. In other words, they are exchanging a pion or have temporarily formed a bound state. Obviously, this can only happen within a nucleus. In this interaction, two nucleons are ejected from the nucleus leaving two holes in the nuclear shell states and hence the name. Examples of 2p2h process are



The corresponding Feynman diagram is

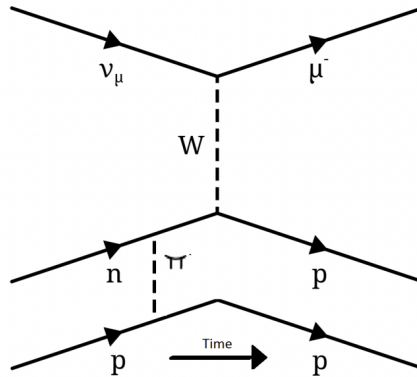


Figure 1.6: Feynman diagram of 2p2h process on np pair, where proton is the spectator nucleon. A variant happens when the spectator nucleon is a neutron.

The figure above is taken from Ethan Miltenberger's MS Thesis [9].

### 1.3.5 Deep and Shallow Inelastic Scattering (DIS and SIS)

QE scattering, delta resonance and 2p2h process are interactions with nucleons made up of quarks. Deep inelastic scattering happens when a neutrino is so energetic that it interacts at the quark level with the other quarks as spectators. An individual quark cannot come out though due to quark confinement and instead results in the production of a large number of hadrons due to hadronization. These hadrons will still typically produce a single proton or neutron in the final state, because baryon number is conserved, but may produce as many pions and kaons as they have energy. It is naturally a high energy and momentum transfer process. This thesis is limited to  $q_3 < 1.2$  GeV except for the discussion on structure functions in QE in Chapter 2 and so this process is less important. An example of a Feynman diagram representing a DIS is shown below. This process needs to use the energy to create a quark anti-quark pair so that there is at minimum one baryon and one pion in the final state.

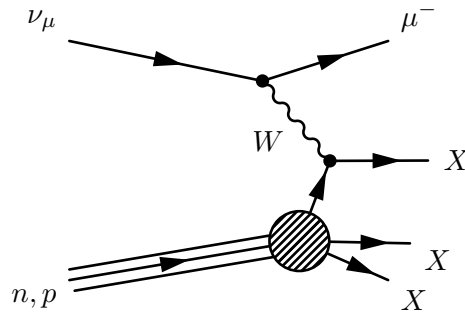


Figure 1.7: Feynman diagram of deep inelastic scattering

$X$  in the figure is just to represent the production of hadrons and three lines approaching the blob represent three quarks inside a nucleon.

DIS played an important role in the discovery of quarks although an electron beam instead of a neutrino beam was used to probe the inside of nucleons. Electrons or neutrinos traveling at a high momentum have a very short wavelength since wavelength associated with the matter wave is inversely proportional to the momentum. Because of having a short wavelength, highly energetic electrons or neutrinos can probe inside of a nucleus and “see” a single quark and notice other quarks nearby.

Shallow Inelastic Scattering (SIS) is DIS with a specific condition. Different research groups and authors use similar but not the same definition of SIS. Some authors define SIS as DIS with  $Q^2 < 1 \text{ GeV}^2$  while others define SIS as DIS with  $W < 2 \text{ GeV}$ . In the context of MINERvA, the SIS region is  $W < 2 \text{ GeV}$ . At these energy transfers, only one or at most two pions are produced. The boundary between SIS reactions on quarks and resonance reactions on nucleons is fuzzy both experimentally and theoretically.

### 1.3.6 Coherent Pion Production

All the interactions described above happen when a neutrino interacts with a nucleon inside a nucleus. Coherent pion production refers to an interaction of a neutrino with a whole nucleus that leads to the production of  $\pi^+$ . This interaction dominates at low momentum transfers so that the nucleus remains intact and can even remain in its ground state. This can also be understood on the basis of momentum-wavelength explanation given above. To probe the nucleus as a single object without a substructure, a longer

wavelength is required, which is possible only with low momentum transfer.

The Feynman diagram of coherent pion production is

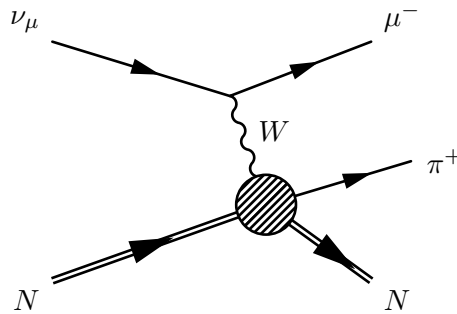


Figure 1.8: Feynman diagram of coherent pion production

where  $N$  represents a nucleus.

When an antineutrino interacts with a nucleus as a whole, it produces a  $\pi^-$  instead of a  $\pi^+$  and there is a neutral current version that produces a  $\pi^0$ .

## 1.4 Introduction to MINERvA Detector

There are many different neutrino experiments running right now or have run in the past. One of the most common type of neutrino experiment is neutrino oscillation experiment. Neutrino oscillation refers to the change in flavor of a neutrino as it travels a certain distance. Experiments like T2K and NOvA are long-baseline (hundreds of km) experiments searching for oscillation between muon neutrino and electron neutrino. How many muon neutrinos and electron neutrinos are present in the beam, how many are expected to interact in the detector, and what's their energy distribution is determined by their interaction with matter. Oscillation phenomena are measured by deviations from the predictions of ordinary interactions, so the interaction cross section must be well-modeled.

MINERvA is the first experiment to measure the interaction cross-section for five

different nuclear targets: helium, iron, lead, water and carbon. It also modeled neutrino interactions with oxygen and hydrogen. My thesis focuses on the interaction with the scintillator, which is plastic made up of equal number of carbon and hydrogen in MINERvA. Whenever I discuss the Valencia Model in the thesis, it is always on carbon nucleus whereas any discussion on MINERvA Monte Carlo (MC) or data is on scintillator.

To write this section on MINERvA detector, I have taken a lot of information from the paper titled “Design, calibration, and performance of the MINERvA detector” [10]. It is a complete report and readers of this thesis can refer to that paper for more details.

#### 1.4.1 MINERvA neutrino beam flux

MINERvA ran its experiment using Neutrinos at the Main Injector (NuMI) beamline facility at Fermilab shown in the following figure taken from [11].

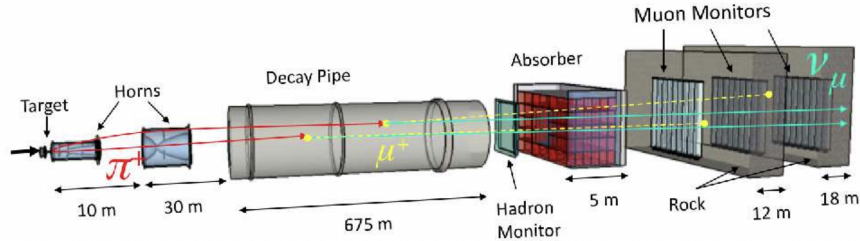


Figure 1.9: NuMI beamline at Fermilab used to generate a neutrino beam that enters the MINERvA detector (not shown) located a few tens of meters downstream of the final muon monitor

NuMI begins with a proton beam of 120 GeV hitting a graphite target and generating secondary pions and kaons. These secondary hadrons are then focused by magnetic horns into the 675 metre long decay pipe. Horns can change their polarity. When horns focus positively charged hadrons (called Forward Horn Current), the beam primarily consists of antimuons and muon neutrinos. When horns focus negatively charged hadrons (called Reverse Horn Current), the beam primarily consists of muons and muon antineutrinos. Hadron monitor measures the number of undecayed hadrons before the

beam can enter the absorber. Absorbers made of rocks absorb muons (antimuons) and let antineutrinos (neutrinos) pass. Then, muon monitor measures the muons left in the beam. The muons that escape the absorbers are called rock muons. They were used by MINERvA for setting energy scale and timing calibration.

MINERvA had two separate eras: Low Energy Era (LE) when MINERvA ran from 2009 to 2013 and Medium Energy Era (ME) when MINERvA ran from 2013 to 2019. In LE Era, the neutrino beam peaked at 3 GeV while in ME era, the neutrino beam peaked at 6 GeV. This thesis uses events only from the ME era.

### 1.4.2 MINERvA Detector

MINERvA Detector is placed downstream of the NuMI beamline, and it is followed by MINOS Near Detector. Its schematic is shown in Fig. 1.10 taken from [10].

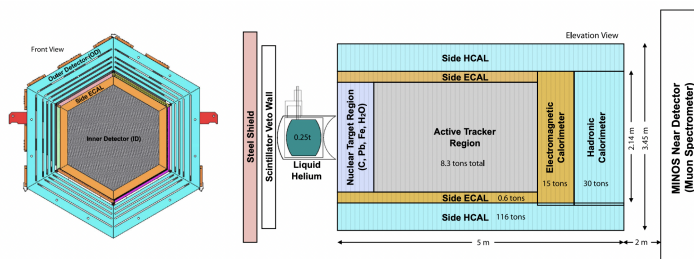


Figure 1.10: Front and Elevation View of MINERvA Detector

MINERvA contains a liquid helium tank placed between the veto wall and the main detector. Veto wall monitors the hadrons which might be produced by the interaction of neutrinos when they pass through rocks. In addition to helium, MINERvA has nuclear targets such iron, lead, carbon and water placed in the nuclear target region. Nuclear target region is followed by active tracker region, which is followed by electromagnetic calorimeter (ECAL) and hadronic calorimeter (HCAL). All these are surrounded by side ECAL and side HCAL (also called Outer Detector). Both outer detector and tracker are hexagonal in shape.

Every region in the detector contains “modules”. A module is made up of two

scintillator planes mounted in one frame. These planes are oriented at 60 degrees with respect to each other. There are three orientations in total, called X, U and V, with U and V oriented  $\pm 60$  degrees from the X orientation. The modules alternate between UX and VX combination of planes. The reason behind this 60 degree orientation is the 3D reconstruction of the trajectory of particles produced in the interaction. In particular, it enables unambiguous reconstruction of the directions of two particles at once; even if their trajectory overlaps in one view, there will be separate measurements in at least two views. The 60 degree rotation also explains why the detector has a hexagonal shape.

### **Active Tracker Region**

The active tracker region is a pure scintillator region consisting of 62 tracking modules or 124 scintillator planes. Every scintillator plane consists of 127 triangular scintillator strips with an optical fiber inside. These fibers let the light generated when a neutrino interacts in the tracker to travel toward photomultiplier tubes (PMTs). The light is collected there and converted into electrical signals which can further be turned into measurable quantities. My thesis includes those neutrino interactions whose interaction vertex lies in the active tracker region.

### **Electromagnetic Calorimeter (ECAL)**

ECAL has 10 modules very similar to tracking modules with the only difference that each module contains a 0.2 cm thick lead sheet on the downstream end of each scintillator plane. Electromagnetic interaction probabilities go as the square of the charge of the nucleus  $Z^2$ . With lead  $Z = 82$ , the high probability for electron and photon interactions produces a shower or cascade. This prevents energy from escaping the detector and produces accurate energy reconstruction.

### **Hadronic Calorimeter (HCAL)**

HCAL has 20 modules in total that are similar to tracking modules with the only difference that it contains only one plane of scintillator strips. The other plane is made of 1 inch thick steel plate. From the perspective of a hadron, the density and thickness of the steel produces 10x as much energy loss and interactions as one plane of scintillator.

This makes the HCAL an inexpensive and compact sampling calorimeter that contains most of the hadron energy, enabling their accurate energy reconstruction while still tracking muons into the MINOS near detector.

### **Outer Detector (OD), also called Side HCAL**

Outer Detector has similar function and steel structure as HCAL. They are made of steel and scintillators. OD measures the energy deposited by hadrons leaving the detector from the side.

## **1.5 Selection Cuts, Neutrino Flux, Nuclear Effects and Modeling in MINERvA**

The previous section mentions that 120 GeV protons hit the graphite target leading to the production of pions and kaons which further decay to produce a neutrino beam and an antineutrino beam. The number of protons hitting the target during the running period of the experiment is called Proton on Target (POT). POT during the run of MINERvA ME beam, called Data POT, are  $1.0606 \cdot 10^{21}$  and POT in the MC simulated beam are  $4.10343 \cdot 10^{21}$ . Since  $\text{MC POT} \approx 4 \times \text{Data POT}$ , the number of simulated events have to be divided by a factor of 4 before they can be compared to the data events. Experiments aim to simulate 4 to 10 times the statistics as the real data so the statistical uncertainties on the simulation are half or a third as much.

### **1.5.1 Muon Reconstruction and its limitations**

A muon is always present in the outgoing particles of the charged-current events studied in this thesis. It has to enter MINOS for its energy (or momentum magnitude) to be reconstructed. The minimum muon momentum that can be reconstructed is 1.5 GeV. A muon with less momentum has a high chance of depositing all its energy in MINERvA detector and not entering MINOS at all. We set an upper limit of 60 GeV on muon momentum. A muon traveling with a higher momentum encounters resolution issues. MINOS uses two methods to determine muon momentum: range method and curvature method. Range method works only if the muon stops in the calorimeter region of the

MINOS, which is about the first 40% region of MINOS. This method is based on the relation between the distance a muon travels and the amount of energy it has. MINOS has a spectrometer region in the last 60% of its volume. It contains a magnetic field that is used to determine the muon momentum based on how much it curves in the magnetic field. Since this is the latter region of MINOS, generally high energy muons enter this region. The range method has lower uncertainties and better resolution, so when some muons are measured using both methods, the value from the range method is always chosen.

In addition to momentum limitations, detector geometry also imposes a constraint on muon angle: for example a muon travelling at about 20 degrees with respect to the neutrino enters MINOS and is successfully reconstructed only about 1 in 10 times. Because the muon angle distribution is neutrino energy dependent, and a muon angle selection is baked into the geometry of the detectors, a study purposely making more restrictive angle cuts in angle is part of the latter half of the thesis.

### 1.5.2 $\nu - e$ scattering constrained flux is the MINERvA's default flux

There are various ways to determine neutrino flux such as inverse muon decay,  $\nu - e$  scattering and low- $\nu$  technique. The default flux of MINERvA comes from a simulation of the beam line, the pion and kaon production, and the focusing elements. The simulation is then modified using a constraint from the  $\nu - e$  scattering technique [12]. That flux is used in this thesis except for in Chapter 5 where the flux determined by Rob Fine using low- $\nu$  technique [13] is also used and the results of two fluxes are compared. The following figure taken from [12] shows the default flux of MINERvA before  $\nu - e$  constraints were applied. The figure gives an idea of how the flux looks as a function of neutrino energy. The comparison of unconstrained flux and  $\nu - e$  constrained flux can be found in [12].

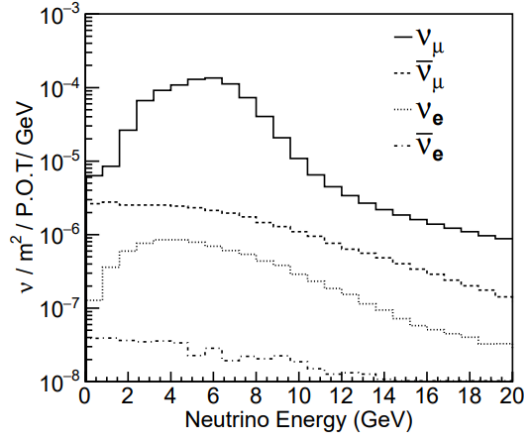


Figure 1.11: Default MINERvA flux before applying neutrino-electron scattering constraints

Fig. 1.11 shows four different fluxes corresponding to  $\nu_\mu$ ,  $\bar{\nu}_\mu$ ,  $\nu_e$  and  $\bar{\nu}_e$ . My work is on muon neutrinos, so I have used the  $\nu_\mu$  flux distribution. It peaks around 6 GeV.

In the latter chapters of the thesis, energy dependence in neutrino models is studied and to do that, the neutrino flux is divided into three neutrino energy ranges: LowEnu (1 - 4 GeV), MidEnu (4 - 7) GeV and HighEnu (7 GeV and higher). The basic idea behind this choice is to cover the left tail, peak and right tail of the distribution separately as they have different level and sources of uncertainties. The flux around the beam peak is most accurately known. Another feature of this choice is that the statistical power of the three samples is similar.

### 1.5.3 Neutrino Event Generators and Nuclear Effects

Neutrino-nucleus simulation is done using neutrino event generators such as GENIE, GiBUU, NEUT and NuWro. These event generator codes contain a comprehensive set of models for all the processes mentioned above, plus a few more that are not relevant for this thesis. Sometimes they have multiple different models to choose from and always have the option to vary the parameters of the models. GENIE uses C++ and is a primary generator for all Fermilab experiments such as MINERvA, NOvA and MicroBooNE. J-PARC experiments in Japan such as T2K and Super-K use NEUT as an

event generator. GiBUU has the most sophisticated FSI model until now. NuWro is also a C++ based event generator. Although experiments such as MINERvA primarily use only one event generator, it is fairly common in neutrino physics experiments to use different generators and compare their results. MINERvA uses GENIE and introduces its own empirical corrections to the models simulated in the generator. These corrections are based on fits to the experimental data and are called “tunings”. The tune used in this thesis is known as MnvTune v1. Event simulation in GENIE is based on Monte Carlo technique [14, 15].

Since a neutrino interacts with a nucleon inside a nucleus, nuclear effects are also incorporated in the simulation. They have an effect on structure functions which are used to define the interaction cross-section. Some of the nuclear effects are

- Fermi Motion: A bound nucleon is always in motion as opposed to a free nucleon that is at rest. Since a nucleus is so tightly localized inside a nucleus, Heisenberg’s Uncertainty Principle proposes an uncertainty in the momentum of the nucleon, and hence the Fermi motion. Several different variations of a Fermi gas are used. The version used by MINERvA is just a regular Fermi gas, the one used by the Valencia calculation is a local Fermi gas. In this model, a nucleon has an increasing probability with increasing momentum until it drops all the way to 0 at the momentum of 220 MeV, called Fermi momentum. This deviation from zero for the momentum vector of the initial state has consequences for the momentum of the measurable products of the reaction. My thesis is based on this model. However, electron scattering results have shown that there is a small non-zero probability for a nucleon to have a momentum higher than Fermi momentum. Bodek and Ritchie [16] first suggested a simple way to add this feature to neutrino interaction models and since this probability lies at high end of the probability distribution, it is called Bodek-Ritchie Tail.
- Random Phase Approximation (RPA): RPA is introduced to implement a screening effect. This is similar to the screening of an electrically charged particle in a polarizable medium but it is a screening effect of weak interaction. It arises due to interactions between nucleons inside a nucleus which results in a change

in electroweak couplings between them [17, 18]. Due to RPA, the interaction cross-section is reduced. Using the Valencia Model predictions for quasi-elastic processes, Gran [19] has investigated the scaling of RPA effect and shown the results which confirm that RPA is dominant at low energy and momentum transfers. As  $Q^2 \rightarrow 0$ , the cross-section drops by about 60% due to RPA. RPA has almost no effect above  $Q^2 = 0.5 \text{ GeV}^2$ .

- **Pauli Blocking:** Pauli blocking is based on Pauli’s Exclusion Principle. According to this principle, no two fermions can exist together in a quantum state with same quantum numbers. If a new nucleon is produced in an interaction and some other nucleon is in the same state already, the production of the new nucleon is suppressed or blocked; the reaction is unphysical and not allowed. Every model for interactions with nucleons implements Pauli blocking, either as limits to the integral over allowed kinematics or using an accept-reject loop to reject interactions with final nucleon momenta below the Fermi-motion limit. Bodek [20] among others has characterized Pauli blocking as being significant only at low energy and momentum transfers, such that  $Q^2 < 0.2 \text{ GeV}^2$  or  $q_3 < 0.44 \text{ GeV}$ .
- **Removal Energy:** Just like some energy, called ionisation energy or binding energy, must be supplied to an electron to eject it from an atom, some energy, called removal energy, must be supplied to eject a nucleon from a nucleus. Sometimes, a nucleon is in an excited state and this reduces the removal energy. An average removal energy for a nucleon in a ground state carbon nucleus is 25 MeV. MINERvA neutrino beam is of the order of GeV and thus, removal energy would seem to be too small to make a difference in MINERvA experimental results. However, MINERvA can measure hadron energies down to zero with few MeV resolution; the 25 MeV removal energy is significant on this scale.

There is one “nuclear effect” which is not included in the list above. It is called “Final State Interactions (FSI)”. FSI is different from all the nuclear effects mentioned above. Nuclear effects such as Fermi motion, RPA, Pauli blocking and removal energy affect the cross-section of a neutrino-nucleus interaction but once the interaction has happened and the outgoing hadrons are produced, these four nuclear effects are out of

the picture. A hadron coming out of the reaction, say a proton in a quasielastic scattering, inside a nucleus still has to go through the nucleus and with substantial probability will interact with other nucleons before it can exit the nucleus. These interactions after a hadron is produced and before it exits the nucleus are called Final State Interactions, or sometimes called intranuclear rescattering. These interactions can change the energy, electric charge, momentum or the hadron itself. It is also possible that the hadron gets absorbed inside the nucleus and does not exit the nucleus at all. FSI of  $\pi^+$  are studied in Chapter 7 and one such FSI is pion absorption in which the pion gets absorbed by two or more nucleons and never exits the nucleus.

There are two most commonly used models of FSI. They are “Effective” cascade model (hA) and Semi-classical cascade model (hN) [21]. Though it has the virtue of being extremely simple and anchored to data, hA is an old FSI model. It makes predictions directly based on hadron scattering data. hN is a newer model and calculates the probability of the hadron interaction in discrete steps using nuclear density models. GENIE version 2 is used in this thesis and MINERvA ran it only with the hA FSI model. Since both hA and hN are anchored to relevant data, it is not so clear which one is better. Each experiment debates which is the best choice for the physics they need to simulate to achieve their analysis goals.

In a neutrino-nucleus interaction, muons are also produced. In principle, their energy is affected by the choice of removal energy strategy, which leads to a set of systematic uncertainties. It is also affected by radiative processes where the muon sheds a photon (like in Bremsstrahlung) during the interaction, and electron-neutrino scattering is even more affected. Though there is recent work on this topic, these radiative corrections are not simulated in GENIE and are not considered in this thesis.

Once a particle is produced, whether a muon or a hadron, and it has exited the nucleus after final state interactions, the particle has to go through the detector. It interacts with various nuclei and materials such as carbon, titanium, oxygen, hydrogen, steel, lead and plastic. The simulation of the particle interaction with the detector and the change in its energy and momentum spectrum as it travels is modeled using Geant4

[22]. Effects simulated within Geant4 are not considered in detail in this thesis.

#### 1.5.4 Modeling of various neutrino-nucleus interactions in GENIE and MINERvA tunings

There are many theoretical models available in the literature for various neutrino-nucleus interactions. QE scattering, delta resonance and 2p2h process are the main focus in this thesis, so their modeling requires a bit more attention.

Quasielastic scattering model is available from the work of Llewelyn Smith [23]. His model was originally for free nucleons and when applied to nucleus, it assumes impulse approximation, which in simple terms means ignoring the short-range correlations between nucleons. MINERvA reweighted Llewelyn Smith’s model up to approximate Valencia RPA effect. So, the QE model in MINERvA simulations is like a hybrid between Llewelyn Smith’s Model and Valencia RPA [17, 18].

Valencia Group has given a whole QE Model, including RPA effect. Chapter 2 uses this exact model directly from their FORTRAN code. However, MINERvA only uses a special feature, i.e. RPA of this model.

Delta resonance can be modeled using: Berger-Sehgal Model [24] and Lalakulich-Paschos Model [25]. These are based on two different ways of theoretical calculations and their detailed analysis is given in Ishmam Mahbub’s thesis [26]. Berger-Sehgal Model has slightly improved modeling than Rein-Sehgal Model [27] but there are some issues with it about describing MINERvA data. This work’s and MINERvA’s choice is Rein-Sehgal Model to simulate delta and higher resonances. There are additional models becoming available to experimenters in the near future.

Valencia Group has also given a 2p2h model [28], which is directly used by MINERvA following the technique described in [29]. This model is also used in 2p2h structure function analysis in Chapter 2 directly from the Valencia FORTRAN code. However, MINERvA makes an enhancement in the “dip” region. “Dip” region is the region between delta resonance and QE scattering in the triangle diagram [8]. Phil Rodrigues

proposed an empirical enhancement in this region based on a fit to MINERvA data. This enhancement is used and described in Gran *et al.* [30] and Ascencio *et al.* [6]. The 2p2h enhancement is added when using the MINERvA Monte Carlo simulation in this thesis, but not when using the Valencia Model directly through their code.

## 1.6 Prior Work

The energy dependence work in this thesis is inspired by the work of Ishmam Mahbub, a former MS student at University of Minnesota Duluth, who defended his MS thesis in 2021 [26]. He studied the energy dependence in Llewelyn Smith's model of quasielastic scattering on free nucleons. His finding was that energy independent term containing Llewelyn's form  $B(Q^2)$ , which I have shown is same as structure function  $W_2$  in section 2.1.2 for QE, is big enough to describe MINERvA data and the other terms containing energy dependence are too small. He also studied energy dependence in delta resonance based on structure functions extracted from Lalakulich-Paschos Model and had the same finding that energy independent term containing  $W_2$  is the dominant term and other structure functions which are a part of  $1/E$  and  $1/E^2$  terms can be ignored. He also compared the results of three different delta resonance models, Rein-Sehgal Model, Berger-Sehgal Model and Lalakulich-Paschos Model, with each other. Ishmam applied muon angle cuts on data and MC to see whether energy dependence is well-modeled or not. He found discrepancies with specific muon angle cuts, which inspired the work in this thesis on muon angle cuts and angle acceptance. Another systematic effect that he studied was Muon Kludge. He tried to study if an unmodeled energy dependence arises from an error in muon kludge. The starting point for Ishmam's thesis work was a preliminary study by undergraduate Alec Lovlein in 2016-2017.

## Chapter 2

# An Introduction to Structure Functions and their Analysis for QE and 2p2h Process

In general, any interaction is described by cross-section. For the sake of understanding, cross-section of an interaction can be treated as the probability of that interaction. An interaction with a higher cross-section has a higher chance of occurring. Cross-section can be either total or differential. The difference between these two types of cross-sections and a detailed explanation of cross-section can be found in [31, 32]. However, an explanation is given here to get a general idea. It must be noted that the explanation given here assumes that the particle scatters off the target with some size and area, and uses that to describe the idea of cross-section, though quantum mechanics and wave packets don't really work like this.

Imagine a particle incident on a target. In a classical billiard ball scenario, the incident particle can go in any direction depending on its distance from the target (called impact parameter). If the particle passes through unaffected, it means that the particle did not interact or the interaction was too feeble. For it to interact with the target, it has to come closer to the target. Total cross-section is defined as the effective area around

the target through which an incident particle should pass to have an interaction. Differential cross-section is a bit more subtle. It can be one-dimensional, two-dimensional or higher-dimensional. “Dimension” here refers to the parameter with respect to which the probability of an interaction is determined. For a simple explanation, the differential cross-section  $d\sigma/d\theta$  can be considered, where  $d\theta$  is differential variation in the angle between the direction of incidence and the direction of scattering. The whole term  $d\sigma/d\theta$  means that the differential target area  $d\sigma$  is the area in which a neutrino particle/beam should hit, so that it scatters in the “direction”  $d\theta$ .

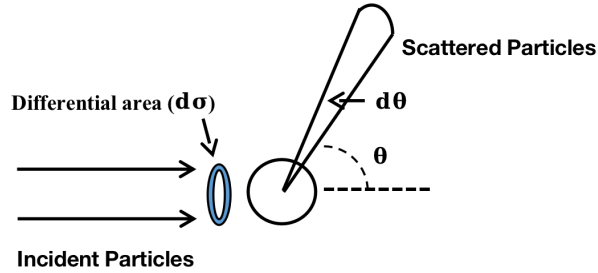


Figure 2.1: An incident particle beam traveling in the differential area ( $d\sigma$ ) scatters in the differential angle ( $d\theta$ )

The two differential cross-sections that will mostly be used in this thesis are:

- Single-differential cross-section:  $d\sigma/dQ^2$
- Double-differential cross-section:  $d^2\sigma/dq_0dq_3$

where,  $Q^2$ ,  $q_0$  and  $q_3$  refer to the negative of four-momentum transfer squared, energy transfer, and three-momentum transfer respectively.

A differential cross section is like a probability distribution function whose purpose is to be integrated. Single-differential cross-section can be obtained from a double-differential cross-section by integrating it with respect to one of the two parameters. For example,  $d^2\sigma/dq_0dq_3$  can be integrated with respect to  $q_3$  to obtain  $d\sigma/dq_0$ , which is also used in Section 2.2.6. This can be integrated one more time to give the total cross-section that any such scattering occurred.

## 2.1 Introduction to Form Factors

As described above, every interaction is described in terms of cross-section. What cross-section depends on is governed by the type of interaction. For example, in the case of neutrino-nucleus scattering, a neutrino interacts with a nucleon present inside the nucleus. Hence, the cross-section depends on the nuclear effects also. On the other hand, when a neutrino interacts with a free nucleon, such as when a neutrino interacts with a hydrogen nucleus which is effectively a free proton, no nuclear effects are present and the cross-section depends only on the structure of the free nucleon. Neutrinos do not have any structure as they are the so-called fundamental particles. Nucleons have a more complicated structure than just a spherical ball of uniformly distributed electric charge. For example, a neutron is electrically neutral, which means it has no overall electric charge. However, it is made up of one up quark and two down quarks, which are individually charged, and their asymmetric distribution leads to a non-uniform charge distribution inside a neutron. The articles [33, 34] present a detailed description of the electric charge distribution inside a neutron and a proton. Similarly, nucleons have a magnetization distribution.

Charge distribution or magnetization distribution as a function of radial position cannot be measured experimentally and hence, they are not directly useful in determining interaction cross-section. An alternative is to use form factors. Their exact definition and usage is too complicated to be explained here and is better left off for the quantum field theory books to explain. However, their physical interpretation can be given in simple terms. First of all, form factors are functions of a relativistic invariant  $Q^2$ . References [35, 36] describe the four form factors, which are a part of electroweak interactions. They are Vector Form Factors, Axial Form Factor and Pseudoscalar Form Factor.

There are two Vector form factors, Dirac  $F_1(Q^2)$  and Pauli  $F_2(Q^2)$  form factors, first proposed by Yennie *et al.* [37], which are used to write down neutrino-nucleus interaction cross-section in the upcoming sections. These can be further written in terms of Sachs electric ( $G_E$ ) and magnetic ( $G_M$ ) form factors as follows with  $\tau = Q^2/4M^2$ , where  $M$

is the average nucleon mass:

$$F_1 = \frac{G_E + \tau G_M}{1 + \tau} \qquad F_2 = \frac{G_M - G_E}{1 + \tau} \qquad (2.1)$$

Sachs *et al.* [38, 39] proposed this transformation as electric and magnetic form factors can be interpreted physically. In the Breit frame,  $G_E(Q^2)$  and  $G_M(Q^2)$  are the Fourier transforms of the electric charge and magnetization distributions. Breit frame is a frame used in lepton-nucleon scattering experiments to determine the electromagnetic form factors of the nucleon. This frame is defined such that the virtual photon exchanged in the interaction has zero energy and the momentum of the incident photon is antiparallel to that of the initial momentum of the nucleon [40, 41].

Earlier experiments and analyses used to describe electromagnetic form factors by dipole approximation. Dipole approximation means that the electric charge spatial distribution and magnetization spatial distribution of a free proton or neutron can be treated as exponential [42]. In this approximation,  $G_E^{proton} \approx G_D$ ,  $G_M^{proton} \approx \mu_p G_D$ ,  $G_E^{neutron} \approx 0$  and  $G_M^{neutron} \approx \mu_n G_D$ , where  $G_D = (1 + Q^2/M_V^2)^{-2}$ ,  $M_V = 0.84$  GeV, and,  $\mu_p$  and  $\mu_n$  are the magnetic moment of the proton and neutron respectively, whose value can be found in [43]. However, the dipole form factor and an exponential charge distribution out to infinity are not realistic, and modern experiments and theoretical calculations rarely use the dipole form.

Since neutrinos interact only via weak interaction and electromagnetic factors no longer dominate, it is up to neutrino experiments to determine axial form factor. Axial form factor characterizes the axial charge spatial distribution, which is a fairly important property of a nucleon. It determines the contribution of the up quark and down quark intrinsic spin to the total nucleon spin of 1/2. It is also an important factor in neutron decays [44].

The first and the simplest assumption of the axial form factor was dipole approximation such that

$$F_A(Q^2) = F_A(0) (1 + Q^2/M_A^2)^{-2} \qquad (2.2)$$

where,  $F_A(0)$  is known to a high precision from nuclear beta decay [43]. My thesis also uses this approximation with  $M_A = 0.99$  GeV for quasielastic scattering and  $M_A = 1.12$  GeV for delta and higher resonances. These values of axial mass were first determined from the data of deuterium bubble chamber experiments conducted in 1970s.

Since the past decade, there has been a lot of research going on in this area. Dipole approximation is no longer used by experiments as it does not describe the experimental data well. There are three different results available in the literature. One result given by Meyer *et al.* [45] is based on the  $z$  expansion analysis used in conjunction with bubble chamber data to determine axial form factor. The second result comes from the lattice QCD calculations [46]. The third one comes from the recent publication by MINERvA Collaboration in which they have done the first high-statistics measurement of the antineutrino-proton scattering to extract nucleon axial charge radius [47]. These three results are not in agreement with each other.

The fourth form factor is pseudoscalar form factor  $F_P$ . When contributing to the total cross-section, this form factor is suppressed by a factor of  $m_l^2/M^2$ , where  $m_l$  is the lepton mass (muon mass when muon neutrino undergoes charged-current interactions) and  $M$  is the average nucleon mass, in the neutrino-nucleus interactions studied in this work. In the pion pole dominance ansatz which has been shown to work very well [48], it can be directly determined from the experimentally measured axial form factor as follows

$$F_P(Q^2) = \frac{4M^2 F_A(Q^2)}{Q^2 + m_\pi^2}, \quad (2.3)$$

where  $m_\pi$  is the charged pion mass.

### 2.1.1 Introduction to Structure Functions and their energy dependence

Until now, form factors have been discussed, which are an important part of the neutrino-nucleus interaction cross-section, but are not enough to describe interactions

when the struck nucleon is in a nuclear medium. Nuclear effects also have to be included in the calculations.

To write the general neutrino-nucleon interaction cross-section for a free nucleon, leptonic  $L_{\mu\nu}$  and hadronic  $W_{\mu\nu}$  tensors are used.  $L_{\mu\nu}$  contains the information about the incoming neutrino and the muon produced in the charged-current interactions.  $W_{\mu\nu}$  contains information about the struck nucleon and four-momentum transfer, and is written in terms of six structure functions  $W_1, W_2, W_3, W_4, W_5$  and  $W_6$  [17, 18]. The inner product  $L_{\mu\nu}W^{\mu\nu}$  ultimately enters the expression of cross-section and only the first five structure functions survive in this inner product.

The expression for the charged-current double-differential cross-section that is applicable to all interaction processes such as QES, Resonance and DIS is [49]:

$$\frac{d^2\sigma}{dq_0dq_3} = \frac{G_F^2 \cos^2\theta_C q_3}{2\pi E_\nu^2} \bar{L}_{\mu\nu} \bar{W}^{\mu\nu}, \quad (2.4)$$

where,

$$\begin{aligned} \bar{L}_{\mu\nu} \bar{W}^{\mu\nu} = & W_1 (Q^2 + m_l^2) + W_2 \left( 2E_\nu(E_\nu - q_0) - \frac{m_l^2 + Q^2}{2} \right) \pm \frac{W_3}{M} (E_\nu Q^2 \\ & - \frac{q_0}{2} (m_l^2 + Q^2)) + \frac{W_4}{M^2} \left( \frac{Q^2 m_l^2 + m_l^4}{2} \right) - \frac{W_5}{M} m_l^2 E_\nu \end{aligned} \quad (2.5)$$

and, the symbols  $G_F, \theta_C, E_\nu, m_l$  and  $M$  represent Fermi coupling constant, Cabibbo angle, incoming neutrino energy, lepton mass, and the average nucleon mass respectively. The average nucleon mass means the average of the mass of proton and neutron. The “+” sign in the expansion of  $L_{\mu\nu}W^{\mu\nu}$  refers to neutrino interactions and “-” refers to antineutrino interactions. “Bar” over leptonic and hadronic tensor represents the average over final spins.

In general, structure functions are two-dimensional. They are a function of both  $q_0$  and  $q_3$ . This can be seen directly in the case of delta resonance which has a width in the triangle diagram even for a free nucleon. The width corresponds to a wide range of invariant masses because of the very short lifetime of the delta baryon and the

time-energy expression of the Heisenberg's uncertainty principle. On the other hand, quasielastic scattering on a free nucleon is just a curve on the triangle diagram and hence, structure functions are single-dimensional and just the function of  $Q^2$ . This is the reason why structure functions can be directly related to the quasielastic scattering model for a free nucleon. However, when neutrino strikes a nucleus and interacts with a bound nucleon, nuclear effects must be included in the structure functions. References [35, 50, 51] show how these effects can be included and how free nucleon structure functions are related to the structure functions containing nuclear effects. For the purpose of this thesis, it will be assumed that the structure functions contain nuclear effects unless otherwise mentioned.

### Energy dependence of the charged-current neutrino-nucleus interactions

One of the main aims of this thesis is to analyze the energy dependence of charged-current neutrino-nucleus interactions. The starting point would be to separate terms in Eq. 2.4 based on the order of neutrino energy ( $E_\nu$ ) such that

$$\begin{aligned} \frac{\bar{L}_{\mu\nu}\bar{W}^{\mu\nu}}{E_\nu^2} = & \frac{1}{E_\nu^2} \left[ W_1 (Q^2 + m_l^2) - \frac{W_2}{2} (m_l^2 + Q^2) \mp \frac{q_0 W_3}{2M} (m_l^2 + Q^2) \right. \\ & \left. + \frac{W_4}{M^2} \left( \frac{Q^2 m_l^2 + m_l^4}{2} \right) \right] + \frac{1}{E_\nu} \left[ -2q_0 W_2 \pm \frac{W_3 Q^2}{M} - \frac{W_5 m_l^2}{M} \right] + 2W_2 \quad (2.6) \end{aligned}$$

$W_2$  is the only structure function with an energy independent factor associated with it. So, at higher neutrino energies such that of MINERvA, it is expected that  $W_2$  would be the most dominant structure function for the neutrino scattering since the other terms are suppressed, and the cross-section can be approximated to  $2W_2$ . In lower energy experiments such as NOvA, T2K and DUNE, the next lower order  $E_\nu$  term i.e. the term governed by  $1/E_\nu$  would be of significance and couldn't be ignored. In this term,  $W_2$ ,  $W_3$  and  $W_5$  structure functions are present. However,  $W_5$  is suppressed by  $m_l^2/M$ , and, hence, only  $W_2$  and  $W_3$  have a significant contribution to the  $1/E_\nu$  term.

To say again, most of MINERvA's measurements at 6 GeV constrain only the  $2W_2$  term. NOvA's beam peaks at 2 GeV, as is the oscillation max for DUNE. So the  $1/E$  terms are 3 times more significant than at MINERvA and the  $1/E^2$  terms are 9

times more significant. Conceptually, NOvA could use MINERvA measurements as the uncertainty on  $2W_2$  and assign theory motivated uncertainties on the other terms. By extension, the experiments at and below 1 GeV (T2K, SBN) might not benefit at all from MINERvA's  $2W_2$  constraint.

### 2.1.2 Llewelyn Smith Model for QE Scattering and Comparison of Form Factors and Structure Functions

Llewelyn Smith wrote a detailed paper on QE Scattering on a free nucleon [23]. The paper was summarised by Anthony Mann in a technical (pedagogical) note posted to MINERvA and NOvA [52]. This section takes a lot of content from the Mann's work on the Llewelyn Smith model of quasielastic scattering. The section is concluded by describing the similarity between the structure functions and form factors for this model.

Eq. 2.5 expands the inner product of leptonic tensor and hadronic tensor in terms of structure functions. The same inner product can be expanded in terms of form factors for a QE scattering on a free nucleon. The corresponding expression taken from [52] is

$$\bar{L}_{\mu\nu}\bar{W}^{\mu\nu} = (4M^2)^2 A(Q^2) \mp \frac{(s-u)}{M^2}(4M^2)^2 B(Q^2) + \frac{(s-u)^2}{M^4}(4M^2)^2 C(Q^2) \quad (2.7)$$

where “bar” over the tensors represents the average over final spins. The “-” sign corresponds to neutrino interactions and the “+” sign corresponds to antineutrino interactions.  $s$  and  $u$  are Mandelstam variables, which are Lorentz-invariant.  $s - u$  is given by the following equation in terms of mass of nucleon ( $M$ ), energy of the incident neutrinos ( $E_\nu$ ), four-momentum transfer ( $q$ ) and mass of lepton ( $m_l$ ).

$$s - u = 4ME_\nu + q^2 - m_l^2 \quad (2.8)$$

$A(Q^2)$ ,  $B(Q^2)$  and  $C(Q^2)$  are Llewelyn's forms, usually, written in terms of the dimensionless  $\tau = -q^2/4M^2 = Q^2/4M^2$ . They are related to form factors as follows:

$$\begin{aligned}
A(\tau) &= 4\tau \left[ |F_A|^2 (1 + \tau) - |F_V^1|^2 (1 - \tau) + |\xi F_V^2| \tau (1 - \tau) + 4F_V^1 \xi F_V^2 \tau \right] \\
B(\tau) &= -4\tau F_A (F_V^1 + \xi F_V^2) \\
C(\tau) &= \frac{1}{4} \left[ |F_A|^2 + |F_V^1|^2 + \tau |\xi F_V^2|^2 \right]
\end{aligned} \tag{2.9}$$

where,  $F_A$  represents the axial form factor,  $F_V^1$  and  $F_V^2$  represent the vector form factors [53] and  $\xi$  denotes the difference between the magnetic moment of proton and neutron.

For quasielastic scattering on a free nucleon, the differential cross-section is given by

$$\frac{d\sigma}{dQ^2} = \frac{G_F^2 \cos^2 \theta_c}{128\pi E_\nu^2 M^2} \bar{L}_{\mu\nu} \bar{W}^{\mu\nu} \tag{2.10}$$

which can be further expanded to

$$\frac{d\sigma}{dQ^2} = \frac{G_F^2 \cos^2 \theta_c M^2}{8\pi E_\nu^2} \left[ A(\tau) \mp B(\tau) \frac{s-u}{M^2} + C(\tau) \frac{(s-u)^2}{M^4} \right] \tag{2.11}$$

Using Eq. 2.8 in Eq. 2.7, the energy dependent terms in the cross-section can be separated on the basis of the order of neutrino energy as follows

$$\begin{aligned}
\frac{\bar{L}_{\mu\nu} \bar{W}^{\mu\nu}}{E_\nu^2} &= \frac{1}{E_\nu^2} \left[ A(Q^2) \mp B(Q^2) \frac{(4ME_\nu - Q^2 - m_l^2)}{M^2} + \frac{C(Q^2)}{M^4} \left( 16M^2 E_\nu^2 + \right. \right. \\
&\quad \left. \left. (Q^2 + m_l^2)^2 \right) - 8ME_\nu (Q^2 + m_l^2) \right] \\
&= \frac{1}{E_\nu^2} \left[ A(Q^2) \pm B(Q^2) \frac{(Q^2 + m_l^2)}{M^2} + \frac{C(Q^2)}{M^4} (Q^2 + m_l^2)^2 \right] + \\
&\quad \frac{1}{E_\nu} \left[ \mp \frac{4B(Q^2)}{M} - \frac{8C(Q^2)}{M^3} (Q^2 + m_l^2) \right] + \frac{16C(Q^2)}{M^2}
\end{aligned} \tag{2.12}$$

This equation expresses energy dependence in terms of Llewellyn Smith's  $A(Q^2)$ ,  $B(Q^2)$  and  $C(Q^2)$ , which are a function of form factors, and Eq. 2.5 expresses energy dependence in terms of structure functions. For the quasielastic scattering on a free nucleon, the corresponding orders of neutrino energy can be compared between the two expressions. This is possible since the structure functions are also one-dimensional for

QE scattering on a free nucleon.

With that start from Llewelyn Smith and Mann, comparing the energy independent term between the two expressions gives

$$W_2 = 8C(Q^2)/M^2. \quad (2.13)$$

Similarly, comparing the sign-altering term in  $1/E$  term gives

$$W_3 = -4B(Q^2)/Q^2 \quad (2.14)$$

while the other terms give, using Eq. 2.13,

$$W_5 = W_2 \left( 1 + \frac{Q^2}{m_l^2} - \frac{2q_0 M}{m_l^2} \right) \quad (2.15)$$

From  $1/E^2$  term, comparing sign-altering terms gives

$$W_3 = -\frac{2B(Q^2)}{q_0 M} \quad (2.16)$$

while the other terms give, using Eq. 2.13,

$$W_1 + \frac{W_4 m_l^2}{2M^2} = \frac{A(Q^2)}{Q^2 + m_l^2} + \frac{4C(Q^2)}{M^2} + \frac{C(Q^2)}{M^4} (Q^2 + m_l^2) \quad (2.17)$$

Additionally, comparing Eq. 2.14 and Eq. 2.16 yields

$$\frac{Q^2}{2Mq_0} = 1 \quad (2.18)$$

as it should be because this is the condition for quasielastic scattering on a free nucleon.

Using Eq. 2.18 in Eq. 2.15, the following QE specific relation is obtained.

$$W_2 = W_5. \quad (2.19)$$

This section shows how different structure functions can be related to form factors for a quasielastic scattering on a free nucleon. Ref. [35] does this in detail and gives

an exact relation between structure functions and form factors where pseudoscalar form factor and other small terms are not neglected.

## 2.2 Analysis of QE structure functions

As discussed earlier, QE scattering is just a 1D curve with negligible, delta-function-like width in the triangle diagram for a free nucleon. One more way to understand this is using the concept of invariant mass. Just like  $q_0$  and  $q_3$ , invariant mass ( $W$ ) and  $Q^2$  can also be used to get a 2D plot. For a free nucleon,  $W$  is fixed at 938 MeV and only  $Q^2$  varies. Thus, it is a 1D plot and structure functions are a function of  $Q^2$  only.

There is little point in talking about free neutrons since they do not exist as a source or a target. On the other hand, a free proton is just hydrogen and it is readily available. When QE scattering happens in a nucleus on a bound nucleon, Fermi motion of the nucleon plays an important role. When a nucleon is free, it is assumed to be at rest. However, due to Fermi motion inside a nucleus, QE scattering has a width in the triangle diagram and is actually a 2D plot. Thus, QE scattering can be analyzed both as a 1D plot and a 2D plot inside a nucleus. The method to analyze it in 1D is discussed in the next section.

Mahbub [26] analyzed the energy dependence of the cross section for interactions on a free nucleon, as a function of the natural variable. Here I am repeating and extending that analysis using the Valencia calculation for QE reactions on nucleons in carbon. The difference is that the distribution is now two dimensional in the lab frame because of the motion of the nucleons in carbon. Their calculation also includes Pauli blocking and a nuclear screening effect known as Random Phase Approximation (RPA). There is only one specific subsection where RPA is not considered for the purpose of analyzing the effect of RPA on interaction cross-section. Except for that, it is a part of every calculation and plot.

Figures come from running the original Valencia FORTRAN code for the  $^{12}\text{C}$  nucleus, both with and without RPA in QE, and 2p2h Model. The Valencia code is called

by the C++ code, written by Federico Sanchez, Professor, Université de Genève (at the time was at IFAE, Universitat Autònoma de Barcelona), and Richard Gran, Professor, University of Minnesota Duluth, that accesses quantities within the FORTRAN routines directly [8]. Additionally, all the plots in this chapter contain the cross-section per carbon nucleus with its 6 protons and 6 neutrons.

### 2.2.1 Structure Functions in 1D

The cross-section  $d^2\sigma/dq_0dq_3$  for QE scattering is two-dimensional for a bound nucleon. However, it can be analyzed in one-dimension as  $d\sigma/dQ^2$  such that variables are changed from  $(q_0, q_3)$  to  $(q_0, Q^2)$  or  $(q_3, Q^2)$  in the first step using the transformation rules as described in [54]. The second step is to integrate  $q_0$  or  $q_3$  over its range, which is 0 to  $E_\nu$  (only approximately for  $q_3$ ), so that  $Q^2$  is the only variable left.

The variable change used to obtain plots in this section is

$$q_0, q_3 \rightarrow q_0, Q^2 = q_3^2 - q_0^2 \quad (2.20)$$

The Jacobian of the transformation is  $1/2q_3$ , and hence, the one-dimensional cross-section per nucleus at a particular  $Q^2$  can be obtained using:

$$\int \frac{1}{2q_3} \frac{d^2\sigma}{dq_0dq_3} dq_0. \quad (2.21)$$

Alternatively, it can be obtained by integration over  $q_3$  instead of  $q_0$  as mentioned earlier, the Jacobian being  $1/2q_0$ . However, it is convenient to integrate over  $q_0$  as its upper limit is  $E_\nu$ , and depends solely on the energy of the incoming neutrino. Without a careful thought, it might seem that the upper limit of  $q_3$  should also be  $E_\nu$ , energy and momentum of the neutrino being equal. However, inside a nucleus, nucleons are always in motion [55] and thus the upper limit of  $q_3$  goes beyond the expected value and must be carefully taken from the two-dimensional plots such as Fig. 2.2.

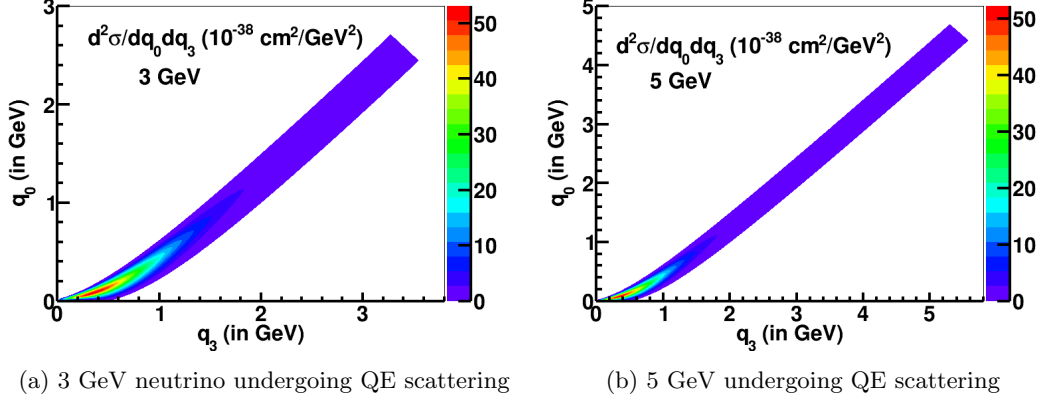


Figure 2.2: Double differential cross-section depicting Fermi motion when a neutrino undergoes QE scattering with a nucleon

Fig. 2.2 shows that the two-dimensional plots extend by about 0.55 GeV past  $E_\nu$  on the  $q_3$ -axis for both the neutrino energies. QE Scattering is just an infinitesimally thin curve in the case of free nucleons but it attains a width due to their Fermi motion in the nucleus. The width of the plots is similar for both neutrino energies. This behaviour is expected since the Fermi motion across different energies is uniform. QE cross-section maximum is not exactly in the middle of the colored area. It is slightly shifted upward.

The kinematic restriction due to the energy and momentum of the neutrino, and extra kinematic space due to Fermi motion is easily visible in single-differential cross section versus  $Q^2$  plots. In Fig. 2.2, the two cut-off ends in the upper right corner correspond to  $Q^2$  (in  $\text{GeV}^2$ ) = 3.35 and 6.53 for 3 GeV neutrino, and to  $Q^2$  (in  $\text{GeV}^2$ ) = 5.99 and 11.49 for 5 GeV neutrino, with smaller  $Q^2$  corresponding to the upper vertex. For  $Q^2 > 6.53 \text{ GeV}^2$  for 3 GeV neutrino, no event is expected and the cross-section should drop down to zero as shown in Fig. 2.3. Similar behaviour is expected from 5 GeV neutrino for  $Q^2 > 11.49 \text{ GeV}^2$ .

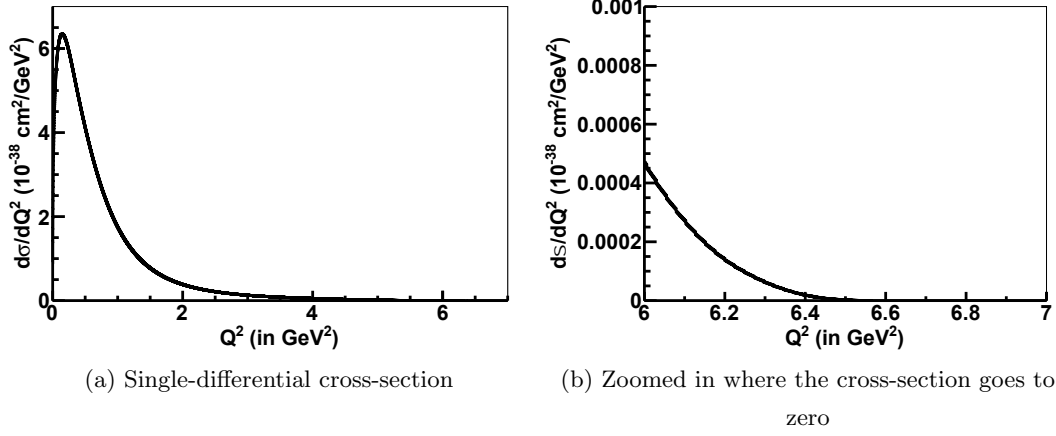


Figure 2.3: Single-differential cross-section per nucleus goes to zero around  $Q^2 = 6.53$   $\text{GeV}^2$  for 3 GeV neutrino

The behaviour of the cross-section around the other limit of  $Q^2$  for neutrinos is apparent when the ratio of the plots for two energies is taken.

A new terminology is introduced here to study the structure functions along with the kinematic terms in 1D. The names are as used in the code, and are defined with numerical integration. There is no equivalent convention in the literature for this quantity. The resulting quantity is a function of  $Q^2$ .

$$\begin{aligned}
 ww1int &= \int \frac{1}{2q_3} \frac{W_1(Q^2 + m_l^2)}{E_\nu^2} q_3 dq_0 \\
 ww2int &= \int \frac{1}{2q_3} \left( 2W_2 - \frac{2q_0 W_2}{E_\nu} - \frac{W_2(Q^2 + m_l^2)}{2E_\nu^2} \right) q_3 dq_0 \\
 ww3int &= \pm \int \frac{1}{2q_3} \left( \frac{W_3 Q^2}{E_\nu M} - \frac{q_0 W_3(Q^2 + m_l^2)}{2M E_\nu^2} \right) q_3 dq_0 \\
 ww4int &= \int \frac{1}{2q_3} \frac{W_4 m_l^2 (Q^2 + m_l^2)}{2M^2 E_\nu^2} q_3 dq_0 \\
 ww5int &= - \int \frac{1}{2q_3} \frac{W_5 m_l^2}{M E_\nu} q_3 dq_0
 \end{aligned} \tag{2.22}$$

In all these expressions, the term  $\frac{G_F^2 \cos^2 \theta_C}{2\pi}$  is always multiplied. Since it is a constant and won't affect the energy dependence analysis, it is not written again and again for the sake of brevity. The following figure shows these quantities as a function of  $Q^2$ .

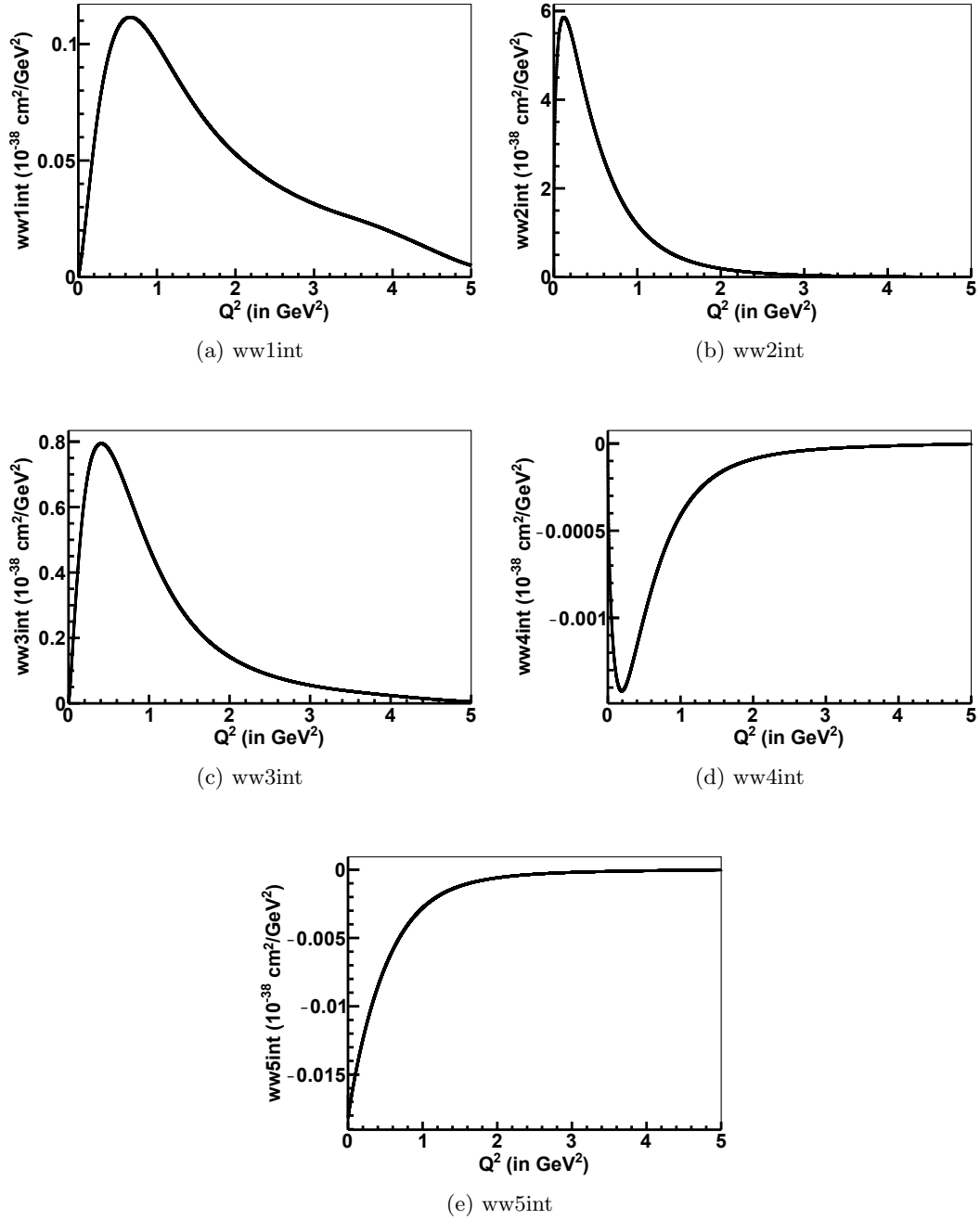


Figure 2.4: Structure functions ( $wwint$ 's) for 3 GeV neutrinos. The cross section is the simple sum of the five panels, where  $W_2$  is by far the largest at this energy.

As explained earlier, the term containing  $W_2$  dominates the cross-section in general which is also shown in Fig. 2.4. The second dominant contribution comes from  $W_3$  as it is present in the next lower order of  $E_\nu$ .  $W_5$  also has  $1/E_\nu$  attached to it but it is suppressed by its kinematic factors.  $W_1$  and  $W_4$  terms contain the energy dependence as  $1/E_\nu^2$ . This factor and their kinematic terms make them sub-dominant.

### 2.2.2 Ratios across different energies

When a ratio is taken of structure function contributions for different energies, it is expected that the ratio of  $ww1int$ ,  $ww4int$  and  $ww5int$  for  $E_{high}/E_{low}$  should be constant and equal to  $(E_{low}/E_{high})^2$ ,  $(E_{low}/E_{high})^2$  and  $E_{low}/E_{high}$  respectively using Eq. 2.22. However, the ratios of  $ww2int$  and  $ww3int$  have  $E_\nu$  and  $Q^2$  dependence. Carefully analysing their expressions, it can be seen that their ratios should increase with the increase in  $Q^2$ . Additionally, the rise would be flatter for ratio of 15 GeV/5 GeV terms compared to the ratio of 5 GeV/3 GeV terms.

The expected constant ratios of  $ww1int$ ,  $ww4int$  and  $ww5int$  for 5 GeV/3 GeV are 0.36, 0.36 and 0.6 respectively. It can be seen in Fig. 2.5 that the ratios adhere to the expected behaviour till  $Q^2$  of about 3.5 GeV<sup>2</sup>, after which all of them start rising up at a much higher rate. This  $Q^2$  value corresponds to the top vertex explained earlier and for  $Q^2$  higher than this value, the events of 3 GeV neutrinos start dropping due to kinematic restrictions while the events of 5 GeV neutrinos remain unaffected. That's why the ratio starts rising up. Similar behaviour is expected from the plots of ratio 15 GeV/5 GeV around  $Q^2 = 5.99$  GeV<sup>2</sup>.

MINERvA typically works on  $Q^2 < 1.5$  GeV<sup>2</sup> and this strange behaviour is beyond its domain. However, for NOvA, T2K and other experiments operating at lower energies, this analysis is important and must be understood. The following figure shows the 1D structure function quantities ( $wwint$ 's) ratio for 5 GeV to 3 GeV neutrino energy.

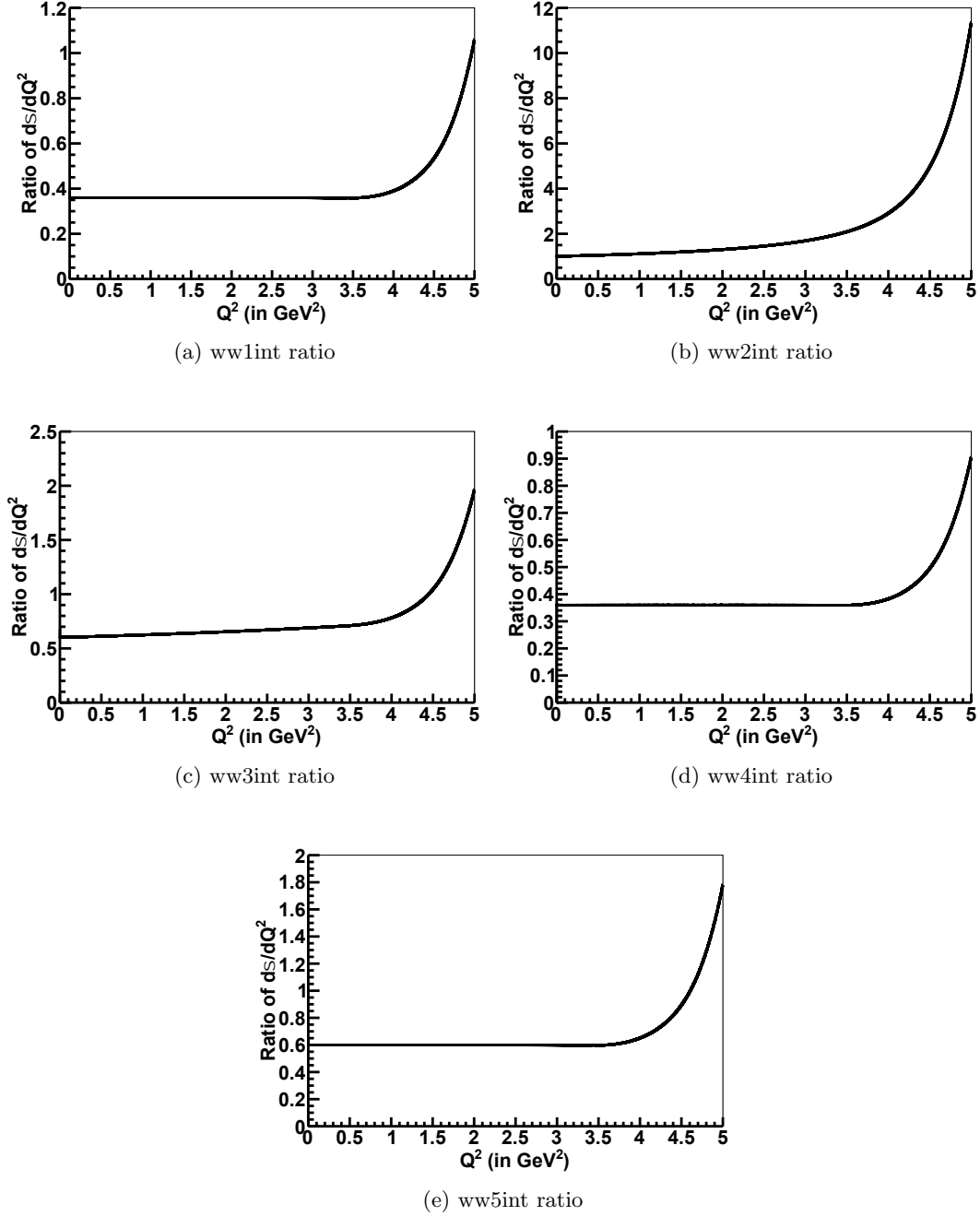


Figure 2.5: Ratio of structure function contributions  $5 \text{ GeV} / 3 \text{ GeV}$ . The ratios are 1.0, 0.6, and 0.36 until about  $Q^2 = 4 \text{ GeV}^2$  when the ratio is affected by the kinematic boundary visible in the 2D plots in the earlier figure.

Although the ratio of structure functions increases or remains constant, the total cross-section, which is dominated by the second and the third structure function as shown in the next section, decreases with increase in  $Q^2$  as shown in Fig. 2.6, and exhibits the similar stranger behaviour around  $Q^2 = 3.5 \text{ GeV}^2$  as seen above. The figure also contains a zoomed in plot for  $Q^2 < 1.5 \text{ GeV}^2$  which shows that the ratio of cross-section 5 GeV/ 3 GeV drops by about 6% in this  $Q^2$  range. This cross-section ratio of about 0.95 for 5 GeV and 3 GeV neutrinos is small enough and MINERvA is unlikely to measure it experimentally.

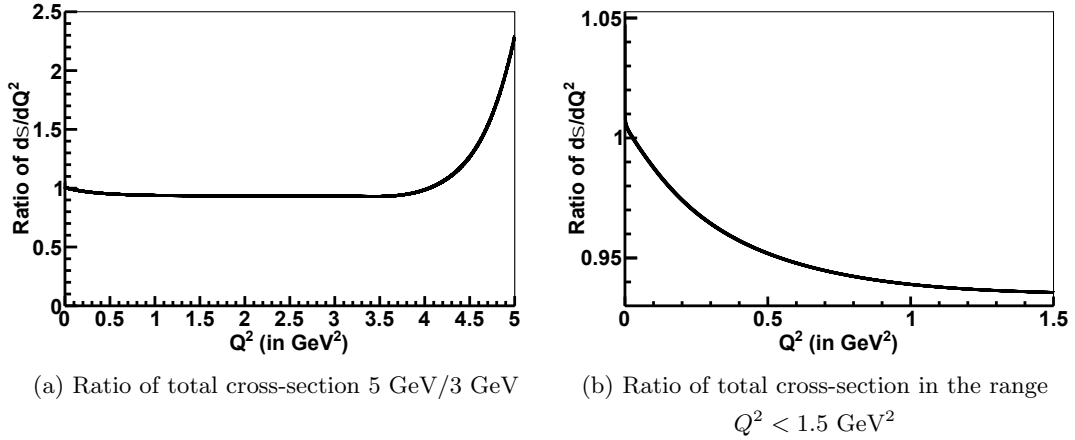


Figure 2.6: Ratio of  $d\sigma/dQ^2$  for 5 GeV/3 GeV neutrinos drops by about 6% in the range  $Q^2 < 1.5 \text{ GeV}^2$

At the end of this section, it must be clarified that the term “total cross-section” used in this section simply refers to the summation of the structure functions along with their kinematic terms. Generally, it means the integration of the differential section as defined at the beginning of this chapter. However, for the purpose of the structure function study, whether one-dimensional or two-dimensional, it is simply the summation of terms containing structure functions.

### 2.2.3 Fractional Contribution of Different Structure Functions in Total Cross-Section

$W_2$  makes an energy-independent dominant term, so it is expected to have the maximum contribution.  $W_3$  and  $W_5$  have  $1/E$  energy dependence, so they are expected to have the second-dominant contribution. This subsection compares the relative sizes to gain intuition about where in kinematic space energy dependence will appear first. However, the kinematic term  $m_l^2/M$  associated with  $W_5$  makes it much smaller compared to other structure function terms. The next dominant terms should be  $W_1$  and  $W_4$ , however,  $W_4$  tags along an extra  $m_l^2/M^2$  kinematic term which makes it much smaller just like  $W_5$  term.

The paragraph above comments on the dominance of structure functions based on the kinematic factors associated with them. However, it is possible that individual structure function value outweighs the kinematic factor dependence. For example,  $W_1$  might be smaller for one interaction and not for other. Thus, it is fine as a starting point to use kinematic factors to draw initial conclusions about the relative contribution of structure functions but it should always be checked with actual calculations or plots (or data). For QE and 2p2h as we see in this and the next section, the initial comments are proven to be true.

The magnitude of the first three structure functions can be directly compared in Fig. 2.7. This is a subset of the terms in Fig. 2.5 but combines in a single plot in the style of Mahbub's thesis [26].

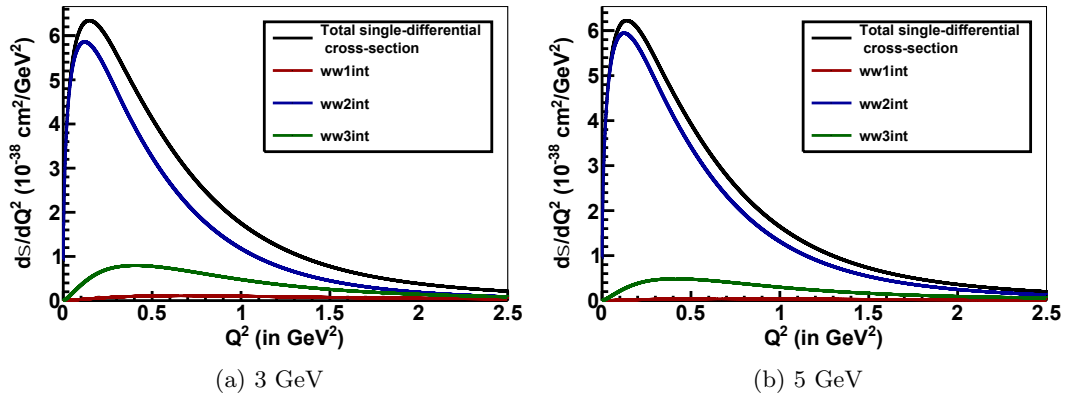


Figure 2.7: The first three structure functions and the total cross-section for 3 GeV and 5 GeV neutrinos

The second structure function is pretty close to the total cross-section and it gets even closer at higher energy. On the other hand, the first structure function and the third structure function have a reduction in their fractional contribution.

The exact fractional contribution of each structure function can be depicted by plotting the ratio of structure functions and the total cross-section as in Fig. 2.8.

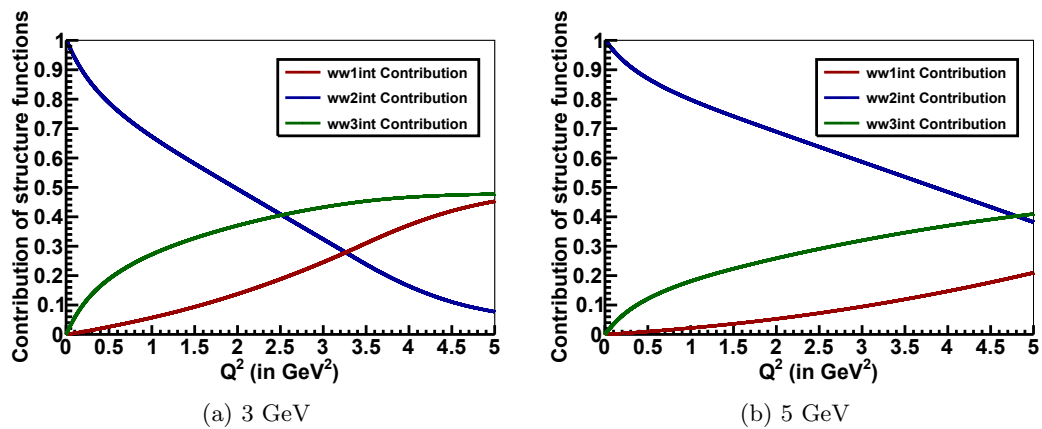


Figure 2.8: Fractional contribution of the first three structure functions in the total cross-section for 3 and 5 GeV neutrinos

As can be seen in Fig. 2.8, within the range of interest of MINERvA, structure functions stick to the expected dominance behaviour. At higher  $Q^2$ ,  $Q^2$  dependent terms in the expression Eq. 2.22 become significant and change the order of dominance. This happens at higher  $Q^2$  for 5 GeV neutrinos as compared to 3 GeV neutrinos. There is an energy dependence at high  $Q^2$  (and high  $q_3$  in the 2D plots) because the kinematic cutoff starts earlier in  $q_3$  for 3 GeV neutrinos. There is a second source of energy dependence at high  $Q^2$  because the intrinsic  $Q^2$  dependence means that  $W_1$  and  $W_3$  structure functions overtake it.

Table. 2.1 shows the approximate dominance of each structure function term for 3 GeV and 5 GeV neutrinos.

Table 2.1: Fractional contribution of different structure functions in total cross-section for 3 GeV and 5 GeV neutrinos for different values of  $Q^2$  (in  $\text{GeV}^2$ )

Str. Func.	Energy	$Q^2 = 0.5$	$Q^2 = 1.0$	$Q^2 = 1.5$
ww1int	3	0.03	0.06	0.09
	5	0.01	0.02	0.04
ww2int	3	0.78	0.66	0.57
	5	0.87	0.79	0.73
ww3int	3	0.19	0.28	0.34
	5	0.12	0.19	0.23

For both the energies, the contributions of the three structure functions add up to 1. This means that the contribution of  $ww4int$  and  $ww5int$  is tiny and negligible in comparison to that of other structure functions. Their fractional contribution can be seen in Fig. 2.9. The figure shows that  $ww4int$  and  $ww5int$  terms are negative and have the least contribution in general, which decreases even more for the higher energy.  $ww4int$  term is negative because  $W_4$  itself is negative for QE process. On the other hand,  $ww5int$  term is negative because it carries a minus sign and  $W_5$  is positive for the QE process. It is shown in Section 2.1.2 that  $W_5 = W_2$  for a free nucleon and  $W_2$  is always positive. Although this relation doesn't necessarily hold for a bound nucleon, it still gives a possible reason why  $W_5$  might be positive for QE scattering inside a nucleus.

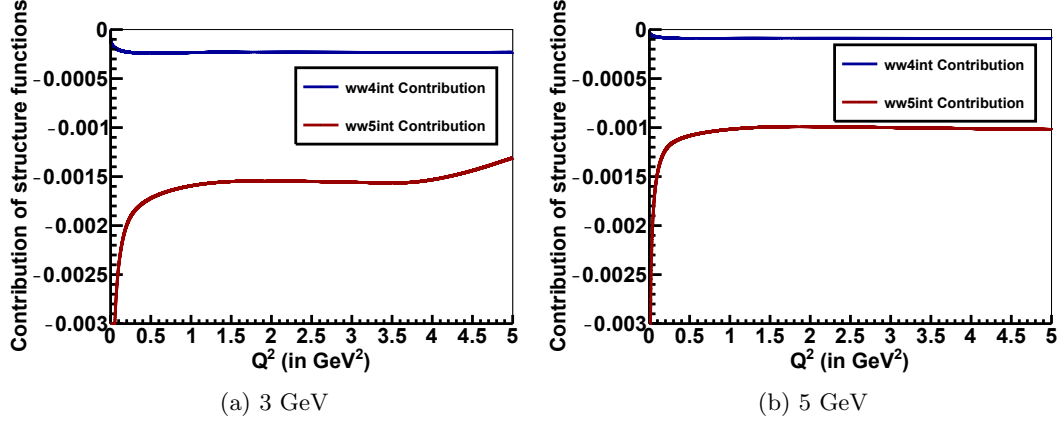


Figure 2.9: Fractional contribution of the fourth and fifth structure functions in the total cross-section for 3 and 5 GeV neutrinos

Fig. 2.9 shows that  $ww5int$  might have a larger contribution as  $Q^2 \rightarrow 0$ . Table. 2.2 summarises the fractional contribution of all the structure functions in the first bin, i.e.  $0 < Q^2 < 0.001 \text{ GeV}^2$ .

Table 2.2: Fractional contribution of all the structure functions in total cross section for 3 GeV and 5 GeV neutrinos as  $Q^2 \rightarrow 0$

Str. Func.	3 GeV	5 GeV
ww1int	0.00032	0.00012
ww2int	1.01755	1.01079
ww3int	0.00026	0.00017
ww4int*	-0.00004	-0.00002
ww5int	-0.01815	-0.01106

\*  $ww4int$  has the first bin as  $-\infty$  for some reason for both the energies. Hence, the fractional contribution of  $ww4int$  stated in the table is the average of 0 and its fractional contribution in the second bin.

The fractional contributions given in Table 2.2 cannot be verified theoretically in this work. However, the ratio of the fractional contributions of  $-ww5int$  and  $ww2int$

can be verified under the assumption that  $W_2 \approx W_5$  and energy-dependent terms in  $ww2int$  can be ignored in comparison to the term containing  $2W_2$ . Using Eq. 2.22,

$$\begin{aligned} ww2int &\approx \frac{G_F^2 \cos^2 \theta_C}{2\pi} \int \frac{1}{2q_3} (2W_2) q_3 dq_0 \\ ww5int \text{ (scaled by -1)} &= \frac{G_F^2 \cos^2 \theta_C}{2\pi} \int \frac{1}{2q_3} \frac{W_5 m^2}{ME_\nu} q_3 dq_0 \end{aligned} \quad (2.23)$$

Using the relation  $W_2 \approx W_5$  for quasielastic scattering on a bound nucleon gives

$$\begin{aligned} \frac{-ww5int}{ww2int} &= \frac{m^2}{2ME} \\ &= \frac{0.00595}{E_\nu \text{ (in GeV)}} \end{aligned} \quad (2.24)$$

Hence, the ratio should be 0.00198 and 0.00119 for 3 GeV and 5 GeV neutrinos respectively.

At low  $Q^2$ , nuclear effects such as Pauli Blocking [20] and RPA [19] start dominating and impulse approximation [56] no longer holds. The approximations used in deriving Eq. 2.24 hold for high  $Q^2$  only. Because of this, the calculated and actual ratios match for only  $Q^2 > 0.2 \text{ GeV}^2$  as shown in Fig. 2.10. Table 2.2 shows that the actual ratio is 0.0178 and 0.0109 for 3 GeV and 5 GeV neutrinos respectively as  $Q^2 \rightarrow 0$ .

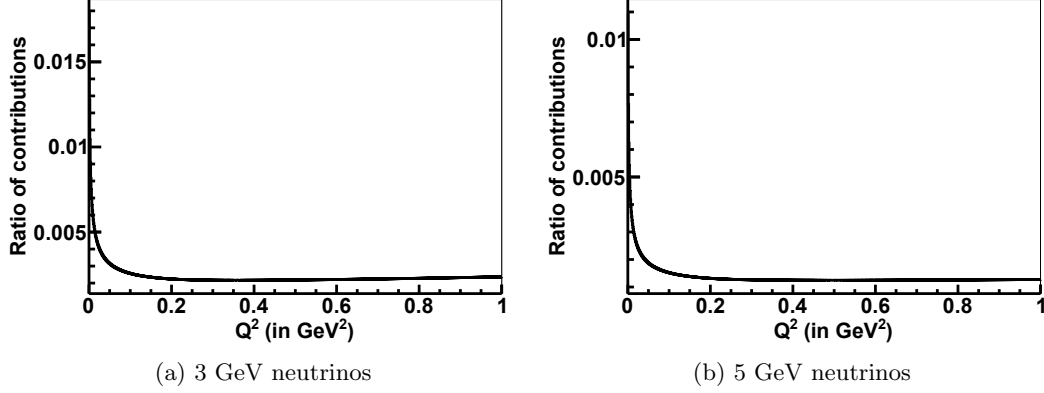


Figure 2.10: Ratio of contribution of the fifth (scaled by -1) and the second structure functions in the total cross-section for 3 and 5 GeV neutrinos

#### 2.2.4 Structure Functions in 2D

From here onwards,  $ww$ 's means the corresponding terms in the double-differential cross-section similar to  $wwint$ 's without the integration. Also, the physics focus will be on  $q_3 < 2$  GeV where MINERvA measurements are robust and the RPA and Pauli Blocking effects are most noticeable, but away from the high  $Q^2$ , high  $q_3$  kinematic cutoffs.

Writing them explicitly,

$$\begin{aligned}
 ww1 &= \frac{W_1 (Q^2 + m_l^2)}{E_\nu^2} \\
 ww2 &= W_2 \left( 2 - \frac{2q_0}{E_\nu} - \frac{(Q^2 + m_l^2)}{2E_\nu^2} \right) \\
 ww3 &= \pm W_3 \left( \frac{Q^2}{E_\nu M} - \frac{q_0 (Q^2 + m_l^2)}{2ME_\nu^2} \right)
 \end{aligned} \tag{2.25}$$

where the factor  $\frac{G_F^2 \cos^2 \theta_C q_3}{2\pi}$  is always multiplied and “+” sign is used for neutrino-nucleus interactions. Since this work is on neutrino interactions, the natural choice is “+” sign.

Two-dimensional  $ww$ 's, means structure functions with kinematic factors, can be plotted with respect to  $q_0$  and  $q_3$  where the color of the plot describes the magnitude of the structure functions. The first three structure functions are shown in Fig. 2.11 for 3 GeV neutrinos.  $ww_4$  and  $ww_5$  are not shown here since they are too small in comparison to other structure functions and can be safely ignored.

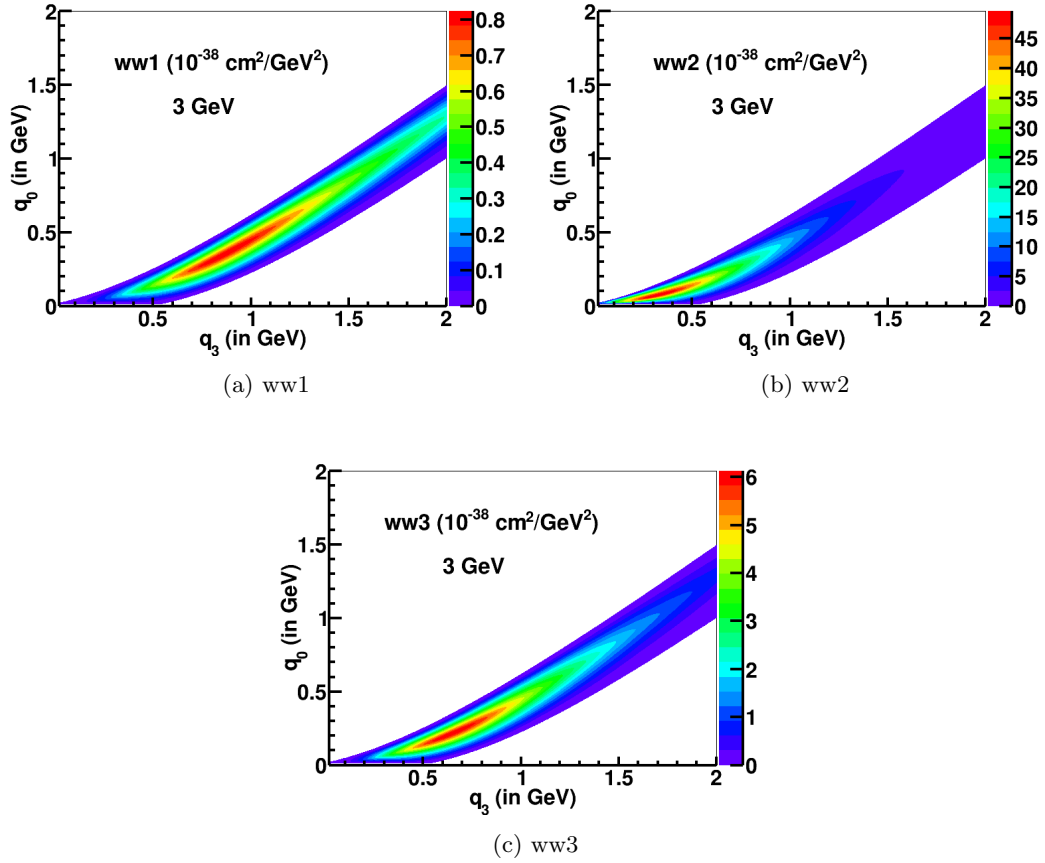


Figure 2.11: The first three structure function terms for 3 GeV neutrinos

$q_3$ -axis in the figure starts from 0.02 GeV instead of 0.0 GeV. This is because the code that is available has some error in that  $q_3$  range and gives unreasonably high values of structure functions.

Fig. 2.11 shows structure functions along with kinematic factors containing terms

of various order of energy dependence. Energy Independent Term containing  $2W_2$ ,  $1/E$  term in  $ww2$  and  $1/E^2$  term in  $ww2$  can be plotted separately. Similarly, individual terms of different orders of energy can be plotted for  $ww3$ . All these terms are shown in Appendix A.

In the interest of analyzing the energy dependence of neutrino-nucleus interactions, it is imperative that the Energy Independent Term in the cross-section, which is  $2W_2$  along with its kinematic factors, and  $1/E$  Term are plotted together so that a comparison can be made.  $1/E$  Term is simply obtained by collecting all the terms in Eq. 2.6 of the order of  $1/E$ . Thus,  $1/E$  Term is

$$1/E \text{ Term} = \frac{1}{E} \left( \frac{W_3 Q^2}{M} - 2q_0 W_2 \right) \quad (2.26)$$

where the factor  $\frac{G_F^2 \cos^2 \theta_C q_3}{2\pi}$  is always multiplied, and the term containing  $W_5$  is not included even though it has the order of  $1/E$  since it is negligible compared to terms containing  $W_2$  and  $W_3$ . Energy Independent Term and  $1/E$  Term can be plotted together as follows. The text inside the figure uses the symbol  $\omega$ , which is same as  $q_0$ .

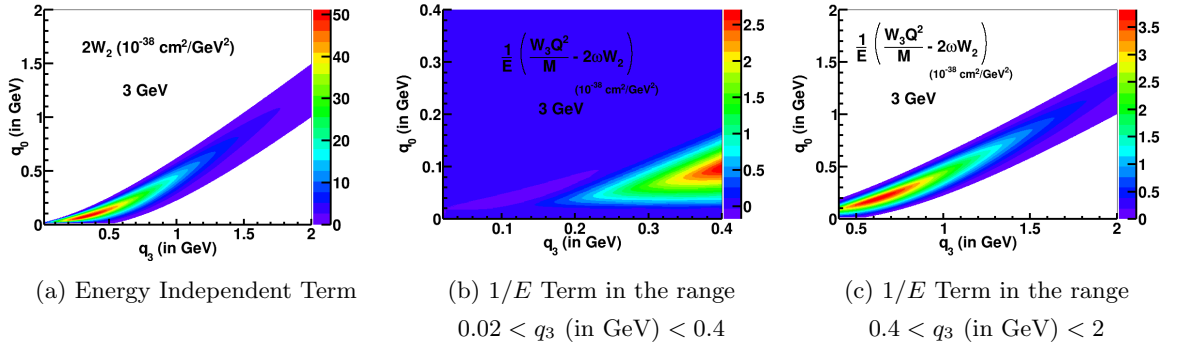


Figure 2.12: Energy Independent Term and  $1/E$  Term for 3 GeV neutrinos

In Fig. 2.12, the first figure shows the whole Energy Independent Term although the text inside the figure is just  $2W_2$ . It is just a representation of the term.  $1/E$  Term is broken down into two  $q_3$  ranges, 0.02 GeV to 0.4 GeV and 0.4 GeV to 2 GeV. The

reason is that for  $q_3 < 0.4$  GeV,  $1/E$  Term is both negative and positive for QE scattering. Because of this reason, ROOT assigns a color to every point in the plot where the  $1/E$  Term goes to 0 and thus, the whole plot looks colored.  $1/E$  Term is positive everywhere for  $q_3 > 0.4$  GeV, so this visual artifact is not a problem.

It is clear from the figure that  $1/E$  Term is about 15 times smaller than Energy Independent Term containing  $2W_2$  at a neutrino energy of 3 GeV. Similarly, it is 30 times smaller for the MINERvA peak of 6 GeV. This shows that  $W_2$  dominates the cross-section by a large amount at MINERvA energies. The  $W_3$  enters into the picture for lower energy experiments such as MicroBooNE and T2K, preferentially enhancing the higher  $q_3$  and  $Q^2$  parts of the cross-section. The cross-section for the NOvA experiment is in the middle, the  $1/E$  Term at 2 GeV is 10 times smaller than the Energy Independent Term.

### 2.2.5 Ratio of structure functions indicating the energy dependence introduced by RPA

The ratio of  $ww1$ ,  $ww4$  and  $ww5$  between energies  $E_{high}$  and  $E_{low}$  is straightforward and is equal to  $(E_{low}/E_{high})^2$ ,  $(E_{low}/E_{high})^2$  and  $E_{low}/E_{high}$  respectively. The ratio of  $ww2$  between the two energies can be evaluated as

$$\begin{aligned} \frac{ww2(\text{at } E_{high})}{ww2(\text{at } E_{low})} &= \frac{2W_2 - \frac{2q_0W_2}{E_{high}} - \frac{W_2(Q^2+m_l^2)}{2E_{high}^2}}{2W_2 - \frac{2q_0W_2}{E_{low}} - \frac{W_2(Q^2+m_l^2)}{2E_{low}^2}} \\ &= \frac{2 - \frac{2q_0}{E_{high}} - \frac{(Q^2+m_l^2)}{2E_{high}^2}}{2 - \frac{2q_0}{E_{low}} - \frac{(Q^2+m_l^2)}{2E_{low}^2}} \end{aligned} \quad (2.27)$$

Eq. 2.27 clearly shows that the ratio depends on both  $q_0$  and  $Q^2$ , or  $q_3$ . To get an approximate expression at MINERvA energies, the term of the order  $1/E^2$  can be ignored and the approximate expression will be

$$\frac{ww2(\text{at } E_{high})}{ww2(\text{at } E_{low})} = \left( \frac{E_{low}}{E_{high}} \right) \left( 1 + \frac{E_{high} - E_{low}}{E_{low} - q_0} \right) \quad (2.28)$$

At high energies or low energy transfer, the ratio of  $ww2$  tends to 1. Otherwise, it is always greater than 1. The ratio of  $ww3$  can be evaluated as

$$\begin{aligned} \frac{ww3(\text{at } E_{high})}{ww3(\text{at } E_{low})} &= \frac{\frac{W_3 Q^2}{ME_{high}} - \frac{q_0 W_3 (Q^2 + m_l^2)}{2ME_{high}^2}}{\frac{W_3 Q^2}{ME_{low}} - \frac{q_0 W_3 (Q^2 + m_l^2)}{2ME_{low}^2}} \\ &= \left( \frac{E_{low}}{E_{high}} \right)^2 \left( 1 + \frac{E_{high} - E_{low}}{E_{low} - \frac{q_0}{2} \left( 1 + \frac{m_l^2}{Q^2} \right)} \right) \end{aligned} \quad (2.29)$$

The ratio of  $ww3$  also depends on both  $q_0$  and  $Q^2$ , or  $q_3$ . In general,  $Q^2 \gg m_l^2$ , so the approximate expression for the ratio of  $ww3$  is given by

$$\frac{ww3(\text{at } E_{high})}{ww3(\text{at } E_{low})} = \left( \frac{E_{low}}{E_{high}} \right)^2 \left( 1 + \frac{E_{high} - E_{low}}{E_{low} - \frac{q_0}{2}} \right) \quad (2.30)$$

The ratio for both  $ww2$  and  $ww3$  should increase with an increase in energy transfer and be independent of a change in  $q_3$ .

For the ratio between 5 GeV and 3 GeV, the ratio for  $ww1$ ,  $ww4$  and  $ww5$  is expected to be 0.36, 0.36 and 0.6 respectively, while for  $ww2$  the ratio should be 1 and greater and for  $ww3$  the ratio should be 0.6 and greater.

Fig. 2.13 on the next page shows the ratio between the structure functions at 5 GeV and 3 GeV. It can be seen that the ratios do not stick to their expected behaviour. The ratio of  $ww1$ ,  $ww4$  and  $ww5$  is not constant but has a slight variation of about 2%. The ratio of  $ww2$  and  $ww3$  varies with  $q_3$  also. This deviation from the expected behaviour and additional energy dependence is coming not from Fermi motion or Pauli blocking but from RPA as shown next.

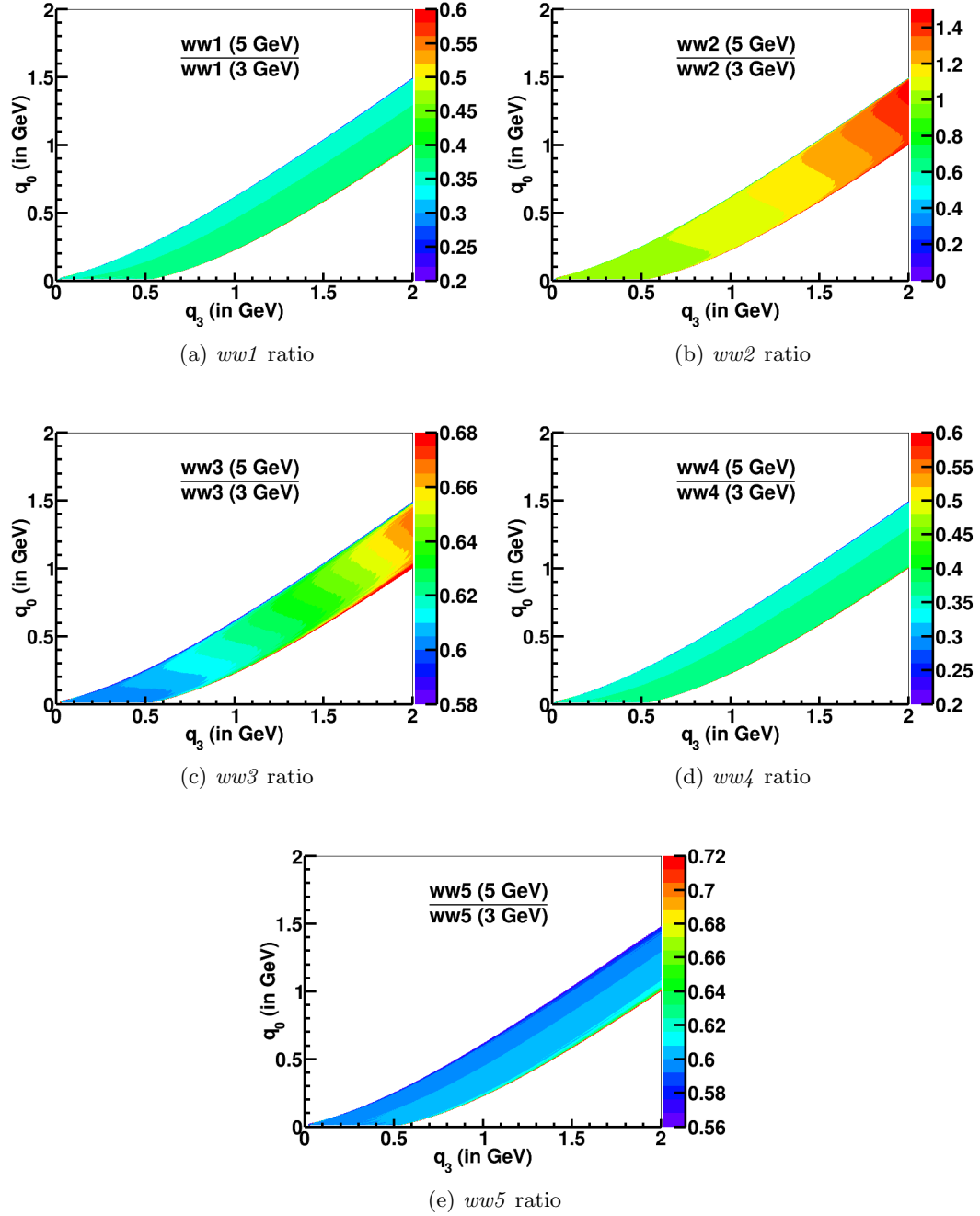


Figure 2.13: Ratio of structure function contributions 5 GeV / 3 GeV. The ratios show a slight variation from their constant values of 0.36 and 0.6, and a slight variation along the  $q_3$ -axis.

### 2.2.6 Energy Dependence coming from RPA and its uniformity across different structure functions

A free nucleon is bereft of any nuclear effects. However, a nucleon in a nucleus is affected by Pauli Blocking [20], Random Phase Approximation (RPA) [19], Fermi Motion [55] and Removal Energy [57] to name a few. RPA was introduced in the place of the impulse approximation [36] and is one of the most interesting pieces of nuclear physics in this calculation by the Valencia group. Impulse approximation is an approach to lepton-nucleus scattering in which it is assumed that there is no interaction between the nucleons and the incoming lepton interacts with only single nucleon in the case of quasielastic scattering. In reality, nucleons are not independent and the interactions between them, called correlations, exist. The RPA screening effect is usually considered a kind of long-range correlation. The 2p2h process is a form of short-range correlation. Impulse approximation breaks down as  $Q^2 \rightarrow 0$ . This is referred to as the low- $Q^2$  problem [56]. RPA approximation was proposed as a resolution to this problem. It is primarily a screening effect that suppresses the cross-section at low  $Q^2$ . To the neutrino exchanging little energy and momentum, the target nucleon looks like half a nucleon. This subsection attempts to separate the energy dependence of this effect from the structure function effects in the Valencia calculation.

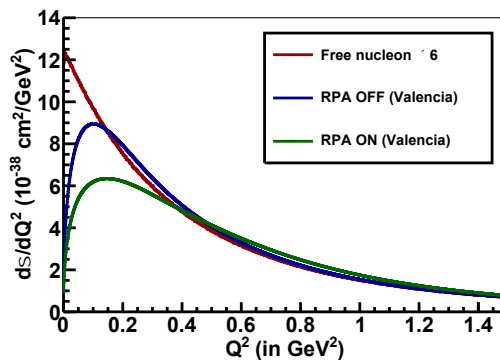


Figure 2.14: Single differential cross-section comparison of free nucleon (times 6), carbon nucleus ( $^{12}\text{C}$ ) with RPA OFF and RPA ON

Fig. 2.14 compares the cross-section of six free nucleons with that of a  $^{12}\text{C}$  nucleus with RPA OFF and ON. Cross-section is smaller when a neutrino interacts with a

neutron in a nucleus due to nuclear effects especially Pauli blocking at low  $Q^2$ . If RPA is ON, it reduces the cross-section even more at low  $Q^2$  and enhances the cross-section by a small amount at high  $Q^2$ . This observation is in agreement with the results presented in [19].

### **Additional Energy Dependence introduced by RPA**

In this work, we find the Valencia Model for RPA changes the energy dependence of the cross-section, and it can be seen when the ratio of structure functions is taken. As shown in Fig. 2.13, the ratios do not stick to the expected values. This behaviour disappears when the ratio is taken with RPA turned off.

Fig. 2.15 on the next page shows that the ratio of  $ww1$ ,  $ww4$  and  $ww5$  is constant and equal to 0.36, 0.36 and 0.6 respectively for 5 GeV and 3 GeV neutrinos. The ratio of  $ww2$  and  $ww3$  is also not dependent on  $q_3$ . The structure functions recover their expected values, and the gradient in  $ww1$ ,  $ww4$ , and  $ww5$  disappears when RPA is turned off. This shows that RPA introduces an additional energy dependence in structure functions. Since this additional energy dependence is about 2%, it can be safely ignored for the purpose of experimental analysis since the uncertainties in the MINERvA data are greater than 2%.

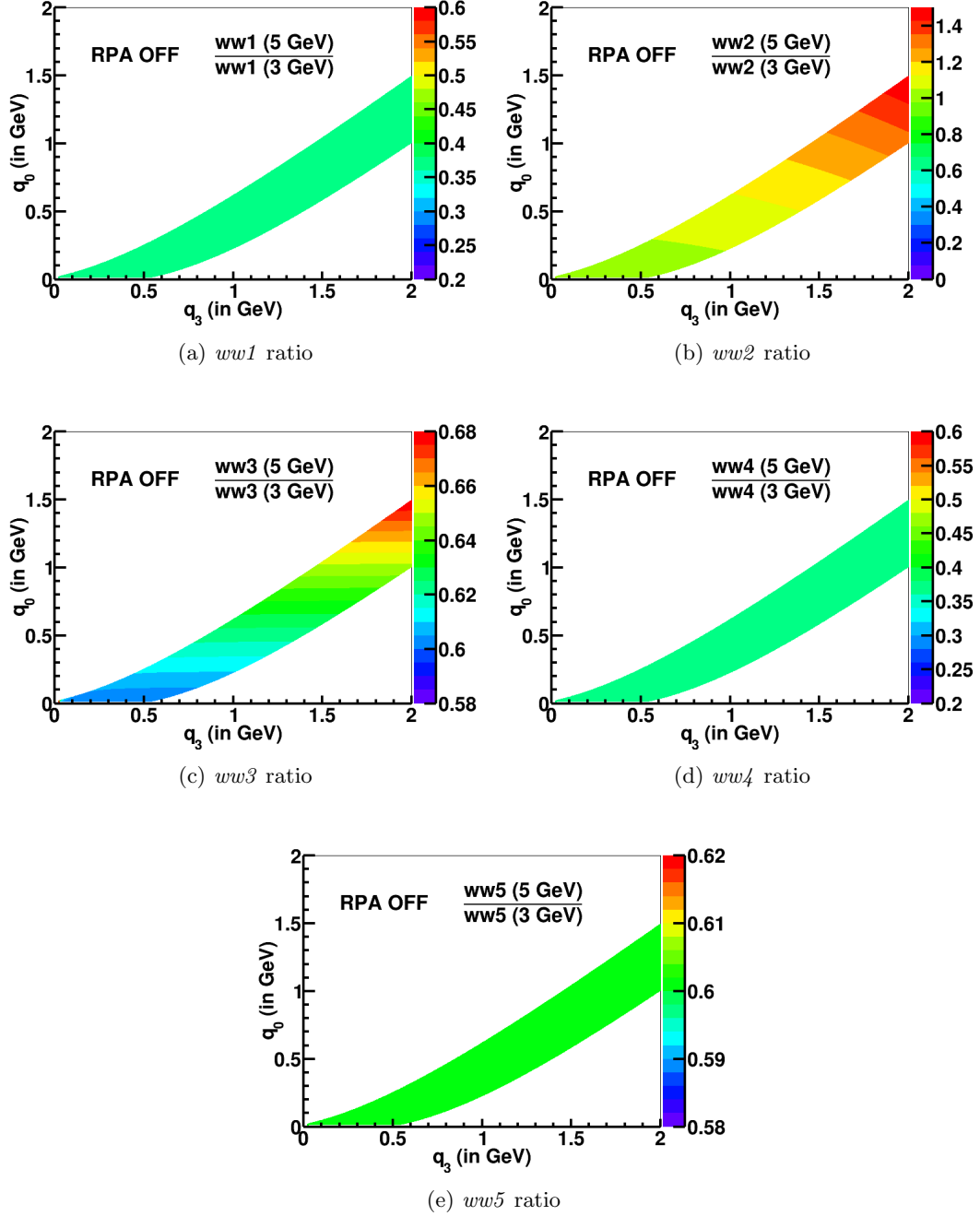


Figure 2.15: Ratio of structure functions between 5 GeV and 3 GeV neutrinos with RPA OFF. The gradient has disappeared in the ratios of  $ww1$ ,  $ww4$  and  $ww5$ . The ratios of  $ww2$  and  $ww3$  are also no longer varying with  $q_3$ .

### Uniformity of RPA across different structure functions

To observe the effect of RPA on different structure functions, ratio can be taken between  $ww$ 's when RPA is ON and OFF. These are like the comparisons in Gran *et al.* [8] and Gran [19], but separated into the individual five structure functions.

It is important to determine whether it is uniform across all structure functions or not. This is connected to the extraction of structure functions discussed in the next chapter. If RPA is significantly non-uniform, then the method discussed in the next chapter will have to incorporate this non-uniformity carefully. Luckily, it is uniform for all practical purposes as shown in Fig. 2.16. It therefore does not modify the energy dependence in the way a  $W_3$ -only effect or a major change in the form factors will. It varies a bit but that is beyond the MINERvA threshold.

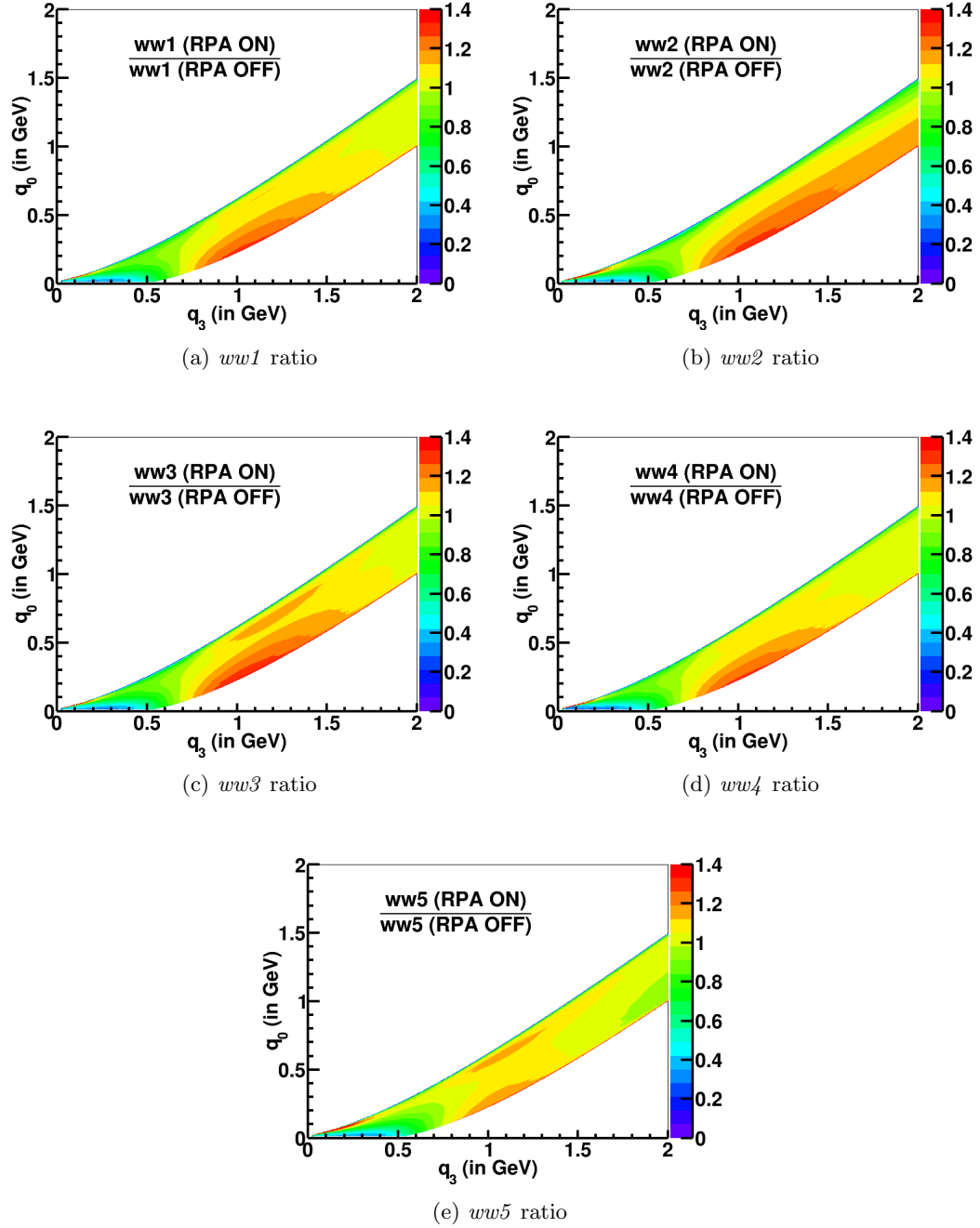


Figure 2.16: Ratio of structure functions between RPA ON and RPA OFF at 3 GeV

Fig. 2.16 shows that the effect of RPA is almost uniform across all the structure functions. To do a better comparison, the single-differential cross-section can be compared between the dominant structure functions,  $ww2$  and  $ww3$ , as a function of energy transfer.

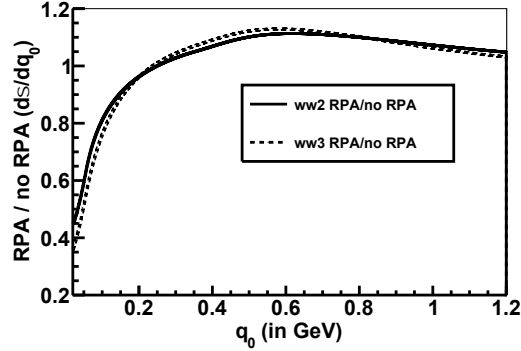


Figure 2.17: Comparison of the effect of RPA across  $ww2$  and  $ww3$  for 3 GeV

In addition to the uniform effect of RPA on structure functions, Fig. 2.17 shows that RPA suppresses the cross-section for  $q_0 < 0.2$  GeV and varies by a small amount after that, which is also supported by the results in Ref. [19].

### 2.2.7 Fractional Contribution of Structure Functions

Moving away from the RPA effect and back to the bigger picture, Section 2.2.3 and 2.2.4 have already given a clear evidence that  $ww2$  has the largest contribution followed by  $ww3$ . Their fractional contribution can be plotted in 2D also. Fig. 2.18 compares the fractional contribution of the first three structure functions against each other and between 3 GeV and 5 GeV neutrinos. The reader must keep in mind that the color scale changes from plot to plot. There are three important observations from the figure:

- In the low-recoil sample ( $q_3 < 1.2$  GeV),  $ww2$  has the largest contribution followed by the contribution of  $ww3$  and  $ww1$ . It is above 70% for  $ww2$ , below 25% for  $ww3$  and below 5% for  $ww1$  in this sample. Due to the uncertainties in MINERvA data,  $ww1$  can be safely ignored.

- The contribution of  $w_2$ , although more than any other structure function, decreases with an increase in neutrino energy. On the contrary, the contribution of  $w_3$  and  $w_1$  increases with an increase in neutrino energy.
- The contribution of  $w_1$  and  $w_3$  increases with an increase in energy transfer or momentum transfer, while  $w_2$  has just the opposite behaviour.

Fig. 2.18 shows the fractional contribution of structure functions. These 2D plots show only a little additional structure compared to their integral in the  $Q^2$  plots in Section 2.2.3.

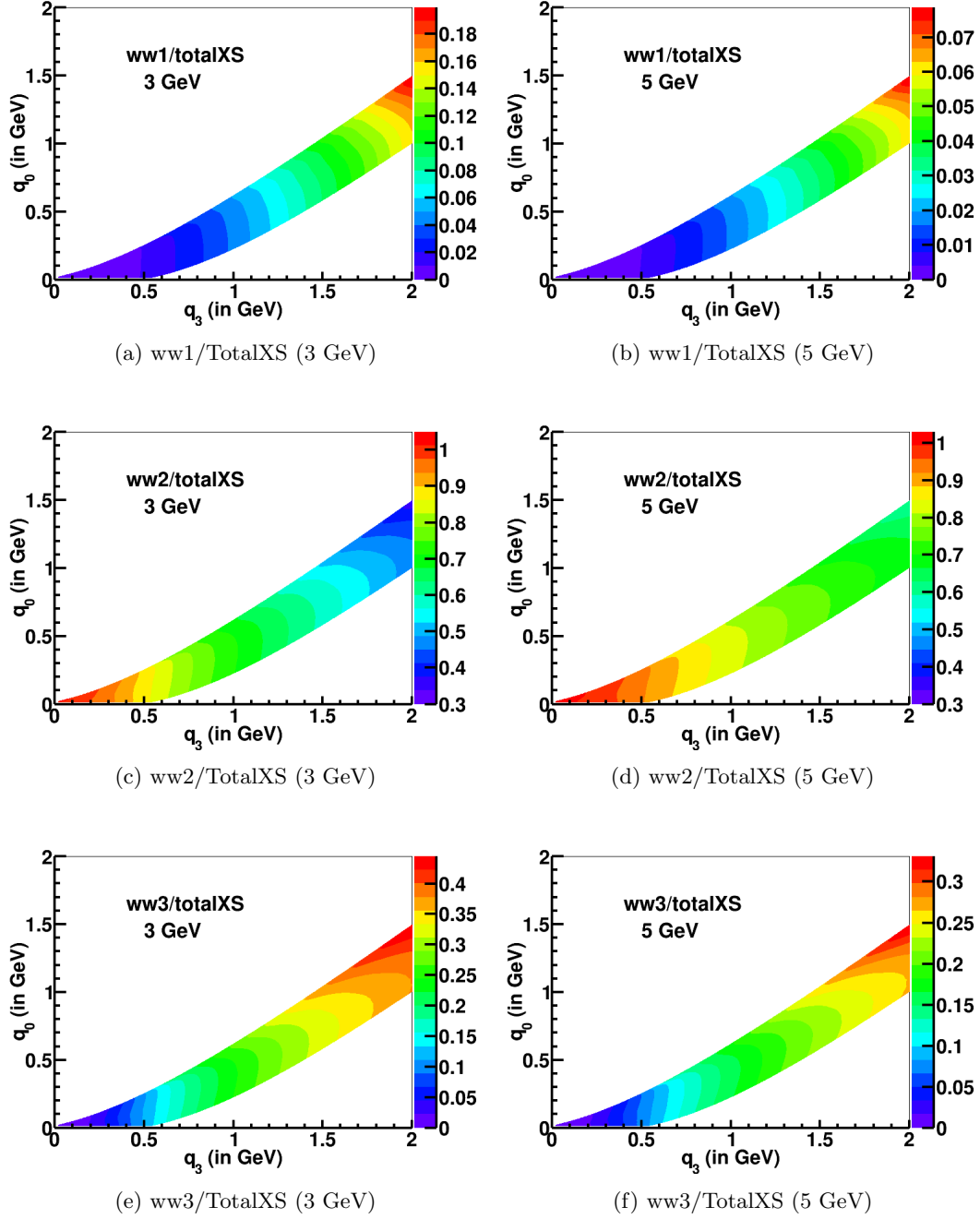


Figure 2.18: Fractional contribution of structure functions in total cross section (totalXS) of QE scattering for 3 GeV and 5 GeV neutrinos. Caution, the color scale changes from plot to plot, so blue to red in one plot shows the trend but are not the same values as in another plot.

To determine the contribution of Energy Independent Term and  $1/E$  Term in the total cross-section, they can be plotted separately. Fig. 2.12 shows the plots of these terms already and depicts that  $1/E$  Term is much smaller in comparison to Energy Independent Term. Fig. 2.19 shown here compares the fractional contributions of energy-independent term and  $1/E$  Term between 3 GeV and 5 GeV neutrinos.

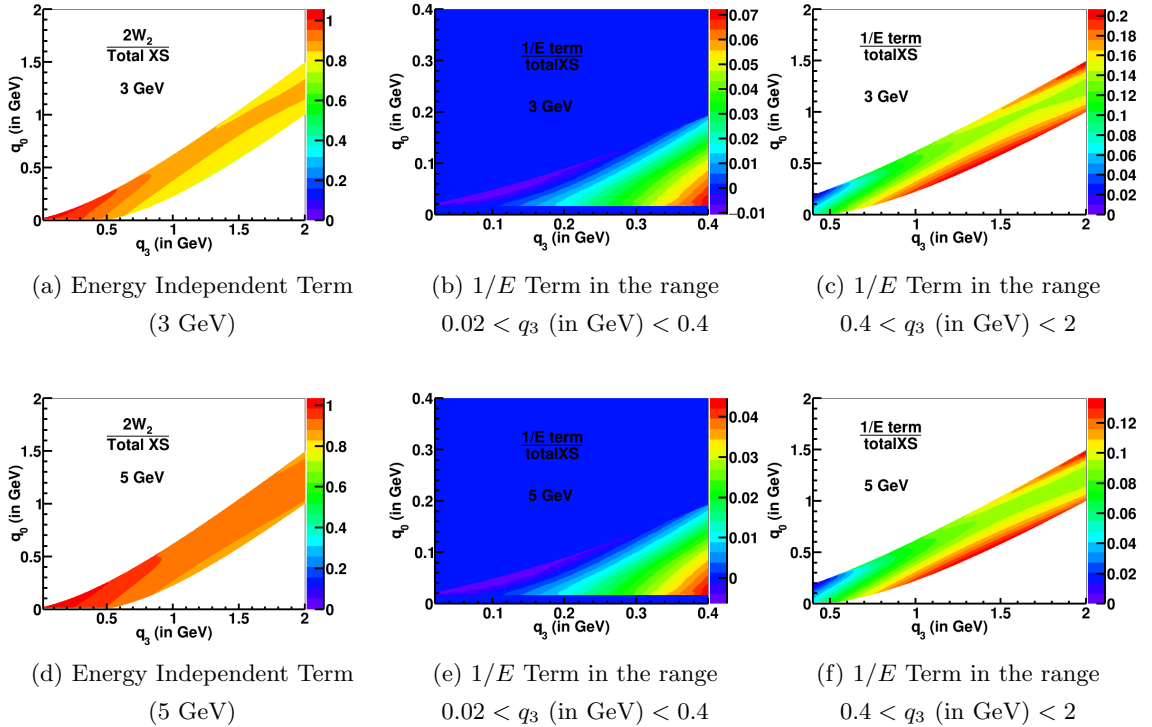


Figure 2.19: Fractional contribution of Energy Independent Term and  $1/E$  Term for 3 GeV and 5 GeV neutrinos. The middle plot is zoomed in on the lowest  $q_3$ , and here  $1/E$  Term goes negative, so the plotting package colors all the zero values blue in that case.

The figure above shows that Energy Independent Term has a contribution greater than 80% everywhere and 85% in the low-recoil sample for 3 GeV neutrinos. Both of these percentages rise up to 90% for 5 GeV neutrinos. On the other hand, the contribution of  $1/E$  Term is less than 20% everywhere and almost always less than 15% in the low-recoil sample. The corresponding percentages reduce to almost 10% for 5 GeV

neutrinos.

This analysis shows that energy dependence is very small at MINERvA energies and the cross-section is dominated by  $W_2$ . In particular, MINERvA data can, in principle, set a strong constraint on the  $W_2$  term but a relatively weak constraint on the  $1/E$  Term. Such a constraint could be used by NOvA to produce a mix of MINERvA empirical and form factor prediction for their 2 GeV data.

### 2.3 Analysis of 2p2h Structure Functions

Valencia code is available for both QE Scattering and 2p2h. It also provides structure functions separately for each process. The analysis of structure functions for 2p2h in this section is similar to that done in the previous section for QE scattering. The general idea is plotting structure functions for 2p2h and studying their contribution in the total cross-section to see how the energy dependent parameters for 2p2h differ from QE. To analyze the energy dependence, Energy Independent Term and  $1/E$  Term will also be plotted.

Although the analysis is similar for the 2p2h process compared to QE scattering, the two processes are different. QE scattering happens on a single nucleon, which is neutron when the incident beam consists of neutrinos, and 2p2h happens on a pair of nucleons. This pair can be of two neutrons (nn pair), a proton and a neutron (pn pair) and two protons (pp pair).

This work includes only nn and pn pairs. The cross-section of an interaction of a neutrino with a pp pair is not available from the Valencia code. Such a charge-changing neutrino reaction necessarily produces a  $\Delta^{++}$  in the final state which decays to a proton and a  $\pi^+$ . The Valencia group left this process off their calculation because they were interested in reactions that had zero pions in the final state. The Valencia 2p2h model does allow the production of delta resonances, but only when they are accompanied by the de-excitation of the delta through pion exchange with another nucleon. As such, the model has both QE-like and delta-like components in the kinematic space, even though

no pions and only virtual deltas are involved.

The other difference is that QE scattering can be interpreted in 1D as a function of  $Q^2$ . The integration can still be done (as a background to compare to an experimental QE distribution) but it also integrates over multiple cross section structures since 2p2h does not have a 1D analogue. 2p2h happens due to short-range correlations between the two nucleons and this correlation is not present in the case of free nucleons. On top of that, free neutrons also do not exist outside a nucleus.

### **2.3.1 Structure Functions**

Structure functions along with their kinematic factors (ww's) can be plotted and they are as follows

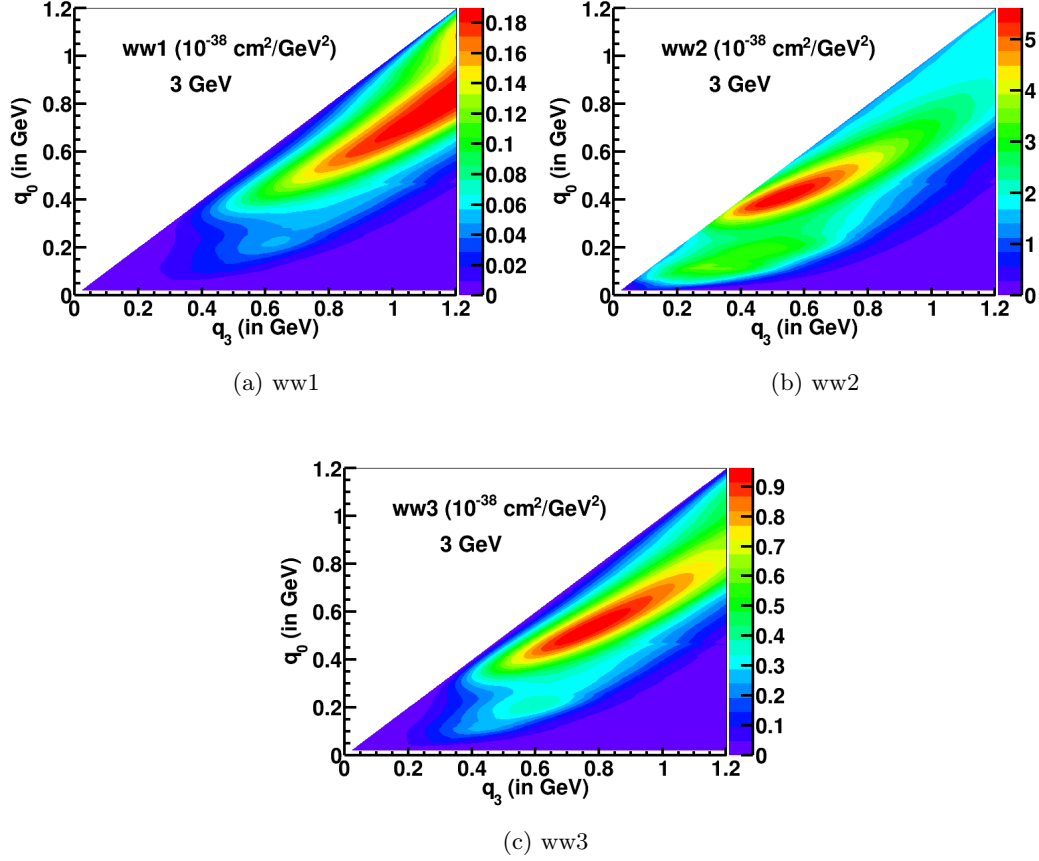


Figure 2.20: The first three structure function terms for 3 GeV neutrinos

Fig. 2.20 shows a stark difference between QE and 2p2h. QE scattering is limited to a small region in the plot. It is a line for free nucleons and gets a small width due to Fermi motion of nucleons inside a nucleus. However, 2p2h happens on a pair of nucleons and this leads to the presence of a non-zero cross-section in the whole kinematic space. The kinematic space corresponding to  $q_0 > q_3$  has zero cross-section (it is white) no matter which process it is since  $q_0 > q_3$  implies  $Q^2 < 0$  and  $Q^2$  has to be greater than 0 for an interaction to happen. The kinematic space in the lower right corner of the plot has predicted cross-sections that are not possible from the QE scattering with Fermi motion alone.

In all the plots of Fig. 2.20, the reddish region lies in the delta region. It appears that delta component is prominent in 2p2h process. This is not an actual delta production but only a virtual delta resonance produced through the mechanism explained at the beginning of this section. Just like QE scattering,  $ww2$  clearly dominates the cross-section followed by  $ww3$  and  $ww1$ .

Fig. 2.20 shows the structure functions with all the kinematic factors and energy dependence.  $ww1$  has only  $1/E^2$  dependence. The breakdown of  $ww2$  and  $ww3$  into individual energy components of the double-differential cross-section is provided in Appendix A.

To understand the energy dependence in 2p2h process, it is important to plot Energy Independent Term and  $1/E$  Term separately and compare them with each other. They are as follows

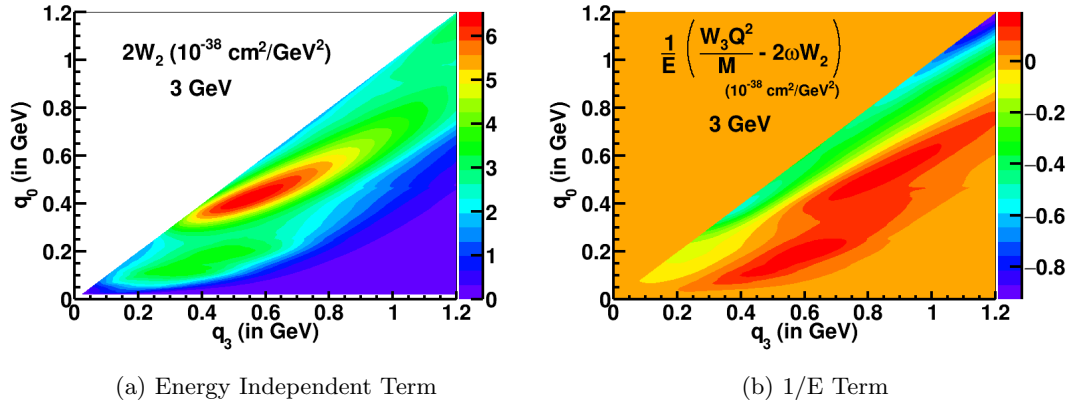


Figure 2.21: Energy Independent Term and  $1/E$  Term for 3 GeV neutrinos. As with other 2D plots, the plot on the right has substantial negative components, and the graphic program displays 0.0 as an orange color instead of white.

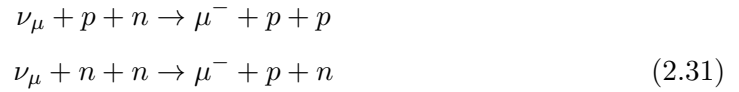
The  $1/E$  Term in Fig. 2.21 is not broken down into  $q_3$  ranges like QE Scattering because the  $1/E$  Term is negative in a lot of places and breaking it down into two plots won't be beneficial. It can be observed that Energy Independent Term, dictated by

$2W_2$ , is pretty big compared to the  $1/E$  Term. Where Energy Independent Term is maximum, it is bigger than the  $1/E$  Term by a factor of 20. This factor increases to 40 for a 6 GeV neutrino. Thus, at MINERvA energies, the  $1/E$  Term can be safely neglected for a 2p2h process and  $W_2$  structure function is enough to describe the interaction cross-section. Despite that simple statement, the 2p2h process has an extremely rich structure compared to the QE scattering, even in the region where the QE scattering overlaps.

If one assumed the energy dependence in 2p2h was like the QE process (or the delta process not studied in this thesis but in Ishmam Mahbub's thesis [26]), the data might have surprising energy dependence because of the complexity of the 2p2h process.

### 2.3.2 pn and nn contribution in $ww2$ and total cross-section

Valencia code has pn and nn initial state process encoded in the 2p2h process. The two processes are as follows:



These processes add up to give the cross-section of every structure function shown in Fig. 2.20. It is enough to show the cross-section coming from pn and nn in  $ww2$  since it is similar for all the structure functions. The other reason is that  $ww2$  has the largest contribution in the total cross-section so its analysis is the most important. Also, the plots for pn and nn are drawn at 3 GeV since the distribution of pn and nn in the total cross section is almost same in the MINERvA energy range.

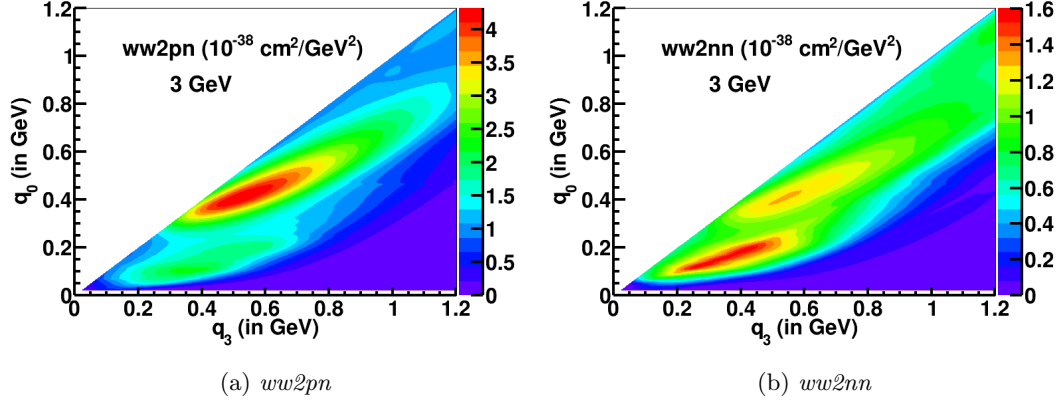


Figure 2.22: Breakdown of  $ww2$  into  $ww2pn$  and  $ww2nn$  for 3 GeV neutrinos

It can be seen from the plots that pn is the dominant process and its contribution is more than 50% in the whole kinematic space. In addition to the dominance coming from the cross-section calculations of a pn pair and a nn pair, the number of possible pn pairs is higher the number of possible nn pairs in a carbon nucleus. The nn pairs have a relatively stronger QE component (the lower red peak in the right plot in Fig. 2.23 shown below) because a QE-like process can only happen on neutrons in the nucleus. Absolute values of  $ww2pn$  and  $ww2nn$  are maximum in delta region and just below the dip region [58] respectively. The dip region is jargon for the region between the QE and the Delta peaks. Without Fermi motion or a 2p2h process, there should be zero cross section there. Like an atomic electron that cannot exist between the 1s state with an energy -13.6 eV and 2s state with an energy -3.4 eV, so also there should be no allowed value of  $W$  for baryons between 938 and 1232 GeV.

The exact contribution of  $ww2pn$  and  $ww2nn$  in the total cross-section can be seen by taking a ratio of the two and plotting them as follows

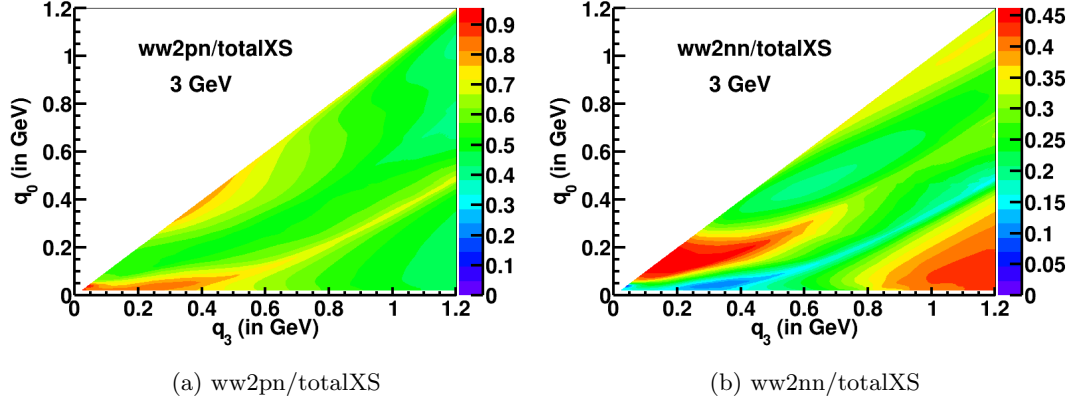


Figure 2.23: Fractional contribution of  $ww2pn$  and  $ww2nn$  in totalXS (pn + nn) for 3 GeV neutrinos

Fig. 2.23 confirms that pn is the dominant process. It can be seen that nn has the maximum contribution in dip region and the bottom right corner of the kinematic space, while it is minimum just below the QE region. This behaviour of maximum and minimum is due the interference between QE-like and  $\Delta$ -like terms [8].

It would be interesting to see the contribution of pn and nn for all the structure functions in the total cross-section. As other structure functions are added to  $W_2$ , it is possible that some features of the plots shown in Fig. 2.23 change. The corresponding plots are

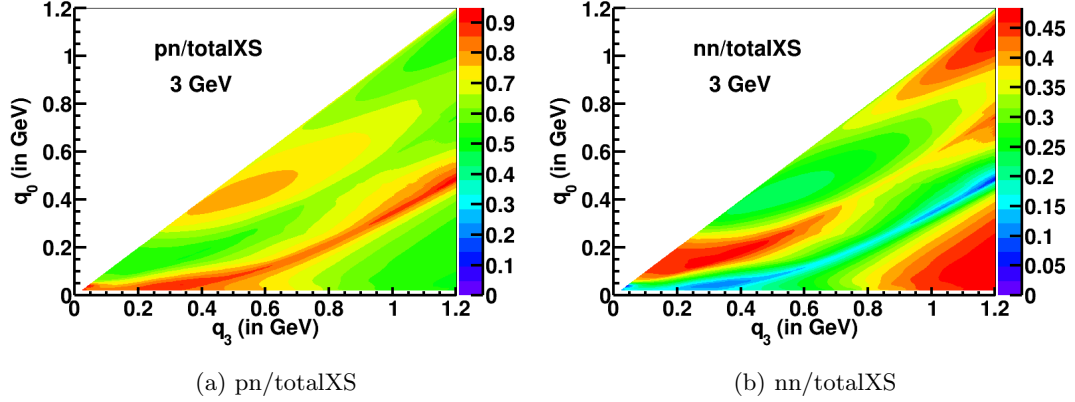


Figure 2.24: Fractional contribution of pn (total) and nn (total) in totalXS (pn + nn) for 3 GeV neutrinos

pn has a bigger contribution everywhere and it is maximum around the delta region and just below the QE region. nn has the maximum contribution, less than pn though, in dip region and the two corners of the kinematic space. This maximum of nn in the upper right corner is not so much apparent in the plot of  $ww2pn$ . Other structure functions such as  $ww1$  and  $ww3$  have a bigger value in this corner as shown in Fig. 2.20. The reason behind this maximisation in the corners can be attributed to the interference between the QE-like and  $\Delta$ -like terms. The other possible reason is related to the range of validity of the Valencia 2p2h model. The corners are actually at the far edge of the phase space the model is designed to predict. Around that edge, there are some aspects of Valencia Model that are non-relativistic. Another 2p2h model, Super scaling approximation model (SuSA) [59], is fully relativistic and performs better in that area.

### 2.3.3 Fractional Contribution of Structure Functions

Although it is clear from all the analysis till now that  $W_2$  is the most dominant structure functions followed by  $W_3$  and  $W_1$ . It is important to look at the plots of their fractional contribution in the total cross-section to get an exact idea. The plots are as follows:

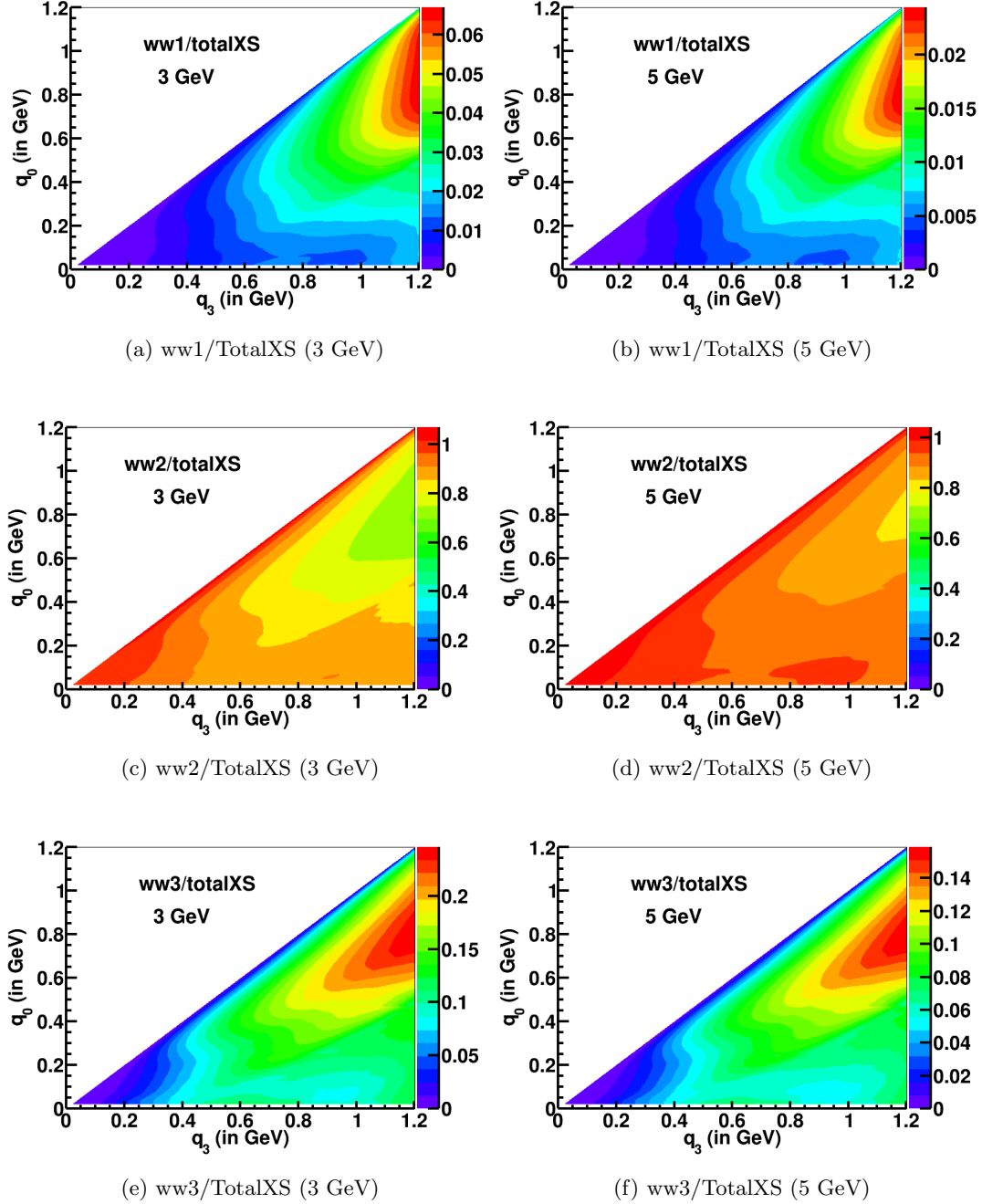


Figure 2.25: Fractional contribution of structure functions in total cross section (totalXS) for 2p2h process corresponding to 3 GeV and 5 GeV neutrinos

It can be observed that  $ww2$  has fractional contribution greater than 80% for a 3 GeV neutrino in all of the kinematic space except for in an upper right corner where  $ww1$  and  $ww3$  have a maxima. This percentage rises up to 85% for a 5 GeV neutrino. The fractional contribution of  $ww3$  is less than 20% almost everywhere for a 3 GeV neutrino and less than 15% for a 5 GeV neutrino. The corresponding percentages are 5% and 2% for  $ww1$ . The percentages mentioned here do not add up to 100% as they might correspond to different regions in the plot. Another observation is that the contribution of  $ww2$  increases as energy transfer decreases. The behaviour of  $ww3$  and  $ww1$  is just the opposite of this.

The takeaway is that  $W_2$  describes the cross-section in a big part of the kinematic space.  $W_3$  has a non-negligible but a small contribution.  $W_1$  is totally ignorable as its contribution lies within the uncertainties present in the experimental data of MINERvA.

This chapter can be concluded by looking at the plots of fractional contribution of Energy Independent Term and  $1/E$  Term. It is important for the energy dependence analysis of 2p2h process.

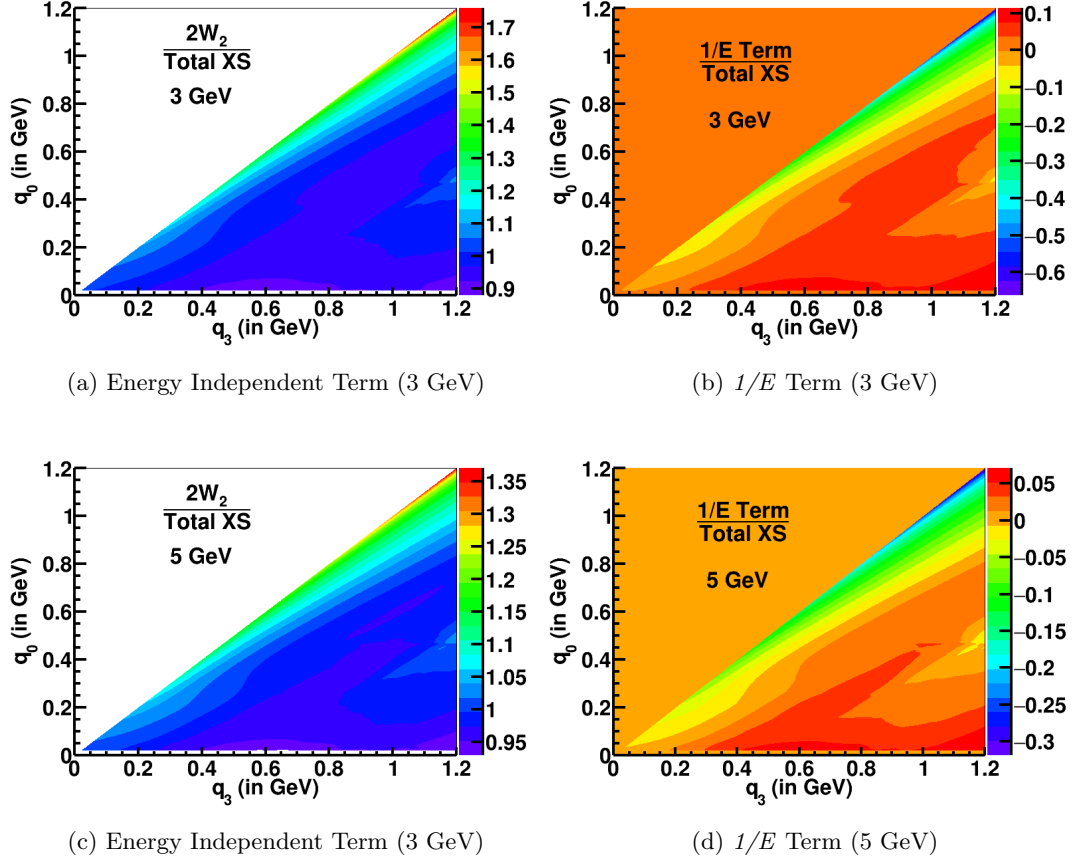


Figure 2.26: Fractional contribution of Energy Independent Term and  $1/E$  Term for 3 GeV and 5 GeV neutrinos. The right plot has negative values along the diagonal, and the value zero is represented by orange rather than white.

The figure above shows that the contribution of Energy Independent Term, dictated by  $2W_2$ , is in the range  $(100 \pm 10)\%$  everywhere for a 3 GeV neutrino and in the range  $(100 \pm 5)\%$  everywhere for a 5 GeV neutrino. It goes above 100% where  $1/E$  Term is negative. Consequently, the contribution of  $1/E$  Term is less than 10% everywhere for a 3 GeV neutrino and less than 5% for a 5 GeV neutrino. If one wanted to use MINERvA data as a  $W_2$  constraint, looking toward NOvA data at 2 GeV, the constraint must be restricted to lower  $q_3$ . There is a small region at the top edge of the plot where the contribution of Energy Independent Term goes up to 140% for a 3 GeV neutrino. In

this region also the Valencia Model becomes unphysical because part of the calculation is non-relativistic. That unphysical portion might be stronger in the  $W_2$  structure function and produced the dramatic trend.

The takeaway of this section and of the whole chapter is that  $W_2$  is good enough to describe the MINERvA data, or the other way around, MINERvA is only able to reliably constrain the  $W_2$  term.  $W_3$  is small enough such that its contribution is comparable to the uncertainties present in MINERvA data. Though beyond this thesis (or the MINERvA experiment), these observations support the use of MINERvA data to constrain the  $W_2$  structure function to predict the cross section at NOvA energies.

## Chapter 3

# Extraction of Structure Functions from MINERvA MC and Data

The previous chapter discussed about  $1/E$  Term present in a neutrino-nucleus interaction (for QE and 2p2h) and showed its contribution relative to the Energy Independent Term. It is less than 10% for MINERvA energies. The plots shown in that chapter were made using structure functions extracted from Valencia code directly and hence, were purely theoretical and did not contain any uncertainties or resolution smearing.

The goal of this chapter is to develop a method to extract Energy Independent Term, dictated by  $2W_2$ , and  $1/E$  Term from MINERvA MC and data directly, and compare it to the theoretical values available from Valencia code. The motivation behind this extraction is that if these values match with each other, then these values can be instrumental in predicting the interactions for lower energy neutrino experiments.

There is no published work that attempts this in the low momentum transfer region and this may be the first attempt ever to have tried such a thing. It is conceptually related to the so-called low- $\nu$  method used by the NOMAD and MINERvA experiments with deep inelastic scattering samples.

### 3.1 Description of the method

The method is based on using the general expression relating the number of events with the total cross-section and other detector parameters. The expression is:

$$\text{No. of events} = \sigma \times Flux \times POT \times \text{No. of neutrons} \quad (3.1)$$

where no. of neutrons is the number of neutrons in the tracker region and protons on target (POT) is a scaling factor for how many neutrinos were in the neutrino beam (and the simulated beam) over the duration of the data period. This work uses the number of neutrons instead of the number of nucleons since the Valencia code against which the results of the method will be compared gives the results per carbon nucleus, which is directly related to the per neutrons result.

$\sigma \times Flux$  can be expanded as follows when flux is also binned in terms of neutrino energy with bin width  $\Delta E$

$$\begin{aligned} \sigma \times Flux &= \sum_E \left[ \left( \int \frac{d^2\sigma}{dq_0 dq_3} dq_0 dq_3 \right) \cdot Flux \right] \Delta E \\ &= \sum_E \left[ \left( (En. Ind. Term) + \frac{1}{E} (1/E Coeff.) + \frac{1}{E^2} (1/E^2 Coeff.) \right) \cdot Flux \right] \cdot \Delta E, \end{aligned} \quad (3.2)$$

where *En. Ind. Term* refers to the 2D integration of  $2W_2$  term (along with other kinematic factors) with respect to  $q_0$  and  $q_3$ , and *1/E Coeff.* refers to the coefficient of  $1/E$  Term as defined in the Chapter 2. It can be obtained by integrating  $1/E$  Term with respect to  $q_0$  and  $q_3$ , and multiplying the result of integration with neutrino energy. Mathematically, it can be written as

$$\begin{aligned} \text{En. Ind. Term} &= \frac{G_F^2 \cos^2 \theta_C}{2\pi} \int 2W_2 q_3 dq_0 \\ 1/E \text{ Coeff.} &= \frac{G_F^2 \cos^2 \theta_C}{2\pi} \int \left( \frac{W_3 Q^2}{M} - 2q_0 W_2 \right) q_3 dq_3 dq_0, \end{aligned} \quad (3.3)$$

where “+” has been chosen for  $W_3$  since this section is devoted to neutrino-nucleus interactions.  $1/E^2$  Coeff. can be defined similarly.

It is important to be clarified at this point that one term is called “En. Ind. Term” just because it is the only energy-independent term in the cross-section expression. However, if  $1/E$  is removed from  $1/E$  Term, then  $1/E$  Coeff. is left and it is also energy-independent. So, both “En. Ind. Term” and “ $1/E$  Coeff.” are energy-independent and their titles or names are just for the notation purpose and to relate them back to the original cross-section expression. To be pedantic, both these terms have a tiny ( $< 0.5\%$ ) energy-dependence coming from RPA but it is well within the statistical uncertainties, and hence, there is no practical problem in treating them as energy-independent.

As Chapter 2 showed, the contribution of  $1/E^2$  terms is negligible compared to that of the other terms, so it suffices to consider the *En. Ind. Term* and *1/E Term* only. Now, since *En. Ind. Term* and *1/E Coeff.* are independent of neutrino energy, they can be taken out of the summation in Eq. 3.2 and the resulting equation would be

$$\sigma \times Flux = (En. Ind. Term) \cdot \Delta E \cdot \left( \sum_E Flux \right) + (1/E Coeff.) \cdot \Delta E \cdot \left( \sum_E \frac{Flux}{E} \right) \quad (3.4)$$

which can be further written using Eq. 3.1 as

$$(En. Ind. Term) \cdot \left( \sum_E Flux \right) + (1/E Coeff.) \cdot \left( \sum_E \frac{Flux}{E} \right) = \frac{\text{No. of events} \times 1/\Delta E}{\text{POT} \times \text{No. of neutrons}} \quad (3.5)$$

This thesis uses 90% of each of the MINERvA medium-energy era Monte Carlo playlists and all of the data. The missing 10% was used to train a Machine Learning algorithm for Nafis Fuad for his Duluth M.S. thesis [60] which is not used in this thesis. POT is  $4.10343 \cdot 10^{21}$  for MC and  $1.0606 \cdot 10^{21}$  for data. Number of neutrons in the tracker is  $1.65 \cdot 10^{30}$  as given in [61]. Flux details are obtained from the Ancillary files of [12]. The bin width in the file is  $\Delta E = 0.5$  GeV.

Right Hand Side (RHS) of Eq. 3.5 is a constant for a particular energy range. Summation over flux and energy-weighted summation of flux on the Left Hand Side (LHS) are also constant for that energy range. The two variables are *En. Ind. Term* and *1/E Coeff.* Thus, the equation is a linear equation in two variables and we can create a system of two equations for the two unknown variables and solve them. The energy ranges used in this analysis are 3-5 GeV, 4-6 GeV, 5-7 GeV, and 7+ GeV (means 7 GeV and higher). The reason behind choosing four energy ranges and not just two is that four energy ranges form six pairs of energy ranges and hence, give six sets of solutions to the Eq. 3.5. Since the solutions are energy-independent, these six different solutions should be same or at least close to one another. An inconsistency in the result indicates the presence of a systematic uncertainty or be used to diagnose flaws or bugs in the method.

For the energy range 5-7 GeV, the flux details are as follows [12]:

Table 3.1: Flux in each bin in the energy range 5-7 GeV

Bin Low (GeV)	Bin High (GeV)	Flux (neutrinos/ $m^2$ /POT/GeV)
5.0	5.5	$1.179888 \cdot 10^{-4}$
5.5	6.0	$1.238293 \cdot 10^{-4}$
6.0	6.5	$1.193707 \cdot 10^{-4}$
6.5	7.0	$1.046674 \cdot 10^{-4}$

where the flux is assumed to be centered at bin center, such as 5.25 GeV in the case of bin (5 - 5.5 GeV).

This method is tested on MINERvA MC since everything about an interaction is available in MC and that makes the test easier. In MINERvA jargon, this is called a closure test. A well designed analysis performed on Monte Carlo “mock data” samples should return the correct answer. Simultaneously, the method is applied to data to compare the results with MINERvA MC.

To demonstrate how the equation is written, the number of events in Mid  $q_3$  range and 5-7 GeV energy range given by MINERvA MC are 860168.87, which is not a whole

number because most MC events are given a non-integer weight that transforms from one MC model to a slightly different model. Thus, the RHS of Eq. 3.5 is

$$\begin{aligned} \frac{\text{No. of events} \times 1/\Delta E}{\text{POT} \times \text{No. of neutrons}} &= \frac{860168.87 \times 1/0.5}{(4.10343 \cdot 10^{21}) \times (1.65 \cdot 10^{30})} \text{GeV}^{-1} \\ &= 2.5408717 \cdot 10^{-46} \text{GeV}^{-1} \end{aligned} \quad (3.6)$$

The flux terms in the LHS of Eq. 3.5 for the energy range 5-7 GeV are

$$\begin{aligned} \sum_E \text{Flux} &= (1.179888 + 1.238293 + 1.193707 + 1.046674) \cdot 10^{-4} \\ &= 4.658562 \cdot 10^{-4} \\ \sum_E \frac{\text{Flux}}{E} &= \left( \frac{1.179888}{5.25} + \frac{1.238293}{5.75} + \frac{1.193707}{6.25} + \frac{1.046674}{6.75} \right) \cdot 10^{-4} \\ &= 7.86152 \cdot 10^{-5} \end{aligned} \quad (3.7)$$

The final equation (per neutron) for the energy range 5-7 GeV and Mid  $q_3$  is

$$46.58562 \cdot (\text{En. Ind. Term}) + 7.86152 \cdot (1/E \text{ Coeff.}) = 254.08717 \quad (3.8)$$

where the units of *En. Ind. Term* and *1/E Coeff.* are  $10^{-39} \text{ cm}^2$  and  $10^{-39} \text{ cm}^2\text{-GeV}$  respectively.

Similarly, equations for other energy ranges can be written for different ranges of  $q_3$ , and they can be solved simultaneously for a pair of energy ranges. It must be mentioned that no muon angle cut is applied in this initial study since it introduces an extra energy dependence in the equations.

### 3.2 Differences between Valencia MC and MINERvA MC leading to efficiency correction

True values of *En. Ind. Term* and *1/E Coeff.* can be obtained from Valencia MC by simply integrating over the 2D cross-section plots, such as those in figures 2.12 and

2.21. Since Valencia MC gives the values per nucleus and neutrino interactions generally happen on a neutron, that value has to be divided by 6 before it can be used to compare with the values obtained from MINERvA MC. Here, dividing by 6 is equivalent to assuming that the total cross-section of a nucleus is the summation of the cross-section of neutrons. This is the statement of an impulse approximation, which works well for  $q_3 > 0.4$  GeV [56]. For  $q_3 < 0.4$  GeV, this work includes Random Phase Approximation (RPA) [19] and because of that, dividing by 6 works well for that  $q_3$  range also.

The values of *En. Ind. Term* and *1/E Coeff.* for QE scattering and 2p2h process obtained from Valencia code, and expressed per neutron i.e. per nucleus divided by 6, corresponding to 3 GeV neutrinos are as follows:

Table 3.2: *En. Ind. Term* obtained from Valencia code for QE scattering and 2p2h process expressed per neutron corresponding to 3 GeV neutrinos for Low  $q_3$ , Mid  $q_3$  and High  $q_3$  in the unit  $10^{-39}$  cm<sup>2</sup>

Interaction	Low $q_3$	Mid $q_3$	High $q_3$
QE Scattering	1.2991	3.1366	1.9470
2p2h Process	0.2906	1.1253	1.1015
Sum of the two interactions	1.5896	4.2619	3.0485

Table 3.3: *1/E Coeff.* obtained from Valencia Code for QE Scattering and 2p2h Process expressed per neutron corresponding to 3 GeV neutrinos for Low  $q_3$ , Mid  $q_3$  and High  $q_3$  in the unit  $10^{-39}$  cm<sup>2</sup>-GeV

Interaction	Low $q_3$	Mid $q_3$	High $q_3$
QE Scattering	0.0946	0.9111	0.9082
2p2h Process	-0.0194	-0.0360	-0.1344
Sum of the two interactions	0.0751	0.8751	0.7738

The values mentioned above are determined for 3 GeV neutrinos but they can be used for all other neutrino energies also. The only energy dependence in them comes

from RPA and that is less than 0.5%.

Now that values from Valencia MC are available, it is important to point out the differences between Valencia MC and MINERvA MC/data before going forward. The differences between the two are:

- Valencia provides the values for only QE and 2p2h while MINERvA MC and data also have other interactions such as delta resonance.
- MINERvA MC or data has resolution smearing present in  $q_3$ .
- MINERvA MC or data has angle acceptance effect and thus efficiency correction.
- MINERvA MC or data has statistical and systematic uncertainties.
- MINERvA MC or data has Final State Interactions (FSI) in it.

Values available from Valencia for (QE + 2p2h) can give a general idea about the values expected from MINERvA data even though they do not contain delta resonance. Resolution smearing in MINERvA MC or data can be dealt with by unfolding but that is beyond the scope of this work. MINERvA uses D'Agostini prescription of unfolding [62, 63] and implements it using the RooFit toolkit [64]. Comments given throughout this chapter deal with this and explain how much it is going to affect the extraction method. Angle acceptance effect is the easiest to deal with here and has been explained as this section progresses. MINERvA uncertainties cannot be removed, at least for this work, and although FSI can be turned off in the MC, it is deliberately kept since it is always present in data and the ultimate goal of this work is to extract the  $1/E$  Coeff. from MINERvA data itself.

Muons produced by a neutrino interaction in the tracker have to go into the MINOS Spectrometer where their energy and momentum is determined. The efficiency of muons, or how many muons enter the MINOS and are accurately tracked, depends on the angle at which they are produced with respect to the incoming neutrino beam. The practical cutoff of the efficiency is around 20 degrees, where the efficiency is less than 10%. This means that one out of ten neutrino events is counted. Since Valencia does not have

this angle acceptance effect, MINERvA MC and data needs to be corrected by a factor  $1/\text{Efficiency}$  to bring it one step closer to Valencia. To determine the muon efficiency, Fig. 3.1 is used that is taken from a study by MINERvA colleague Dr. Abigail Waldron [65]. Waldron’s sample covers a similar range of three-momentum transfer.

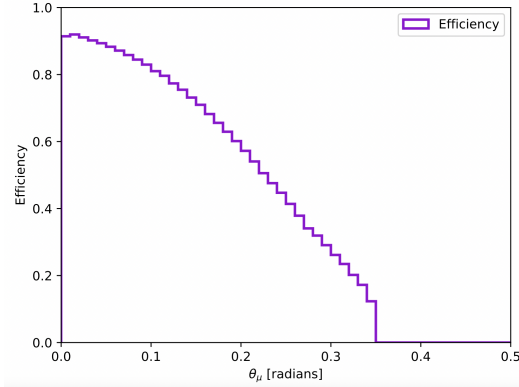


Figure 3.1: Efficiency for antineutrino interactions as a function of antimuon angle

Although the plot is for antineutrino interactions and antineutrino interactions produce an antimuon instead of a muon, it is assumed that the efficiency or angle acceptance effect is purely a detector geometry effect. That is why the same plot is used to study neutrino interactions in this chapter. To use this plot in the form of a programming code, a few points were selected on the plot and a four-degree polynomial was fitted through them. The chosen points were (0 rad, 92%), (0.11 rad, 80%), (0.2 rad, 58%), (0.22 rad, 50%), (0.3 rad, 31%) and (0.33 rad, 20%). The function `numpy.polyfit()` from Python 3.10.6 was used to fit a polynomial through these points and the polynomial obtained was

$$\begin{aligned} \text{Efficiency}(\theta_\mu) = & (-1.55 \cdot 10^{-3}) \cdot \theta_\mu^4 + (6.78 \cdot 10^{-2}) \cdot \theta_\mu^3 - 1.06 \cdot \theta_\mu^2 \\ & + 2.52 \cdot \theta_\mu + 92.0 \quad (3.9) \end{aligned}$$

This was the polynomial that was obtained and fed into the code directly. As can be seen, a quadratic polynomial would have sufficed for the efficiency since the coefficients of higher order terms are within the uncertainties and including them would not make a big difference.

### 3.3 Extraction from MINERvA MC and Data

The method developed in the previous section is applied to MINERvA MC and data. Out of the energy ranges 3-5 GeV, 4-6 GeV, 5-7 GeV and 7+ GeV, two energy ranges are chosen at once and the corresponding equation (Eq. 3.5) for each energy range is written, and they are solved simultaneously. The 3-5 GeV energy range is included for both Low  $q_3$  and Mid  $q_3$  but not for High  $q_3$  since for this  $q_3$  and  $E_\nu$  range, the muon angle goes beyond 20 degrees and detector geometry comes into play. The tables below present the results for both MINERvA MC and data.

Table 3.4: *En. Ind. Term* and *1/E Coeff.* for both MINERvA MC and data for Low  $q_3$  in the units  $10^{-39}$  cm<sup>2</sup> and  $10^{-39}$  cm<sup>2</sup>-GeV respectively

Energy Range (in GeV)	MINERvA MC		MINERvA data	
	<i>En. Ind. Term</i>	<i>1/E Coeff.</i>	<i>En. Ind. Term</i>	<i>1/E Coeff.</i>
7+, 5-7	0.882	3.170	1.130	2.746
7+, 3-5	0.964	2.457	1.086	3.123
7+, 4-6	0.869	3.282	0.995	3.920
3-5, 5-7	1.081	1.986	1.024	3.372
3-5, 4-6	1.314	1.058	1.425	1.772
4-6, 5-7	0.830	3.475	0.591	5.938

Table 3.5: *En. Ind. Term* and *1/E Coeff.* for both MINERvA MC and data for Mid  $q_3$  in the units  $10^{-39}$  cm<sup>2</sup> and  $10^{-39}$  cm<sup>2</sup>-GeV respectively

Energy Range (in GeV)	MINERvA MC		MINERvA data	
	<i>En. Ind. Term</i>	<i>1/E Coeff.</i>	<i>En. Ind. Term</i>	<i>1/E Coeff.</i>
7+, 5-7	4.903	8.280	5.352	7.285
7+, 3-5	4.920	8.135	4.840	11.752
7+, 4-6	4.691	10.129	4.646	13.446
3-5, 5-7	4.944	8.039	4.101	14.702
3-5, 4-6	5.768	4.753	5.560	8.880
4-6, 5-7	4.055	13.308	2.525	24.034

Table 3.6: *En. Ind. Term* and *1/E Coeff.* for both MINERvA MC and data for High  $q_3$  in the units  $10^{-39} \text{ cm}^2$  and  $10^{-39} \text{ cm}^2\text{-GeV}$  respectively

Energy Range (in GeV)	MINERvA MC		MINERvA data	
	<i>En. Ind. Term</i>	<i>1/E Coeff.</i>	<i>En. Ind. Term</i>	<i>1/E Coeff.</i>
7+, 5-7	6.628	2.018	6.520	4.052
7+, 4-6	6.196	5.784	5.657	11.572
4-6, 5-7	4.900	12.260	3.069	24.500

Tables 3.4, 3.5 and 3.6 present the terms extracted from MINERvA MC and data. The expectation was that no matter which pair of energy ranges is chosen, the terms should not change since they do not depend on neutrino energy. However, the tables show that the values obtained are not the same. This variation can be attributed to the uncertainties present in the MC and data. *En. Ind. Term* is relatively stable across different energy ranges in comparison to *1/E Coeff.* since *1/E Coeff.* is sensitive to uncertainties and resolution smearing, and hence, a small change in the number of events brings about a big change in it. Another observation is that MINERvA MC and data produce results closer to each other but neither match the values given in tables 3.2 and 3.3. This is due to the differences listed in the previous section, especially the presence of delta resonance and resolution smearing.

The conclusion of all the points mentioned in this paragraph and observation of values given in the tables is that although it cannot be determined for certain whether the values are actually correct, the relatively smaller variation of values across different energies and similarity in values between MINERvA MC and data is a strong hint that the method works and can do a better job with smaller uncertainties and less resolution smearing. The extraction technique in this work is applied to  $q_3$  bins of width 0.4 GeV but it could also be applied to smaller subsets or 2D bins such as used by MINERvA colleague Marvin Ascencio [6].

That even small uncertainties in the data and MC can lead to the variation in the

values of *En. Ind. Term* and *1/E Coeff.* across different energy ranges can be demonstrated by changing the number of events in every energy range by a small percentage so that all the values converge to a particular value. However, these percentages are different for different energy ranges indicating that they might not be the correct uncertainty but serve well to demonstrate the idea. Also, it is important to mention that this technique of convergence by varying the number of events does not lead to a unique point of convergence. Trying a different set of percentages can lead to a different point of convergence. To constrain these percentages and limit the range of points of convergence, smaller uncertainties and tighter constraints on percentages are required. That the solutions can be converged to any desirable values is demonstrated in Appendix B.

To do this demonstration of convergence, the following changes are made to the number of events in MINERvA MC

- Low  $q_3$  : 7+ GeV (+3.02%), 5-7 GeV (-0.9%), 3-5 GeV (+0.5%), 4-6 GeV (-3.39%)
- Mid  $q_3$  : 7+ GeV (+2.6%), 5-7 GeV (+2.47%), 3-5 GeV (+2.6%)
- High  $q_3$  : 7+ GeV (-3%), 5-7 GeV (+2.1%), 4-6 GeV (+0.4%)

and the following changes are made to the number of events in MINERvA data

- Low  $q_3$  : 7+ GeV (+2%), 5-7 GeV (+2.88%), 3-5 GeV (+1.1%), 4-6 GeV (-2.5%)
- Mid  $q_3$  : 7+ GeV (+2%), 5-7 GeV (+3.6%), 3-5 GeV (-2.5%), 4-6 GeV (-3%)
- High  $q_3$  : 7+ GeV (-1%), 5-7 GeV (+3.25%), 4-6 GeV (-2.9%)

where (+%) and (-%) represent the increase and decrease in the number of events respectively by the percentage mentioned. For a sense of scale, these changes are at a few percent level, which is larger than the statistical uncertainty but are the same size or smaller than changes in event rate due to many kinds of uncertainties in the interaction or detector model.

After making these changes, *En. Ind. Term* and *1/E Coeff.* are calculated again and are presented here.

Table 3.7: *En. Ind. Term* and *1/E Coeff.* for both MINERvA MC and data for Low  $q_3$  in the units  $10^{-39} \text{ cm}^2$  and  $10^{-39} \text{ cm}^2\text{-GeV}$  respectively after reweighting the number of events

Energy Range (in GeV)	MINERvA MC		MINERvA data	
	<i>En. Ind. Term</i>	<i>1/E Coeff.</i>	<i>En. Ind. Term</i>	<i>1/E Coeff.</i>
7+, 5-7	1.026	2.238	1.122	3.060
7+, 3-5	1.026	2.238	1.122	3.062
7+, 4-6	1.026	2.237	1.122	3.062
3-5, 5-7	1.026	2.238	1.122	3.062
3-5, 4-6	1.026	2.240	1.122	3.062
4-6, 5-7	1.027	2.235	1.122	3.064

Table 3.8: *En. Ind. Term* and *1/E Coeff.* for both MINERvA MC and data for Mid  $q_3$  in the units  $10^{-39} \text{ cm}^2$  and  $10^{-39} \text{ cm}^2\text{-GeV}$  respectively after reweighting the number of events

Energy Range (in GeV)	MINERvA MC		MINERvA data	
	<i>En. Ind. Term</i>	<i>1/E Coeff.</i>	<i>En. Ind. Term</i>	<i>1/E Coeff.</i>
7+, 5-7	5.048	8.344	5.236	9.379
7+, 3-5	5.048	8.346	5.232	9.409
7+, 4-6	5.048	8.349	5.231	9.424
3-5, 5-7	5.048	8.348	5.228	9.429
3-5, 4-6	5.049	8.342	5.239	9.385
4-6, 5-7	5.046	8.358	5.216	9.500

Table 3.9: *En. Ind. Term* and *1/E Coeff.* for both MINERvA MC and data for High  $q_3$  in the units  $10^{-39} \text{ cm}^2$  and  $10^{-39} \text{ cm}^2\text{-GeV}$  respectively after reweighting the number of events

Energy Range (in GeV)	MINERvA MC		MINERvA data	
	<i>En. Ind. Term</i>	<i>1/E Coeff.</i>	<i>En. Ind. Term</i>	<i>1/E Coeff.</i>
7+, 5-7	5.675	8.533	5.805	9.676
7+, 4-6	5.675	8.536	5.804	9.684
4-6, 5-7	5.674	8.541	5.802	9.697

These tables show that the values converged to a point after a slight reweighting of the number of events. Conversely, if all the values converged to a point across different neutrino energies which they should, uncertainties in the number of events can change these values in a non-uniform manner.

### 3.4 Are the values after convergence correct? Sensitivity of *1/E Coeff.* necessitates smaller uncertainties

Before commenting on the convergence and the correctness of the values obtained, it is imperative to understand why there is a variation in the values before convergence and why *1/E Coeff.* has a bigger range of variation in comparison to that of *En. Ind. Term.* The idea is to determine the sensitivity to the *1/E Coeff.* at MINERvA energies.

Eq. 3.8 is written for the energy range 5-7 GeV and Mid  $q_3$  range. The LHS of the equation is

$$\text{LHS} = 46.58562 \cdot (\text{En. Ind. Term}) + 7.86152 \cdot (1/E \text{ Coeff.}). \quad (3.10)$$

The true values obtained from Valencia code for *En. Ind. Term* and *1/E Coeff.*, also given in Tables 3.2 and 3.3, are 4.2619 and 0.8751 respectively, with the units as specified in the tables. Now, the two terms contributing to the LHS evaluate to

$$\begin{aligned}
\text{1st Term in LHS} &= 46.58562 \times 4.2619 \\
&= 198.5432 \\
\text{2nd Term in LHS} &= 7.86152 \times 0.8751 \\
&= 6.8796
\end{aligned} \tag{3.11}$$

Comparing the contribution of the two terms in LHS of Eq. 3.8 gives

$$\text{1st term in LHS} \approx 30 \text{ times 2nd Term in LHS} \tag{3.12}$$

The true value of  $1/E$  *Coeff.* is already 5 times smaller than that of *En. Ind. Term.* MINERvA peak at 6 GeV makes the whole term smaller by an additional factor of 6. Thus, determining  $1/E$  *Coeff.* is equivalent to determining a term with a tiny contribution to the equation. This is the reason behind the sensitivity to the  $1/E$  *Coeff.* and why it has a bigger range of variation in comparison to that of *En. Ind. Term.* This analysis also gives an explanation why determining the coefficient of  $1/E^2$  Term will be even more difficult. It will have an additional factor of 6 coming from neutrino energy. Also, the true value of its coefficient is a few times smaller than that of  $1/E$  *Coeff.*, thus its contribution will be effectively at least 200 times smaller than that of *En. Ind. Term* making it extremely difficult to determine its value from MINERvA MC and data with any uncertainties present. I briefly explored this term by making three equations and three unknowns, but it clearly did not work and I do not report on it here.

After all the analysis, the question is whether the obtained values before or after the convergence are correct or not even for the MC only, the desired closure test. It cannot be stated with certainty at this point whether the values are correct or not. One of the reasons is that true values are available only for QE scattering and 2p2h process at this point. On top of that, GENIE version 2 that is used in this work to run simulations and generate events uses a slightly modified QE scattering model and thus, the values obtained from Valencia code are not exactly right.

The other reason is the use of the efficiency correction plot in this analysis. The plot was developed for antineutrino interactions originally and describes the efficiency

of an antimuon and not a muon. It is a good approximation that the efficiency does not depend on whether it is a muon or an antimuon but only on the detector geometry. However, it is still possible that the efficiency for muons is slightly different and thus, the efficiency correction used in this work might not be perfect.

Resolution smearing changes the values of *En. Ind. Term* and *1/E Coeff.*, and thus, it is not easy to compare their calculated values using the extraction technique to the true values directly without unfolding, which basically means reverting the resolution smearing to some extent. Now, smearing and uncertainties lead to a non-uniform set of values across different energies. It is good that the non-uniformity is not too vast and MINERvA MC and data values are closer if not exactly same. This is a strong indication that the method works. MINERvA MC and data are not expected to produce the same values since they are different as various plots in this work depict.

The technique of convergence is discussed in this chapter. However, the point of convergence can be changed easily by adjusting the percentages. Even if one convergence point was identified as better, using the MC or a  $\chi^2$  test, the uncertainties would lead to a range of points and thus the uncertainty on the result. The challenges enumerated above, especially extracting the true result from the GENIE model, were too challenging to pursue a sensitivity analysis in further detail.

Sensitivity to the *1/E Coeff.* is not very good at MINERvA energies. It would be better if we had a longer “lever arm” in energy, such as including data from NOvA (peaks at 2 GeV), or using data from the DUNE experiment. Even lower energy data is available such as MicroBooNE (peaks at 1 GeV) and T2K (peaks at 600 MeV). The lower the energy of an experiment, the better measurement of the *1/E Coeff.* can be made. Experiments with energies of a few hundreds of keV or a few MeV, such as Coherent CAPTAIN-Mills, CHANDLER and ICARUS, will be sensitive to the coefficient of  $1/E^2$  Term also. In fact, the data at energies of keV or MeV will have strong contributions from  $1/E$  and  $1/E^2$  terms, and the cross-section may not look anything like the MINERvA data where 90% is determined by  $2W_2$ .

## Chapter 4

# Muon Angle Analysis and Energy Dependence

A muon is always produced in a charged-current neutrino-nucleus interaction and it can travel at any angle with respect to the neutrino beam depending on the neutrino energy, energy transfer and momentum transfer. It has already been mentioned in the previous chapters that how well a muon is tracked and its energy and momentum reconstructed depends on its angle among other factors such as its energy and how far interaction vertex is from MINOS. For its reconstruction, a muon has to enter MINOS and due to this geometry constraint, a muon traveling at an angle above 20 degrees does not enter MINOS on an average 9 out of 10 times. Thus, understanding the dependence of muon angle on neutrino energy, energy transfer and momentum transfer is important for its reconstruction although that is not a part of this thesis.

Muon angle has another important role, which is also the core of this thesis. Since muon angle distribution is dependent on neutrino energy, selecting a subsample of events with a specific range of muon angle implies including an additional energy dependence in the sample. Neutrino experiments have observed that theoretical models are not perfect and do not describe the experimental data completely. One deeper question is that even if interactions are not well-modeled, whether at least energy dependence is well-modeled. Applying muon angle cuts on a sample is one way to test the modeling of

energy dependence. However, a care must be taken in the interpretation. It is possible that a discrepancy between data and MC seemingly coming from mismodeled energy dependence is coming from the interaction cross-section directly and shows up as an energy dependence discrepancy due to the chosen muon angle cuts. This subtlety will come up several times in the next chapters and reaches a conclusion in Chapter 7.

## 4.1 Parallel/Longitudinal and Perpendicular Momentum of a Muon

Muon angle and momentum can be written as a function of its parallel/longitudinal momentum ( $p_{\parallel}$ ) and traverse momentum ( $p_{\perp}$ ), both of which are relative to the original neutrino direction and can be written in terms of  $E_{\nu}$ ,  $q_0$  and  $q_3$ . This thesis chooses  $q_0$  and  $q_3$  as independent variables and writes or discusses everything else such as muon angle and momentum in terms of those. It was mentioned in Section 1.3 that  $W$  and  $Q^2$  can also be treated as two independent quantities. Similarly,  $p_{\parallel}$  and  $p_{\perp}$  can also be treated as independent quantities and everything else can be written in terms of them. Kleykamp *et al.* [66] and Ruterbories *et al.* [67] make this choice and measure  $p_{\parallel}$  and  $p_{\perp}$  experimentally. However, in this thesis, we stick to the choice of  $q_0$  and  $q_3$ . This section describes how the muon angle varies in this kinematic space and with  $E_{\nu}$ .

### 4.1.1 Expressions for the muon's momentum parallel and transverse to that of the neutrino

Let's assume that the muon neutrino was traveling with momentum  $p_{\nu}$  and energy  $E_{\nu}$  before it hit the neutron, and produced a muon at an angle  $\theta_{\mu}$  with respect to the direction of the neutrino. Thus, the muon's momentum  $\vec{p}_{\mu}$  can be broken down into two components, longitudinal or parallel momentum  $p_{\parallel}$  and traverse momentum  $p_{\perp}$ . The following relation, derived in Appendix C, relates  $p_{\parallel}$  with  $Q^2$  and muon energy.

$$Q^2 = 2E_{\nu} (E_{\mu} - p_{\mu} \cos \theta_{\mu}). \quad (4.1)$$

Using  $p_{\mu} \cos \theta_{\mu} = p_{\parallel}$ , it can be rearranged to obtain  $p_{\parallel}$  in terms of  $E_{\mu}$  ( $= E_{\nu} - q_0$ ), and  $Q^2$  as follows

$$p_{\parallel} = E_{\mu} - \left( \frac{Q^2 + m_{\mu}^2}{2E_{\nu}} \right). \quad (4.2)$$

Einstein's mass-energy relation [68], along with the Pythagorean relation  $p_{\mu}^2 = p_{\parallel}^2 + p_{\perp}^2$ , can be used to obtain  $p_{\perp}$ .

$$\begin{aligned} p_{\perp}^2 &= E_{\mu}^2 - p_{\parallel}^2 - m_{\mu}^2 \\ &= (E_{\nu} - q_0)^2 - p_{\parallel}^2 - m_{\mu}^2 \end{aligned} \quad (4.3)$$

Putting the expression of  $p_{\parallel}$  in the above equation gives

$$p_{\perp} = \sqrt{\frac{E_{\mu}}{E_{\nu}} (Q^2 + m_{\mu}^2) - \left( \frac{Q^2 + m_{\mu}^2}{2E_{\nu}} \right)^2 - m_{\mu}^2} \quad (4.4)$$

It should be noted that these expressions are valid for all the processes (QE, 2p2h, Delta Resonance, DIS, ...). In general, any interaction is randomly picked by nature or GENIE MC. Energy and momentum transfer,  $W$  and  $Q^2$ , or in this expression energy transfer and  $Q^2$  are all viable for 2D basis kinematics.

#### 4.1.2 Range of $Q^2$ and $q_3$

For the  $p_{\perp}$  to be real in Eq. 4.4,

$$\frac{E_{\mu}}{E_{\nu}} (Q^2 + m_{\mu}^2) - \left( \frac{Q^2 + m_{\mu}^2}{2E_{\nu}} \right)^2 - m_{\mu}^2 \geq 0$$

which can be rewritten as,

$$Q^4 + (2m_{\mu}^2 - 4E_{\mu}E_{\nu}) Q^2 + 4m_{\mu}^2 E_{\nu} (E_{\nu} - E_{\mu}) + m_{\mu}^4 \leq 0 \quad (4.5)$$

and we get a quadratic equation inequality in  $Q^2$ . For the real solutions to exist, discriminant of the quadratic equation, i.e.  $16E_{\nu}^2 (E_{\mu}^2 - m_{\mu}^2)$ , has to be greater than or equal to 0, which is always true. Furthermore, the range of  $Q^2$  which satisfies the inequality is

$$Q^2 \in \left[ 2E_{\nu}E_{\mu} - m_{\mu}^2 - 2E_{\nu}\sqrt{E_{\mu}^2 - m_{\mu}^2}, 2E_{\nu}E_{\mu} - m_{\mu}^2 + 2E_{\nu}\sqrt{E_{\mu}^2 - m_{\mu}^2} \right]. \quad (4.6)$$

The lower limit corresponds to the perfectly forward muon and the upper limit corresponds to the perfectly backward muon. Eq. 4.6 provides a range of  $Q^2$  in terms of  $E_\nu$  and  $q_0$  (since  $E_\mu = E_\nu - q_0$ ). It is obvious that  $Q^2$  can never be 0. The  $Q^2$  corresponding to the transverse muon can be obtained by setting Eq. 4.2 to 0. It gives

$$Q_{transverse}^2 = 2E_\nu E_\mu - m_\mu^2 \quad (4.7)$$

To get an idea of the range of  $Q^2$  for different muon energies, the following table presents the values of  $Q^2$  for the forward, transverse and backward muon, for  $q_0 = 0.8$  GeV. This comparison corresponds to a horizontal line in the triangle diagram, Fig. 1.3, as it crosses lines of constant  $Q^2$ .

Table 4.1: Range of  $Q^2$  (in  $GeV^2$ ) for  $q_0 = 0.8$   $GeV$

Energy (in GeV)	Forward	Transverse	Backward
5 (MINERvA ME)	0.002	41.989	83.976
3 (MINERvA LE)	0.004	13.189	26.374
2 (NOvA, DUNE 1st max)	0.008	4.789	9.570
1 (T2K, MicroBooNE, DUNE 2nd max)	0.049	0.389	0.728

Since  $Q^2 = q_3^2 - q_0^2$ , only a range of  $q_3$  is possible for a particular neutrino energy and energy transfer. The important point is that the maximum value of  $q_3$  is  $E_\nu$ , so the maximum value of  $Q^2$  is limited by that. It is more restrictive than the table above. The table of  $q_3$  corresponding to Table. 4.1 is

Table 4.2: Range of  $q_3$  (in  $GeV$ ) for  $q_0 = 0.8$   $GeV$

Energy (in GeV)	Forward	Transverse	Backward
5 (MINERvA ME)	0.801	6.529	9.199
3 (MINERvA LE)	0.802	3.719	5.198
2 (NOvA, DUNE 1st max)	0.805	2.330	3.195
1 (T2K, MicroBooNE, DUNE 2nd max)	0.830	1.014	1.170

It can be seen in the table above that transverse and backward muons are obtained only when  $q_3 > E_\nu$ . For MINERvA,  $q_3$  is generally less than  $E_\nu$ , so we do not expect

to see any muons traveling at such higher angles.

It is easy to show that  $q_3$  cannot be less than  $E_\nu$  for a transverse muon.

$$\begin{aligned} q_3^2(\text{transverse}) &= Q_{\text{transverse}}^2 + q_0^2 \\ &= q_0^2 - 2E_\nu q_0 + (2E_\nu^2 - m_\mu^2), \end{aligned} \quad (4.8)$$

where, Eq. 4.7 is used to write the expression for  $Q_{\text{transverse}}^2$ . For  $q_3 < E_\nu$ ,  $q_0$  has to be in the range  $(E_\nu - m_\mu, E_\nu + m_\mu)$ . However,  $q_0$  is always less than  $E_\nu - m_\mu$ . Thus,  $q_3$  must be greater than  $E_\nu$  for the production of a transverse muon.

Since  $Q^2$  and by an extension  $q_3$  has a lower limit when a massive muon comes from a charge-changing reaction, the value  $Q^2 = 0$  or  $q_3 = 0$  is not possible. In general, this lower limit is so close to 0 and beyond the experimental threshold, it can practically be taken to be 0.

### 4.1.3 Variation of $p_\perp$ with $q_3$ and $q_0$

Since  $\sin(\theta_\mu)$  is directly proportional to  $p_\perp$ , it is important to determine how  $p_\perp$  varies with a change in  $q_0$  and  $q_3$  for the intuition of both muon angle and working in 2D kinematic space.

Using Eq. 4.4 the following expression for the change in the transverse momentum with three-momentum transfer can be worked out at constant energy transfer

$$2p_\perp \left. \frac{\partial p_\perp}{\partial q_3} \right|_{\text{const. } q_0} = \frac{q_3}{E_\nu^2} (2E_\nu E_\mu - m_\mu^2 - Q^2) \quad (4.9)$$

In the range  $Q^2 \in [2E_\nu E_\mu - m_\mu^2 - 2E_\nu \sqrt{E_\mu^2 - m_\mu^2}, 2E_\nu E_\mu - m_\mu^2]$ ,  $\frac{\partial p_\perp}{\partial q_3} > 0$  and thus,  $p_\perp$  increases with an increase in the value of  $q_3$  at constant  $q_0$ . Similarly, in the range  $Q^2 \in (2E_\nu E_\mu - m_\mu^2, 2E_\nu E_\mu - m_\mu^2 + 2E_\nu \sqrt{E_\mu^2 - m_\mu^2}]$ ,  $\frac{\partial p_\perp}{\partial q_3} < 0$  and thus,  $p_\perp$  decreases with an increase in the value of  $q_3$  at constant  $q_0$ . This decrease represents the muon becoming more and more backward.

Similarly, using Eq. 4.4 the expression for change in  $p_{\perp}$  with the change in  $q_0$  can be written for constant momentum transfer

$$2p_{\perp} \left. \frac{\partial p_{\perp}}{\partial q_0} \right|_{\text{const. } q_3} = \frac{-1}{E_{\nu}^2} (q_0 - E_{\nu}) (q_0^2 - 2E_{\nu}q_0 - (q_3^2 + m_{\mu}^2)) \quad (4.10)$$

In the range of physically realizable  $q_0$ ,  $\frac{\partial p_{\perp}}{\partial q_0} < 0$  for constant  $q_3$ , and thus  $p_{\perp}$  decreases with an increases in energy transfer for constant  $q_3$ .

## 4.2 Behaviour of $\theta_{\mu}$ with variation of $q_3$ , $q_0$ and $E_{\nu}$

The MINERvA detector has geometrically limited acceptance for muon angles beyond 20 degrees. Understanding of muon angle's variation with  $q_3$ ,  $q_0$  and  $E_{\nu}$  is crucial to understand the effect of efficiency on the analysis coming in due to detector geometry limitations.

Using basic trigonometry relations, muon angle  $\theta_{\mu}$  can be related to transverse momentum ( $p_{\perp}$ ) and total muon momentum ( $p_{\mu}$ ) as follows

$$\sin^2 \theta_{\mu} = \frac{p_{\perp}^2}{p_{\mu}^2}. \quad (4.11)$$

### 4.2.1 Behaviour of $\theta_{\mu}$ with variation in $q_3$ keeping $q_0$ and $E_{\nu}$ fixed

As shown in Section 4.1.3,  $p_{\perp}$  increases with an increase in  $q_3$  until  $q_3$  reaches the value of  $E_{\nu}$ . Since  $p_{\mu}^2 = (E_{\nu} - q_0)^2 - m_{\mu}^2$ ,  $p_{\mu}$  is independent of  $q_3$  and thus, the behaviour of  $\theta_{\mu}$  directly depends on  $p_{\perp}$ . Following the argument, it can be stated that  $\theta_{\mu}$  increases with an increase in  $q_3$  for a constant energy transfer and neutrino energy until  $q_3$  reaches the value of  $E_{\nu}$ . It keeps increasing even after that but the value of  $p_{\perp}$  starts decreasing.

### 4.2.2 Behaviour of $\theta_{\mu}$ with variation in $q_0$ keeping $q_3$ and $E_{\nu}$ fixed

Variation of  $\theta_{\mu}$  with a variation in  $q_0$  is a little more subtle. Both  $p_{\perp}$  and  $p_{\mu}$  decrease with an increase in  $q_0$ . I am limiting the analysis in this subsection to  $q_3 < E_{\nu}$  since that is in the range of interest of MINERvA. The analysis can be extended to higher

values of  $q_3$ .

Differentiating both sides of the Eq. 4.11 with respect to  $q_0$  at constant  $q_3$ ,

$$\begin{aligned} \sin(2\theta_\mu) \left. \frac{\partial \theta_\mu}{\partial q_0} \right|_{\text{const. } q_3} &= -(q_0 - E_\nu) (q_0^2 - 2E_\nu q_0 + (2E_\nu^2 - q_3^2 - m_\mu^2)) \\ &\quad \times \frac{(q_0^2 - 2E_\nu q_0 + (q_3^2 - m_\mu^2))}{2E_\nu^2 [(E_\nu - q_0)^2 - m_\mu^2]^2} \end{aligned} \quad (4.12)$$

The discriminant of the quadratic polynomial  $(q_0^2 - 2E_\nu q_0 + (2E_\nu^2 - q_3^2 - m_\mu^2))$  is negative, which means that the polynomial is always positive for all values of  $q_0$ .  $(q_0 - E_\nu)$  is always negative for the physically realizable  $q_0$ . Within the range of physical  $q_0$ , the second polynomial is positive in the range  $q_0 \in [0, E_\nu - \sqrt{E_\nu^2 - q_3^2 + m_\mu^2})$  and negative in the range  $q_0 \in (E_\nu - \sqrt{E_\nu^2 - q_3^2 + m_\mu^2}, E_\nu - m_\mu)$ , becoming 0 and giving the maximum muon angle for

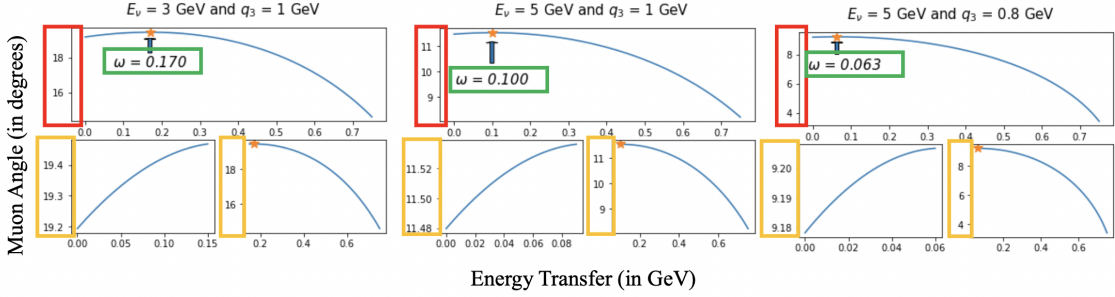
$$q_{0(max)} = E_\nu - \sqrt{E_\nu^2 - q_3^2 + m_\mu^2}. \quad (4.13)$$

Thus,  $\theta_\mu$  increases as  $q_0$  increases from 0 to  $E_\nu - \sqrt{E_\nu^2 - q_3^2 + m_\mu^2}$  and decreases after that. This point of maxima gets closer to  $q_0 = 0$  as  $E_\nu$  increases and gets farther away from it as  $q_3$  increases.

The angle corresponding to the maxima can be found by using the Eq. 4.13 in the Eq. 4.11 and it is given by

$$\theta_{\mu(max)} = \sin^{-1} \left( \frac{q_3}{E_\nu} \right) \quad (4.14)$$

A better explanation of the variation of  $\theta_\mu$  with  $q_0$  is shown in Fig. 4.1



(a) Muon angle vs Energy Transfer

Figure 4.1: Muon angle first increases and then decreases with an increase in energy transfer. The lower plots zoom in on the details and have different vertical scales.

Fig. 4.1 shows that the peak moves left and down with an increase in  $E_\nu$  for constant  $q_3$  while it moves right and up with an increase in  $q_3$  for constant  $E_\nu$ .

#### 4.2.3 Behaviour of $\theta_\mu$ with variation in $E_\nu$ keeping $q_0$ and $q_3$ fixed

To obtain this behaviour, Eq. 4.2 can be used. For MINERvA energies,  $E_\mu \gg \frac{Q^2 + m_\mu^2}{2E_\nu}$ , and thus,

$$\begin{aligned}
 p_{\parallel} &\approx E_\mu \\
 \text{or, } \cos\theta_\mu &\approx \frac{E_\mu}{p_\mu} \\
 &\approx \frac{1}{\sqrt{1 - \left(\frac{m_\mu}{E_\mu}\right)^2}}
 \end{aligned} \tag{4.15}$$

Since  $E_\mu$  increases with an increase in  $E_\nu$ ,  $\cos\theta_\mu$  increases and thus,  $\theta_\mu$  decreases with an increase in neutrino energy. In the context of MINERvA, the same energy and momentum transfer reactions will have more forward muons at higher neutrino energy, and it is more likely that the muon will be measured in the MINOS Near Detector and accepted into the sample.

### 4.3 Ineffective angle cuts

Based on the previous sections, the following points will help in understanding the trend of muon angle and which muon angle is affected by a particular angle cut.

- $\theta_\mu$  increases with an increase in  $q_3$ .
- $\theta_\mu$  first increases and then decreases with an increase in  $q_0$ .
- $\theta_\mu$  decreases with an increase in  $E_\nu$ .
- $Q^2 = 0$  events, along the diagonal with  $q_0 = q_3$ , always have a small muon angle.

To determine whether an angle cut would affect the events or not, the points stated above are important.

Following on the work of I. Mahbub [26], the following classification of energy ranges is made: Low  $E_\nu$  (1-4 GeV), Mid  $E_\nu$  (4-7 GeV) and High  $E_\nu$  (7 GeV and higher). Since the neutrino flux distribution peaks at 6 GeV, the classification is made such that there is an energy range behind the peak, one around the peak and another after the peak.

Similarly, three-momentum transfers can be classified as: Low  $q_3$  (0.0 - 0.4 GeV), Mid  $q_3$  (0.4 - 0.8 GeV) and High  $q_3$  (0.8 - 1.2 GeV). It must be mentioned that although Low  $q_3$  range includes 0.0, that value of  $q_3$  is physically not approachable. This was seen in section 4.1.2 where the minimum value of  $Q^2$ , and thus  $q_3$  is non-zero for all values of  $E_\nu$  and  $q_0$ .

To get the maximum muon angle in a particular energy range and  $q_3$  range, the idea is to choose the minimum energy value and maximum  $q_3$  value in the range, and then use Eq. 4.14 and Eq. 4.13 to get the maximum angle and the corresponding  $q_{0(max)}$  respectively.

The following table can be constructed specifying the angle cuts which won't have any effect on the events in a particular range of  $E_\nu$  and  $q_3$ .

Table 4.3: Maximum angle in an energy range and  $q_3$  range, and the corresponding ineffective angle cuts

Energy range (in GeV)	$q_3$ range (in GeV)	$q_{0(max)}$ (in GeV)	$\theta_{\mu(max)}$ (in deg.)	Ineffective angle cut (in deg.)
High $E_\nu$	High $q_3$	0.103	9.871	10.00
	Mid $q_3$	0.045	6.562	6.75
	Low $q_3$	0.011	3.276	3.50
Mid $E_\nu$	High $q_3$	0.183	17.458	17.75
	Mid $q_3$	0.079	11.537	11.75
	Low $q_3$	0.019	5.739	6.00
Low $E_\nu$	High $q_3$	0.824	81.890	None
	Mid $q_3$	0.391	53.130	None
	Low $q_3$	0.078	23.578	None

In Table. 4.3, the upper value of  $q_3$  used in the High  $q_3$  range for Low  $E_\nu$  is taken to be 0.99 GeV since  $q_3$  cannot exceed  $E_\nu$ . For Low  $E_\nu$ , all angle cuts will have an effect because the maximum angle is always greater than 20 degrees.

#### 4.4 Energy Dependence Discrepancies when Muon Angle Cuts are applied

Experimental results show that neutrino-nucleus interaction models are not perfect as they do not describe the data well. MINERvA shows this for neutrino energy range 1 to 20 GeV. A deeper question is whether energy dependence in the cross-section is well-modeled or not even though the absolute cross-section might not be well-modeled. Previous chapters have already shown that energy dependence comes from  $W_3$  and  $W_2$ . So, if energy dependence mismodeling is coming from the cross-section directly, it could mean that either  $W_3$  or  $W_2$  is not right. However,  $W_2$  has less chances of being wrong since it also governs the Energy Independent Term and is constrained very well.

#### 4.4.1 Method to test whether energy dependence in data is well-modeled or not

One way to test the energy dependence is by taking the ratio of data events of two different energy ranges, say HighEnu and MidEnu, and comparing it with the ratio of the same energy ranges for Monte Carlo. If the ratios match, it means that the energy dependence is well-modeled and if they don't, it means that it is not well-modeled. The following figure shows the ratios HighEnu/MidEnu and MidEnu/LowEnu for High  $q_3$ , Mid  $q_3$  and Low  $q_3$  with only the default muon angle cut of 20 degrees. This muon angle cut will not affect any event in HighEnu and MidEnu sample as shown in the previous section. However, LowEnu events have a muon angle greater than 20 degrees and they will gain an additional energy dependence due to this angle cut.

The horizontal axis in the figure is labeled “recoil energy in tracker (GeV)”. This is a reconstructed calorimetric quantity and an equivalent of available energy. Available energy, introduced in [69], is an experiment-centered energy from hadrons. Compared to energy transfer, it excludes neutrons and also the energy cost to remove nucleons from the nucleus.

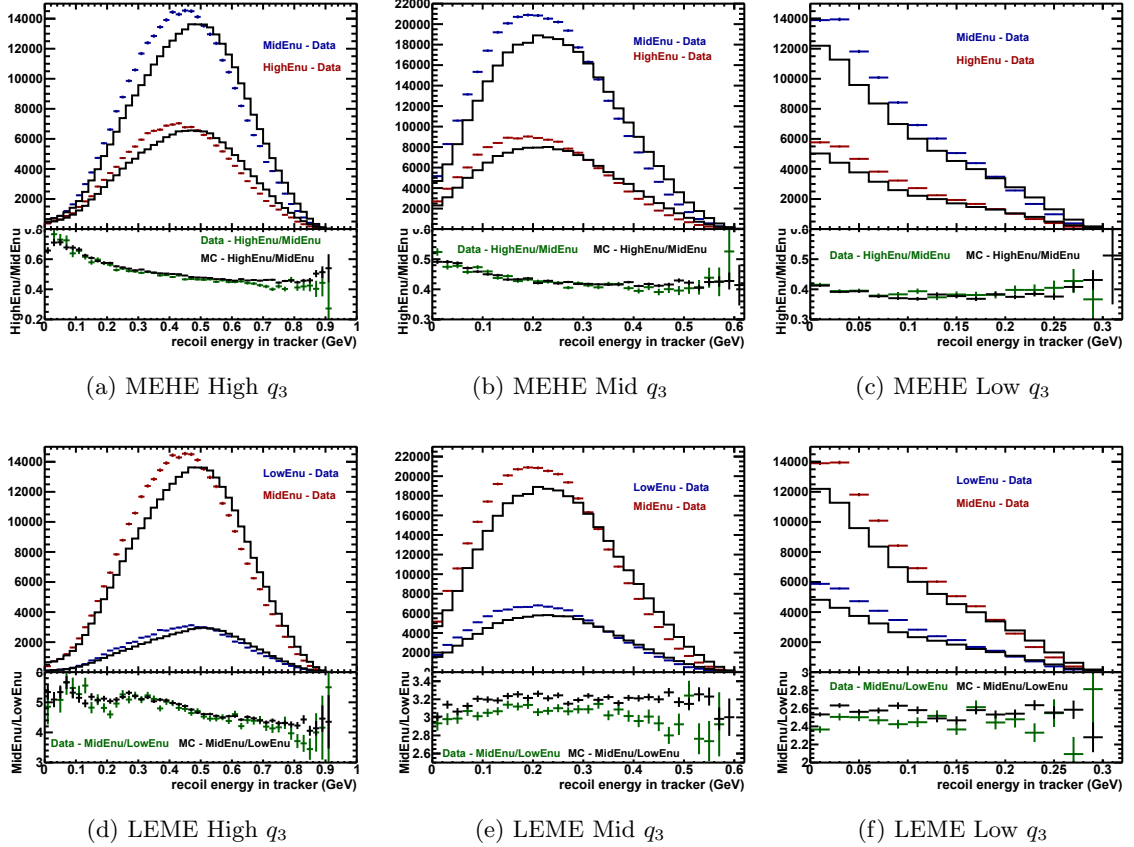


Figure 4.2: Plots of the ratios HighEnu/MidEnu and MidEnu/Low Enu for three different ranges of  $q_3$  with the default muon angle cut of 20 deg.

Energy dependence is generally well-modeled for the ratio HighEnu/MidEnu except for in the region of high energy in tracker where the ratio of MC is greater than the ratio of data. This is the region of low  $Q^2$ . Mahbub [26] has studied these plots in his thesis and pointed out that this discrepancy could be coming from mismodeled energy dependence in low  $Q^2$  suppression, which is the suppression of resonances at low  $Q^2$ .

Energy dependence in MidEnu/LowEnu is well-modeled in High  $q_3$  range except for the region of low  $Q^2$  which could be due to mismodeled energy dependence in low  $Q^2$  suppression also. However, there is an energy dependence discrepancy in Mid  $q_3$  and Low  $q_3$  because the black and green points in the lower panels in plots (e) and (f) in

Fig. 4.2 disagree by more than their statistical error bars. This may be coming from mismodeled energy dependence in cross-section itself, which implies that  $W_3$  could be mismodeled. It is possible that this mismodeling affects the ratio of HighEnu/MidEnu also but due to high neutrino energy, the energy dependent term is suppressed. For the MidEnu/LowEnu ratio, angle acceptance due to angle cut cannot be neglected either.

I will not go into further details about these plots here. The point I want to make is that if no extra source of energy dependence such as a strong muon angle cut can be identified, it is likely that the discrepancy is due to mismodeled  $W_3$  in the cross-section itself. However, if there is no energy dependence discrepancy without any angle cut, for example the ratio of HighEnu/MidEnu in High  $q_3$ , and the discrepancy appears after applying an angle cut, it is likely due to a particular mismodeled interaction that shows up as an energy dependence discrepancy due to the chosen angle cut. We will see soon that a discrepancy appears in the ratio HighEnu/MidEnu for High  $q_3$  when an angle cut of 5 degrees is applied.

#### 4.4.2 Smaller angle cuts introduce an additional energy dependence

I will use the plot of HighEnu and MidEnu in High  $q_3$  range to make my point. It is directly applicable to other neutrino energy and  $q_3$  ranges also.

Fig. 4.2 in the previous section showed that there is almost no energy dependence discrepancy for the selected energy range and  $q_3$  range with no muon angle cut (20 degrees cut is equivalent to no angle cut for HighEnu and MidEnu). This indicates that the energy dependence in the cross-section itself is well-modeled. The following figure shows that there is still no discrepancy when an angle cut of 0 to 10 degrees is applied but a discrepancy appears when an even stronger angle cut of 0 to 5 degrees is applied. Also, there is no discrepancy when events with muon angle from 5 to 10 degrees are selected.

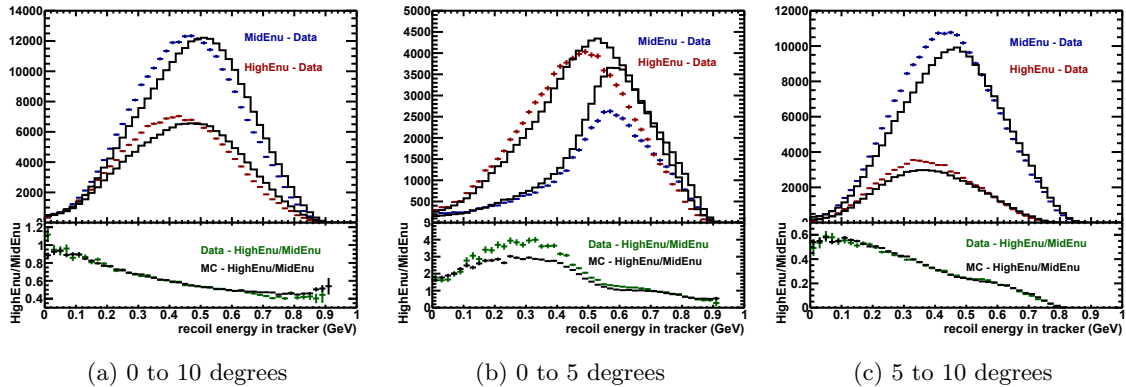


Figure 4.3: Plots of the ratios HighEnu/MidEnu High  $q_3$  with the angle cut of 0 to 10 degrees, 0 to 5 degrees and 5 to 10 degrees. There is a large energy dependence discrepancy in the middle plot.

The events with muon angle up to 5 degrees have an energy dependence discrepancy and those with muon angle from 5 to 10 degrees do not have a discrepancy but when these two set of events are plotted together, the discrepancy disappears. I have already said that there is no energy dependence discrepancy coming from the cross-section but it does not mean that the cross-section is well-modeled.

I have shown in latter chapters that this discrepancy is due to mismodeling of pions and I will use that information here to explain what is going on. Low energy pions are underestimated in MC and high energy pions are overestimated in MC. When a bigger angle cut of 0 to 10 degrees is applied, almost all the pions are selected and their overestimation and underestimation balances each other out and we do not see a discrepancy. Similarly, a muon angle cut of 5 degrees primarily selects high energy pions which are overestimated in MC. This mismodeling shows up as an energy dependence discrepancy here. It is possible that the angle cut of 5 to 10 degrees also selects pions in such a way that the mismodeling of low and high energy pions balances itself.

The takeaway is that angle cuts impose an additional energy dependence and if an energy dependence discrepancy appears, it could be due to mismodeled cross-section that shows up there due to the angle cut. It is still possible that energy dependence

in cross-section is not well-modeled but to verify that, we should take a step back and remove additional energy dependence sources such as angle cuts before reaching a conclusion.

In the latter chapters, we will see that even smaller angle cuts such as 0 to 2 degrees and 2 to 4 degrees can also be applied to study energy dependence.

## 4.5 Changing QE axial mass ( $M_A$ ) and RPA effect

The discrepancy that looks like mismodeled energy dependence in Fig. 4.3 is where, without angle cuts, the QE population peaks. Even though an angle cut is applied, the region of interest still has a large number of QE events indicating that an imperfect QE model could be part of the cause. In addition, the event rate distributions in the upper part of most plots demonstrate that the QE model and other models are not perfect. Changing form factors and the RPA effect are already familiar from Chapter 2.2. The first part of this section demonstrates how much improvement in describing the data event rate is obtained by adjusting them, then whether the discrepancy is also reduced. Although we learn later that the apparent energy dependence discrepancy is coming from the pion model, we studied the effect of varying QE parameters. This section reports on the resulting insights.

Bubble chamber experiments were conducted in the 1970s on deuterium. They remain an important data set and their measurements of the protons, pions, and muons are extremely precise. At that time deuterium was believed to have minimal nuclear effects that would be easy to model since a deuterium nucleus consists of only a proton and a neutron. Recent re-interpretations of data have suggested that nuclear effects in deuterium are not as easy to model as it was expected. Nevertheless, bubble chamber was a high precision experiment and provided the first measured value of quasielastic scattering axial mass as  $M_A = 0.99$  GeV. The extraction of axial form factor from bubble chamber data was based on the naive dipole approximation. Recent work by Meyer *et al.* [45] fits the better motivated z-expansion parametrization to the same data. The form factor itself is not very different because it is the same data, but the

uncertainty budget is much more realistic. Lattice QCD calculations predict the form factor is quite different, approximately the difference between dipole form factors with  $M_A = 0.99$  GeV and  $M_A = 1.24$  GeV. One interpretation is that the Lattice QCD result is the true form factor and the bubble chamber result is modified by unexpectedly strong nuclear effects. This section evaluates the consequences of such a hypothesis.

#### 4.5.1 Comparison between the effect of $M_A = 1.08$ GeV and $M_A = 1.24$ GeV on the plot with MINERvA Default $M_A = 0.99$ GeV

For this work, I am choosing two  $M_A$  values in addition to the bubble chamber and MINERvA default 0.99 GeV. One is 1.08 GeV which is  $1\sigma$  above the mean axial mass value as determined in the uncertainty budget in Meyer et al. [45] for the z-expansion, but re-expressed by Dr. Gran in terms of  $M_A$  for use within MINERvA. The other is 1.24 GeV which is predicted by Lattice QCD [46].

The goal is to see the effect of changing  $M_A$  from 0.99 GeV to 1.08 GeV and 1.24 GeV. This change in axial mass is applied to HighEnu and MidEnu sample in High  $q_3$  range. I'm showing the plots of only High  $q_3$  range and not Mid  $q_3$  and Low  $q_3$  because the axial form factors are pinned at  $F_A(Q^2 = 0)$  to a value extracted from neutron decay, so variations of form factors always have largest effects at high  $Q^2$ . The goal here is not the energy dependence. It is to determine if changes to the form factor can improve the agreement with the data in the upper panel, and the simple data/MC ratio is in the lower panel. In effect, the goal is to improve the model for the structure function  $2W_2$ . Also, the next plot shows that the change of  $M_A$  from 0.99 GeV to 1.08 GeV is not big enough. One  $q_3$  range is enough to convey that point here. We created the plots for only 0 to 10 degrees as our test as other angles which are not included in this thesis had the same effect with a change in axial mass.

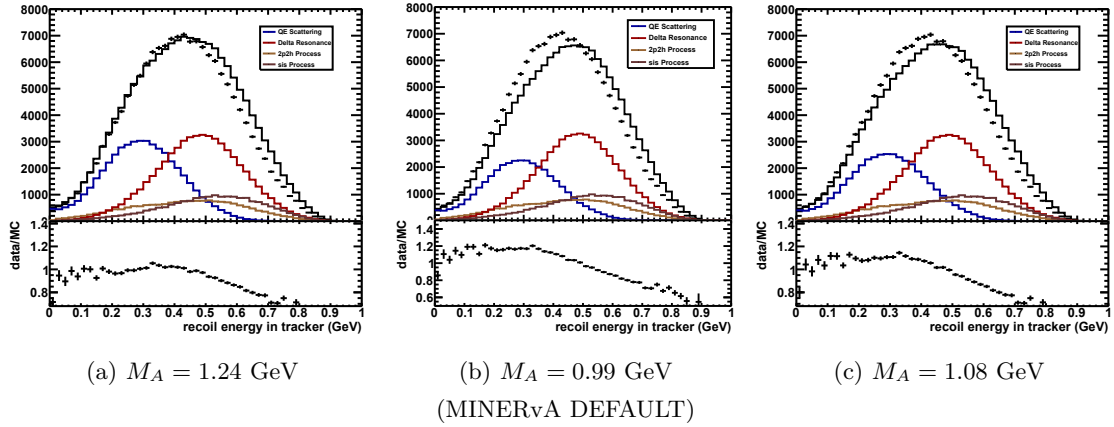


Figure 4.4: Plots of HighEnu for High  $q_3$  and muon angle cut 0 to 10 degrees to draw a comparison between three different quasielastic axial masses

In the above figure, it can be seen that increasing axial mass increases the simulated cross-section, and hence the number of events, since the ratio data/MC has come down.  $M_A = 1.24$  GeV brings the ratio down by about 15 to 20% while  $M_A = 1.08$  GeV brings the ratio down by less than 10% in comparison to the ratio in the plot of MINERvA DEFAULT. The effect of a change in axial mass can be studied for MidEnu also.

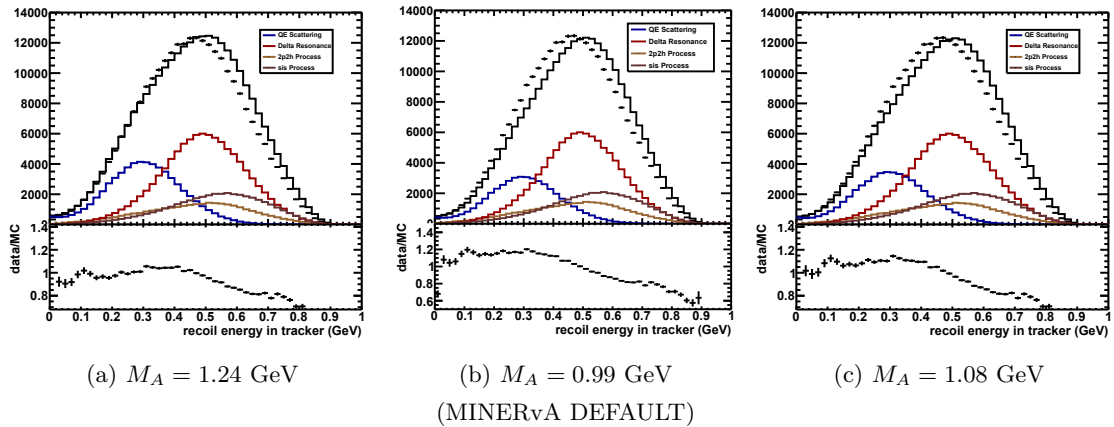


Figure 4.5: Plots of MidEnu for High  $q_3$  and muon angle cut 0 to 10 degrees to draw a comparison between three different quasielastic axial masses

Ratios have come down for MidEnu also and  $M_A = 1.24$  GeV brings the ratio down by a bigger percentage in comparison to  $M_A = 1.08$  GeV. Also, because this form factor and structure function change only affects the QE component, the shape of the ratios changes noticeably. Hypothetically obtaining the correct model for all processes will yield flat ratios that are within flux uncertainty of 1.0.

From now on,  $M_A = 1.24$  GeV will be used to draw any comparison since its effect is bigger and easier to observe. This might not seem so important in High  $q_3$  but in lower  $q_3$  ranges, the effect of a change in  $M_A$  is too small and thus, a relatively bigger change is required for an easier observation.

#### **4.5.2 Comparison between the effect of $M_A = 1.24$ GeV and RPA effect ( $1\sigma$ away from nominal) on the plot with MINERvA Default $M_A = 0.99$ GeV and nominal RPA**

Gran [19] has showed that nominal RPA used by MINERvA reduces the free-nucleon cross-section as  $Q^2 \rightarrow 0$  by 60%. This percentage decreases until there is no reduction around  $Q^2 = 0.5$  GeV<sup>2</sup>. RPA then slightly enhances the cross-section at higher  $Q^2$ . Since RPA is dominant at low  $Q^2$  and hence low energy and momentum transfers, we will see in the upcoming plots that changing RPA has the biggest effect on Low  $q_3$  range and that too on the left side of the plots which corresponds to the low energy in tracker.

We propose that reduction of cross-section by 60% is a bit too much and that is why the data/MC ratio in the MINERvA DEFAULT plots is greater than 1. We will reduce the RPA effect by  $1\sigma$  from its nominal value and thus, reduce the data/MC ratio by increasing the interaction cross-section. The definition of  $\pm 1\sigma$  is to go 25% of the distance from RPA nominal to RPA off, and then go the same amount in the opposite direction.

The following plots compare the effect of changing only  $M_A$  from 0.99 GeV to 1.24 GeV with the effect of changing RPA from its nominal value to a smaller value. The following page has the plots for HighEnu and the page after that has the plots for MidEnu. We checked for LowEnu separately that the effect is same.

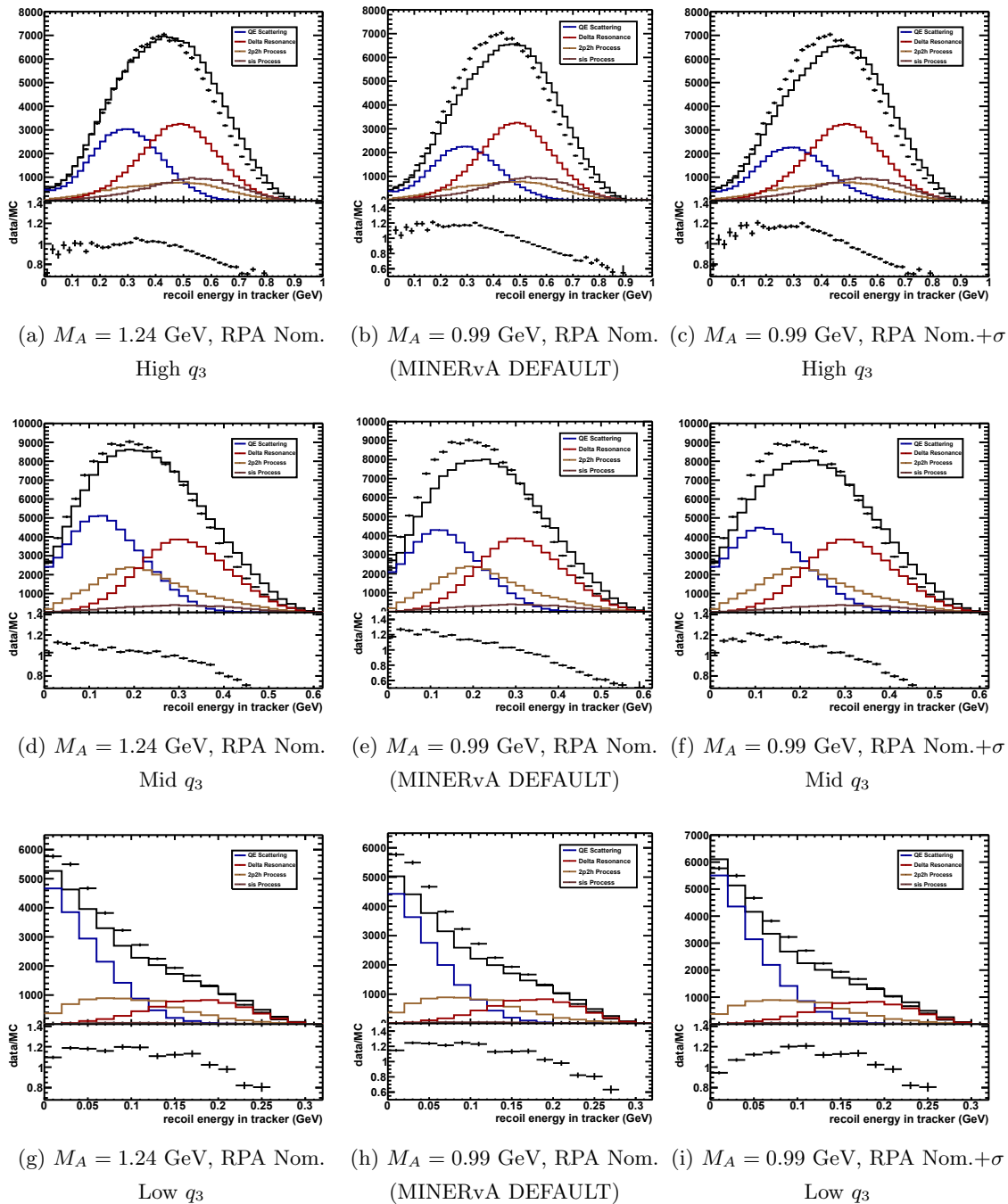


Figure 4.6: Increasing  $M_A$  brings the data/MC down by the largest amount in High  $q_3$ . Reducing RPA brings the data/MC down by the largest amount in Low  $q_3$ . Plots are of HighEnu High  $q_3$ , Mid  $q_3$  and Low  $q_3$  with a muon angle cut of 0 to 10 degrees.

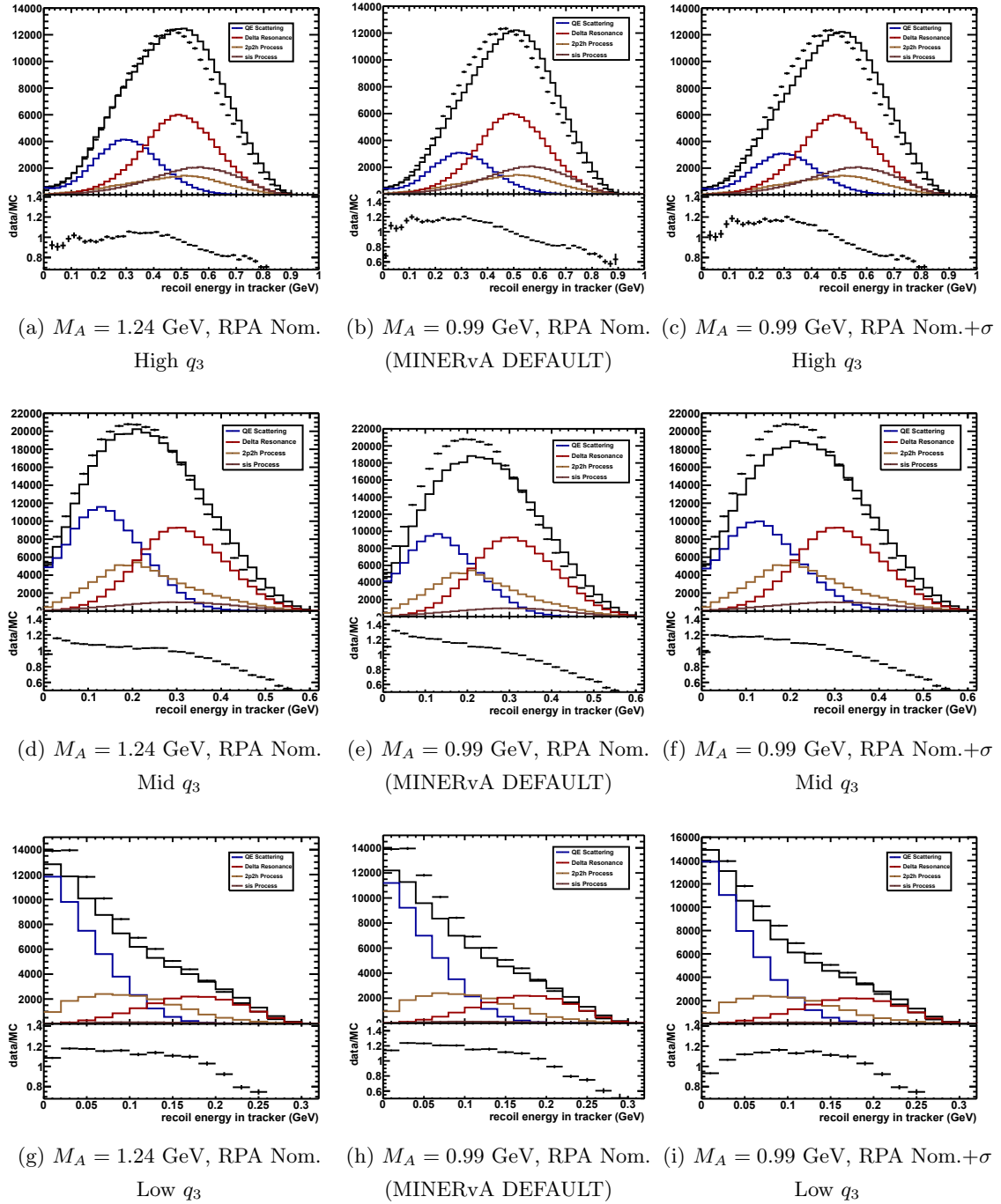


Figure 4.7: Increasing  $M_A$  brings the data/MC down by the largest amount in High  $q_3$ . Reducing RPA brings the data/MC down by the largest amount in Low  $q_3$ . Plots are of MidEnu High  $q_3$ , Mid  $q_3$  and Low  $q_3$  with a muon angle cut of 0 to 10 degrees.

All the figures drawn above have shown that  $M_A = 1.24$  GeV has the biggest effect on High  $q_3$  and a significant effect on Mid  $q_3$ . It brings data and MC closer in the low energy in tracker region by increasing the cross-section of quasielastic scattering and hence the number of simulated events. It has a small effect on Low  $q_3$ .

The figures indicate that the default RPA in MINERvA is a bit more than required. Reducing it by  $1\sigma$  brings data and MC closer since reducing RPA means increasing quasielastic cross-section. Reducing RPA has a big effect on Low  $q_3$ , a significant effect on Mid  $q_3$  and a negligible effect on High  $q_3$ .

In conclusion, both  $M_A = 1.24$  GeV and RPA smaller by  $1\sigma$  bring data and MC closer and hence, may be a better choice than the default values. However, neither change produces distributions that are flat at 1.0 across the whole range. If they are better, other aspects of the model would also need adjustment, or even those other aspects could cure the discrepancy with no change in  $M_A$  or RPA.

### 4.5.3 Varying $M_A$ and RPA effect to observe their effect on the energy dependence discrepancy

Coming back to the energy dependence discrepancy shown in Fig. 4.3 corresponding to HighE<sub>nu</sub> and MidE<sub>nu</sub> in High  $q_3$  range when a muon angle cut of 0 to 5 degrees is applied, this discrepancy is present in the region where QE peaks. Thus, when we first encountered this discrepancy it was natural to try varying the QE parameters, such as  $M_A$  and RPA effect, to see if that reduces the discrepancy. Before actually varying QE parameters, we should look at the following figure which shows the peaks of various interactions.

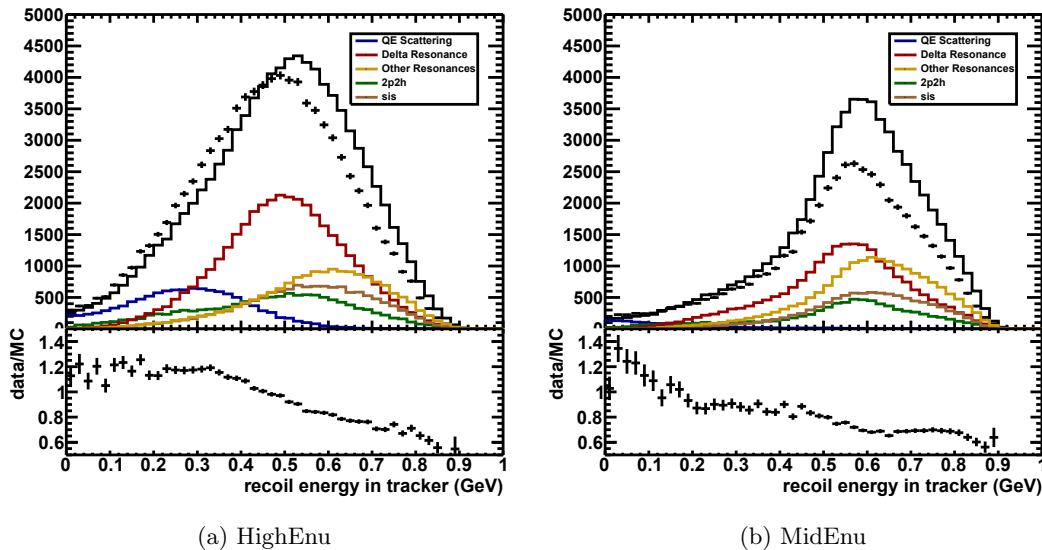


Figure 4.8: Plots of HighEnu and MidEnu in High  $q_3$  range when a muon angle cut of 0 to 5 degrees is applied showing that the discrepancy region is populated by QE events only in HighEnu. QE events do not pass the angle cut in MidEnu

The figure above indicates that the discrepancy shown in Fig. 4.3 lies in the region where QE peaks for HighEnu. MidEnu does not have a QE peak in that region but this significant difference in QE events between MidEnu and HighEnu, and possibly imperfect QE model, could be a contribution to the discrepancy when angle cuts are applied. The previous subsections have indicated that  $M_A = 1.24$  GeV and RPA smaller by  $1\sigma$  might be a better choice. Thus, we tried these values and compared the new plot with the original plot to see if the discrepancy has gone away.

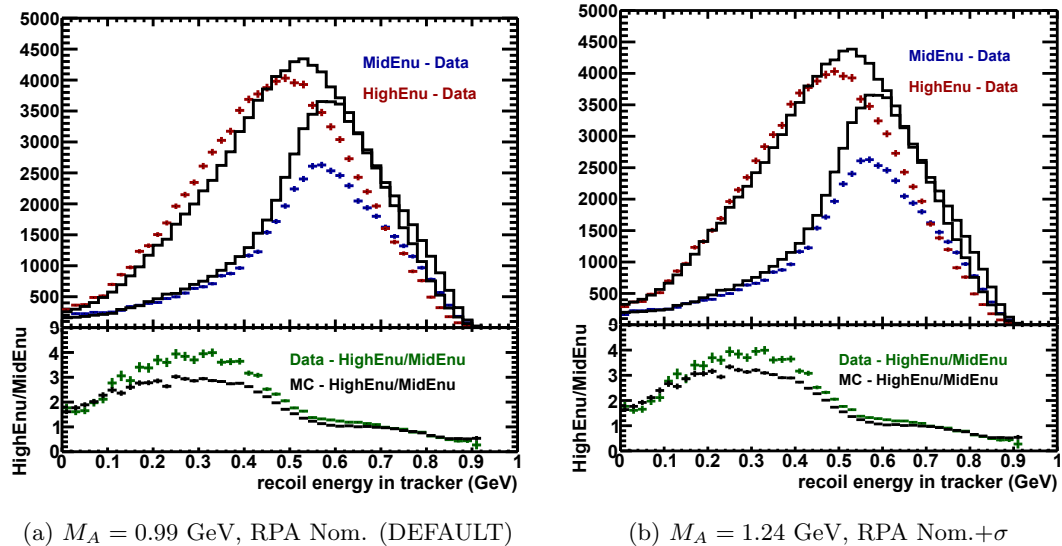


Figure 4.9: Plots of HighEnu and MidEnu in High  $q_3$  range when a muon angle cut of 0 to 5 degrees is applied showing that the discrepancy region is reduced by a small amount when the  $M_A$  and RPA effect in QE are changed

The figure above shows that the discrepancy reduces by a small amount when  $M_A$  and RPA effect are changed. This indicates that there must be some other interaction that is mismodeled and can remove the discrepancy completely. The other problem here is that there is no consensus in the neutrino physics community that a value of  $M_A$  as large as 1.24 GeV could be right.

By the end of the thesis, it will become clear that pion production is responsible for the energy dependence discrepancies and pions are produced by delta resonance and not by QE scattering. Since we changed the  $M_A$  of QE scattering and RPA affects only QE scattering, it was natural for these changes to have little effect on the energy dependence discrepancies. It also hints that at MINERvA energies, making such dramatic changes to the form factors produces little intrinsic energy dependence discrepancy itself. At some lower energy they must have a significant effect.

## Chapter 5

# Neutrino Flux Analysis

In accelerator neutrino experiments, a neutrino beam is generated through the decay of pions and kaons, which are produced when a proton beam hits a graphite target. Neutrinos further interact in the near detector with nuclei. MINERvA can predict and calibrate the number and energy spectrum of neutrinos passing through and interacting in the detector. In order to analyze the data obtained from interactions, it is important that neutrino flux is well-modeled but it is affected by uncertainties. The production of hadrons when proton beam hits the graphite target and their distribution is the major source of uncertainties along with beam focusing and alignment. Smaller uncertainties come from horn currents [11].

The analysis of energy dependence in this thesis is closely related to a flux-constraint technique called the low- $\nu$  method [70, 13]. This chapter explores the interplay between the two approaches to beam data and flux uncertainties.

### 5.1 Neutrino Flux Measuring Techniques

MINERvA uses three techniques to constrain the neutrino flux. One is based on the neutrino-electron scattering. Mostly, a neutrino interacts with a nucleus but sometimes it scatters off atomic electrons ( $\nu e^- \rightarrow \nu e^-$ ). The scattering cross-section is about a thousand times smaller than the neutrino-nucleus cross-section but it is very well modeled [71]. The details of MINERvA constraining neutrino flux using neutrino-electron

scattering is provided in references [72, 12]. My work uses this flux unless mentioned otherwise. The second technique uses Inverse Muon Decay (IMD) in which a muon neutrino interacts with an electron and produces an electron neutrino and a muon. IMD ( $\nu_\mu e^- \rightarrow \nu_e \mu^-$ ) can be used to predict neutrino flux with small uncertainties. Its energy threshold is approximately 11 GeV and is thus, used to predict the high-energy tail of MINERvA neutrino beam [73]. Its cross-section up to one-loop electroweak corrections is given in reference [74]. MINERvA calls these processes “Standard Candles”.

The third technique that is central to this section is based on the low- $\nu$  method. The symbol  $\nu$  comes from deep inelastic scattering on nucleons and is defined as  $p \cdot q/m_N$  where the four-vector dot product in the numerator ensures the quantity is a relativistic invariant.  $p$  and  $q$  are the initial four-momentum of the struck nucleon and the four-momentum transfer respectively, and  $m_N$  is the mass of the struck nucleon. In the special case of the lab reference frame, this quantity evaluates simply to the reaction energy transfer which is called  $q_0$  or  $\omega$  in nuclear physics and throughout this thesis. It is the vertical axis in the triangle diagram and related to the tracker energy in most of the other plots.

Low- $\nu$  technique was developed by CCFR/NUTEV collaborations and has been used by MINOS collaboration [75]. MINERvA has used it to include correction to the MINOS muon energy scale [70] and for a flux constraint in the low energy data era [76]. However, MINERvA hasn't explored the individual three-momentum transfer ranges and that the flux obtained through this method might bring data and Monte Carlo closer to each other in all those ranges. The idea is that at low  $\nu$  values, or as  $\nu/E_\nu \rightarrow 0$  where  $E_\nu$  is the incoming neutrino energy, the cross-section is independent of neutrino energy. Hence, the number of events are directly proportional to the neutrino flux. In a way, this method is used to constrain the SHAPE of neutrino flux.  $\nu - e$  scattering method mentioned above is a rate-based constraint and hence, is more useful in constraining the actual value of the flux, so the two methods are complementary.

The inclusive differential cross-section for charged-current neutrino (or antineutrino)-nucleon interaction is given by [76]

$$\frac{d\sigma^{\nu,\bar{\nu}}}{d\nu} = A \left( 1 + \frac{B}{A} \frac{\nu}{E_\nu} - \frac{C}{A} \frac{\nu^2}{2E_\nu^2} \right) \quad (5.1)$$

where A, B and C are the integrals of neutrino-quark deep inelastic scattering structure functions  $F_1 = MW_1(x, Q^2)$ ,  $F_2 = \nu W_2(x, Q^2)$  and  $F_3 = \nu W_3(x, Q^2)$  [77, 78], where  $x = Q^2/(2M\nu)$  is the Bjorken scaling variable,  $Q^2$  is the negative of four-momentum transfer squared and  $M$  is the proton mass. Bjorken variable is a relativistic invariant that gives a measure of the fraction of the incoming neutrino energy transferred to the struck quark. It is no surprise that structure functions for neutrino-quark scattering in the deep inelastic scattering regime have a similar pattern to the structure functions for neutrino-nucleon scattering for quasielastic, 2p2h, and delta reactions at low momentum transfer. This connection is what we wanted to explore in detail.

The expressions of A, B and C are as follows:

$$\begin{aligned} A &= \frac{G_F^2 M}{\pi} \int_0^1 F_2(x) dx, \\ B &= -\frac{G_F^2 M}{\pi} \int_0^1 (F_2(x) \mp xF_3(x)) dx, \\ C &= B - \frac{G_F^2 M}{\pi} \int_0^1 F_2(x) \tilde{R} dx, \end{aligned} \quad (5.2)$$

where “-” sign corresponds to neutrinos and “+” sign corresponds to antineutrinos.  $\tilde{R}$  has a slightly complicated expression dependent on structure functions. It is not a part of the main story, and that’s why it is not written here but it can be found in the reference [76].

In the limit  $\nu/E_\nu \rightarrow 0$ , Eq. 5.1 simplifies to

$$\frac{d\sigma^{\nu,\bar{\nu}}}{d\nu} \approx A. \quad (5.3)$$

Thus, the cross-section depends only on  $F_2(x)$ , and is independent of the neutrino energy, and hence, the only energy dependence present in the data is due to flux. By analyzing this energy dependence, neutrino flux can be constrained. This technique can be used by DUNE in future as its energy range overlaps with MINERvA [79].

## 5.2 Rob Fine's Low- $\nu$ Flux and its Analysis

Dr. Rob Fine, a former member of the MINERvA collaboration, used the low- $\nu$  method incorporating the 3.6% muon energy shift given in [70] and presented his results on neutrino flux in his Ph.D. thesis [13]. He also included  $\nu - e$  scattering corrections to low- $\nu$  method but those results were not fully developed by the time his thesis was written and that is why they were not investigated as a part of my thesis.

Rob Fine's low- $\nu$  flux is shown relative to MINERvA's previous best flux, which incorporates the  $\nu - e$  scattering constraint. This figure is taken from Fine's thesis.

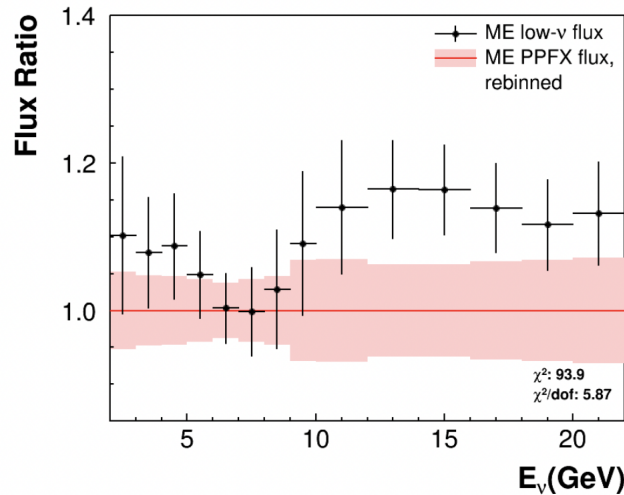


Figure 5.1: Rob Fine's low- $\nu$  flux estimate expressed as a ratio of low- $\nu$  flux to the MINERvA's default  $\nu - e$  scattering flux

Fig. 5.1 shows that low- $\nu$  flux and MINERvA's default  $\nu - e$  scattering flux meet in the range 6 to 7 GeV, which is slightly on the high side of ME neutrino beam peak event rate. This is expected since low- $\nu$  method constrains the shape of flux and  $\nu - e$  scattering method constrains the rate of incoming neutrinos in the flux, and both of these are best estimated around the ME beam peak. The low- $\nu$  flux has a substantially different spectrum, by up to 30% on the high energy side, compared to the default flux.

C. Wilkinson *et al.* [80] have presented some concerns for the use of low- $\nu$  technique to determine flux below 5 GeV of neutrino energy. This technique has a constant cross-section assumption for low energy transfers. The authors of [80] have shown that this assumption and low- $\nu$  flux constraints are severely dependent on the models used which in turn are related to the ansatz that there is negligible energy dependence of the cross section at MINERvA ME beam energies in this thesis. They have addressed other concerns related to the selection of a low energy transfer sample from the data. Rob Fine has incorporated some of these concerns in his thesis resulting in big error bars in the region of low neutrino energy.

Since Rob Fine's flux is not available as a code, it was manually parametrized by selecting a few data points and fitting a polynomial through them. The parametrization is almost as shown, cartoon style, in the following picture. The actual polynomial and parametrization is given in Appendix D.

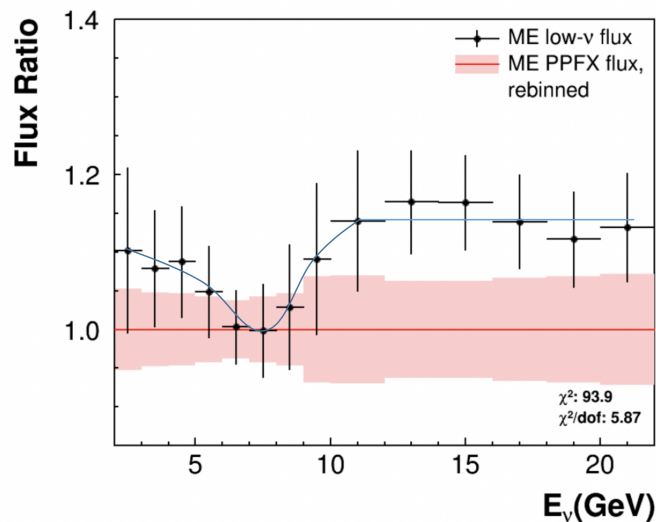


Figure 5.2: Rob Fine's low- $\nu$  flux parametrization

The main goal of this section is to compare data with Monte Carlo for the MINERvA default  $\nu - e$  scattering flux and Rob Fine's low- $\nu$  flux. That comparison will inform our interpretation of the energy dependence of the cross section and which differences between the data and the model could simply be attributed to flux uncertainties. To

do that, three different ranges of three-momentum transfer can be plotted together and compared between the two fluxes.

The figure 5.3 on the next page is divided into two pads for both the fluxes for a different quantity that has not been presented thus far in this thesis: the event rate vs neutrino energy. In fact, it is displaying the integral of each of the three  $q_3$  ranges defined earlier, but in finer energy bins than the three that have been used up to now. It is projecting out the same samples in a graphically complementary way. Since data is unaffected by any change in the Monte Carlo, this pad doesn't change. The bottom pad shows the ratio of data/MC showing a distortion on the right that is the inverse (because the MC is in the denominator) of the parametrization. If neutrino-nucleus interaction models, neutrino flux modeling and detector simulations were perfect, the data/MC ratio would be 1. However, they are not perfect and so, the ratio deviates from 1. A green horizontal line is drawn corresponding to the ratio of 1 in the bottom pad to guide the eye for an easier comparison of the two fluxes. There is an additional line at the ratio of 1.1 since the Low  $q_3$  plot has an almost constant offset for the low- $\nu$  flux.

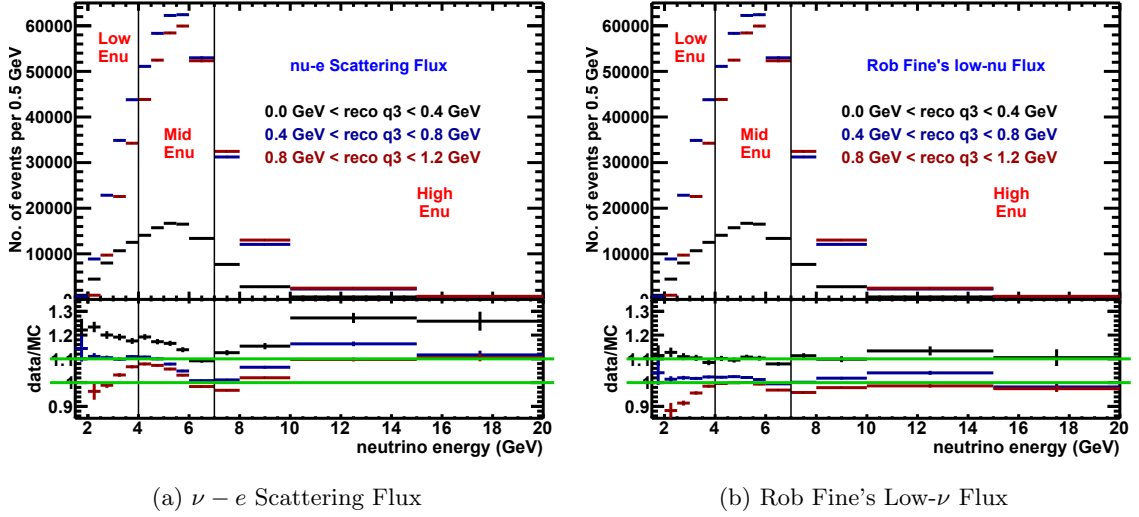


Figure 5.3: Comparison of data and MC for two different fluxes by dividing three-momentum transfer into three different ranges

Fig 5.3 clearly shows that data/MC ratio is closer to 1 for Rob Fine's low- $\nu$  flux. Also, the wiggles that are present for the  $\nu - e$  scattering flux have almost disappeared and the ratio plot is much flatter. This is an expression of an additional energy dependence introduced by the low- $\nu$  flux. The ratio between 6 and 7 GeV is practically unchanged. The  $\nu - e$  method constrains these bins best, and the low- $\nu$  method appears to agree.

A strength of Rob Fine's low- $\nu$  approach is that the absolute flux on the high side is pinned to  $\mathcal{O}(5\%)$  precise flux and DIS cross section measurements made by CCFR [81, 82], NuTeV [83, 84], and NOMAD [85, 86]. Given this, the deviation from 1.0 in the second figure (b) of Fig. 5.3 at high energies is directly illustrating actual shortcomings of the neutrino interaction model for the different  $q_3$  ranges. Actually, the energy spectrum of CCFR is from 30 GeV to 600 GeV and it imposes a constraint on cross-section in those energy  $\nu$  ranges. NOMAD peaks at 24.3 GeV and its high energy range overlaps with the low energy range of CCFR, thus NOMAD is constrained by CCFR data. Now, the low energy range of NOMAD overlaps with the high energy range of Rob Fine's and MINERvA's neutrino beam, and thus imposes constraints on the neutrino flux in

HighEnu range.

Below the peak at 6 GeV, the low- $\nu$  flux has lowered the data/MC ratio by 5 to 8%. The nominal flux uncertainty in the  $\nu - e$  scattering flux is about 3.9% [12] and this lowering of ratio is within  $2\sigma$  of the nominal flux uncertainty.

One of the other important observations from the figure is that although wiggles have mostly disappeared, the ratio of High  $q_3$  deviates at the lowest energies from the ideal ratio of 1. The two most probable reasons behind this could be angle acceptance and energy dependence from the cross-section itself. Another important observation is that Low  $q_3$  has a constant offset of about 10% with the low- $\nu$  flux. This hints at a possible energy-independent error creeping in from the QE cross-section itself since QE is predominant at low momentum transfers. Angle acceptance is not significant for the Low  $q_3$  range. All these possibilities are explored in the next subsections. There will be comments about the Mid  $q_3$  range also.

A potential criticism of using the low- $\nu$  flux method for this low three-momentum transfer sample is that many of the events in data are common to the two analyses. The ratios in Fig. 5.3 could be flat by construction if the sample overlap was perfect. This circularity does not detract from the demonstration of how the methods relate to each other conceptually, that there is no surprise effect coming from the QE, 2p2h, and delta resonances, or when the data are binned in  $q_3$ . For a cross-section measurement like in Ascencio *et al.* [6] where the event rate is divided by a flux, this flux might not be suitable. Special consideration of the systematic uncertainties would be needed and the fraction of events that are common to the two analyses have to be taken into account.

### 5.2.1 Angle Acceptance showing up in the data/MC ratio

As we saw in Chapter 4, muon angle increases as neutrino energy decreases and three-momentum transfer increases. This statement can be used to understand the deviation of High  $q_3$  from being flat and being near 1 for LowEnu.

In the energy range  $2.5 \text{ GeV} < E_\nu < 4 \text{ GeV}$ , the order of muon angle is High  $q_3 >$

Mid  $q_3 > \text{Low } q_3$ . Thus, we expect the least effect of angle acceptance on Low  $q_3$  range. We chose the lower limit of neutrino energy as 2.5 GeV here since that is the lower limit of neutrino energy in the original plot of Rob Fine as shown in Fig. 5.1 and is not far off from 2 GeV. Hence, it does not affect the analysis. The maximum muon angle for each  $q_3$  range in this energy range is as follows:

Low  $q_3$  (0.0 GeV < true  $q_3$  < 0.4 GeV): 9.207 deg.

Mid  $q_3$  (0.4 GeV < true  $q_3$  < 0.8 GeV): 18.663 deg.

High  $q_3$  (0.8 GeV < true  $q_3$  < 1.2 GeV): 28.686 deg.

where  $q_3$  of 0.0 GeV is in red since  $q_3$  can be 0.0 GeV only approximately as shown in section 4.1.2. Also, the maximum muon angle is determined theoretically using the Eq. 4.14 and thus gives the maximum angle only for true  $q_3$  range. However, the resolution smeared  $q_3$  won't have a significantly different maximum muon angle and thus, these muon angle values serve the purpose of the analysis here.

As the maximum muon angle values indicate, Low  $q_3$  is not affected by angle acceptance by a large amount. Looking at the Fig. 3.1, this  $q_3$  range corresponds to an efficiency of over 60% for LowEnu. Mid  $q_3$  range is affected by angle acceptance since efficiency drops significantly above 15 degrees. However, High  $q_3$  has the maximum angle acceptance effect. It goes even beyond the 20 degree mark.

All these observations show that Low  $q_3$  has the least angle acceptance effect and because of that, its energy dependence does not show up in the low- $\nu$  plot. Mid  $q_3$  has a big angle acceptance effect but its ratio is still closer to 1. It is possible that angle acceptance shows up for Mid  $q_3$  but it is compensated by energy dependence coming from the cross-section itself. This will be explored in the next subsection. High  $q_3$  has the maximum angle acceptance effect and this could be one of the reasons behind its deviation in LowEnu from the ideal ratio of 1.

### 5.2.2 Cross-section analysis for the observations of the data/MC ratio

Section 3.1 describes carefully the meaning of Energy Independent Term and  $1/E$  Coefficient, and how it can be obtained from the Valencia Code using the Eq. 3.5. These

terms can be directly used here since this section is about understanding the energy dependence creeping in Fig. 5.3.

To understand how big the energy dependence is here and whether it can be ignored can be understood by taking the ratio of  $1/E$  Coefficient and Energy Independent Term.  $1/E^2$  terms can be neglected as they are tiny compared to other terms.

Table 5.1: Comparison of  $1/E$  Coeff. and  $1/E$  Term at 3 GeV with En. Ind. Term for Low  $q_3$ , Mid  $q_3$  and High  $q_3$

Ratio of terms	Low $q_3$	Mid $q_3$	High $q_3$
$1/E$ Coeff./En. Ind. Term	4.724%	20.533%	25.384%
$1/E$ Coeff./En. Ind. Term $\times 1/3$ GeV	1.575%	6.844%	8.461%

The first row in the Table 5.1 is a general expression for all the neutrino energies and energy dependence corresponding to a particular neutrino energy can be obtained by simply dividing the first row by the neutrino energy. Also, the first row is not unitless. Its unit is GeV but it is not mentioned again and again since percentages are of main interest here. The second row is unitless and it shows the energy dependence at 3 GeV since that is the midpoint of LowEnu.

Table 5.1 shows that  $1/E$  Coeff / En. Ind. Term is about 5% for Low  $q_3$ , which brings down the energy dependence in Low  $q_3$  to about 1.6% for 3 GeV. This energy dependence at 3 GeV is maximum for High  $q_3$  standing at about 8.5%. This higher energy dependence in High  $q_3$  can be another reason for deviation in LowEnu.

Until now, both angle acceptance and higher intrinsic energy dependence in High  $q_3$  can be a reason for the deviation in LowEnu. It is possible that angle acceptance is not well-modeled and/or energy dependence term is not well-modeled for High  $q_3$  but it is not possible at this point to determine which one is the case. Mid  $q_3$  also has a higher energy dependence and a significant angle acceptance but they both apparently compensate each other. If angle acceptance is well-modeled, it means that energy

dependence term is not well-modeled for High  $q_3$  but it is well-modeled for Mid  $q_3$ . However, if angle acceptance is not well-modeled, it means that energy dependence is also not well-modeled for Mid  $q_3$ . It might or might not be well-modeled for High  $q_3$ . Energy dependence is more significant for LowEne compared to other neutrino energy ranges. If it is mismodeled, this could be a reason why it would show up only in LowEne.

It must be mentioned that Table 5.1 presents the true values, which means that the values do not include resolution smearing effects. Also, since they come from Valencia code, they do not include processes other than QE and 2p2h such as delta and higher resonances, and deep inelastic scattering. However, as the work in Chapter 3 shows that resolution smearing generally increases energy dependence, the comments stated above can still be used to explain the deviation observed for High  $q_3$ .

Low  $q_3$  is an interesting  $q_3$  range. First of all, angle acceptance is small here as seen in the previous subsection. Additionally, QE dominates by a large amount over other processes, so the numbers given in the table can be easily used for Low  $q_3$ . Since 1.6% energy dependence is not significant and it is below all the uncertainties in MINERvA, it can be ignored and cross-section is approximately energy-independent. Using Eq. 2.4 and 2.6,

$$\frac{d^2\sigma}{dq_0q_3} \approx \frac{G_F^2 \cos^2\theta_C q_3}{2\pi} (2W_2). \quad (5.4)$$

In the Fig. 5.3, Low  $q_3$  does not show observable energy dependence and has a constant offset of about 10%. This indicates a possible error in the known value of  $W_2$  for the QE scattering, the dominant interaction at low momentum transfers. The analysis did not go in this direction, but such an error could be partially corrected with either or both changes in  $M_A$  and the RPA effect described at the end of the previous chapter.

### 5.2.3 Application of low- $\nu$ flux to energy dependence discrepancies

As explained in Chapter 4, muon angle cuts, neutrino energy cuts and three-momentum cuts can be used to analyze the energy dependence in neutrino-nucleus interaction. In

addition to energy dependence coming directly from the cross-section, muon angle cut introduces an additional energy dependence. It has been seen in neutrino experiments that neutrino models are not perfect and data does not match theoretical predictions. MINERvA has the same observation. However, the question explored in this subsection is one step deeper. Even though models are not perfect, the question is whether at least energy dependence is well-modeled or not. The basic idea behind the energy dependence is that if number of events at a particular neutrino energy are known, they can be used to predict the number of events at some other neutrino energy. Now, the individual number at these two different energies might not match between data and Monte Carlo, but the expectation is that the correlation between them should.

Normally, data and Monte Carlo are compared by plotting them together. However, the goal of this section is to analyze the energy dependence and for that, two different energy ranges MidEnu (4 - 7 GeV) and HighEnu (7 GeV and higher) are plotted together in one pad of the figure and the other pad takes the ratio of number of events in HighEnu and MidEnu for data and Monte Carlo separately. If these two ratio plots match, it means that the energy dependence is well-modeled. In general, it is well-modeled but here are some examples where it is not.

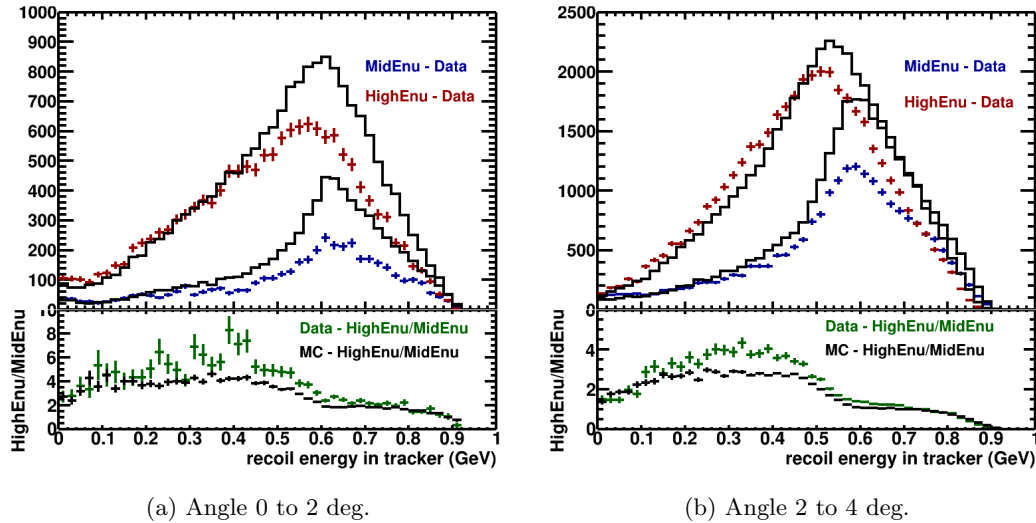


Figure 5.4: Energy dependence discrepancy present corresponding to MidEnu and HighEnu in High  $q_3$  range for muon angle cuts 0 to 2 deg. and 2 to 4 deg.

The figure above shows that energy dependence is not well-modeled for those specific muon angle cuts. There are discrepancies corresponding to other muon angle cuts also but these are enough to run the checks here. Energy dependence could be mismodeled due to mismodeled neutrino flux, mismodeled angle acceptance and mismodeled energy-dependent terms in the cross-section itself. Angle acceptance is very well modeled in MINERvA, so that cannot be the problem here. Chapter 2 has already shown that energy dependent terms can be ignored at MINERvA energies, so even if energy dependence terms are not well-modeled, their effect won't be big enough to create this discrepancy.

It has been demonstrated that Rob Fine's low- $\nu$  flux brings data/MC ratio closer to 1 and introduces an additional energy dependence in the simulation. It is worth testing whether this additional energy dependence resolves the discrepancy present in Fig. 5.4.

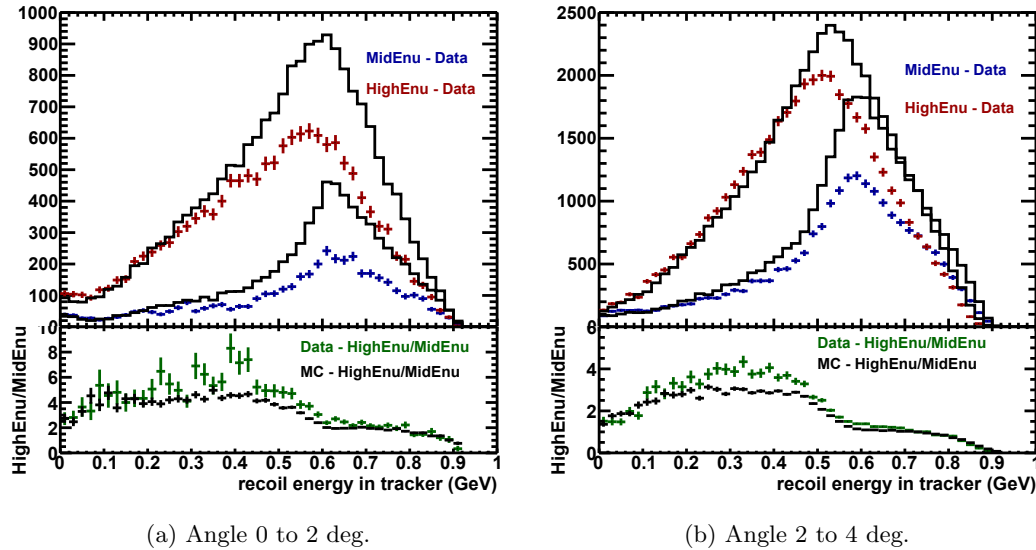


Figure 5.5: Rob Fine’s low- $\nu$  flux to analyze the energy dependence discrepancy present corresponding to MidEnu and HighEnu in High  $q_3$  range for muon angle cuts 0 to 2 deg. and 2 to 4 deg.

Low- $\nu$  flux has no observable effect on the discrepancy present in the figure for muon angle 0 to 2 degrees. There is a tiny effect on the discrepancy present corresponding to the muon angle 2 to 4 degrees but it is not enough to be the main reason behind the energy dependence discrepancy.

There is another possible reason behind the energy dependence discrepancy which will be explored in the next sections. It is due to the energy dependence coming from the cross-section itself. A clarification is required here. Cross-section itself might have well-modeled energy dependence. However, it is possible that cross-section is not well-modeled for all neutrino energies but it shows up as an energy dependence discrepancy due to an interplay with other energy dependent features of the data such as the muon angle cuts.

## Chapter 6

# Outer Detector (OD) Analysis

As shown in the previous section, using Rob Fine's low- $\nu$  flux instead of default  $\nu - e$  scattering flux does not resolve the discrepancies. Neither does a major change in the axial form factor or the strength of the RPA effect. There must be some other reason behind the energy dependence discrepancy. This chapter explores whether the highly energetic particles entering the outer detector could be a reason behind the discrepancy. To determine whether it is charged hadrons or neutral particles, events in the discrepancy region are scanned by eye using an event display. By the end of the chapter, a strong evidence is collected that highly energetic  $\pi^+$  are behind the discrepancy. The outer detector is marked as Side HCAL in Fig. 1.10. Particles are generally highly energetic if they deposit an energy in outer detector because they have to pass through several interaction lengths of steel walls.

This study is of a different style than the others in this thesis. Confronted by a mystery, we first looked for inspiration, in this case a study by Emily Haase [87]. Based on that, we put a subset of events into a list and viewed them (eye-scanned) using a visual event display. That allows us to perceive and measure patterns by eye that we had never yet written an algorithm to study. Then we can followup that insight qualitatively using ordinary analysis tools.

The previous chapter discusses about the discrepancy when muon angle cut of 0 to 2 degrees or 2 to 4 degrees is applied. For this section, it is better to analyse the

discrepancy with an angle cut of 0 to 5 degrees. The reason is that the discrepancies for the angle 0 to 2 degrees and 2 to 4 degrees are present in the plot with 0 to 5 degrees angle cut also. This can be shown by the plot of MidEnu and HighEnu with an angle cut of 0 to 5 degrees as follows

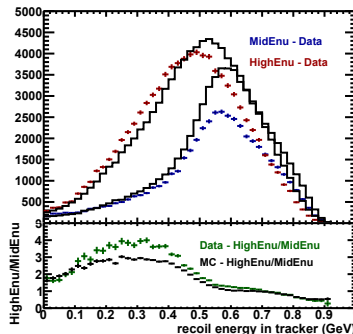


Figure 6.1: Energy dependence discrepancy corresponding to HighEnu and MidEnu in High  $q_3$  range with muon angle cut of 0 to 5 degrees

## 6.1 Effect of OD Cuts on Energy Dependence Discrepancy

The talk given by Duluth undergraduate Emily Haase [87] inspired an idea to try cutting on the amount of energy present in MINERvA's outer detector (OD). Her work explored the events with little or no hadronic energy, an unrelated study looking for evidence of short-range correlated nucleon pairs. This corresponds to low energy in tracker, which is less than 0.2 GeV and is at and just below the region of interest in Fig. 6.1. One of her cut was to remove events in OD having more than 200 MeV of energy. In her sample, this cut affected data and Monte Carlo differently, thus indicating a shortcoming in Monte Carlo. The discrepancy in this work extends from her sample region to about energy in tracker of 0.4 GeV. It is possible that hers and this work are being affected by the same shortcoming in the model. Fig. 6.2 shows the plots with events cut if their outer detector energy is greater than the energy mentioned.

A cut of 2 MeV requires a practically quiet outer detector and about half the events are removed. Raising the cut adds events back to the sample such that with the cut set to 400 MeV, almost no events are cut. As with the Haase's analysis, the cut affects the

simulated events differently than the data.

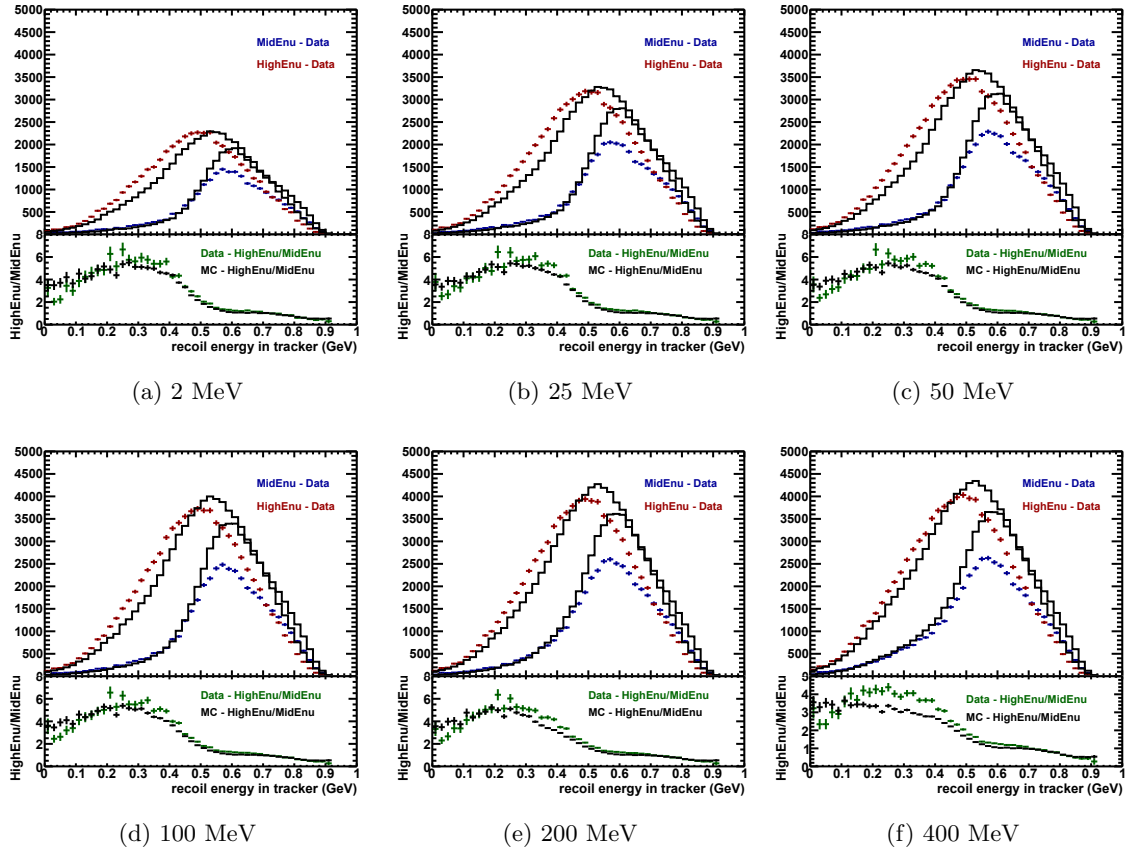


Figure 6.2: Plots of HighEnu and MidEnu in High  $q_3$  range with muon angle cut 0 to 5 degrees and OD events cut above the OD energy mentioned

Fig. 6.2 shows that the discrepancy resolves by a large amount if the events having OD energy greater than 100 MeV are cut. For the energy limit of 200 MeV, the discrepancy starts appearing in the right tail of the plot and at 400 MeV, it is back. Yet stronger cuts from 2 MeV to 100 MeV seem to remain steady with little discrepancy, despite removing almost half of the events. It appears that only higher energy OD events lead to a discrepancy.

That high OD energy events lead to the discrepancy makes sense since high OD

energy implies that particles produced in the interaction deposit a big amount of their energy in OD and a small amount of energy in tracker. This is the reason a high OD energy population can live in low energy in tracker region. In fact, it lines up closely with the energy in tracker region where discrepancy is present.

To see which events are cut by the OD energy limit, it is better to compare two plots that separate the sample into events with OD energy above and below 100 MeV.

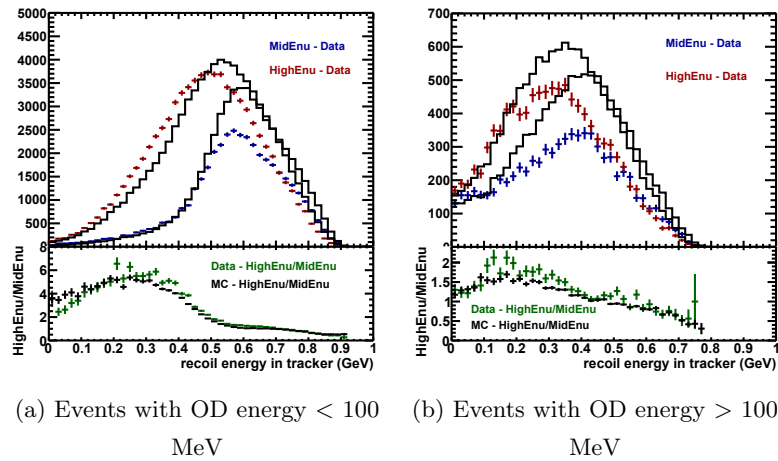


Figure 6.3: Plots of HighEnu and MidEnu in High  $q_3$  range with muon angle cut 0 to 5 degrees and OD events cut above and below 100 MeV respectively

It was expected that there would be a big discrepancy in Fig. 6.3 when events are kept above 100 MeV and that would explain the discrepancy in the original plot with no OD cut. However, numbers play out such that discrepancy is visually small in both the plots of Fig. 6.3 and yet there is a big discrepancy in the original plot.

## 6.2 Scanning of Highly Energetic $\pi^+$ entering the Outer Detector

In this situation we know a population of events are important but not the reason why. A tool to take the next step is the MINERvA visual event display called Arachne [88].

After a study that itemized the calorimetric energy in the tracker and in the OD, it was realized there are simply three kinds of energy deposits possible in the OD:

- Overlay (energy deposits that do not belong to the interaction)
- Neutral particles (neutrons and photons)
- Charged Hadrons (pions and protons)

Overlay is MINERvA jargon for all the activity in the detector unrelated to the neutrino interaction being measured. It comes from the pileup of multiple neutrino interactions as well as remnant muons in each pulse from the high intensity NuMI neutrino beam. The unrelated activity usually does not coincide in time at the nanosecond level with the interaction, but every so often it randomly happens at the same time. The term overlay comes from MINERvA's technique for "simulating" these pileup effects by overlaying actual data activity on top of the simulated neutrino interaction. As such, overlay is accurately "simulated" by construction because it is taken directly from data.

These three categories of events are identified by their energy deposit and location with respect to the interaction vertex. Charged hadrons are fairly easy to identify since their path is connected to the interaction vertex through a continuous energy deposit. Neutral particles are identified when there is no connected path to the interaction vertex. Since overlay activity is random, it can be anywhere in the outer detector, both near and far from the interaction being measured. Energy in the OD far from the interaction is much more likely to be from overlay though. It is much easier to identify an overlay if there is a lot of energy deposit in a region of OD since particles coming out of the tracker do not deposit energy in a large amount.

Most of the time, it is not easy to distinguish between neutrons and photons, and we do not make an attempt to do so. In principle, they have a slightly different behaviour of depositing energy. While a neutron generally deposits energy in one or two scintillators unless it ejects a proton from a nucleus, a photon with a few hundred MeV of energy generally deposits energy in quite a few scintillators. Sometimes, two photons can be identified in the tracker or one in tracker and the other one in OD which is a sign that

a neutral pion  $\pi^0$  was produced during the interaction and it decayed to two photons.

Pions and protons have a similar visual track in the event display. The range of  $q_3$  changes the relative populations in a suggestive way. In Low  $q_3$  sample, QE is dominant and thus, protons are predominantly produced in this range. In Mid  $q_3$ , both pions and protons have similar energy. In High  $q_3$ , which is the OD scanning sample also, pions are predominant and according to the simulation, pions are the ones going into the OD. The reason behind this is that delta resonance process is dominant in High  $q_3$  and it is the largest source of pions.

For a reference, the three different kinds of OD events look as follows in Arachne:

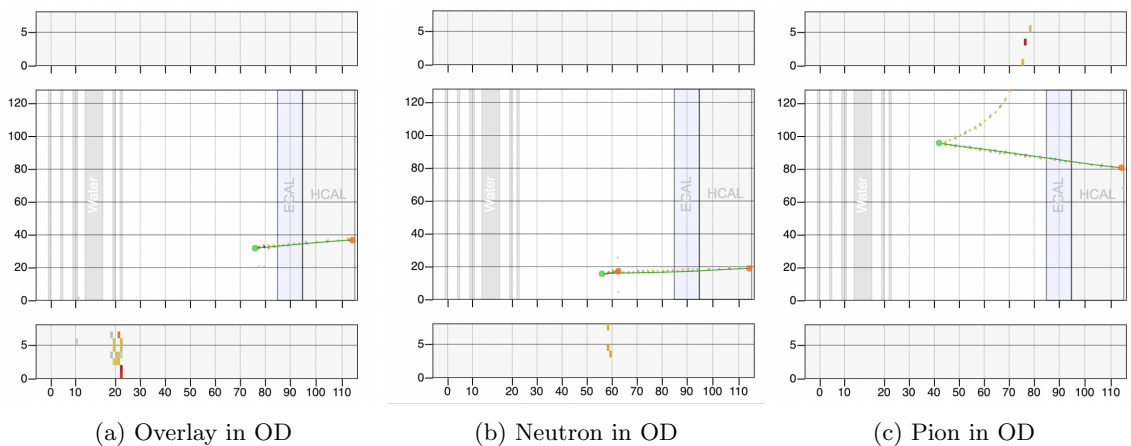


Figure 6.4: An example of overlay, neutron and pion in Outer Detector as viewed in Arachne

### 6.2.1 Scanning results showing that Highly Energetic $\pi^+$ might be overestimated in MC and/or Highly Energetic Neutral Particles might be underestimated in MC

It is much easier to identify charged hadrons in OD as compared to overlay and neutron due to their clear tracks. As a result, 350 events were scanned for the presence of a charged hadron (pion or proton). The subsamples scanned were MidEdu MC, MidEdu

data, HighEnu MC and HighEnu data, for the MidEnu and HighEnu plot in High  $q_3$  range with muon angle cut of 0 to 5 degrees and outer detector energy greater than 100 MeV. The additional constraint on the scanning region was  $0.2 \text{ GeV} < \text{energy in tracker} < 0.3 \text{ GeV}$ , since cuts in outer detector almost resolve the discrepancy in this region as shown in Fig. 6.2. Statistical uncertainty in scanning was determined using the variance formula of binomial distribution [89]. The scanning result is as follows:

Table 6.1: Scanning result of 350 events each for events with outer detector energy greater than 100 MeV for the presence of a charged hadron in OD

$E_\nu$ Range	Data	MC	Diff. b/w Data and MC
Mid	$(20.29 \pm 2.15)\%$	$(38.86 \pm 2.60)\%$	$(18.57 \pm 3.38)\%$
High	$(24.00 \pm 2.28)\%$	$(36.86 \pm 2.58)\%$	$(12.86 \pm 3.44)\%$

Table 6.1 gives a hint that charged hadrons might be oversimulated in MC. Also, as explained earlier, charged hadrons are predominantly pions due to the delta process dominance in High  $q_3$ . However, to ascertain that pions are oversimulated, it is important to estimate the percentage of overlay and neutral particles also, and then, determine the absolute number of events with charged hadrons, neutral particles or overlay in OD.

Overlay is well-modeled in MC as it is taken from data directly. Also, since overlay is not a part of the neutrino-nucleus interaction, its percentage is independent of the neutrino energy. Thus, keeping the scanning region same, 350 MidEnu MC events were scanned and  $(25.43 \pm 2.33)\%$  of those events had pure overlay energy deposit in OD. There were also events with a neutral particle or a charged hadron in addition to overlay but they were few in number. Using the percentage of pure overlay, another table can be constructed showing the percentage of neutral particles in OD events. Subtracting the percentage of overlay and charged hadrons from 100% gives the following table.

Table 6.2: Percentage of events with outer detector energy greater than 100 MeV and having a neutral particle in OD by subtraction

$E_\nu$ Range	Data	MC	Diff. b/w Data and MC
Mid	$(54.29 \pm 3.17)\%$	$(35.71 \pm 3.49)\%$	$(18.57 \pm 4.72)\%$
High	$(50.57 \pm 3.26)\%$	$(37.71 \pm 3.47)\%$	$(12.86 \pm 4.76)\%$

Table 6.2 gives a hint that neutral particles might be undersimulated in MC. However, as mentioned earlier, to determine the exact situation, it is important to look at absolute numbers since total number of events (POT-normalized) are different in data and MC.

### 6.2.2 Confirming that highly energetic $\pi^+$ are oversimulated and highly energetic neutral particles are well-modeled

To get the absolute number, these samples need to be normalized to equivalent beam exposure. This is done by multiplying the MC histograms by the ratio Data POT/MC POT.

Table 6.3: Total number of events (POT-normalized) in the scanning region

Type of events	No. of events
MidEnu data	1267
MidEnu MC	1768
HighEnu data	2181
HighEnu MC	2606

Table 6.3 can be used along with tables 6.1 and 6.2 to determine the actual number of charged hadrons and neutral particles going into OD.

Table 6.4: Number of events with charged hadrons or neutral particles in OD having outer detector energy greater than 100 MeV in the scanning region

Types of particles	$E_\nu$ Range	Data	MC
Charged hadrons	Mid	$257 \pm 27$	$687 \pm 46$
	High	$523 \pm 50$	$961 \pm 67$
Neutral particles	Mid	$688 \pm 40$	$631 \pm 62$
	High	$1103 \pm 71$	$983 \pm 90$

Table 6.5: Comparison of number of events between Data and MC

Types of particles	$E_\nu$ Range	Diff. b/w Data and MC	Diff. in terms of $\sigma$
Charged hadrons	Mid	$430 \pm 53$	8.0
	High	$437 \pm 83$	5.2
Neutral particles	Mid	$56 \pm 74$	0.8
	High	$120 \pm 115$	1.0

Table 6.4 and 6.5 clearly show that charged hadrons are oversimulated in MC and neutral particles are simulated well.

To finish this investigation, Fig. 6.5 shows the breakdown of the sample by the model's interaction modes. The goal is to identify if a single aspect of the model is at fault and to suggest comparisons to other MINERvA analyses that may have observed something similar to Haase and myself. This excess of charged hadrons is primarily due to pions produced on the left side of delta peak as shown in Fig. 6.5. The figure does not have a separate line for the higher resonances but they are included in the figures shown in the next chapter. Those figures clearly show that higher resonances are the second most dominant interactions in the High  $q_3$  range and are also a big producer of pions. SIS and coherent pion production (not shown here but is included in the next chapter) also produce pions but not as much as resonances. 2p2h and QE scattering do not produce pions at all. Although it is possible that a nucleon ejected from a nucleus through QE or 2p2h process undergoes FSI and produces a pion but pions produced that way are significantly less in number compared to pions produced through other

interactions.

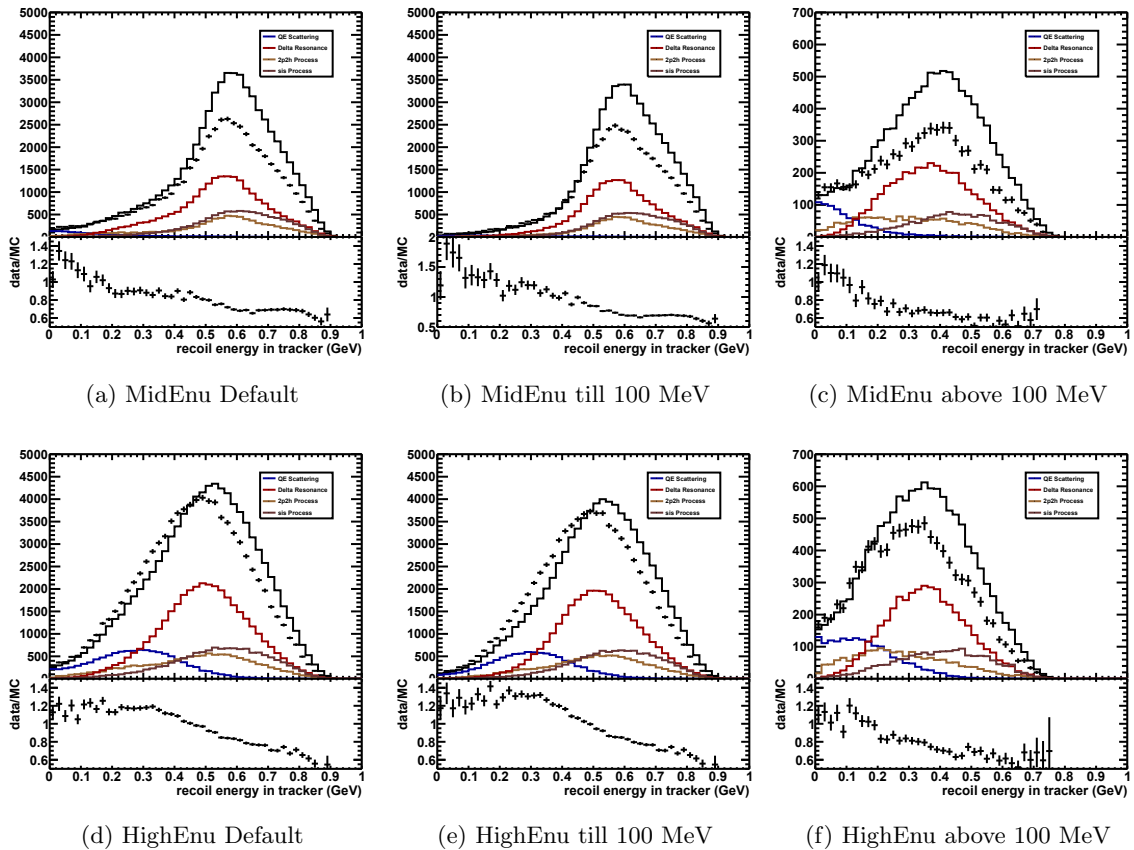


Figure 6.5: Plots of MidEnu and HighEnu in High  $q_3$  range with muon angle cut 0 to 5 degrees depicting the contribution of individual processes (QE, Delta Resonance, 2p2h, SIS) when cuts are applied for outer detector energies

Fig. 6.5 shows a significant increase in the population of QE for higher neutrino energy while delta population increases by a smaller amount. This can be understood using the behaviour of muon angle with change in energy transfer and neutrino energy, as discussed in Chapter 4. QE population has low energy transfer which means a higher muon angle while delta population has a higher energy transfer which means a lower muon angle. Thus, for the angle cut of 0 to 5 degrees, delta population has higher chances of making the cut for the same neutrino energy. When neutrino energy range

is increased from MidEnu to HighEnu, muon angle reduces and more QE events make the cut. Delta population does not change by a lot since many of its events already survived the cut and increasing neutrino energy did not do much.

However, QE and 2p2h do not produce pions and so, it must be delta resonance and partly higher resonances, SIS and coherent pion production that are mismodeled.

Even though neutral particles are simulated well, we can evaluate whether they have the potential to produce a discrepancy. This can be done by changing the weight of events in MC if there is a presence of a neutron beyond a certain energy. The secondary test, as shown in Fig. 6.6, verifies the claim that the discrepancy might not be due to neutral particles since they are well-modeled.

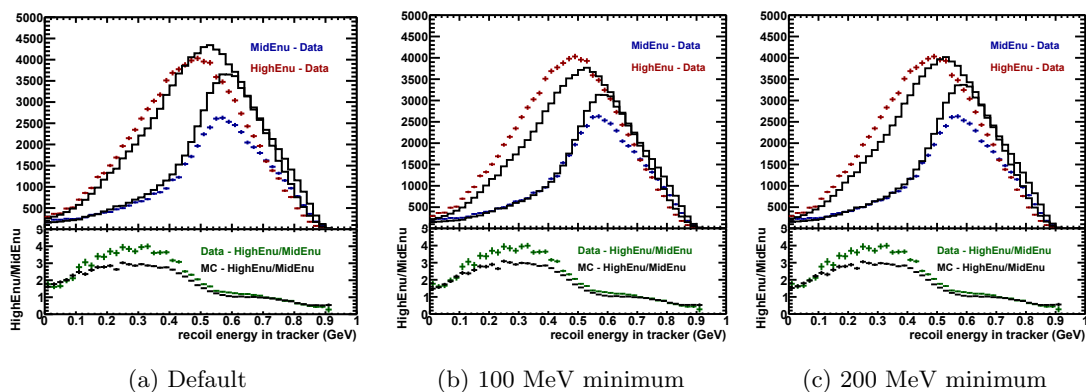


Figure 6.6: Plots of HighEnu and MidEnu in High  $q_3$  range with muon angle cut 0 to 5 degrees and no OD cut with events reweighted by 0.5 remain unchanged if maximum neutron kinetic energy is greater than a certain minimum energy

## Chapter 7

# Pion Kinetic Energy based Reweighting

The previous chapter showed that highly energetic  $\pi^+$  can be a source of the discrepancy. This chapter explores whether low energy  $\pi^+$  also have any contribution to the discrepancy. Also, if pions are, in fact, the reason behind the discrepancy, we can try to narrow down to the specific pion production mode responsible for this shortcoming in MC. Pion production is governed by cross-section calculations and form factors and its energy and momentum distribution while exiting the nucleus is dependent on FSI also. Therefore, this chapter explores both pion production models and different FSI a pion goes through to figure out which of the two is the actual cause behind the discrepancy.

### 7.1 Reweighting events in MC based on the kinetic energy of pions

Like the previous chapter used a selection on a reconstructed quantity (energy in the OD), the next steps benefit from a selection on a Monte Carlo truth quantity. A selection can be applied to the MC based on the presence of a  $\pi^+$  with kinetic energy (KE) more than 150 MeV. If the pion's angle with respect to the beam is high, this is enough energy to reach the outer detector. The value 150 MeV is not chosen at random. It is inspired by Aaron Bercellie's MINERvA result [90] just accepted for publication in

Physics Review Letters. The paper has a plot which shows the interaction cross-section  $d\sigma/dT_\pi$ , where  $T_\pi$  is the kinetic energy of  $\pi^+$ , for three different nuclear targets and compares it with the predictions made by GENIE, NEUT and GiBUU. None of the predictions describe the data very well. GENIEv2 MnvTune v4.2.1 tune (blue line) and the GENIEv2.12.6 untuned (orange line) are the closest to the configuration of MINERvA tunes that I am using. The following figure is taken from the paper.

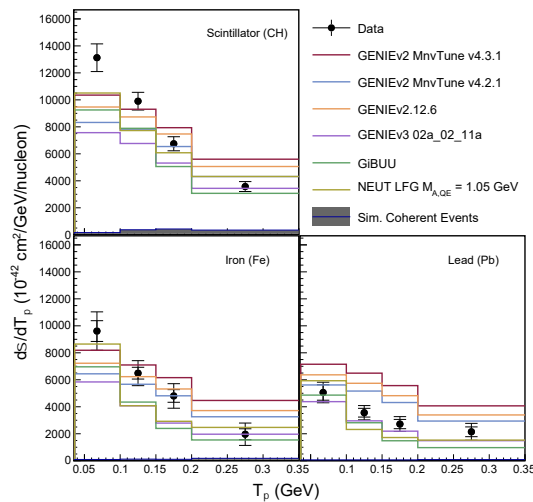


Figure 7.1: Differential cross-section with respect to pion KE is represented by solid point. Its comparison with different versions of GENIE, NEUT and GiBUU shows that none of them define the data perfectly.

Bercellie's plot shows that  $\pi^+$  with  $KE < 100$  MeV are underestimated by all the models and  $\pi^+$  with  $KE > 150$  MeV are overestimated. OD analysis in the previous chapter has showed that High KE  $\pi^+$  could be a source of the discrepancy. OD analysis does not comment on Low KE  $\pi^+$  since those pions do not enter the OD. We can start with increasing the weight of High KE  $\pi^+$  and observing their effect on the discrepancy. In the latter sections, we will reweight Low KE  $\pi^+$  also to confirm whether they are behind the discrepancy or not. In Bercellie's plot, pions are overestimated by about 20% in the KE bin of 150 - 200 MeV. For higher KE, this overestimation goes up to 50%. For this reason, we are applying both 20% and 50% on  $\pi^+$  with KE above 150 MeV. A more careful analysis would apply weights exactly in line with Bercellie's plot,

or even search for a best fit weight, but we do not require that level of detail.

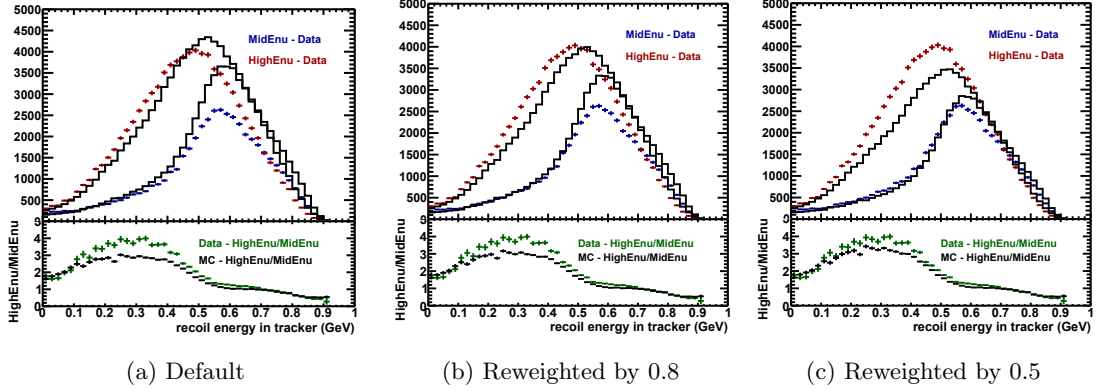


Figure 7.2: Plots of MidEnu and HighEnu in High  $q_3$  range with muon angle cut of 0 to 5 degrees (no OD cut) are reweighted if the kinetic energy of the most energetic pion in the final state is greater than 150 MeV.

As can be seen in Fig. 7.2, reducing the weight of events in Monte Carlo by 20% resolves the discrepancy by a small amount while reducing the weight of events in Monte Carlo by 50% results in a clear and observable reduction in energy dependence discrepancy. This test supports the claim of the previous section in which an excess of  $\pi^+$  in OD was observed and it was proposed as the most probable cause behind the discrepancy.

## 7.2 Final State Interactions of a $\pi^+$

A pion is produced in a neutrino-nucleus interaction through resonance, deep inelastic scattering, and coherent pion production. Quasi-elastic scattering does not produce a pion, however, it can be produced when the proton produced in a neutrino-nucleus interaction undergoes final-state interactions. Similarly, a pion produced through other processes undergoes final state interactions. This thesis covers the final-state interactions of a pion as described below. Ref. [91] has a good explanation of these interactions.

- No FSI - When a pion does not interact with a nucleus at all.

- Charge exchange - When a pion remains a pion after exiting the nucleus but with a different charge.  $\pi^+$  becomes a  $\pi^0$  through charge exchange with a nucleon while a  $\pi^0$  becomes a  $\pi^+$  or a  $\pi^-$  through charge exchange with a nucleon.
- Elastic scattering - The final state nucleus remains in the ground state. Pion's angle with respect to the incoming direction changes by a small amount. Its kinetic energy can change in this scattering. This is modeled as “black disk” diffraction around the whole nucleus as is observed in pion beam data.
- Single nucleon knockout - A nucleon is also ejected from the nucleus along with the pion. This is billiard ball scattering, and the pion gives up some of its energy to the nucleon and its direction is changed.
- Pion absorption - A pion is absorbed on two or more nucleons inside the nucleus and no pion comes out.
- Additional pion production - A pion can lead to the production of more pions through the interaction with nucleus.

The aforementioned final state interactions happen to a pion that is produced inside a nucleus. However, in coherent pion production, a neutrino interacts with a whole nucleus and produces a  $\pi^+$  effectively out of the nucleus which does not undergo final state interactions. This process should be contrasted with the “no FSI” case listed above as in that case, a pion is produced inside the nucleus but it exits it without any interaction.

One other label present in the plots in this section would be “Others”. It corresponds to events in which there was no  $\pi^+$  produced directly in the neutrino-nucleus interaction but there is a  $\pi^+$  in the final state. These pions are produced by nucleons undergoing FSI, and separately by the decay of strange baryons and eta mesons. One more label in the plots will be “No  $\pi^+$ ”, which corresponds to events having no  $\pi^+$  before or after FSI, typical of QE events.

Fig. 6.3 in the previous section showed the plots for OD energy less than or equal to 100 MeV and greater than 100 MeV. Medium energy (MidEnu) and high energy (HighEnu) Monte Carlo plots can be broken into  $\pi^+$  fates. The goal is to determine

the relative contribution of each pion mode. It can be seen in the Fig. 7.3 that No FSI, Elastic Scattering, Pion Absorption and Others are the dominant pion modes. However, there is a subtlety here. Although pion absorption is present in the plot with OD energy above 100 MeV, it does not enter the OD. That pion is absorbed in nucleons and does not exit the nucleus. There must be some other particle, a proton or a neutral particle, that happened to deposit high energy in OD at the same time a pion was produced and absorbed in the nucleus. “Charge exchange” in Fig. 7.3 refers to the interaction when a  $\pi^+$  exchanges a charge with a nucleon and  $\pi^0$  exits the nucleus.

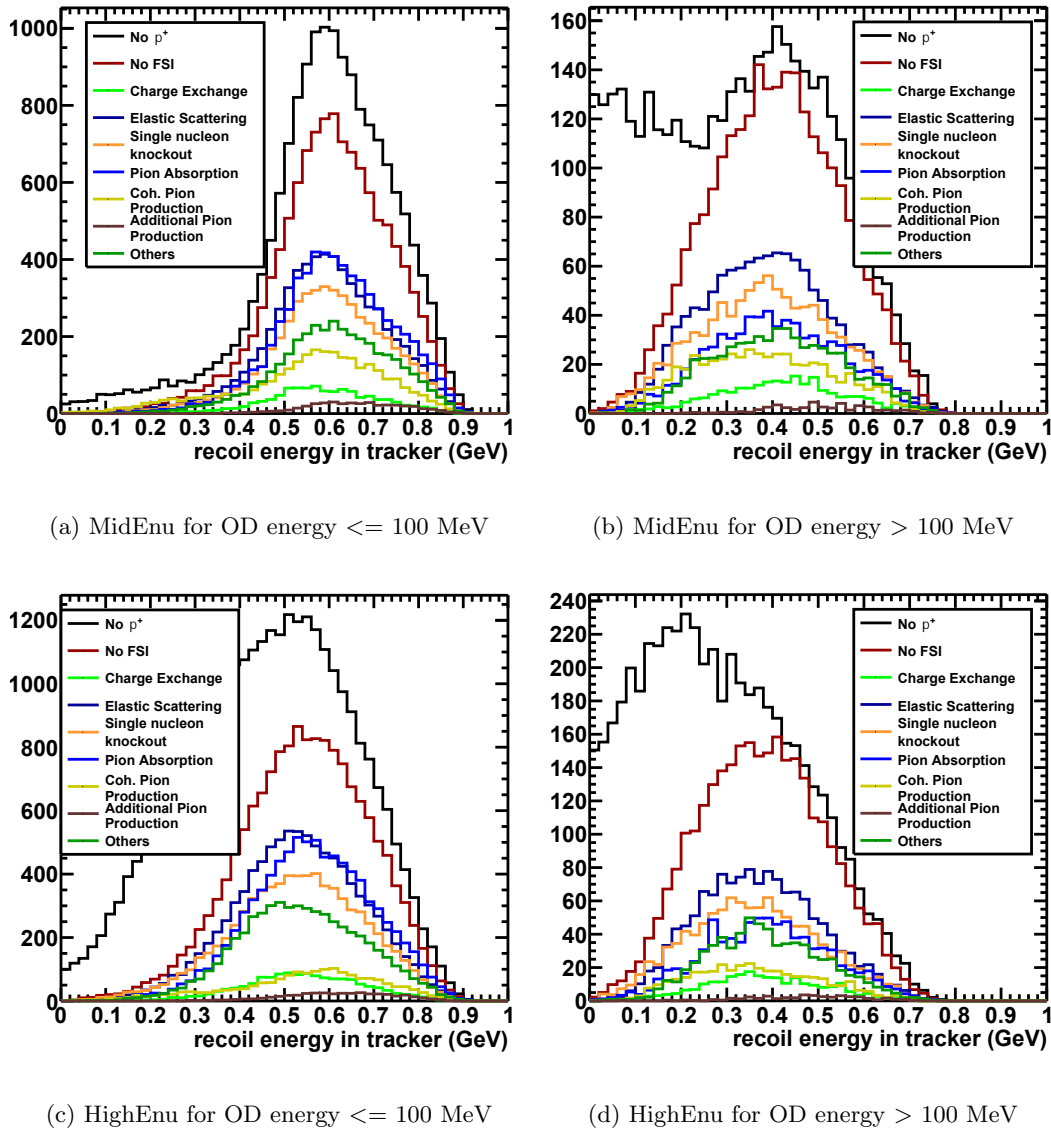


Figure 7.3: Plots of MidEnu and HighEnu in High  $q_3$  range with muon angle cut 0 to 5 degrees and OD cuts broken down into  $\pi^+$  fates

The next figure contains the events due to charge exchange in  $\pi^0$ , which produces a  $\pi^+$ , and does not include “No  $\pi^+$ ” events. The main point of this figure is to show what happens to a  $\pi^+$  in the detector. That is why charge exchange on  $\pi^+$  is replaced with charged exchange on  $\pi^0$  because the former produces a  $\pi^+$  but that  $\pi^+$  does not

enter the detector with its original charge.

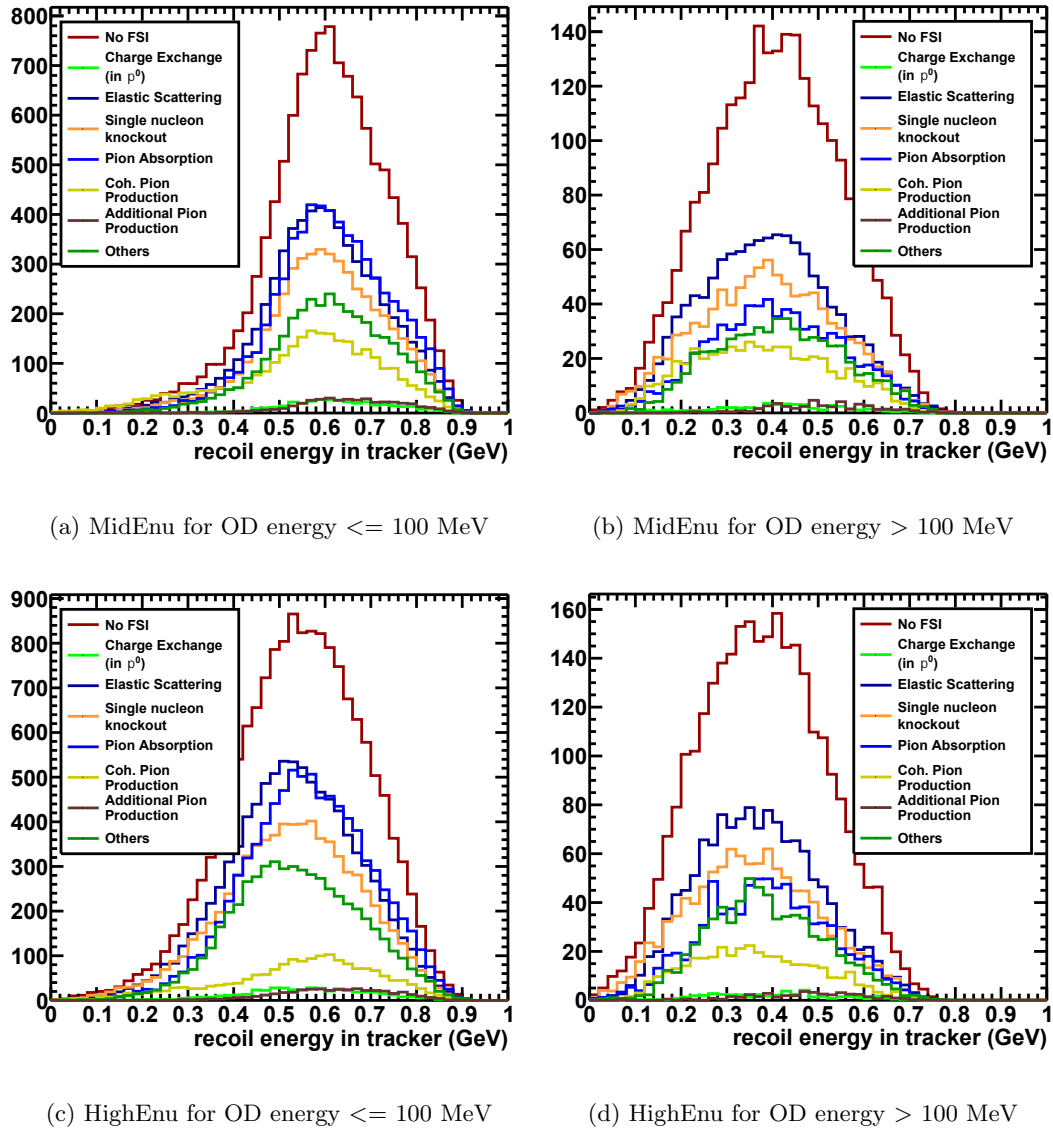


Figure 7.4: Plots of ME and HE High  $q_3$  with muon angle cut 0 to 5 degrees and OD cuts broken down into  $\pi^+$  fates such that a  $\pi^+$  is in the final state.

Charge exchange and additional pion production have significantly less contribution in the production of  $\pi^+$  in the final state as can be seen in Fig. 7.4. Additionally, pion

absorption does not lead to a  $\pi^+$  in the final state since a  $\pi^+$  that is produced through a neutrino-nucleus interaction is absorbed within the nucleus and never gets out.

### **7.3 Determining that FSI of $\pi^+$ is not a major source of the discrepancy**

The work so far presents two possible reasons behind the discrepancy based on the excess of  $\pi^+$  in Monte Carlo. One of them is that the number of  $\pi^+$  produced in the pion production model (pre-FSI) are in excess. The second reason could be that the pion production model is producing the correct number of  $\pi^+$  and it is FSI that increases their number more than it should. As remarked earlier, one or more of the five processes: no FSI, elastic scattering, single nucleon knockout, coherent pion production and Others, could be responsible for this excess. However, none of these processes except for Others change the number of  $\pi^+$  produced in the neutrino-nucleus interaction. They just change its energy and momentum distribution. Others has a small contribution compared to No FSI and elastic scattering, so there is less chance that it could be a dominant reason behind the discrepancy.

#### **7.3.1 Breakdown of $\pi^+$ FSI into individual modes for MidEnu and HighEnu separately**

To ascertain whether FSI have anything to do with the discrepancy or not, a cut of 150 MeV pion kinetic energy can be applied to the breakdown of  $\pi^+$  fates.

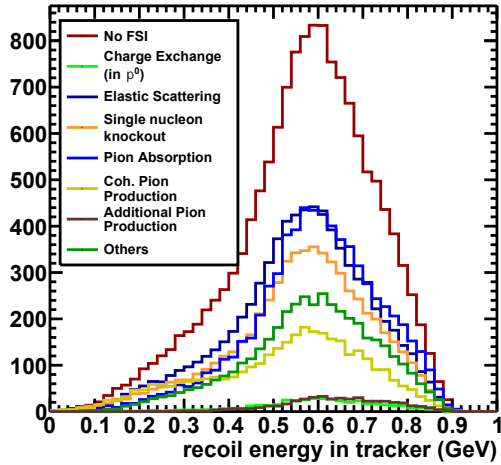
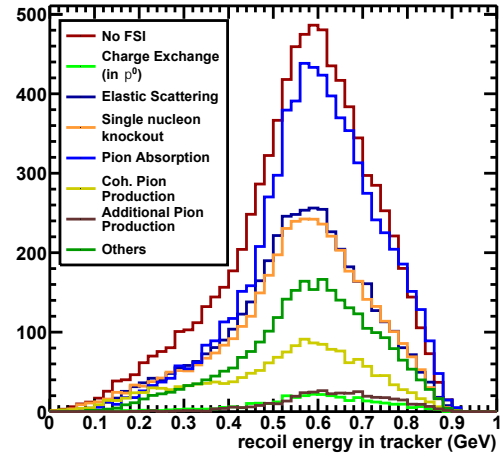
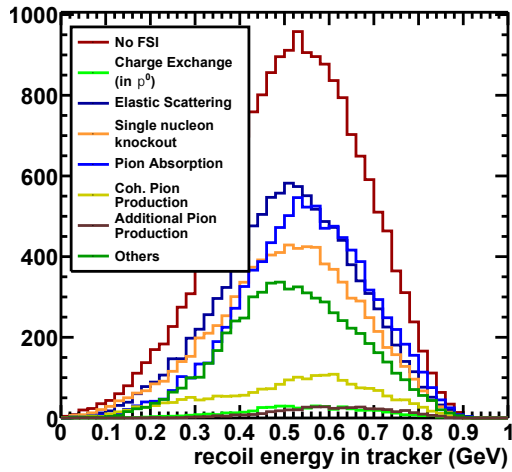
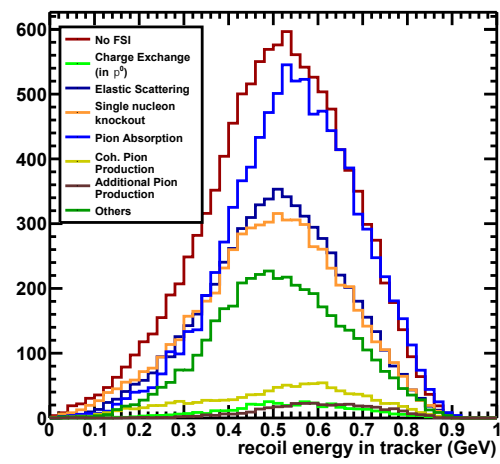
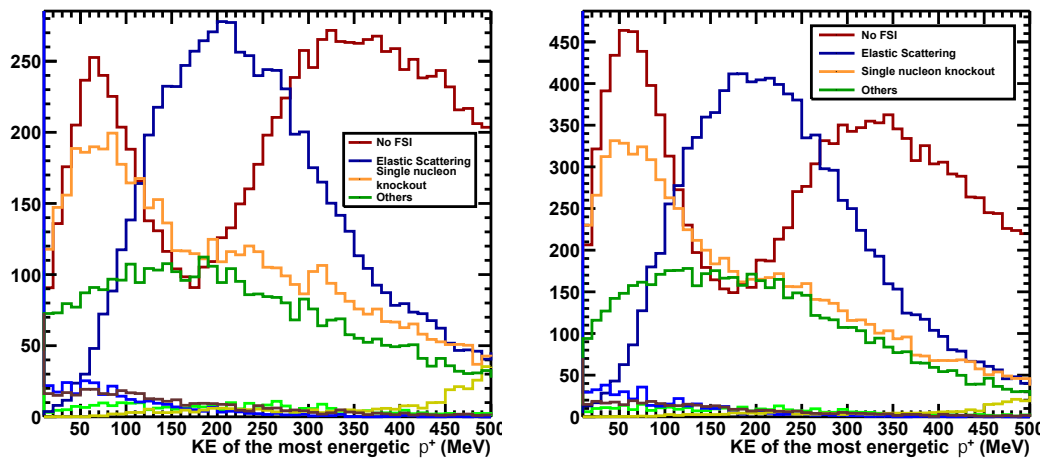
(a) MidEnu with no  $\pi^+$  reweight(b) MidEnu with  $\pi^+$  reweight(c) HighEnu with no  $\pi^+$  reweight(d) HighEnu with  $\pi^+$  reweight

Figure 7.5: Plots of MidEnu and HighEnu in High  $q_3$  range with muon angle cut 0 to 5 degrees and no OD cuts broken down into  $\pi^+$  fates such that the events with the most energetic  $\pi^+$  having kinetic energy greater than 150 MeV are reweighted by 50%

Fig. 7.5 shows that MidEnu has a bigger fraction of high energy  $\pi^+$  compared to HighEnu. Thus, when those events are reweighted, MidEnu events are reduced by a larger amount compared to HighEnu events and the ratio HighEnu(MC)/MidEnu(MC)

goes up in Fig. 7.2. Reading from the vertical scale of the figure, events drop by about 42% in MidEnu and 38% in HighEnu. All the FSI fates have reduced by some amount but coherent pion production has not undergone a big change.

To get a clearer picture, the events can be plotted with the kinetic energy of the most energetic  $\pi^+$  on the horizontal axis. This picture reveals the underlying structure of the FSI process centered pion kinetic energy of 170 MeV and total energy of around 310 MeV (because the mass of pion is 140 MeV), which is enough to excite delta resonance. Recall also that a selection on pion kinetic energy of 150 MeV is also being made in some plots, dividing the FSI subsamples at the delta resonance.



(a) MidEnu breakdown

(b) HighEnu breakdown

Figure 7.6: Plots of MidEnu and HighEnu in High  $q_3$  range with muon angle cut 0 to 5 degrees and no OD cuts broken down into  $\pi^+$  fates as a function of the kinetic energy of the most energetic  $\pi^+$

The legend in the Fig. 7.6 includes only the four dominant processes due to lack of space in the figure. The other processes have the same color-coding as in the others plots of this section. Pion absorption should not be present for higher  $\pi^+$  energy but it lingers at the bottom and at lower pion kinetic energies. These events do not belong to the pion absorption fate in reality. These are those events which have a  $\pi^+$  in the final

state produced due to FSI of nucleons or decay of heavier baryons or mesons. They made the cut because they were present in an event that also had pion absorption separately. Ideally, they belong to “Others” category. Since they are very small in number, they are not a big concern.

Another observation is that no FSI has two peaks in the figure on each side of delta resonance, and the first peak is lower compared to the second peak for MidEnu events and higher for the HighEnu events. If the second peak is taken as a reference, elastic scattering peak has come down a bit in MidEnu breakdown while the first peak has come down by a larger amount. This can be understood using the concept of angle acceptance. Lower kinetic energy of  $\pi^+$  means lower energy transfer, which means higher muon angle. Thus, moving left on the horizontal axis of Fig. 7.6 means moving in the direction of increasing muon angle. Since MidEnu events have a higher muon angle compared to HighEnu events, angle acceptance lowers down the peaks in MidEnu figure by a larger amount as we move left.

### 7.3.2 Reweighting events based on individual FSI fates

To see which  $\pi^+$  fate reduces the discrepancy by the largest amount, MC events can be reweighted for elastic scattering, no FSI, and single nucleon knockout separately. Elastic scattering and no FSI can also be reweighted together since they produce the most energetic  $\pi^+$ . Reweighting coherent pion production events separately is not required since these events are much smaller in number compared to events corresponding to other FSI modes.

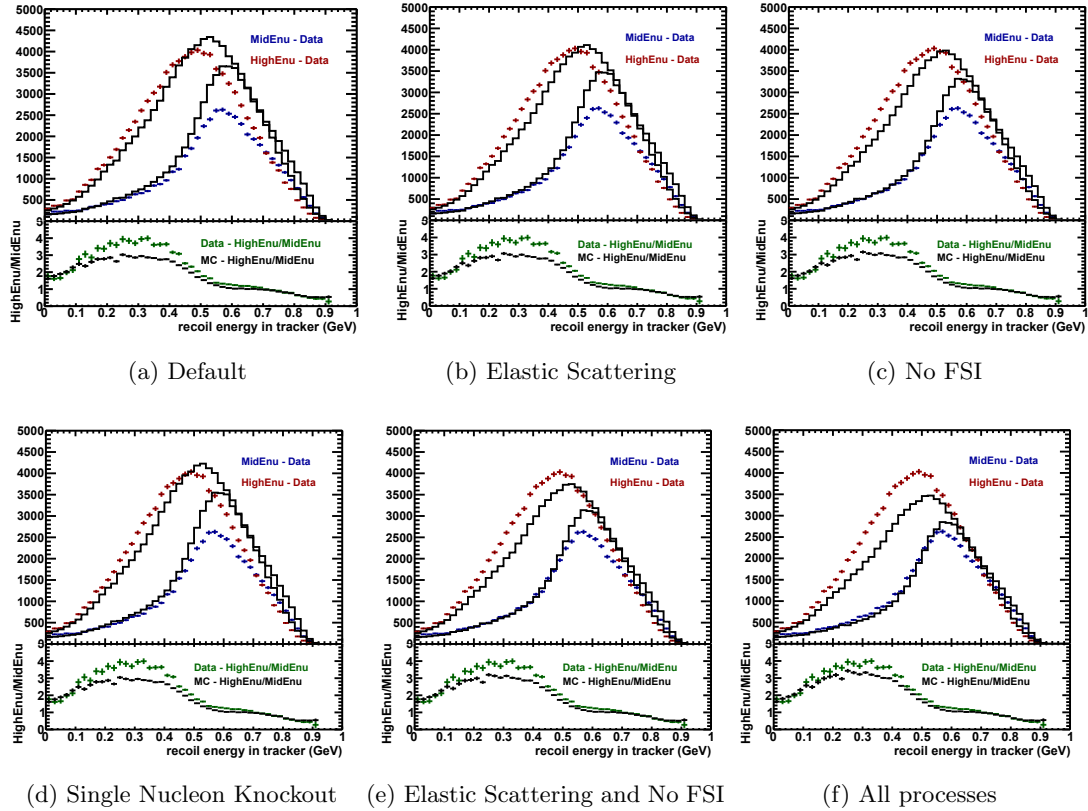


Figure 7.7: Plots of MidEnu and HighEnu in High  $q_3$  range with muon angle cut 0 to 5 degrees with different processes reweighted by 50% if the kinetic energy of the most energetic  $\pi^+$  is greater than 150 MeV

Fig. 7.7 shows that No FSI reweight brings about the maximum change. No FSI and elastic scattering reweight together bring about a big reduction in the discrepancy. This further consolidates the claim that FSI of  $\pi^+$  are not a reason behind the discrepancy but the large number of production of  $\pi^+$  is. The elastic scattering fate in the hA FSI model is a little strange. It produces a small change in the angle of  $\pi^+$  and is quite similar to the fate of No FSI. The implementation of the elastic fate in this GENIE version has additional problems that were identified and corrected by Lauren Harewood for her Duluth M.S. thesis [92]. Those additional problems are present in this sample also but do not appear to be a cause of the discrepancy.

## 7.4 Explanation of why the ratio HighEnu(MC)/MidEnu(MC) goes up when High KE $\pi^+$ events are reweighted

Reweight events reduces the discrepancy since the ratio HighEnu(MC)/MidEnu(MC) goes up in Fig. 7.2. Fig. 7.4 showed that MidEnu events have a larger fraction of High KE  $\pi^+$  in comparison to HighEnu events. This can be easily understood using the angle cuts.

Using Eq. 4.1,

$$p_\mu \cos\theta_\mu = E_\mu - \left( \frac{Q^2 + m_\mu^2}{2E_\nu} \right) \quad (7.1)$$

Under the approximation  $p_\mu \approx E_\mu$ ,

$$E_\mu (1 - \cos\theta_\mu) = \frac{Q^2 + m_\mu^2}{2E_\nu} \quad (7.2)$$

Using trigonometric identities and the relation  $E_\mu = E_\nu - q_0$  gives,

$$E_\nu^2 - q_0 E_\nu - \frac{Q^2 + m_\mu^2}{4} \operatorname{cosec}^2(\theta_\mu/2) = 0, \quad (7.3)$$

which can be solved to get

$$E_\nu = \frac{q_0 + \operatorname{cosec}(\theta_\mu/2) \sqrt{(q_0^2 + m_\mu^2) - q_0^2 \cos^2(\theta_\mu/2)}}{2} \quad (7.4)$$

For smaller angles, such as  $\theta_\mu < 10$  degrees,  $\operatorname{cosec}(\theta_\mu/2)$  is pretty big, because of which, square root term dominates compared to  $q_0$ . Thus, within all the approximations used above, it can be concluded that for the same three-momentum transfer and muon angle, higher neutrino energy corresponds to a smaller energy transfer.

The plots we have worked on so far have muon angle cut of 0 to 5 degrees, and  $0.8 < q_3$  (in GeV)  $< 1.2$ . For the demonstration,  $q_3$  can be chosen to be 1.0 GeV. MidEnu can be represented by 6 GeV and HighEnu can be represented by 10 GeV. In the table that is being constructed now using Eq. 4.11,  $\theta_\mu = 0$  degrees corresponds to a forward muon, which corresponds to the lower limit of  $Q^2$  as given by Eq. ???. The exact value of  $q_0$

can be calculated and it would be different for different neutrino energies. However,  $Q^2$  is approximately 0 for the forward muon and  $q_0$  can be taken to be approximately 1.0 GeV for both the neutrino energies although its exact value would be slightly smaller than this.

Table 7.1: Variation of energy transfer with a change in muon angle corresponding to High  $q_3$  for MidEnu and HighEnu represented by 6 GeV and 10 GeV respectively

Muon Angle	$E_\nu$	$q_0$
0 deg.	6 GeV	1.00 GeV
	10 GeV	1.00 GeV
1 deg.	6 GeV	0.99 GeV
	10 GeV	0.98 GeV
2 deg.	6 GeV	0.98 GeV
	10 GeV	0.94 GeV
3 deg.	6 GeV	0.96 GeV
	10 GeV	0.86 GeV
4 deg.	6 GeV	0.92 GeV
	10 GeV	0.74 GeV
5 deg.	6 GeV	0.87 GeV
	10 GeV	0.53 GeV

Table 7.1 shows that for the same muon angle, HighEnu has a lower energy transfer than that of MidEnu. This difference keeps on increasing as muon angle is increased. Lower energy transfer means lower  $\pi^+$  kinetic energy. This table and observation gives an explanation of why HighEnu events have a smaller fraction of High KE  $\pi^+$  in comparison with MidEnu events, and thus, why the ratio HighEnu(MC)/MidEnu(MC) goes up in Fig. 7.2 when the weight of High KE  $\pi^+$  is reduced.

## 7.5 Reweighting both Low and High KE $\pi^+$

Bercellie's work [90] shows that Low KE  $\pi^+$  (KE < 100 MeV) have a higher cross-section as compared to that predicted by GENIE. Thus, the next idea is to increase the weight

of these events in GENIE and see if the discrepancy reduces. Maybe less number of Low KE pions are also, at least partly, behind the discrepancy. If this is true, trying to reweigh both low energy  $\pi^+$  and high energy  $\pi^+$  together would be the next step, and might be equivalent to changing a form factor in the resonance structure functions or a suppression like Pauli blocking. Another advantage of reweighting both the  $\pi^+$  events is that it keeps the total number of  $\pi^+$  events nearly fixed and just redistributes the events while reweighting only one kind of  $\pi^+$  events with respect to their kinetic energy increases or decreases the events irrationally. The following figure shows that both of these ideas worked and reduced the discrepancy.

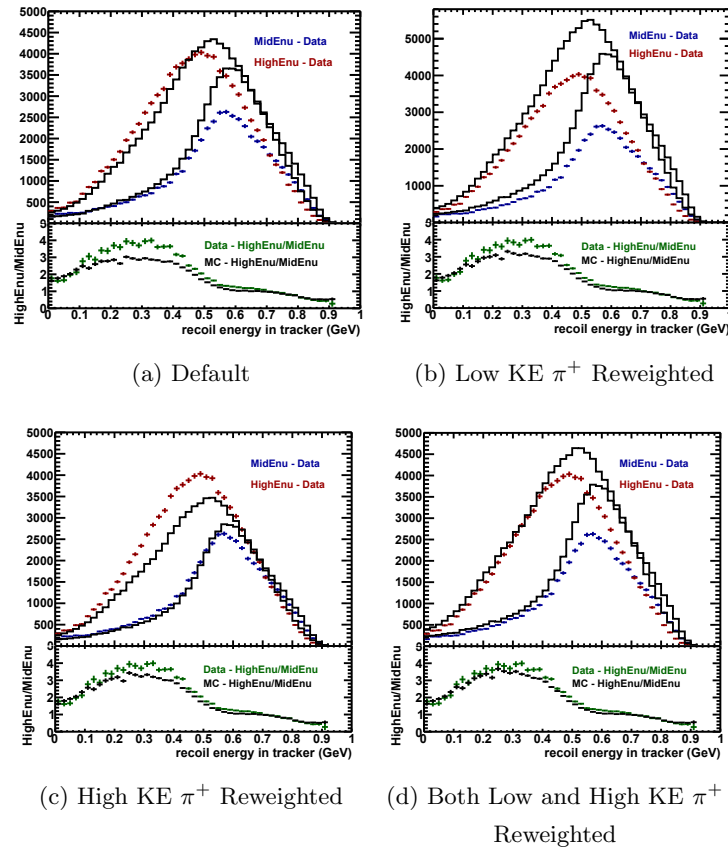


Figure 7.8: Plots of MidEnu and HighEnu in High  $q_3$  range with muon angle cut of 0 to 5 degrees with Low KE  $\pi^+$  (KE < 100 MeV) reweighted by 1.5 and/or High KE  $\pi^+$  (KE > 150 MeV) reweighted by 0.5

Fig. 7.8 shows that reweighting high energy  $\pi^+$  has a bigger effect on the discrepancy in comparison to reweighting the low energy pions for High  $q_3$ . This makes sense since high energy  $\pi^+$  are a larger fraction in this energy range and muon angle cut as can be seen in Fig. 7.6 and explained through Table 7.1. To see these different effects, it is better to take a double ratio. Double ratio is simply the ratio of “green” and “black” plot in the bottom pad of any figure we have used so far. It is like ratio of a ratio. It can be written as

$$\text{Double ratio} = \frac{HighEnuData/MidEnuData}{HighEnuMC/MidEnuMC} \quad (7.5)$$

Since our eyes cannot compare the data and MC ratios which are close enough, double ratio enables us to see additional detail. If energy dependence were perfectly modeled, the double ratio would be equal to 1 for all values of energy in tracker.

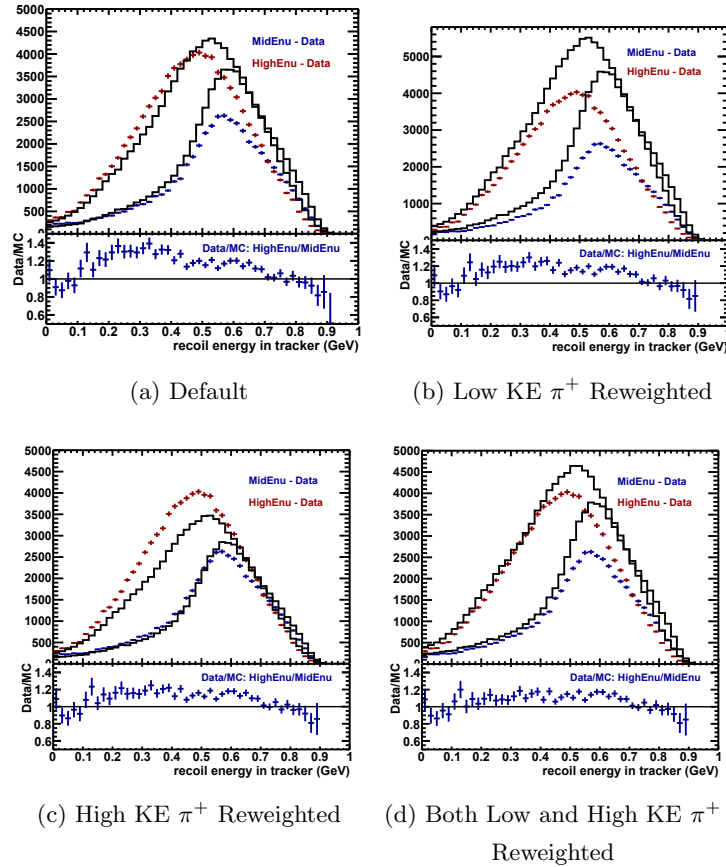


Figure 7.9: Double Ratio Plot for MidEnu and HighEnu in High  $q_3$  range with muon angle cut of 0 to 5 degrees with Low KE  $\pi^+$  (KE < 100 MeV) reweighted by 1.5 and/or High KE  $\pi^+$  (KE > 150 MeV) reweighted by 0.5

Fig. 7.9 shows double ratio plots corresponding to the plots in Fig. 7.8. The figure (a) shows that the default plot does not have a well-modeled energy dependence and there are big bumps present in the double ratio. Reweighting low energy  $\pi^+$  events reduces these bumps and makes the double ratio flatter as shown in (b). Since high energy  $\pi^+$  are a bigger fraction in this selection of energy ranges,  $q_3$  range and muon angle cut, reweighting them makes the double ratio even flatter as shown in (c). Finally, reweighting both low energy and high energy  $\pi^+$  does the best job and brings the double ratio really closer to 1 and makes it pretty flat, as can be seen in (d) better, but  $\chi^2$  test would still reveal that MC does not describe the data.

## 7.6 Application of $\pi^+$ KE reweight to smaller muon angle cuts

Until now, we have analyzed the energy dependence discrepancy present in plots with MidEnu and HighEnu neutrinos in High  $q_3$  range and muon angle cut of 0 to 5 degrees since it is a pretty big discrepancy and is a good discrepancy to run the tests. However, discrepancies are present in smaller muon angle cuts also. We explored whether finer binned angle analysis revealed anything interesting.

Reweighting  $\pi^+$  has the biggest effect on High  $q_3$  sample followed by Mid  $q_3$  and a tiny effect on Low  $q_3$  sample, since smaller momentum transfers is equivalent to smaller energy transfer or energy in tracker and thus, smaller energy of  $\pi^+$ . Thus, some discrepancies are presented here with their reduction after reweighting high energy  $\pi^+$  and reweighting both low energy and high energy  $\pi^+$  together for High  $q_3$  and Mid  $q_3$ . We are not showing the reweighting of Low  $q_3$  events here since QE dominates in the Low  $q_3$  range and it does not produce  $\pi^+$ . Most of the  $\pi^+$  in the Low  $q_3$  range will be coming from FSI of nucleons and they would be in small number.

### 7.6.1 Effect of $\pi^+$ reweight on energy dependence discrepancies present in High $q_3$ range and smaller angle cuts

Discrepancies corresponding to the muon angle cuts 0 to 2 deg., 2 to 4 deg. and 4 to 6 deg. for MidEnu and HighEnu for a High  $q_3$  sample are presented here since they are enough to convey the main point that reweighting  $\pi^+$  reduces the discrepancy. The discrepancy corresponding to the muon angle cut 6 to 8 deg. is also reduced with the pion reweight and those additional plots are included in Appendix E.

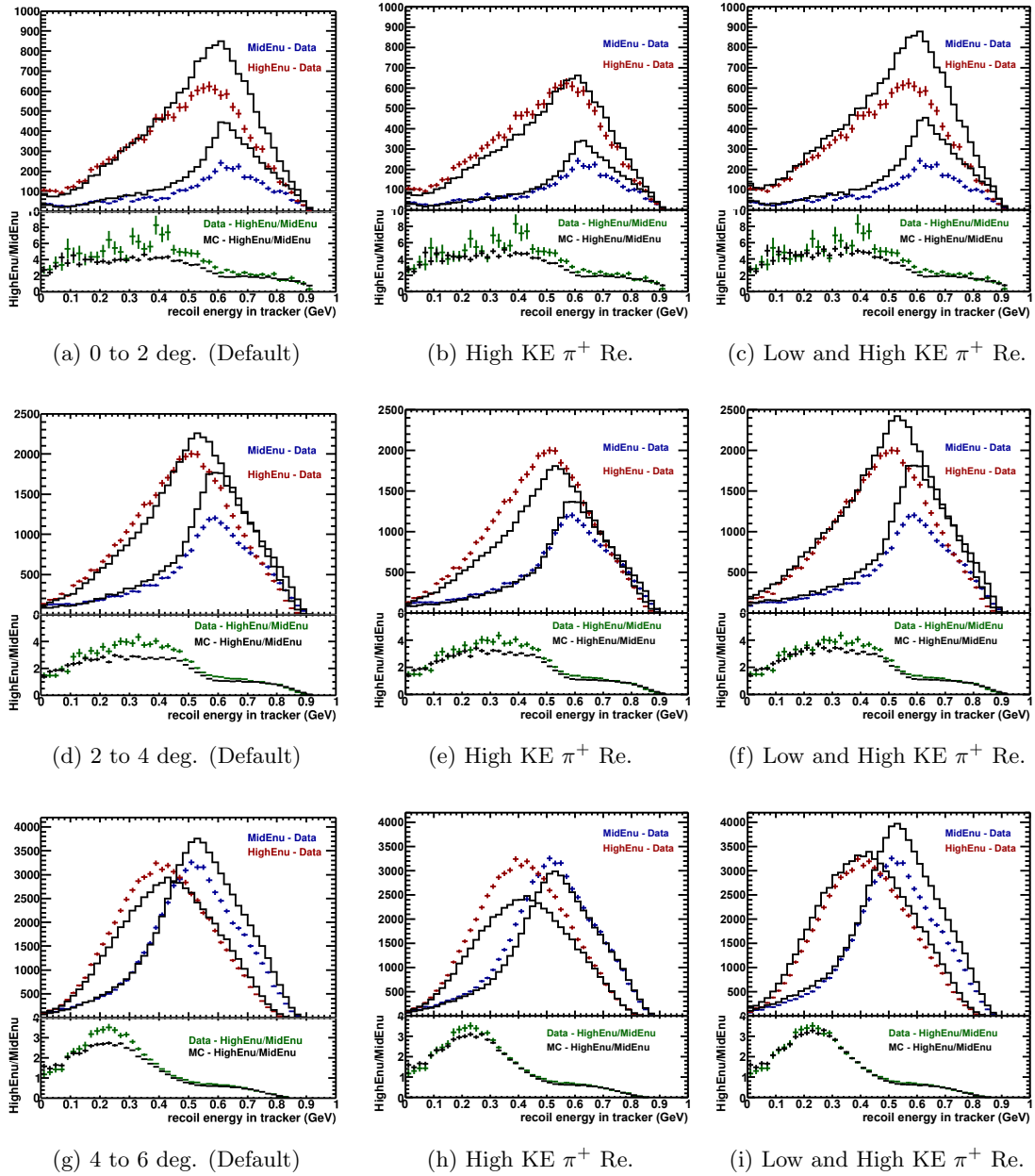


Figure 7.10: Discrepancies present in smaller muon angle cuts for MidEnu and HighEnu in High  $q_3$  range, and their reduction after reweighting only High KE  $\pi^+$  and both Low and High KE  $\pi^+$

Fig. 7.10 provides a comparison between reweighting only High KE  $\pi^+$  and both Low KE  $\pi^+$  and High KE  $\pi^+$ . Discrepancy is reduced in both the reweights and reweighting High KE  $\pi^+$  has a bigger contribution. This can be explained by the bigger fraction of High KE  $\pi^+$  in High  $q_3$  range.

### 7.6.2 Effect of $\pi^+$ reweight on energy dependence discrepancies present in Mid $q_3$ range and smaller angle cuts

Similarly, discrepancies are present in Mid  $q_3$  range also. There are only a few High KE  $\pi^+$  present in this  $q_3$  range. Firstly, we can look at the muon angle cut of 0 to 5 degrees.

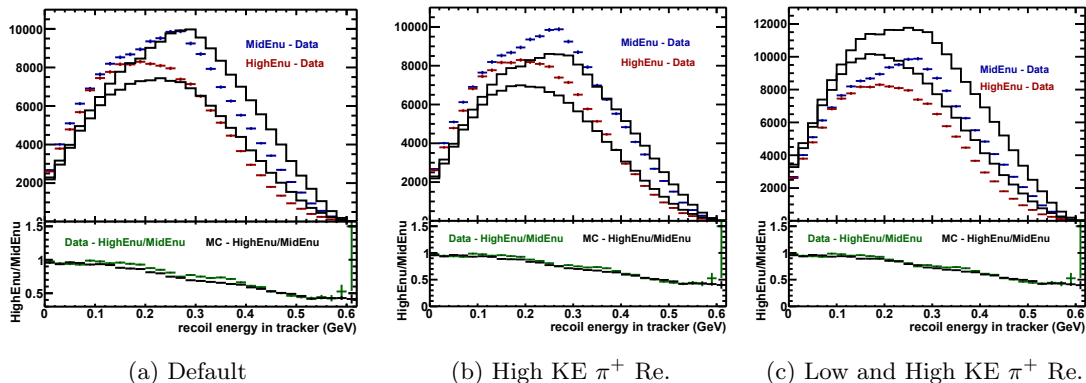


Figure 7.11: Plots of MidEnu and HighEnu in Mid  $q_3$  range with muon angle cut of 0 to 5 degrees with High KE  $\pi^+$ , and both Low KE and High KE  $\pi^+$  reweighted

Reweighting  $\pi^+$  events reduces discrepancies by a small amount. Like High  $q_3$  range, Mid  $q_3$  range also has discrepancies for smaller muon angle cuts. They can be analyzed through the same reweighting idea. The discrepancy corresponding to the muon angle cut 6 to 8 deg. is also reduced with the pion reweight and those additional plots are included in Appendix E.

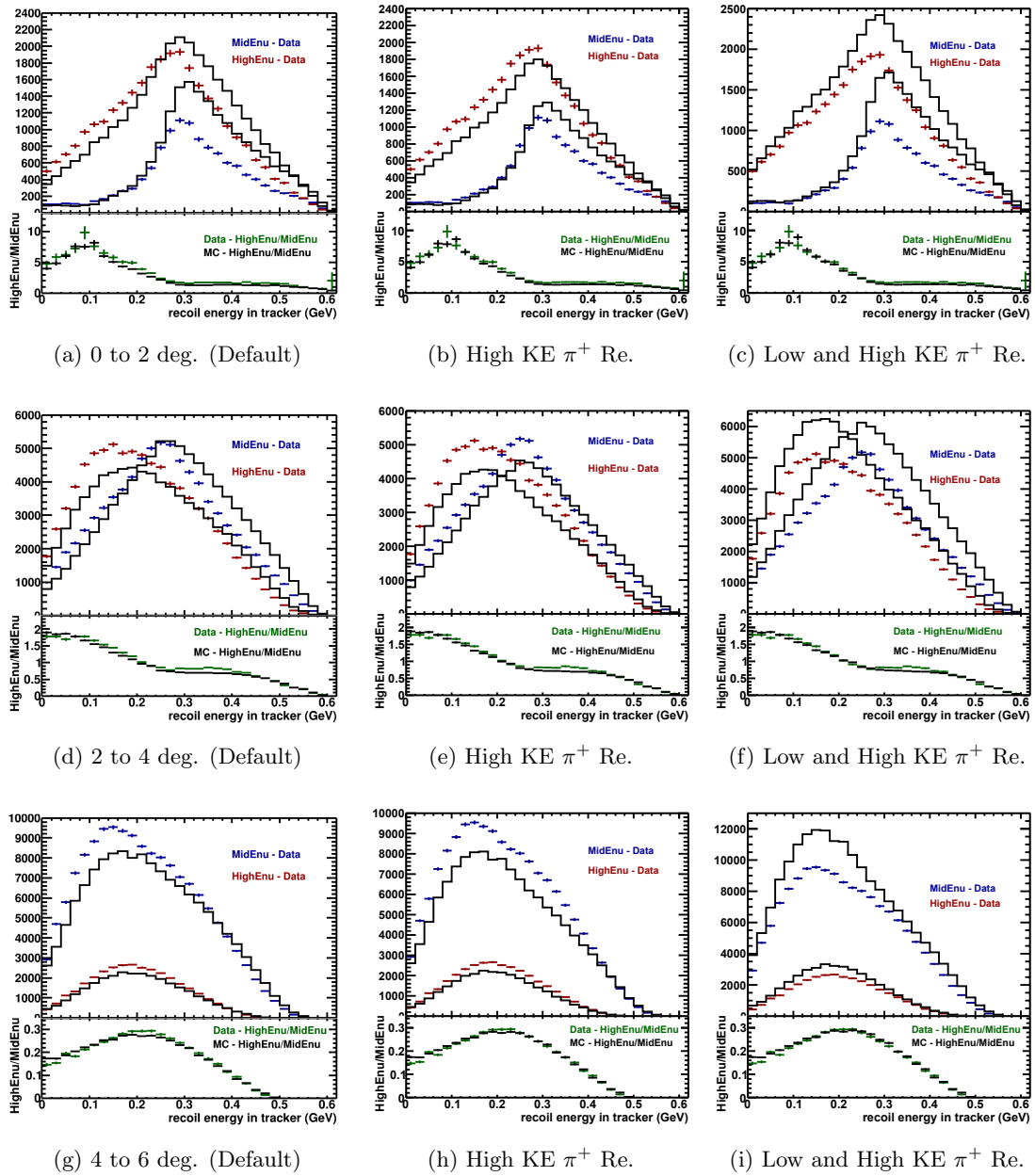


Figure 7.12: Discrepancies present in smaller muon angle cuts for MidEnu and HighEnu in Mid  $q_3$  range, and their reduction after reweighting only High KE  $\pi^+$  and both Low and High KE  $\pi^+$

It can be seen in Fig. 7.12 that reweighting Low KE  $\pi^+$  has a much larger effect compared to reweighting High KE  $\pi^+$  events as expected. Also, discrepancy reduces by a small amount only.

## 7.7 Delta resonance as the major source of pion production

Until now, we have identified that pion production is somehow linked to the discrepancy but we have not established the source of pions, especially  $\pi^+$  in our case. Delta resonance and higher resonances, and deep inelastic scattering (DIS) lead to the production of  $\pi^+$ . Higher resonances correspond to an excited state of protons and neutrons just like delta resonance but with even higher energy. The delta resonance has a rest energy of 1232 MeV and the next resonance has a rest energy of 1535 MeV.

If an event has invariant mass ( $W$ ) less than 2 GeV and is generated through deep inelastic scattering, then that scattering is given a special name and is called “Shallow Inelastic Scattering (SIS)”. Coherent (or diffractive) pion production is the process in which a neutrino interacts with a whole nucleus instead of its nucleons and produces pions. However, it lies at the bottom of the plot, as can be seen in Fig. 7.6, and that’s why it is not plotted here.

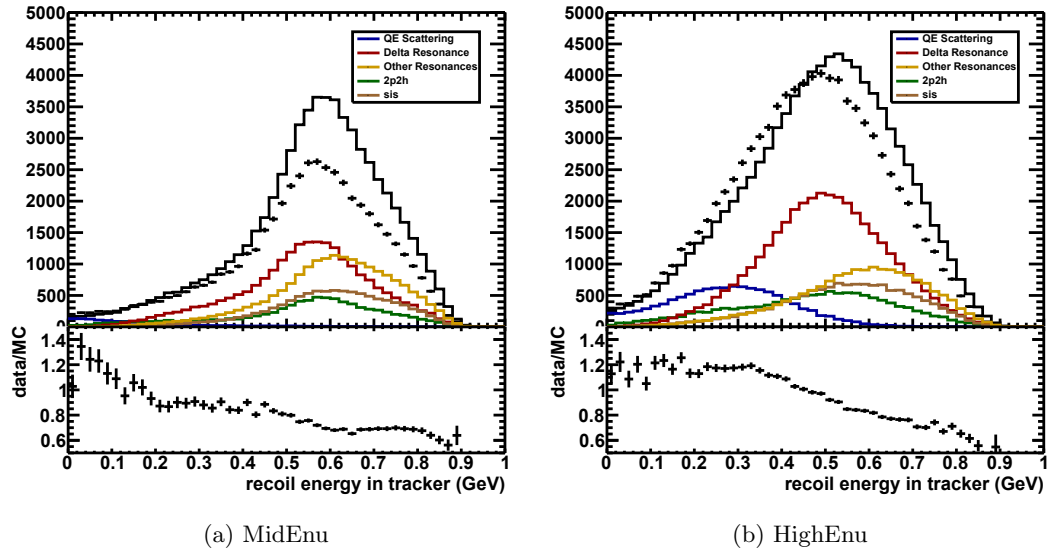


Figure 7.13: MidEnu and HighEnu in High  $q_3$  range with muon angle cut of 0 to 5 degrees depicting the contribution of various neutrino-nucleus interactions

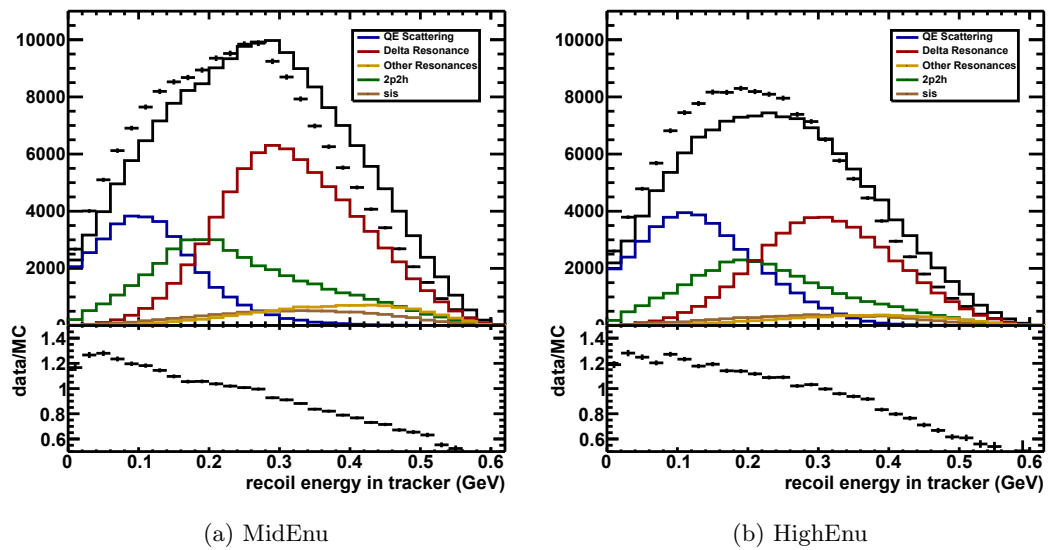


Figure 7.14: MidEnu and HighEnu in Mid  $q_3$  range with muon angle cut of 0 to 5 degrees depicting the contribution of various neutrino-nucleus interactions

It can be seen from the Fig. 7.13 that delta resonance dominates for High  $q_3$  range and its left tail corresponds to the region of discrepancy. This makes sense since reweighting  $\pi^+$  reduced the discrepancy and delta resonance produces  $\pi^+$  in large numbers. Fig. 7.14 shows that delta resonance dominates for MidEnu and dominates for higher energy in tracker for HighEnu. Still, it is the most dominant pion production process.

Although we can get some idea from the figure directly about which process dominates but it does not show the pion production and might mislead in which process produces the maximum number of  $\pi^+$ , so it is better to verify. This can be seen by getting an exact number of events from MC directly. All the tests from now on are done on High  $q_3$  and not Mid  $q_3$  since reweighting pion events has had the biggest effect in High  $q_3$  range.

Table 7.2: Various interactions producing High KE  $\pi^+$  in the discrepancy region  $0.2 \text{ GeV} \leq \text{energy in tracker} \leq 0.3 \text{ GeV}$  and muon angle cut of 0 to 5 degrees corresponding to MidEnu and HighEnu for High  $q_3$  range

Interaction type	MidEnu	HighEnu
All events	4637.42	6942.62
Delta Resonance	1860.82	3404.44
Other Resonances	1154.66	1630.49
Shallow Inel. Scatt.	498.93	1069.60
Deep Inel. Scatt.	53.51	47.97
Coh. Pion Prod.	1068.66	775.50
Remaining	0.82	14.61

The table shows that delta resonance is the dominant source of pion production followed by higher resonances. The subdominant processes that contribute to pion production are SIS and coherent pion production. DIS can be ignored.

Reweighting only delta resonance events by 50% when it produces a  $\pi^+$  with KE greater than 150 MeV is expected to produce an observable reduction in the discrepancy. It might not be big enough though since delta resonance corresponds to less than half

of High KE  $\pi^+$  events in MidEnu and about half of such events in HighEnu. The plots with delta resonance reweighted compared with all events reweighted when a High KE  $\pi^+$  is present are shown below.

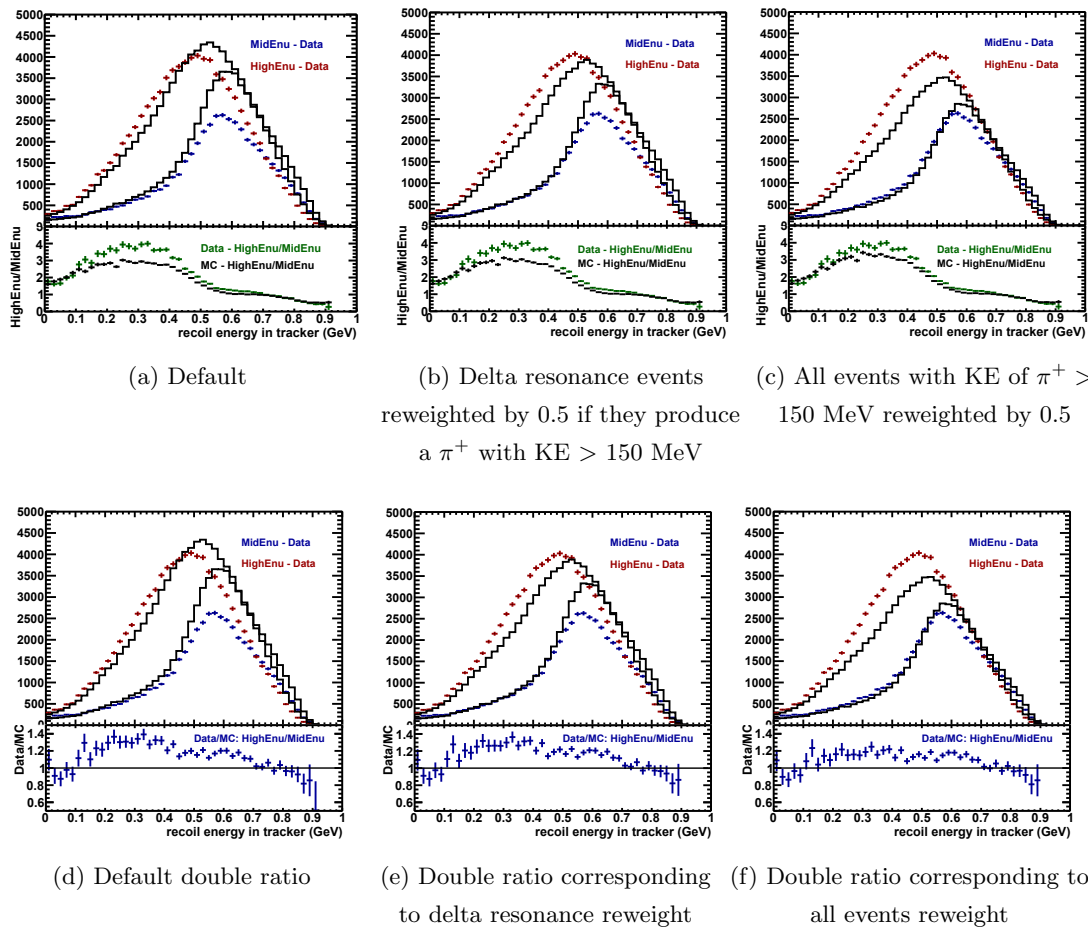


Figure 7.15: Plot of MidEnu and HighEnu in High  $q_3$  range with muon angle cut of 0 to 5 degrees with delta resonance reweighted by 50% if it produces a  $\pi^+$  with KE > 150 MeV compared with the default discrepancy plot and all events reweighted plot

Fig. 7.15 shows that reweighting delta resonance events reduces the discrepancy but that is not big enough to be easily observable without a double ratio plot. This test eliminates the possibility of mismodeled energy dependence in delta resonance and reaffirms a statement made earlier that the discrepancy is due to an excess of pions

produced with the help of the energy-dependent muon angle selections and not due to mismodeled energy dependence.

The second dominant processes producing pions are Other Resonances. So, the next test is to apply the same reweights on all the resonances, including delta resonance, keeping everything else same. This test is to determine if reweighting two dominant processes is enough to bring about an observable change in the discrepancy.

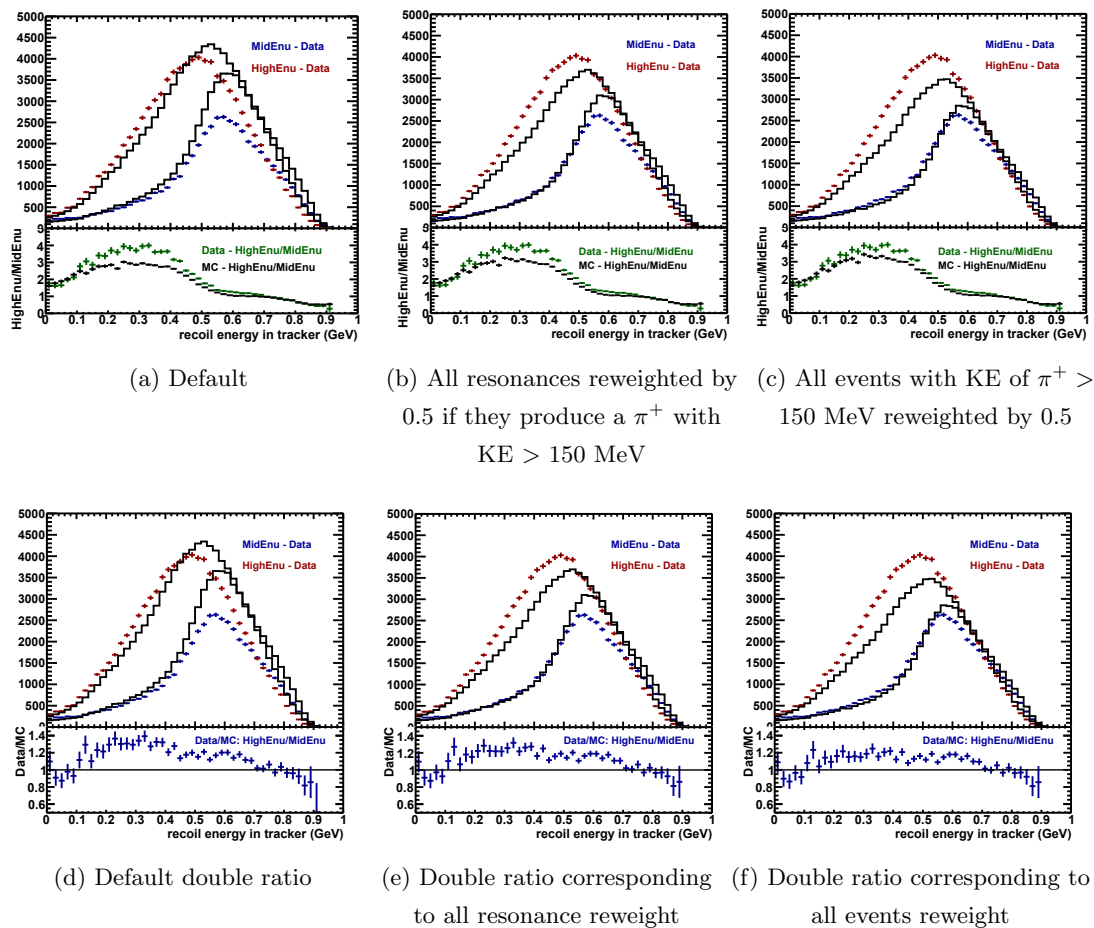


Figure 7.16: Plot of MidEnu and HighEnu in High  $q_3$  range with muon angle cut of 0 to 5 degrees with all resonances reweighted by 50% if it produces a  $\pi^+$  with KE > 150 MeV compared with the default discrepancy plot and all events reweighted plot

Fig. 7.16 shows that reweighting all resonances brings the double ratio down by more than 50% of what it goes down when all the  $\pi^+$  events are reweighted.

All the tests done above confirm that the discrepancy in the plots is due to an excess in pion production. This excess is primarily coming from resonances, especially delta resonance. SIS and coherent pion production might also contribute partly to the excess. However, their contribution in the discrepancy region comes from their left tails, which is notoriously the least reliable feature of models like these.

An interesting and important conclusion of this chapter is to connect the excess of pion production model to the energy dependence discrepancy. Reweighting pions reduces the discrepancy and it seemingly appears that energy dependence is not well-modeled in the pion production model itself. However, we see discrepancy only in smaller angle cuts and not bigger ones such as 0 to 10 degrees or no angle cut which is equivalent to 0 to 20 degrees cut due to detector geometry. This means that angle cut itself introduces an additional energy dependence. It does so by selectively including pion production events of different KE range depending on the angle cut. Muon angle cut of 0 to 5 degrees for High  $q_3$  range selects more pion events with higher KE and less with lower KE. Since High KE pion events are overestimated in MC, it shows up as an energy dependence discrepancy. When a higher angle cut such as 0 to 10 degrees is applied, most of the pion events are included. Underestimation of Low KE pions and overestimation of High KE pions balances each other out. If pion production model itself had energy dependence mismodeled, it would show up in every neutrino energy range and every muon angle cut but it does not.

It is the mismodeling of pion production irrespective of neutrino energy that shows up as an energy dependence discrepancy when muon angle cuts are applied.

## Chapter 8

# Conclusion and Discussion

We showed that the structure function  $W_2$  is big enough to describe QE scattering and 2p2h process at MINERvA energies with more than 90% contribution. The  $1/E$  Term, which contains both  $W_3$  and  $W_2$ , kicks in at lower neutrino energies. Although we did not show it for delta resonance explicitly, experience from Mahbub's thesis [26] is that delta resonance will also follow the same behaviour of structure functions and energy dependence. By taking the ratios of structure functions for QE scattering keeping RPA on and off, we showed that RPA has a slight energy-dependent effect and it introduces a small energy dependence in structure functions also.

We studied 2p2h process on both nn and pn pairs. Plots on contribution of pn and nn pairs in the total cross-section showed that pn has more than 50% contribution in the whole plot. Its contribution is maximum just below the QE peak where it rises up to 90%. 2p2h on nn pair has the maximum contribution in the dip region and the two right corners of the triangle diagram, which is about 45%.

We also studied energy dependence in 2p2h process for Valencia Model. However, we saw some unphysical values in Chapter 2 at the upper edge of 2p2h plots. This is due to a non-relativistic aspect in Valencia Model which is present around that edge. SuSA Model is fully relativistic and it also has very different structure functions whose effects may be interesting if we can access them directly.

A method to extract the structure functions directly from the MINERvA data is developed. Although it is established that the method works, the extraction of  $1/E$  Term is sensitive to the uncertainties present in the MINERvA data. Either smaller uncertainties or going to lower neutrino energies will improve the sensitivity to the  $1/E$  Term and make the extraction more successful. The method was used on MINERvA data obtained during its ME beam era (2013-2019). A direction of future work is to apply the method to the MINERvA data from LE beam era (2009-2013). Since it peaks at 3 GeV, it could improve the sensitivity to the  $1/E$  Term from the factor of 3 GeV/6 GeV. The other limitation we faced is that we applied the extraction method to a resolution-smearred dataset which made comparison of the obtained values with the theoretical values considerably difficult. Unfolding the sample before applying the method will be an interesting thing to try.

Analysis of Rob Fine's low- $\nu$  flux and its comparison with MINERvA's default flux showed that the low- $\nu$  flux brings down the data/MC ratio closer to its ideal value of 1. It also takes the wiggles out of the ratio and makes it flatter. Low  $q_3$  still has a constant offset hinting at an error in the known value of  $W_2$  for QE scattering, such as from the axial form factor or the RPA effect.

There are no energy dependence discrepancies present in a majority of  $E_\nu$  and  $q_3$  ranges but they start appearing when stronger muon angle cuts are applied. These discrepancies can be attributed to mismodeled cross-section whose energy dependence might be perfect but it shows up as an energy dependence discrepancy due to the chosen muon angle cut. We did a thorough analysis of the discrepancy present between HighEnu and MidEnu in High  $q_3$  range when muon angle cut of 0 to 5 degrees is applied. This discrepancy arises due to overestimation of high energy pions and underestimation of low energy pions. Since delta resonance is the dominant model of pion production, it is important to test it further. Varying its vector and axial form factors, and by extension the structure functions, can be a starting point. Also,  $\Delta^{++}$  and  $\Delta^+$  both produce pions, and  $\Delta^+$  has two main decay modes. These three decay modes in total contribute differently to pion production. Their analysis to determine which decay mode is not perfectly modeled can be a step toward improvement in pion production model.

# References

- [1] Wikipedia. Standard Model. [https://en.wikipedia.org/wiki/Standard\\_Model](https://en.wikipedia.org/wiki/Standard_Model). [Online; accessed 7-June-2023].
- [2] The T2K Collaboration. Constraint on the matter–antimatter symmetry-violating phase in neutrino oscillations. *Nature*, 580(1759):339–344, 2020.
- [3] M.A. Acero *et al.* (NOvA). Supernova neutrino detection in NOvA. *Journal of Cosmology and Astroparticle Physics*, 2020(10):014, Oct 2020.
- [4] A. Faessler, R. Hodak, S. Kovalenko, and F. Simkovic. Search for the Cosmic Neutrino Background. *Journal of Physics: Conference Series*, 580(1):012040, Feb 2015.
- [5] M.G. Betti *et al.* (PTOLEMY). Neutrino physics with the PTOLEMY project: active neutrino properties and the light sterile case. *Journal of Cosmology and Astroparticle Physics*, 2019(07):047–047, Jul 2019.
- [6] M.V. Ascencio *et al.* (MINERvA). Measurement of inclusive charged-current  $\nu_\mu$  scattering on hydrocarbon at  $\langle E_\nu \rangle \sim 6$  GeV with low three-momentum transfer. *Physical Review D*, 106(3), Aug 2022.
- [7] Richard Gran. Anti-neutrino reactions with low momentum transfer. *MINERvA-doc-16438-v8*, 2017.
- [8] R. Gran, J. Nieves, F. Sanchez, and M. J. Vicente Vacas. Neutrino-nucleus quasi-elastic and 2p2h interactions up to 10 GeV. *Physical Review D*, 88(11), Dec 2013.

- [9] Ethan Miltenberger. Nuclear effects in neutrino interactions at low momentum transfer. Master's thesis, University of Minnesota Duluth, May 2015.
- [10] L. Aliaga *et al.* (MINERvA). Design, calibration, and performance of the MINERvA detector. *Nuclear Instruments and Methods in Physics Research Section A: Accelerators, Spectrometers, Detectors and Associated Equipment*, 743:130–159, 2014.
- [11] Melissa T. Jerkins *et al.* (MINERvA). Measuring the NuMI Beam Flux for MINERvA. *AIP Conference Proceedings*, 1405:362–367, 2011.
- [12] E. Valencia *et al.* (MINERvA). Constraint of the MINERvA Medium Energy Neutrino Flux using Neutrino-Electron Elastic Scattering. *Physical Review D*, 100(9), Nov 2019.
- [13] Rob Fine. *Measurement of the Medium Energy NuMI Flux Using the Low- $\nu$  and High- $\nu$  Methods at MINERvA*. PhD thesis, University of Rochester, 2020.
- [14] C. Andreopoulos, A. Bell, D. Bhattacharya, F. Cavanna, J. Dobson, S. Dytman, H. Gallagher, P. Guzowski, R. Hatcher, P. Kehayias, A. Mereaglia, D. Naples, G. Pearce, A. Rubbia, M. Whalley, and T. Yang. The GENIE neutrino Monte Carlo generator. *Nuclear Instruments and Methods in Physics Research Section A: Accelerators, Spectrometers, Detectors and Associated Equipment*, 614(1):87–104, 2010.
- [15] C. Andreopoulos, C. Barry, S. Dytman, H. Gallagher, T. Golan, R. Hatcher, G. Perdue, and J. Yarba. The GENIE Neutrino Monte Carlo Generator: Physics and User Manual, 2015, arXiv:1510.05494 [hep-ph].
- [16] A. Bodek and J. L. Ritchie. Fermi-motion effects in deep-inelastic lepton scattering from nuclear targets. *Phys. Rev. D*, 23:1070–1091, Mar 1981.
- [17] J. Nieves, J. E. Amaro, and M. Valverde. Inclusive quasielastic charged-current neutrino-nucleus reactions. *Phys. Rev. C*, 70:055503, Nov 2004.

- [18] J. Nieves, J. E. Amaro, and M. Valverde. Erratum: Inclusive quasielastic charged-current neutrino-nucleus reactions [Phys. Rev. C 70, 055503 (2004)]. *Phys. Rev. C*, 72:019902, Jul 2005.
- [19] Richard Gran. Model uncertainties for Valencia RPA effect for MINERvA, May 2017, arXiv:1705.02932 [hep-ex].
- [20] Arie Bodek. Pauli blocking for a Relativistic Fermi Gas in Quasielastic Lepton Nucleus Scattering, Nov 2021, arXiv:2111.03631 [nucl-th].
- [21] Michael Dolce. NOvA central value tuning & uncertainties for the hN FSI model in GENIE 3. <https://indico.fnal.gov/event/23110/contributions/190679/attachments/131582/161174/2020-07-21-NewPerspectives-hN-tuning.pdf>. [Online; accessed 9-June-2023].
- [22] S. Agostinelli *et al.* Geant4—a simulation toolkit. *Nuclear Instruments and Methods in Physics Research Section A: Accelerators, Spectrometers, Detectors and Associated Equipment*, 506(3):250–303, 2003.
- [23] C.H. Llewellyn Smith. Neutrino reactions at accelerator energies. *Physics Reports*, 3(5):261–379, 1972.
- [24] Ch. Berger and L. M. Sehgal. Lepton mass effects in single pion production by neutrinos. *Physical Review D*, 76(11), Dec 2007.
- [25] Olga Lalakulich and Emmanuel A. Paschos. Resonance production by neutrinos:  $j = 3/2$  resonances. *Phys. Rev. D*, 71:074003, Apr 2005.
- [26] I. Mahbub. Energy dependence in the neutrino scattering data of minerva. Master’s thesis, University of Minnesota Duluth, July 2021.
- [27] Dieter Rein and Lalit M. Sehgal. Neutrino Excitation of Baryon Resonances and Single Pion Production. *Annals Phys.*, 133:79–153, 1981.
- [28] J. Nieves, I. Ruiz Simo, and M. J. Vicente Vacas. Inclusive charged-current neutrino-nucleus reactions. *Physical Review C*, 83(4), Apr 2011.

- [29] J. Schwehr, D. Cherdack, and R. Gran. GENIE implementation of IFIC Valencia model for QE-like 2p2h neutrino-nucleus cross section, 2017, arXiv:1601.02038 [hep-ph].
- [30] R. Gran *et al.* (MINERvA). Antineutrino Charged-Current Reactions on Hydrocarbon with Low Momentum Transfer. *Physical Review Letters*, 120(22), Jun 2018.
- [31] William R. Leo. Techniques for Nuclear and Particle Physics Experiments. chapter 2. Springer-Verlag, 2nd edition, 1994.
- [32] Charles J. Joachain. Quantum Collision Theory. chapter 1. North-Holland Publishing Company, 1975.
- [33] H. Atac, M. Constantinou, Z.-E. Meziani, M. Paolone, and N. Sparveris. Measurement of the neutron charge radius and the role of its constituents. *Nature Communications*, 12(1759), 2021.
- [34] R. Pohl *et al.* The size of the proton. *Nature*, 466:213–216, 2010.
- [35] K.S. Kuzmin, V.V. Lyubushkin, and V.A. Naumov. Quasielastic axial-vector mass from experiments on neutrino–nucleus scattering. *The European Physical Journal C*, 54(4):517–538, Apr 2008.
- [36] H. Gallagher, G. Garvey, and G.P. Zeller. Neutrino-nucleus interactions. *Annual Review of Nuclear and Particle Science*, 61(1):355–378, 2011.
- [37] D. R. Yennie, M. M. Lévy, and D. G. Ravenhall. Electromagnetic Structure of Nucleons. *Rev. Mod. Phys.*, 29:144–157, Jan 1957.
- [38] F. J. Ernst, R. G. Sachs, and K. C. Wali. Electromagnetic Form Factors of the Nucleon. *Phys. Rev.*, 119:1105–1114, Aug 1960.
- [39] R. G. Sachs. High-Energy Behavior of Nucleon Electromagnetic Form Factors. *Phys. Rev.*, 126:2256–2260, Jun 1962.
- [40] H. Kröger and N. Scheu. Physics from Breit-frame regularization of a lattice Hamiltonian. *Physical Review D*, 56(3):1455–1469, Aug 1997.

- [41] Jared A. Rinehimer and Gerald A. Miller. Connecting the Breit Frame to the Infinite Momentum Light Front Frame: How  $G_E$  turns into  $F_1$ . *Physical Review C*, 80(1), Jul 2009.
- [42] Mark Thomson. Modern Particle Physics. chapter 7. Cambridge University Press, 2013.
- [43] C. Patrignani. Review of Particle Physics. *Chinese Physics C*, 40(10):100001, Oct 2016.
- [44] D B Renner, R G Edwards, G Fleming, Ph Hägler, J W Negele, K Orginos, A V Pochinsky, D G Richards, and W Schroers. Calculation of the nucleon axial charge in lattice QCD. *Journal of Physics: Conference Series*, 46(1):152, Sep 2006.
- [45] Aaron S. Meyer, Minerba Betancourt, Richard Gran, and Richard J. Hill. Deuterium target data for precision neutrino-nucleus cross sections. *Physical Review D*, 93(11), Jun 2016.
- [46] Aaron S. Meyer, André Walker-Loud, and Callum Wilkinson. Status of Lattice QCD Determination of Nucleon Form Factors and Their Relevance for the Few-GeV Neutrino Program. *Annual Review of Nuclear and Particle Science*, 72(1):205–232, Sep 2022.
- [47] T. Cai *et al.* (MINERvA). Measurement of the axial vector form factor from antineutrino-proton scattering. *Nature*, 614:48–53, 2023.
- [48] Yong-Chull Jang, Rajan Gupta, Boram Yoon, and Tanmoy Bhattacharya. Axial Vector Form Factors from Lattice QCD that Satisfy the PCAC Relation. *Physical Review Letters*, 124(7), Feb 2020.
- [49] Jan Sobczyk. Recent Work on Multi-Nucleon Correlations. *MINERvA-doc-26551-v2*, 2020.
- [50] R.A. Smith and E.J. Moniz. Neutrino reactions on nuclear targets. *Nuclear Physics B*, 43:605–622, 1972.
- [51] R.A. Smith and E.J. Moniz. Erratum: neutrino reactions on nuclear targets. *Nuclear Physics B*, 101:547, 1975.

- [52] Anthony Mann. Calculate like a Llewellyn. *NOVA-doc-28289-v2*, 2018.
- [53] Francis Halzen and Alan D. Martin. *Quarks and Leptons: An Introductory Course in Modern Particle Physics*. John Wiley & Sons, Inc., 1984.
- [54] R.K. Jain and S.R.K. Iyengar. *Advanced Engineering Mathematics*. chapter 2. Alpha Science International Limited, 2001.
- [55] E. J. Moniz, I. Sick, R. R. Whitney, J. R. Ficenec, R. D. Kephart, and W. P. Trower. Nuclear Fermi Momenta from Quasielastic Electron Scattering. *Phys. Rev. Lett.*, 26:445–448, February 1971.
- [56] Artur M. Ankowski. Breakdown of the impulse approximation and its consequences: the low- $Q^2$  problem, Oct 2008, arXiv:0810.1167 [nucl-th].
- [57] Arie Bodek and Tejin Cai. Removal energies and final state interaction in lepton nucleus scattering. *The European Physical Journal C*, 79(4), Apr 2019.
- [58] Richard Gran. Sensitivity to MEC and RPA using inclusive kinematics. *MINERvA-doc-9842-v1*, 2014.
- [59] J.E. Amaro, M.B. Barbaro, J.A. Caballero, T.W. Donnelly, R. González-Jiménez, G.D. Megias, and I. Ruiz Simo. Neutrino-nucleus scattering in the SuSA model. *The European Physical Journal Special Topics*, 230:4321–4338, 2021.
- [60] Nafis Fuad. Analysis of MINERvA tunings of GENIE based on Hadron Multiplicity using Machine Learning. Master’s thesis, University of Minnesota Duluth, July 2020.
- [61] Cheryl E. Patrick. Introduction to cross sections. *MINERvA-doc-11196-v2*, 2015.
- [62] G. D’Agostini. A multidimensional unfolding method based on Bayes’ theorem. *Nuclear Instruments and Methods in Physics Research Section A: Accelerators, Spectrometers, Detectors and Associated Equipment*, 362(2):487–498, 1995.
- [63] G. D’Agostini. Improved iterative Bayesian unfolding, 2010, arXiv:1010.0632 [physics.data-an].

- [64] Wouter Verkerke and David Kirkby. The RooFit toolkit for data modeling, 2003, arXiv:physics/0306116 [physics.data-an].
- [65] Abigail V. Waldron. Low Recoil Muon Antineutrino Medium Energy (July Meeting). *MINERvA-doc-30875-v1*, 2022.
- [66] J. Kleykamp *et al.* (MINERvA). Simultaneous Measurement of  $\nu_\mu$  Quasielasticlike Cross Sections on CH, C, H<sub>2</sub>O, Fe, and Pb as a Function of Muon Kinematics at MINERvA. *Phys. Rev. Lett.*, 130:161801, Apr 2023.
- [67] D. Ruterbories *et al.* (MINERvA). Simultaneous Measurement of Proton and Lepton Kinematics in Quasielasticlike  $\nu_\mu$ -Hydrocarbon Interactions from 2 to 20 GeV. *Phys. Rev. Lett.*, 129:021803, Jul 2022.
- [68] Albert Einstein. Ist die Trägheit eines Körpers von seinem Energieinhalt abhängig? *Annalen der Physik*, 323(13):639–641, 1905.
- [69] Philip Rodrigues, Callum Wilkinson, and Kevin McFarland. Constraining the GENIE model of neutrino-induced single pion production using reanalyzed bubble chamber data. *The European Physical Journal C*, 76(8), Aug 2016.
- [70] A. Bashyal *et al.* (MINERvA). Use of neutrino scattering events with low hadronic recoil to inform neutrino flux and detector energy scale. *Journal of Instrumentation*, 16(08):P08068, Aug 2021.
- [71] Oleksandr Tomalak and Richard J. Hill. Theory of elastic neutrino-electron scattering. *Physical Review D*, 101(3), Feb 2020.
- [72] J. Park *et al.* (MINERvA). Measurement of neutrino flux from neutrino-electron elastic scattering. *Phys. Rev. D*, 93:112007, Jun 2016.
- [73] D. Ruterbories *et al.* (MINERvA). Constraining the NuMI neutrino flux using inverse muon decay reactions in MINERvA. *Physical Review D*, 104(9), Nov 2021.
- [74] D.Yu. Bardin and V.A. Dokuchaeva. Muon energy spectrum in inverse  $\mu$ -decay. *Nuclear Physics B*, 287:839–851, 1987.

- [75] P. Adamson *et al.* (MINOS). Neutrino and antineutrino inclusive charged-current cross section measurements with the MINOS near detector. *Phys. Rev. D*, 81:072002, Apr 2010.
- [76] A. Bodek, U. Sarica, D. Naples, and L. Ren. Methods to determine neutrino flux at low energies. *The European Physical Journal C*, 72(4), Apr 2012.
- [77] D.F. Geesaman. Nucleon parton distributions and nuclear structure. *Nuclear Physics A*, 527:109–122, 1991.
- [78] W. Seligman. *An Improved Determination of  $\alpha_S$  From Neutrino-Nucleon Scattering*. PhD thesis, Columbia University, 1997.
- [79] A. Abed Abud *et al.* (DUNE). Deep Underground Neutrino Experiment (DUNE) Near Detector Conceptual Design Report. *Instruments*, 5(4), 2021.
- [80] C. Wilkinson, S. Dolan, L. Pickering, and C. Wret. A substandard candle: the low- $\nu$  method at few-GeV neutrino energies. *The European Physical Journal C*, 82(9), Sep 2022.
- [81] B.J. King *et al.* Measuring muon momenta with the CCFR neutrino detector. *Nuclear Instruments and Methods in Physics Research Section A: Accelerators, Spectrometers, Detectors and Associated Equipment*, 302(2):254–260, 1991.
- [82] A. Bodek *et al.* Tests of perturbative QCD using CCFR data for measurements of nucleon structure functions. *Nuclear Physics B - Proceedings Supplements*, 31:271–277, 1993.
- [83] M. Tzanov *et al.* Precise measurement of neutrino and antineutrino differential cross sections. *Physical Review D*, 74(1), Jul 2006.
- [84] G. P. Zeller *et al.* (NuTeV). Precise Determination of Electroweak Parameters in Neutrino-Nucleon Scattering. *Physical Review Letters*, 88(9), Feb 2002.
- [85] P. Astier *et al.* Prediction of neutrino fluxes in the NOMAD experiment. *Nuclear Instruments and Methods in Physics Research Section A: Accelerators, Spectrometers, Detectors and Associated Equipment*, 515(3):800–828, 2003.

- [86] F. Vannucci. The NOMAD Experiment at CERN. *Advances in High Energy Physics*, 2014(129694), 2014.
- [87] Emily Haase. Searching for un-simulated data population SRC region. *MINERvA-doc-31338-v1*, 2022.
- [88] N. Tagg *et al.* Arachne - a web-based event viewer for MINERvA. *Nuclear Instruments and Methods in Physics Research Section A: Accelerators, Spectrometers, Detectors and Associated Equipment*, 676:44–49, Jun 2012.
- [89] Catherine Forbes, Merran Evans, Nicholas Hastings, and Brian Peacock. Statistical distributions. chapter 9. John Wiley & Sons, Inc., 4th edition, 2011.
- [90] A. Bercellie *et al.* (MINERvA). Simultaneous measurement of muon neutrino  $\nu_\mu$  charged-current single  $\pi^+$  production in CH, C, H<sub>2</sub>O, Fe, and Pb targets in MINERvA, Sep. 2022, arXiv:2209.07852 [hep-ex].
- [91] Steven Dytman. Final state interactions in neutrino-nucleus experiments. *Acta Phys. Polon. B*, 40:2445–2460, 2009.
- [92] Lauren Alexandria Harewood. Quasielastic Distributions for Transverse Kinematic Variables. Master’s thesis, University of Minnesota Duluth, June 2019.

## Appendix A

# Individual Terms of Different Orders of Neutrino Energy in QE Scattering and 2p2h Process

In neutrino-nucleus interactions, cross-section is written in terms of structure functions. The two dominant structure functions,  $W_2$  and  $W_3$ , along with their kinematic factors are labeled  $ww2$  and  $ww3$  respectively for this thesis.  $ww2$  has energy-independent,  $1/E$  dependent and  $1/E^2$  dependent terms, while  $ww3$  has  $1/E$  and  $1/E^2$  dependent terms. In this appendix, the subterms are illustrated separately to show their relative size. The complete expressions are as follows:

$$\begin{aligned} ww2 &= W_2 \left( 2 - \frac{2\omega}{E} - \frac{(Q^2 + m^2)}{2E^2} \right) \\ ww3 &= \pm W_3 \left( \frac{Q^2}{EM} - \frac{\omega(Q^2 + m^2)}{2ME^2} \right) \end{aligned} \quad (\text{A.1})$$

where the factor  $\frac{G_F^2 \cos^2 \theta_C q_3}{2\pi}$  is always multiplied.  $\omega$  is another symbol for  $q_0$ , the energy transfer in the interaction.

## A.1 Individual energy terms of $ww2$ and $ww3$ in QE scattering

The individual terms of  $ww2$  and  $ww3$  in quasielastic scattering for 3 GeV neutrinos are shown in Fig. A.1 and A.2 respectively. The minus sign present with the term is not included in the plot.

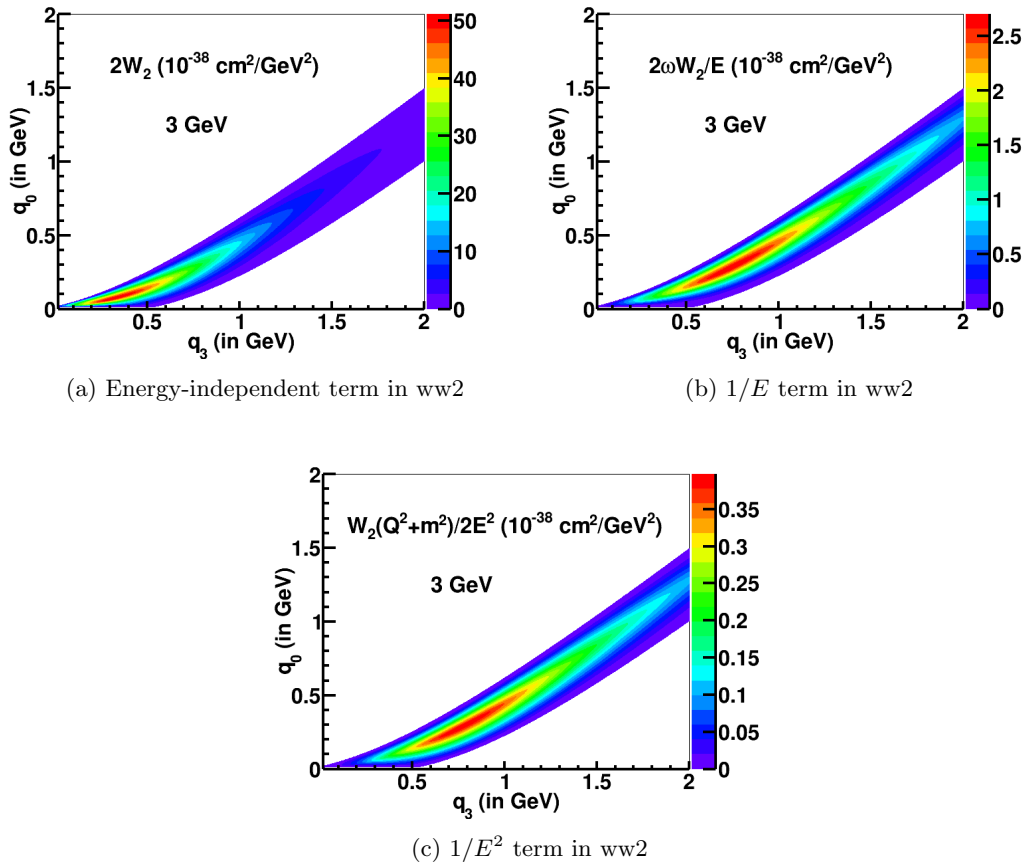


Figure A.1: Terms of different orders of neutrino energy present in  $ww2$  for QE scattering

The energy independent term in  $ww2$  is  $2W_2$ , which is also the energy independent term in the whole cross-section. It is about 20 times bigger than  $1/E$  term in  $ww2$  and about 150 times bigger than the  $1/E^2$  term in  $ww2$  for a 3 GeV neutrino.

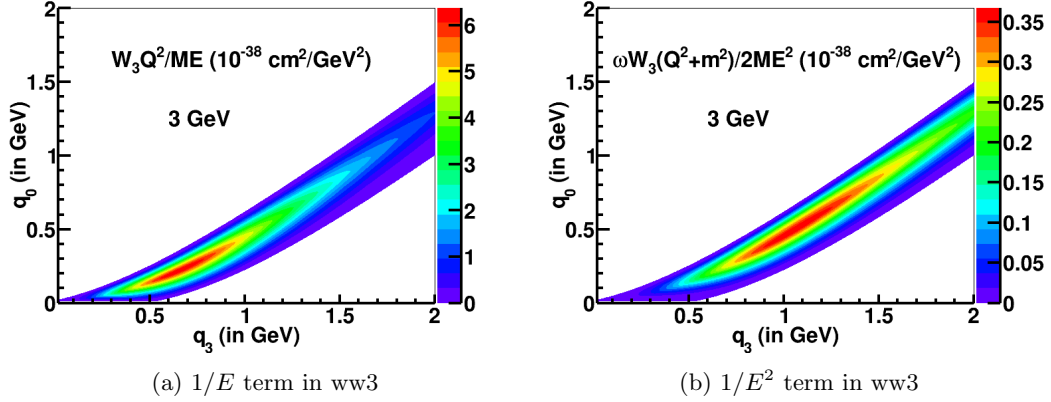


Figure A.2: Terms of different orders of neutrino energy present in  $ww3$  for QE scattering

The  $1/E$  term in  $ww3$  is about 20 times bigger than the  $1/E^2$  term in  $ww3$ .

The  $1/E$  term in  $ww2$  and  $ww3$  together are the  $1/E$  term in the whole cross-section.

## A.2 Individual energy terms of $ww2$ and $ww3$ in 2p2h process

2p2h process is also described by the same expression for neutrino-nucleus interactions in terms of structure functions. The individual terms of  $ww2$  and  $ww3$  for a 3 GeV neutrino are shown in Fig. A.3 and A.4 respectively. Again, minus sign in the expressions is not included in the plot.

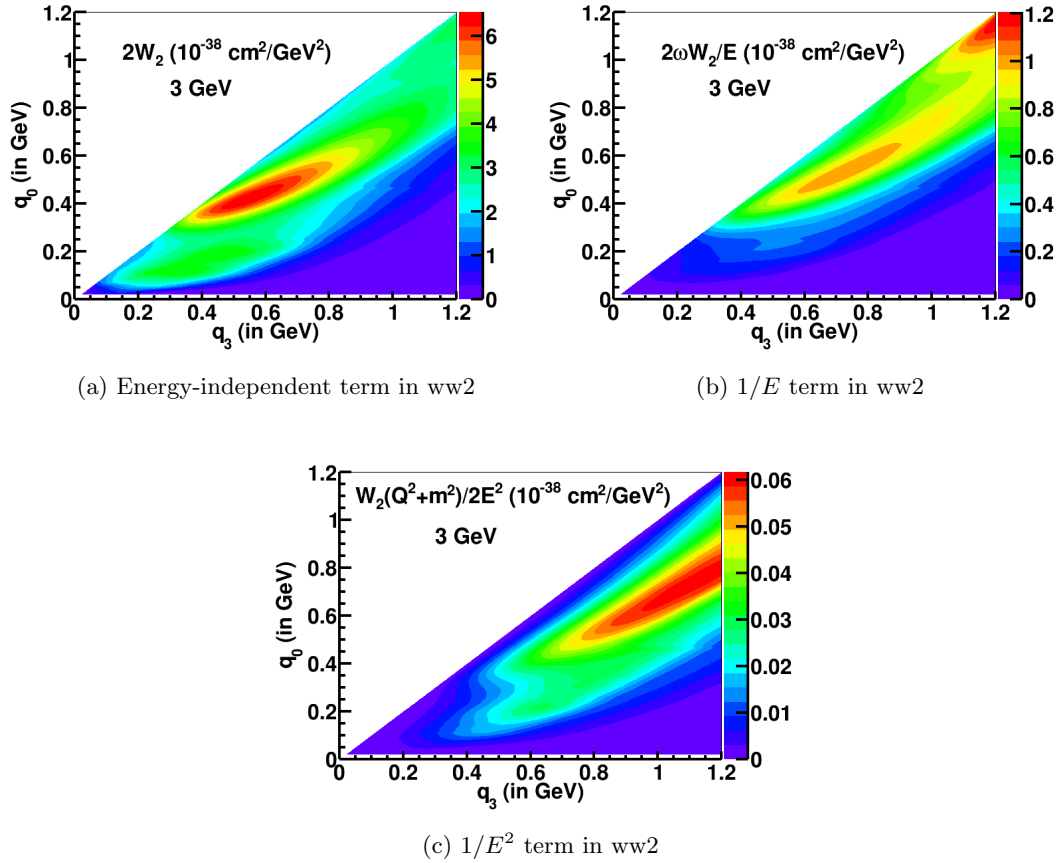


Figure A.3: Terms of different orders of neutrino energy present in  $w\omega 2$  for 2p2h process

The energy independent term in  $w\omega 2$  is  $2W_2$ , which is also the energy independent term in the whole cross-section. It is about 5 times bigger than  $1/E$  term in  $w\omega 2$  and about 100 times bigger than the  $1/E^2$  term in  $w\omega 2$  for a 3 GeV neutrino. Although the maximum values of these three terms are in different places, so comparison between maximum values is not so easy. Still, the relative average magnitude is about the same.

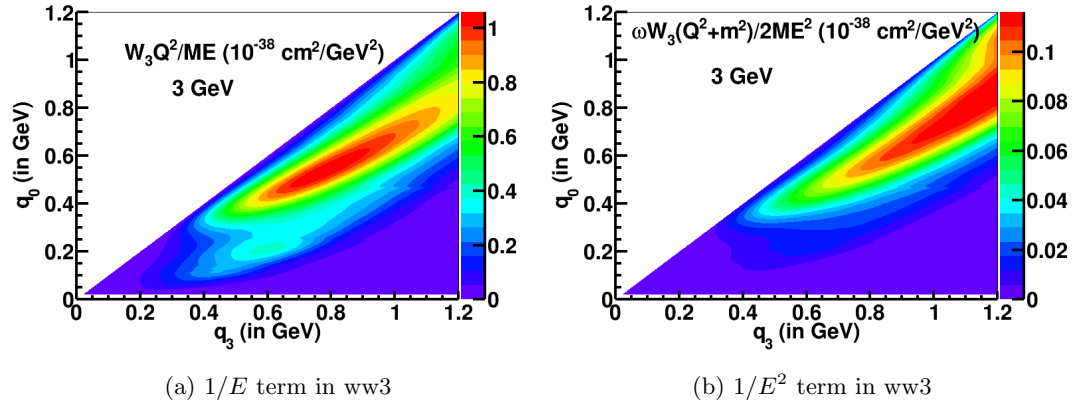


Figure A.4: Terms of different orders of neutrino energy present in  $ww3$  for 2p2h process

The  $1/E$  term in  $ww3$  is about 10 times bigger than the  $1/E^2$  term in  $ww3$ .

The  $1/E$  term in  $ww2$  and  $ww3$  together are the  $1/E$  term in the whole cross-section.

## Appendix B

# Non-unique Convergence in the Extraction of *En. Ind. Term* and *1/E Coeff.*

We defined four neutrino energy ranges 3-5 GeV, 4-6 GeV, 5-7 GeV and 7+ GeV (7 GeV and higher) in Chapter 3. The idea is to choose two energy ranges at a time, write the corresponding equation Eq. 3.5 and solve the two equations simultaneously. Since six pairs of energy ranges can be chosen, six different solutions are possible. However, we saw that the solutions do not match when they should since they are not dependent on neutrino energy.

Then we proposed adjusting the number of events by a small percentage so that the six solutions converge to one solution. This effectively is applying an adjustment for an (unknown) systematic uncertainty, similar to what is often called a nuisance parameter in fitting. In Chapter 3, we commented that there is no unique convergence solution. Using a different set of percentages can lead to a different solution. We will show here how that works.

For an easier demonstration, let us assume that there are only three energy ranges and thus, three possible pairs and three solutions.

For a general demonstration, let's represent the two variables (*En. Ind. Term* and *1/E Coeff.*) by  $x$  and  $y$ . Also, let's say that the coefficients of the variables (which are basically summation over flux and energy-weighted summation over flux) on the LHS of the equation are  $a_1$  and  $b_1$  and the RHS is  $c_1$  for the first energy range. The corresponding coefficients for the other energy ranges can be symbolized by  $a_2$  and  $b_2$ , and  $a_3$  and  $b_3$ . Similarly, the RHS of the remaining two energy ranges can be symbolized by  $c_2$  and  $c_3$ . The three equations can be written as:

$$\begin{aligned} \text{Eq. 1: } & a_1x + b_1y = c_1 \\ \text{Eq. 2: } & a_2x + b_2y = c_2 \\ \text{Eq. 3: } & a_3x + b_3y = c_3 \end{aligned} \tag{B.1}$$

Let's say that the solutions of Eq. 1 and Eq. 2 are  $(x_{12}, y_{12})$ , Eq. 2 and Eq. 3 are  $(x_{23}, y_{23})$  and Eq. 3 and Eq. 1 are  $(x_{31}, y_{31})$ , and these three do not coincide.

Now, we want the solutions to converge to some desired solution, say  $(x_0, y_0)$ . This means the RHS of Eq. B.1 should be

$$\begin{aligned} \text{Desired RHS of Eq. 1: } & a_1x_0 + b_1y_0 \\ \text{Desired RHS of Eq. 2: } & a_2x_0 + b_2y_0 \\ \text{Desired RHS of Eq. 3: } & a_3x_0 + b_3y_0 \end{aligned} \tag{B.2}$$

Finally, the percentage change in the original RHS so that the equations converge to a desired solution is as follows:

$$\begin{aligned} \text{Per. Cha. in RHS of Eq. 1: } & = \frac{\text{Desired RHS of Eq. 1} - \text{Original RHS of Eq. 1}}{\text{Original RHS of Eq. 1}} \times 100\% \\ \text{Per. Cha. in RHS of Eq. 2: } & = \frac{\text{Desired RHS of Eq. 2} - \text{Original RHS of Eq. 2}}{\text{Original RHS of Eq. 2}} \times 100\% \\ \text{Per. Cha. in RHS of Eq. 3: } & = \frac{\text{Desired RHS of Eq. 3} - \text{Original RHS of Eq. 3}}{\text{Original RHS of Eq. 3}} \times 100\% \end{aligned} \tag{B.3}$$

where the desired RHS of equations are given by Eq. B.2 and the original RHS of equations are  $c_1$ ,  $c_2$  and  $c_3$  respectively.

So, using these equations, a suitable percentage adjustment can make the solutions converge anywhere. We can work on the following equations as an example. They are not the equations used in Chapter 3 but some random simple equations for a demonstration.

$$\begin{aligned}\text{Test Eq. 1: } & x + y = 1 \\ \text{Test Eq. 2: } & x + 2y = 2 \\ \text{Test Eq. 3: } & 2x + y = 3\end{aligned}\tag{B.4}$$

The solution of the first two equations is (0, 1), the last two equations is (4/3, 1/3) and the first and the last equations is (2, -1).

Suppose that the desired solution is (1, 0). The desired RHS would be

$$\begin{aligned}\text{Desired RHS of Test Eq. 1: } & 1 \\ \text{Desired RHS of Test Eq. 2: } & 1 \\ \text{Desired RHS of Test Eq. 3: } & 2\end{aligned}\tag{B.5}$$

which means that the percentage change in the test equations should be

$$\begin{aligned}\text{Per. Cha. in RHS of Eq. 1: } &= \frac{1-1}{1} \times 100\% \\ &= 0\% \\ \text{Per. Cha. in RHS of Eq. 2: } &= \frac{1-2}{2} \times 100\% \\ &= -50\% \\ \text{Per. Cha. in RHS of Eq. 3: } &= \frac{2-3}{3} \times 100\% \\ &= -33.33\%\end{aligned}\tag{B.6}$$

These percentage changes lead us to the desired convergence point. Obviously, these percentage changes are pretty big as these equations were chosen at random. However, for the actual extraction method in Chapter 3, the equations are realistic and it takes only a small percentage to get to a convergence point such that all the solutions coincide.

This appendix shows that solutions can be made to converge anywhere by adjusting the RHS of equations by an appropriate percentage. If we think the other way around, while adjusting the percentages by trial and error in the actual equations, we might stumble upon two or more percentages leading to two or more solutions.

That's why it is important to lower the systematic uncertainties and apply stronger constraints on the data, so that the number of possible solutions is reduced and a rational solution with only a small range of variation can be obtained.

The thesis study used a version of the MINERvA analysis that had access only to a few systematic uncertainties. We made the decision to not further pursue how strong the MINERvA systematic constraints actually are in this context, and focused on demonstrating other aspects of the method. The few percent shifts used in the example in the main chapter are typical of the size of systematic effects on the event rate encountered by MINERvA.

## Appendix C

# Derivation of the relation between $Q^2$ , $E_\nu$ , $E_\mu$ , $p_\mu$ and $\theta_\mu$

Let  $k_\nu$  and  $k_\mu$  represent the four-momentum (contravariant) vectors of muon neutrino and muon respectively. They are defined as

$$k_\nu \equiv \begin{pmatrix} E_\nu/c \\ \vec{p}_\nu \end{pmatrix}, \quad k_\mu \equiv \begin{pmatrix} E_\mu/c \\ \vec{p}_\mu \end{pmatrix}, \quad (\text{C.1})$$

where,  $c$  is the speed of light in vacuum.

The four-momentum transfer  $q$  is given by

$$\begin{aligned} q &= k_\nu - k_\mu \\ &= \begin{pmatrix} (E_\nu - E_\mu)/c \\ \vec{p}_\nu - \vec{p}_\mu \end{pmatrix} \end{aligned} \quad (\text{C.2})$$

The magnitude of four-momentum transfer  $q^2 (= -Q^2)$  can be used to obtain  $Q^2$ ,

$$\begin{aligned} Q^2 &= (\vec{p}_\nu - \vec{p}_\mu)^2 - \left( \frac{E_\nu - E_\mu}{c} \right)^2 \\ &= \frac{2E_\nu E_\mu}{c^2} - 2\vec{p}_\nu \cdot \vec{p}_\mu - \left( \frac{E_\nu^2 - p_\nu^2 c^2}{c^2} \right) - \left( \frac{E_\mu^2 - p_\mu^2 c^2}{c^2} \right), \end{aligned} \quad (\text{C.3})$$

where, (+,-,-,-) sign convention is used to obtain the magnitude.

Since the angle between the direction of muon and neutrino is  $\theta_\mu$ ,  $\vec{p}_\nu \cdot \vec{p}_\mu = p_\nu p_\mu \cos\theta_\mu$ . Using the Einstein's mass-energy relation [68],

$$Q^2 = \frac{2E_\nu E_\mu}{c^2} - 2p_\nu p_\mu \cos\theta_\mu - (m_\nu c)^2 - (m_\mu c)^2. \quad (\text{C.4})$$

Eq.(C.4) is the EXACT relation.

The first approximation, which is a very good approximation, is that the neutrino mass is negligible compared to the energies involved, i.e.  $m_\nu \ll m_\mu$  and  $E_\nu \approx p_\nu c$ . Thus,

$$Q^2 = 2\frac{E_\nu}{c} \left( \frac{E_\mu}{c} - p_\mu \cos\theta_\mu \right) - (m_\mu c)^2. \quad (\text{C.5})$$

In natural units, i.e.  $c = 1$ ,

$$Q^2 = 2E_\nu (E_\mu - p_\mu \cos\theta_\mu) - m_\mu^2. \quad (\text{C.6})$$

For the case of charged-current electron neutrino-nucleus scattering in which an electron is produced, another approximation can be made. Electron's mass is generally negligible compared to the energies involved, i.e.  $E_\nu \gg m_e$  and  $E_e \approx p_e$ . Thus,

$$\begin{aligned} Q^2 &= 2E_\nu E_e (1 - \cos\theta_e) \\ &= 4E_\nu E_e \sin^2(\theta_e/2) \end{aligned} \quad (\text{C.7})$$

This approximation may also be valid for high energy DIS scattering with large enough scattering angle  $\theta_\mu$  or equivalently  $Q^2 \gg m_\mu^2$  when a muon is involved.

Prof. Gran notes that MINERvA and others often make the mistake of using this approximation for general charged-current muon neutrino interactions because it often appears this way in the DIS literature, but is a poor approximation in the lowest  $Q^2$  or lowest angle bins of neutrino data.

## Appendix D

# Parametrization of Rob Fine's low- $\nu$ flux

First, the flux ratio was estimated just by eyeballing corresponding to neutrino energy of 2.5 GeV, 3.5 GeV, 4.5 GeV, 5.5 GeV, 6.5 GeV, 7.5 GeV, 8.5 GeV, 9.5 GeV and 11.0 GeV from the Fig. 5.1. The corresponding estimated values are 1.10, 1.08, 1.09, 1.05, 1.01, 1.00, 1.03, 1.09 and 1.14.

The function `numpy.polyfit()` from Python 3.10.6 was used to fit a six-degree polynomial through these points. The value of the polynomial at  $E_\nu = 2.5$  GeV was used for all values of flux ratio below 2.5 GeV, and the value of the polynomial at  $E_\nu = 11$  GeV was used for all values of flux ratio above 11 GeV. The latter respects that the uncertainties in the data are both large enough that we are not sensitive to more detail and that the flux is predicted to be a smooth, featureless exponential beyond this energy.

The final flux parametrization (for  $2.5 \text{ GeV} \leq E_\nu \leq 11 \text{ GeV}$ ) is as follows :

$$\begin{aligned} \text{flux ratio} = & (4.64E - 5)E_\nu^6 - (2.03E - 3)E_\nu^5 + (3.52E - 2)E_\nu^4 - (3.05E - 1)E_\nu^3 \\ & + 1.39 * E_\nu^2 - 3.15 * E_\nu + 3.87, \quad (\text{D.1}) \end{aligned}$$

where the expression  $aE - b$  represents  $a * 10^{-b}$ .

We used this parametrization but even a four-degree polynomial would have sufficed considering the statistical uncertainties.

The constant flux ratio that was used for  $E_\nu < 2.5$  GeV was 1.10 and that for  $E_\nu > 11$  GeV was 1.14, as these were the values of the polynomial at respective neutrino energies.

## Appendix E

# Energy dependence discrepancy corresponding to muon angle cut 6 to 8 degrees reduced by reweighting $\pi^+$

We saw in Chapter 7 that reweighting pions reduces the energy dependence discrepancy. Reweighting High KE  $\pi^+$  (KE > 150 MeV) reduces the discrepancy by a large amount in High  $q_3$  range and reweighting Low KE  $\pi^+$  (KE < 100 MeV) also reduces the discrepancy even further.

For the Mid  $q_3$  range, reweighting High KE  $\pi^+$  does not have a big effect. On the contrary, reweighting Low KE  $\pi^+$  has a big effect in the top pad of the figure and reduces the discrepancy by only a small amount.

We didn't try reweighting pions for discrepancies in Low  $q_3$  range since this range has almost no pions. QE scattering dominates here and it produces protons instead of pions.

The following figures show the plots for LowEnu and MidEnu in High  $q_3$  and Mid  $q_3$  range when a muon angle cut of 6 to 8 degrees is applied. It compares the default

plot with no pion reweight with the plots having a High KE  $\pi^+$  events reweighted and the plots with both Low and High KE  $\pi^+$  reweighted.

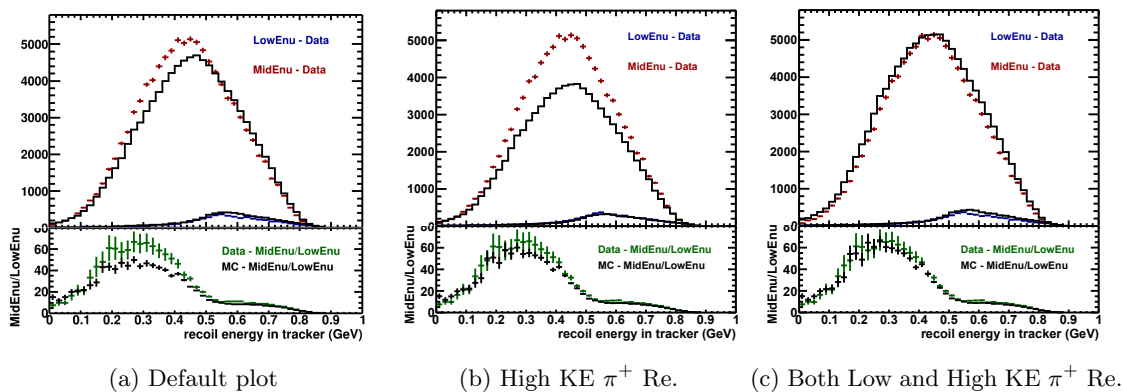


Figure E.1: Plots of LowEnu and MidEnu in High  $q_3$  range with muon angle cut of 6 to 8 degrees comparing the reweight of only High KE  $\pi^+$  and both Low and High KE  $\pi^+$  with the plot having default pion weight

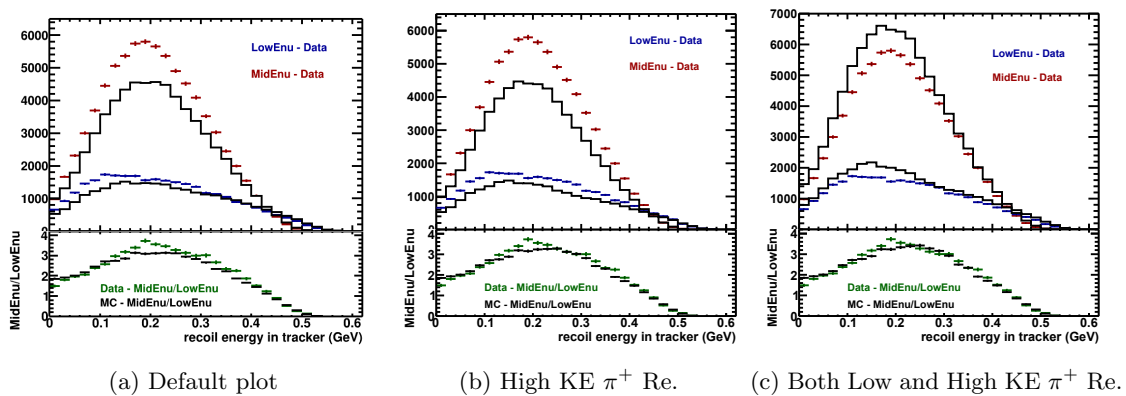


Figure E.2: Plots of LowEnu and MidEnu in Mid  $q_3$  range with muon angle cut of 6 to 8 degrees comparing the reweight of only High KE  $\pi^+$  and both Low and High KE  $\pi^+$  with the plot having default pion weight

As expected from Chapter 7, Fig. E.1 shows that the discrepancy in High  $q_3$  range almost removes when either High KE  $\pi^+$  or both Low and High KE  $\pi^+$  are reweighted.

Reweighting both Low and High KE  $\pi^+$  is better though.

Fig. E.2 shows that reweighting High KE  $\pi^+$  does not have a big effect on the discrepancy in Mid  $q_3$  range. Applying both Low and High KE  $\pi^+$  reweight is almost equivalent to reweighting Low KE  $\pi^+$  only. This reweight reduces the discrepancy by a small amount.

This thesis focused on angle cuts of 0 to 2 deg., 2 to 4 deg., 4 to 6 deg. and 6 to 8 deg. It is easy to extend the analysis to higher angle cuts such as 8 to 10 deg. and 10 to 12 deg, up to 20 deg. However, I have shown in this thesis that resolving discrepancies in smaller angle cuts helps in resolving discrepancies in higher angle cuts also. Angle cuts only move events around. The discrepancy is ultimately coming from the cross-section model.